THREE-DIMENSIONAL MULTIFUNCTIONAL WOVEN COMPOSITES CONTAINING THROUGH-THICKNESS METAL FILAMENTS

A thesis submitted in fulfilment of the requirements for the degree of

Doctor of Philosophy

Sadaf Abbasi

Master of Engineering (M.E) – Mehran UET

School of Engineering

College of Science, Engineering and Health

RMIT University

July 2020

Declaration

I certify that except where due acknowledgement has been made, the work is that of the author alone; the work has not been submitted previously, in whole or in part, to qualify for any other academic award; the content of this thesis is the result of work which has been carried out since the official commencement date of the approved research program; any editorial work, paid or unpaid, carried out by a third party is acknowledged; and ethics procedures and guidelines have been followed. I acknowledge the support I have received for my research through the provision of an Australian Government Research Training Program Scholarship.

Sadaf Abbasi

20 July 2020

Acknowledgements

I would like to sincerely thank my senior supervisor, Distinguished Professor Adrian P. Mouritz for his continuous guidance, dedication, and support throughout this PhD project. I have been extremely lucky to have a supervisor who cared so much about my work, and who responded to my questions and queries so promptly. Thank you for your encouragement and support. I would like to acknowledge the support and mentorship provided by my co-supervisors, Dr. Raj B. Ladani and A/Prof. Lijing Wang (School of Fashion & Textiles).

I would also like to sincerely thank Peter Thatchyk, Julian Bradler, Huw James, Greg Oswald, Patrick Wilkins, Robert Ryan, and Paul Muscat of the RMIT University workshop and laboratory team for all their assistance in my experimental work. Thank you to many of my colleagues and friends at RMIT, including Dr. Anil Ravindran, Dr. Tom Loh, Dr. Alex Gargano, Mr Mukesh Bhasin and Ms Pooneh Attar for their support and encouragement.

I would also like to acknowledge the financial support provided by the RMIT University and Mehran University of Engineering & Technology Jamshoro for giving me study leave to pursue PhD studies.

More importantly, I would like to thank my family, mother (Shamim Abbasi), father (Aftab Ahmed Abbasi), brother (Adeel Ahmed Abbasi) and sisters (Ghazala and Mehwish) for the amazing support, patience and care I have had over my entire academic career. I would like to thank my friend Carol Harrison from United Kingdom for her support and advises. I would like to say special thanks to my best friend (Dr. Mazhar Peerzada) without his encouragement and support my achievements would not have been possible.

Summary

Carbon fibre reinforced composites are used in aircraft, marine craft, automobiles, civil infrastructure and other applications due to their outstanding physical and mechanical properties. However, composites have relatively poor impact resistance and low through-thickness mechanical properties which can limit their uses in structures subjected to out-of-plane loading. Composites are susceptible to delamination cracking which can compromise the integrity and safety of composite structures. Another problem with many composite materials is that their electrical conductivity is low, particularly in the through-thickness direction, because of the dielectric nature of the matrix material and the high resistivity of the fibre-matrix interfaces.

The aim of this PhD project is to design, fabricate and experimentally characterise a novel class of three-dimensionally (3D) woven composite materials with multifunctional properties. The composites contain thin metal z-binders woven into carbon fabric stacks in an orthogonal (through-thickness) pattern. The metals used as the z-binder filaments are copper and stainless steel. For comparison, these materials are compared against 3D woven composite containing z-binders made of carbon tows, which is often used as the through-thickness reinforcement. The 3D woven composites with metal or carbon z-binders are compared against a 2D woven laminate (without z-binders).

The effects of volume content and material properties of the z-binders on a range of functional properties of 3D woven composites is experimentally investigated, including the modes I and II interlaminar fracture toughness and fatigue strength, the low energy impact damage tolerance, and the in-plane mechanical properties. In addition, the effect of z-binders on the through-thickness and in-plane electrical conductivities of 3D woven composites is determined. The use of the woven z-binders for the *in-situ* detection of delamination cracking in 3D composites is also explored. Further, the structural properties of T-joints made of 3D woven composites are experimentally investigated.

An extensive literature review is presented in this PhD thesis into 3D woven composites, including published research into the weaving process, fabric architecture, delamination resistance, impact tolerance, mechanical properties and other functional

properties. Research gaps in the understanding and development of next-generation 3D woven composites is identified based on the literature review.

An experimental research study into the improvements to the modes I and II interlaminar fracture toughness properties of 3D woven composites reinforced with metal or carbon z-binders is conducted. The effect of z-binder material on the interlaminar toughness properties and delamination toughening mechanisms is investigated using copper, steel and carbon z-binders. The steel z-binder gives an outstanding improvement to mode I fracture toughness, followed by the carbon and then copper z-binders. In fact, the 3D woven composite with the steel z-binder has the highest mode I interlaminar toughness value (~30 kJ/m^2) ever measured for a composite material. The z-binders are also effective at increasing the mode II interlaminar fracture toughness properties, but the strengthening effect is less than for mode I. The interlaminar toughness properties were improved by the z-binders forming of large-scale bridging zone along the delamination crack, and the effect of the z-binder material on the bridging process is investigated.

A further research study investigated the modes I and II interlaminar fatigue resistance of 3D woven composites. The fatigue strength increases rapidly with the z-binder content and is dependent on the z-binder material. This improvement is due to the z-binders generating bridging traction loads which resist fatigue crack growth, and the fatigue strengthening mechanisms are determined.

The PhD project investigates the low-velocity impact damage resistance and post-impact compressive properties of 3D woven composites. Two incident impact energies (25 and 50 J) are used to assess the impact damage tolerance of the 3D woven composites. Copper, steel and carbon z-binders are all effective at increasing the impact damage resistance. Also, the compression-after-impact strength of the 3D woven composites is higher (by ~20 - 25 %) when compared to the 2D composite without z-binder reinforcement.

An experimental study into the through-thickness and in-plane electrical conductivities of 3D woven composites is performed. The copper z-binder increases the through-thickness conductivity by about 5700x, whereas the stainless steel and carbon increase the conductivity by ~150x and ~12x respectively. The z-binders also increase the in-plane electrical conductivities, but to a lesser amount than the through-thickness

conductivity. Due to the increased electrical conductivity, it is demonstrated that the z-binders can be used for the *in-situ* detection and monitoring of mode I delamination crack growth within 3D woven composite materials. The z-binders can monitor delamination cracking via changes to the electrical resistivity of the composite material.

An experimental study is conducted into the structural properties of T-shaped composite joints reinforced with copper, steel or carbon z-binders. The z-binders are highly effective at increasing the stiffness and ultimate failure load of the joints. The effect of z-binders on the strengthening and fracture mechanisms of T-joints subjected to high external loading is investigated.

The final research study investigates the in-plane mechanical properties of the 3D woven composites. The flexural, compressive and tensile strengths of the composites decrease with increasing z-binder content due fibre breaks, fibre waviness and ply crimping caused by the weaving process. The reduction to the mechanical properties also depends on the z-binder material, with the steel z-binder reducing the properties more than the carbon and copper z-binders.

This PhD project demonstrates that 3D woven composites with multifunctional properties have superior mode I/II interlaminar fracture toughness, mode I/II interlaminar fatigue resistance, impact damage tolerance, electrical conductivity, *in-situ* delamination monitoring, and structural properties of T-joints.

Publications

- S. Abbasi, R.B. Ladani, C.H. Wang, A.P. Mouritz, Improving the delamination resistance of fibre reinforced polymer composites using 3D woven metal Z-Filaments, *Composites Science and Technology*. 2020; In Press.

- S. Abbasi, R.B. Ladani, C.H. Wang, A.P. Mouritz, mode I fracture toughness of 3D reinforced composite woven with metal and carbon z-binders, *Proceedings of the 22nd International Conference on Composite Materials (ICCM22)*. July 2019.

- S. Abbasi, R.B. Ladani, C.H. Wang, A.P. Mouritz, Boosting the electrical conductivity of polymer matrix composites using low resistivity z-filaments, *Materials and Design*. *(Submitted)*.

- S. Abbasi, R.B. Ladani, C.H. Wang, A.P. Mouritz, Improving the structural properties of composite T-joints using 3D woven metal filaments, *Composite Structures*. *(Submitted)*.

Table of Contents

List of Figures

List of Tables

Chapter 1: Introduction and Background

1.1 Project Background

Carbon fibre reinforced polymer matrix composite materials have been used in aircraft for many years because they offer several beneficial properties, including high specific strength and stiffness, fatigue resistance, and corrosion resistance. However, composites have relatively low out-of-plane (through-thickness) mechanical properties. When subjected to high interlaminar or out-of-plane stresses composites exhibit low resistance to damage and low through-the-thickness mechanical properties. Delamination cracking is a long-standing problem for aircraft composite structures. Delamination damage can be caused by factors such as through-the-thickness static and fatigue loads, edge stresses, environmental degradation, and impact by hail, stone, bird strike etc. Delamination cracks can grow under mode I and/or mode II interlaminar static and fatigue loads, and thereby deteriorate the properties of composite structures. Delamination damage can be particularly challenging to visually detect as it is buried beneath the surface. Delamination damage in composites can lead to serious safety issues, such as reduction of structural properties, which can cause final failure of the composite part as shown for example in Figs. 1.1 and 1.2.

Many incidents have reported of damage to aircraft because of bird strike and impact due to large hail stones or dropped tools. For example, a Boeing 737-700 crashed following the collision with a drone while coming into land at Mozambique airport. The aircraft had 80 passengers, but it was fortunate that the plane landed safely with no injuries. Between 2008 and 2017, there were 16,626 confirmed bird strikes reported to the Australian Transport Safety Bureau (ATSB) [1]. The number of reported bird strikes has increased in recent years, with 2017 having the highest on record with 1,921. Therefore, to ensure continuing safety of the airframe, the Federal Aviation Administration's damage tolerant design regulations [2-4] specify that delamination damage within aircraft composite structures beyond a critical size must be immediately repaired or the entire damaged structure must be replaced. However, the critical damage size depends on many parameters including the loading and geometry of the composite structure and on the location of the damage. Traditional methods used to

repair composite structures are very expensive and require significant time, cost, and for the aircraft to be taken out-of-service.

Fig. 1.1: *Impact damage to the composite nose dome to a Boeing 737-700 aircraft [5].*

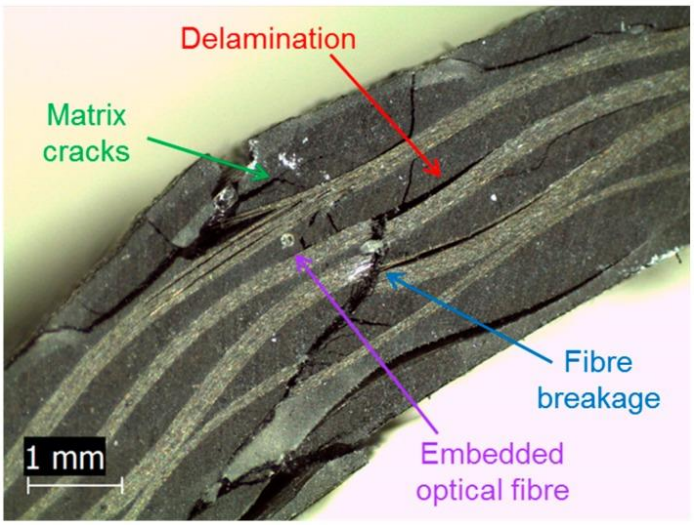

Fig. 1.2: *Cross-section image of delamination cracking in carbon-epoxy composite [6].*

In addition to the problem of delamination damage, composites have low through-thickness electrical conductivity because of the dielectric nature of the polymer matrix and the high resistivity of the fibre-matrix interfaces. This poses challenges in protecting composite aircraft structures against lightning strikes and electromagnetic interference. Lightning strike protection techniques include embedded metal wire mesh, diverter strips, metal picture frames, bonded aluminium foil, and metal foil liners which act as a sacrificial layer designed to ablate during a lightning strike. Although these techniques provide lightning protection, they can partially offset the weight saving benefits of using composite materials.

Modern aircraft structures require multifunctional materials which can provide better structural and damage tolerant properties along with high electrical conductivity [7]. Many research studies have focused on improving the delamination toughness and low energy impact damage resistance using different techniques e.g. 3D fibre architectures (woven, tufted and stitched preforms), nanotubes, short carbon fibres, graphene, and z-pinning [8-13]. These techniques result in high interlaminar fracture toughness and impact damage resistance, and some techniques are also effective at increasing the electrical conductivity. However, to-date very few studies have developed multifunctional composites that exhibit high interlaminar fracture toughness and high through-the-thickness electrical conductivity. Thus, this research will focus on developing multifunctional composite materials with high static and fatigue damage resistance, impact resistance, damage tolerance and electrical properties.

1.2 Aims and Scope of PhD Project

The overarching objective of this PhD project is to design and create a new class of three-dimensional (3D) woven composite material with high damage tolerance under static and fatigue interlaminar loads with high electrical properties and also resistance to impact loads. These properties will be controllably tailored by weaving metal or carbon z-binders in an orthogonal pattern into stacks of 2D woven fabric used in polymer matrix composite materials. Three-dimensional weaving is a versatile manufacturing process for producing technical textiles with in-plane fibres (warp and weft) and through-thickness fibres (called z-fibres or z-binders). 3D woven fabrics offer significant improvements to the lay-up time, ease of handling, delamination toughness and impact damage resistance. However, existing 3D woven fabrics have two deficiencies that limit their applications. Firstly, they are a single-function material designed to have only one superior functional property (usually delamination toughness) [14]. Secondly, in-plane fibre waviness and crimping remain a limiting factor for the mechanical properties of 3D woven composites [15].

This PhD project incorporates metal z-binders into carbon-epoxy composite to improve delamination toughness, delamination fatigue resistance, high electrical properties, excellent impact damage tolerance whilst retaining high in-plane mechanical properties and improve the structural properties of 3D woven composite T-joints. The key innovation of this project

is the creation of novel 3D woven fabrics for composites having (i) high delamination and damage tolerance properties and (ii) multifunctional properties tailored for high-performance components in aircraft, wind turbine blades and other light-weight systems.

This project includes an experimental investigation into the increased interlaminar fracture toughness under static and fatigue loading obtained using metal z-binders. This project also experimentally evaluates different types of metal z-binders on the through-the-thickness and in-plane electrical properties of 3D woven composites. It is shown that metal z-binders give outstanding improvements to the electrical conductivity and damage detection properties. Along with improvements in fracture toughness and electrical properties, metal z-binders also improve the impact damage resistance of composites and the structural properties of composite T-joints. The concept that the mechanical, interlaminar toughness, impact resistance, and electrical properties can be controlled using z-binders depends on wide-range and in-depth research and development of these composite materials. The work presented in this PhD thesis outlines progress on this concept.

1.3 Thesis Outline

The next chapter presents an extensive review of published research into 3D woven composite materials. The literature review examines the effect of the z-binder on the interlaminar fracture toughness, impact resistance, damage tolerance and in-plane mechanical properties of 3D woven composites. Based on the literature findings, the key research gaps in 3D woven composites are identified.

Chapter 3 presents an experimental investigation into the mode I and mode II interlaminar fracture toughness properties and delamination toughening mechanisms of multifunctional 3D woven composites. Composite materials were fabricated using stacked plies of woven carbon fabric, which were woven with metal or carbon z-binders in an orthogonal (through-thickness) pattern. The fabrics were infused with epoxy resin using the vacuum bag resin infusion technique. The effects of z-binder material (copper, steel or carbon) and z-binder volume content on the mode I and II fracture toughness properties are described. Chapter 4 presents an investigation into the fatigue resistance of the same 3D woven composites when subjected to mode I and mode II interlaminar cyclic loading. The effects of z-binder material and volume content on the critical and threshold strain energy release rate to initiate delamination crack growth values as well as Paris curves were determined. Fractographic

analysis was performed into the interlaminar fatigue strengthening mechanism due to the z-binders.

Chapter 5 presents an analytical and experimental investigation into the electrical properties of 3D woven composites. Metal z-binders improve the current flow in the through-the-thickness direction, which is responsible for a large increase to the electrical conductivity of 3D composites. Chapter 6 presents the experimental study into the *in-situ* delamination damage detection in 3D woven composites using the z-binders. Metal and carbon z-binders were used for the real-time detection of delamination cracks in 3D woven composites via measurable changes to the electrical resistivity.

The effect of z-binder material and volume content on the impact damage resistance and post-impact compression properties of the 3D woven composites is examined in Chapter 7. The materials were impacted at low and high energy levels, and then the compression-after-impact (CAI) properties were measured.

An investigation is presented in Chapter 8 into the effect of z-binders on the structural properties T-joints made of 3D woven composite material. Metal or carbon z-binders were woven into the skin-flange region of the T-joints, and then the structural properties were determined under the stiffener pull-off load condition. The stiffness, load-at-first failure, ultimate load and extension-to-failure properties of the different T-joints were measured.

Chapter 9 presents an experimental investigation into the in-plane mechanical properties (tension, compression, flexure) of the 3D woven composites.

The final chapter summarises the main conclusions of this PhD project, and also briefly describes several future research topics to further develop multifunctional 3D woven composite materials.

Chapter 2: Literature Review

Abstract

This chapter presents a comprehensive literature review on 3D woven fabrics and their use in polymer matrix composite materials. The 3D weaving process and the types of 3D woven fabrics are described. Published research into the interlaminar fracture toughness properties, impact damage resistance, mechanical properties and other properties of 3D woven composites is reviewed. This includes a review into the effects of fabric architecture as well as the material type and volume content of z-binders on the properties of 3D woven composites. A research gap analysis, based on the published research, reveals there is a limited understanding on several key topics of 3D woven composites, and some of these are investigated further in this PhD research project. This includes improvements to the interlaminar fracture toughness, interlaminar fatigue strength, impact damage resistance and tolerance, electrical properties and joint strength of 3D woven composites reinforced with metal z-binders.

2.1 3D weaving process

Weaving is the process of producing single ply fabric by interlacing two sets of yarns (warp and weft) which are aligned at 90° to each other (called 2D fabric), and are the most commonly used textile fabric for composite reinforcement. 2D woven fabric is used extensively in the aerospace, automotive, marine and other industries. However, a long-standing problem with 2D woven laminates is their relatively low resistance to cracking and failure when loaded in the through-thickness direction. The absence of through-thickness fibres combined with the low strength and toughness of the polymer matrix phase and fibre-matrix interfaces results in 2D woven laminates being susceptible to delamination damage.

To overcome this problem, there is increasing interest in the 3D weaving of multilayer, net-shaped fabric containing through-thickness reinforcing fibres for use in composite materials. 3D woven composites have superior ballistic impact damage resistance [16] and higher impact damage tolerance [17-21] compared to 2D woven laminates. 3D weaving is the

modified version of single-layer (or 2D) weaving process. 3D weaving is the process in which an integrated multi-layer fabric consisting of multiple ply layers of warp and weft yarns in the in-plane directions and z-binder yarns (z-yarn) woven in the through-thickness direction. The basic principle of the 3D weaving process is presented in Fig. 2.1. The important parameter of the 3D weaving process is the dual-directional shedding operation. Through this operation the multiple layer warp can be displaced to form alternately multiple column-wise and row-wise sheds. Subsequent picking of wefts in the corresponding sheds of the two directions results in the complete interlacing of the multiple layer warp (Z) with the two mutually perpendicular sets of wefts (X and Y). 3D woven fabrics are often produced by using highly automated, computer-controlled looms for fast production and high-quality products [22]. 3D woven fabrics can be manufactured using Jacquard and rapier weaving looms as shown in Fig. 2.2**.** Jacquard controlled looms are the most popular for manufacturing 3D woven fabric due to the individual lifting mechanism of warp yarn. There are two main types of 3D woven fabrics used in composite materials: orthogonal and layer interlock [23-26].

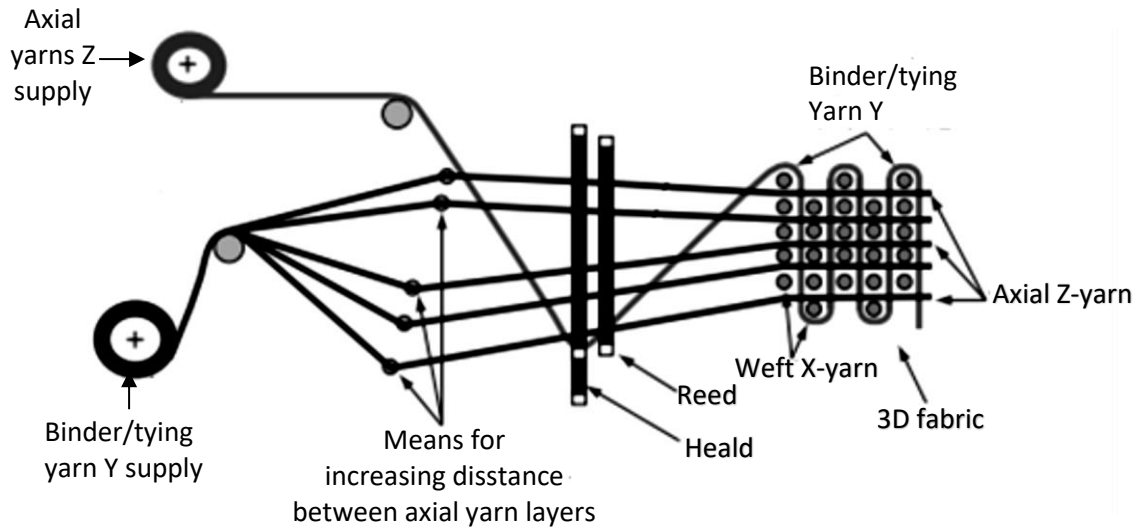

Fig. 2.1: *Principle of 3D weaving process [22].*

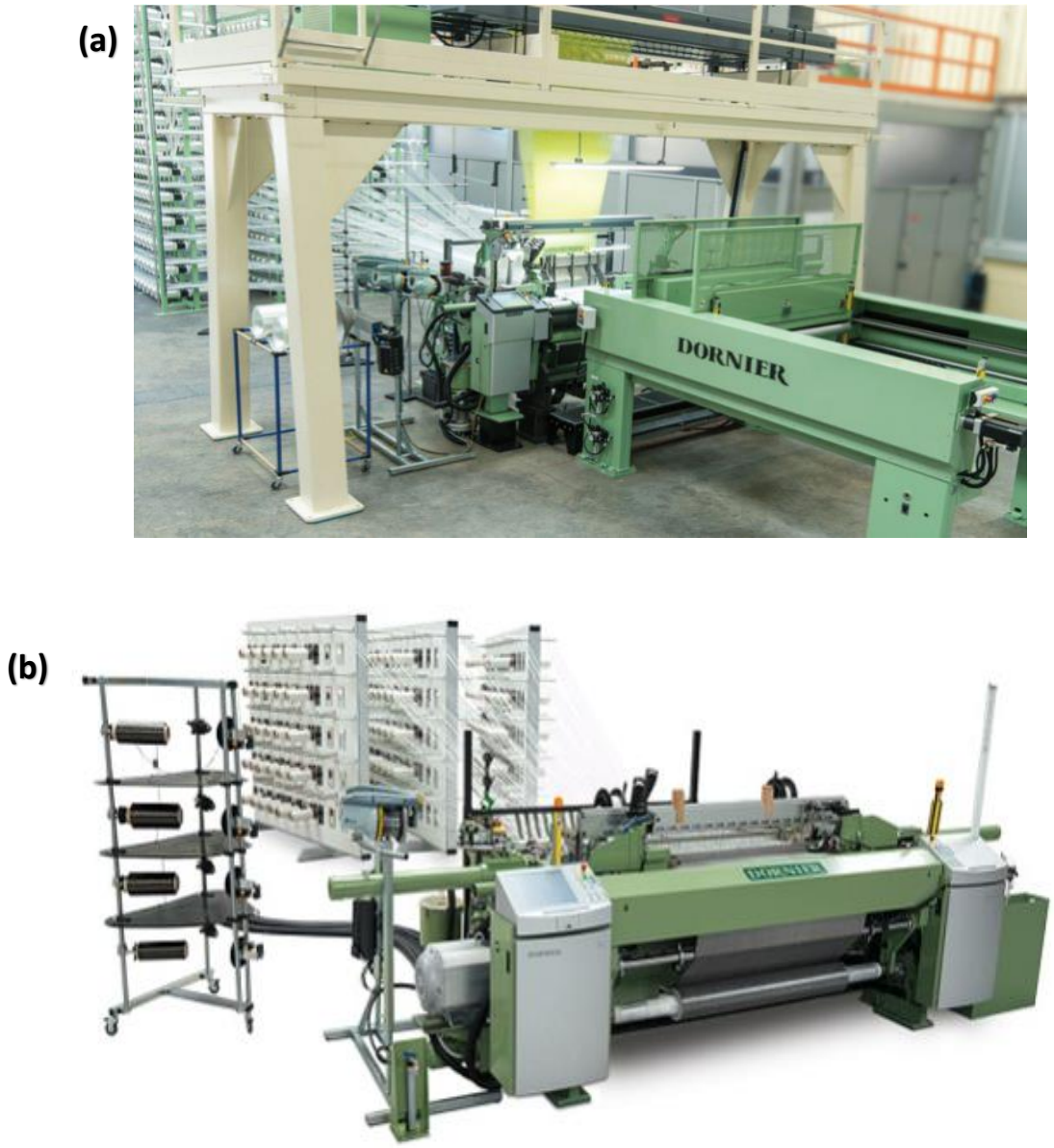

Fig. 2.2: *3D weaving looms for 3D woven fabric manufacturing based on (a) Jacquard and (b) rapier principles [22].*

2.1.1 Orthogonal woven fabrics

The orthogonal weave architecture consists of warp and weft yarns stacked in multiple layers without interlacing, and the entire fabric is bound by z-binder yarns woven in an orthogonal pattern as illustrated in Fig. 2.3(a). The non-interlaced pattern minimises crimp of the warp and weft yarns, and this leads to retention of the in-plane stiffness and strength properties when used in a composite material [27]. There are two main types of orthogonal fabrics: (i) fabrics with one through-thickness z-binder yarn are termed as 'ordinary

orthogonal fabrics', and (ii) fabrics with two z-binders woven in opposing directions, and are known as 'enhanced orthogonal fabric' as shown in Fig. 2.3(b). The enhanced orthogonal fabrics usually have a higher areal density of z-binder yarns compared with ordinary orthogonal fabrics.

2.1.2 Layer interlock woven fabrics

The basic manufacturing of 3D interlock fabrics is based on the 2D weaving technique [28]. The main difference between the 3D interlock fabric manufacturing with 2D fabrics are the distribution of weft yarns inside the shed to obtain a 3D fabric comparatively thicker than 2D fabrics, and in the selection of warp yarns, divided into three types: the weaver warp yarns, the surface warp yarns, and the stuffer warp yarns [29]. Layer interlock fabrics are woven using a set of straight weft yarns and a set of warp yarns that weave with the weft in a diagonal through- thickness direction as shown in Fig. 2.3(c). These fabrics are also known as layer-to-layer fabrics. The fabrics have four sets of yarns: filling, bias and stuffer yarns (warp). Bias yarns are oriented in the thickness direction and interlaced with several weft yarns. Bias yarns have a zig-zag type pattern in the thickness direction and change the course of the structure in the machine direction.

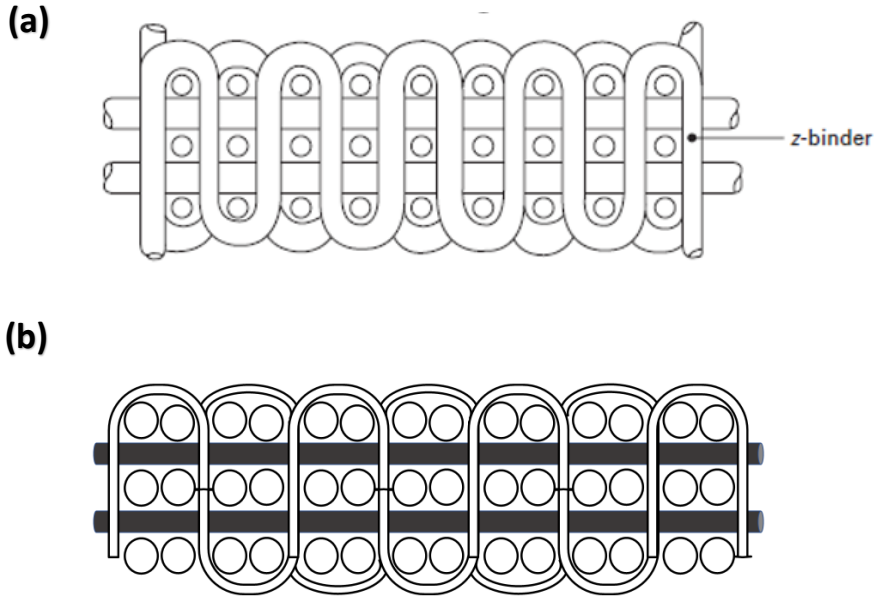

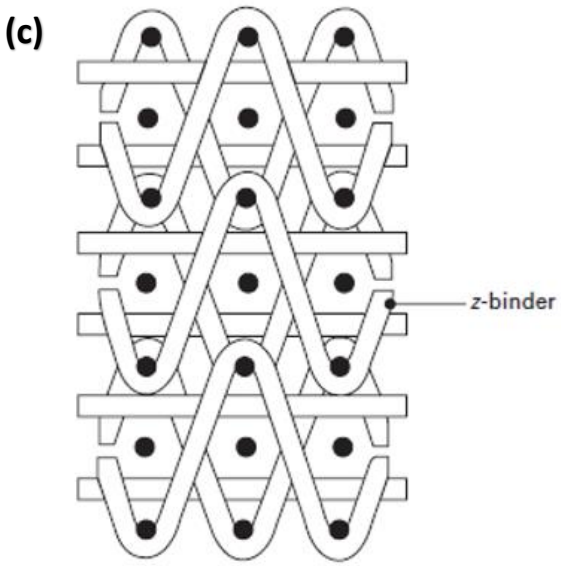

Fig. 2.3: *Types of 3D woven fabrics: (a) orthogonal (b) modified orthogonal and (c) layer interlock [30].*

2.1.3 Damage to tows and in-plane fibre during weaving process

Despite the advantages and potential applications of 3D woven composites, there is a major drawback that the in-plane mechanical properties may be reduced due to the weaving process or weave architecture. The tension, compression, flexural and other in-plane properties of 3D woven composites are up to 10-20% lower than 2D laminates with an equal proportion of load-bearing yarns [15, 31, 32]. The reduction to the in-plane mechanical properties is often due to the crimping, distortion and breakage of fibres during the insertion of z-binder in the weaving process.

During the weaving process, the abrasion, breakage and distortion of warp, weft and z-binder yarns is hard to avoid. For example, warp yarns crossover the series of weaving machine parts with considerable frictional contact which causes the abrasion and, in some instances, breakage of filaments. Lee et al. [33, 34] report that as the yarns slide through the guides and other parts of the weaving machine, the friction causes abrasion damage and breakage of fibres (Fig. 2.4). This damage reduces the tensile failure stress of yarns. Lee et al.

[34] further investigated the failure stress of E-glass yarns after different stages of 3D weaving process. They found that the yarn strength decreased about 30% after the tensioning, warping and take-up operations of weaving process.

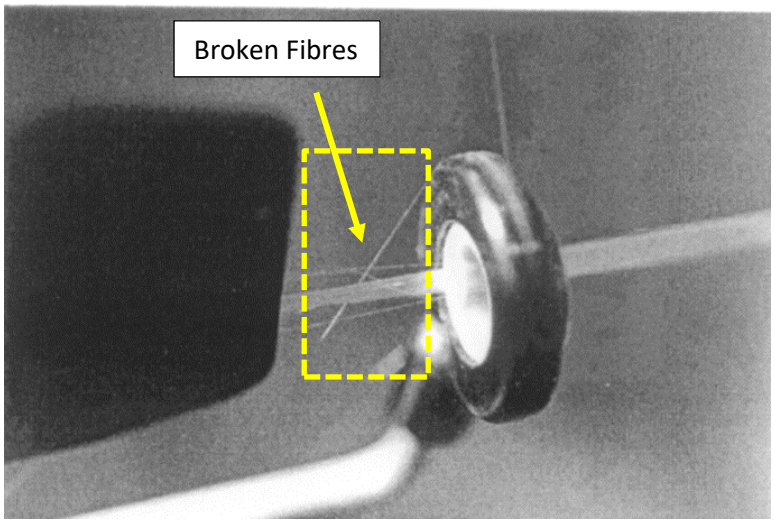

Fig. 2.4: *Broken fibres in a yarn at the guide to a weaving machine [35].*

Yarn distortions known as in-plane waviness and out-of-plane crimp can also occur during the 3D weaving process. Waviness can occur in fabrics where the yarns crossover and interlace each other, with the distortion angle typically in the range of 4-12° [36-38]. The highest misalignment reported is greater than 12°, particularly for yarns close to z-binder yarns in 3D woven fabric. During weaving process, when the carrier (for example, needle) insert a z-binder yarn it pushes the in-plane yarns aside which creates the waviness in yarns and resin-rich pockets (Fig. 2.5) at every z-binder location. The severity of waviness and size of resin-rich areas in 3D woven fabrics is dependent on the diameter of z-binder yarn and needle. This damage can be minimized by controlling the operation of z-binder yarns into warp and weft yarns; for example, by weaving non-crimp orthogonal woven fabric in which the z-binder yarns fit between the in-plane yarns and therefore do not cause excessive waviness.

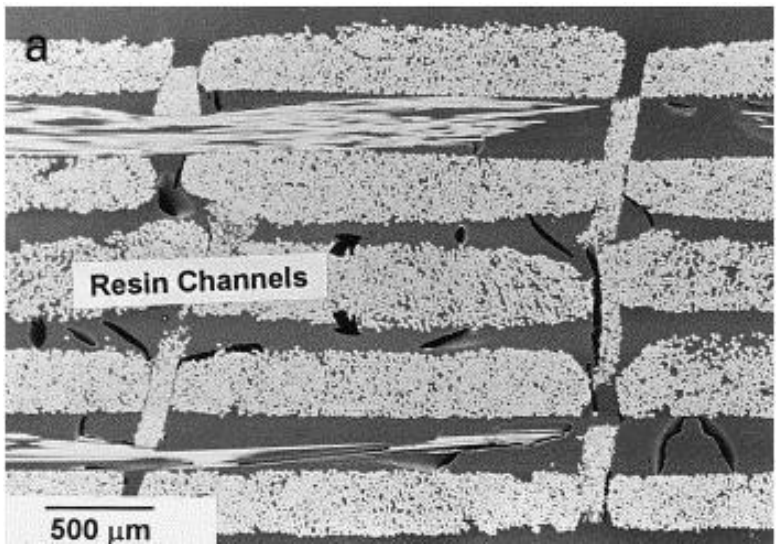

Fig. 2.5: *Resin-rich pockets in 3D woven fabric on z-binder location [37].*

Damaged or broken fibres within woven yarns are important causes for the reduction to the mechanical properties of 3D woven composites. The in-plane yarns are often damaged by the operation of insertion of z-binder yarn. During z-binder insertion, friction stresses are generated which lead to breakage of fibres. The stresses created in between in-plane yarns, z-binder yarns and its carrier are often created by friction, which are partly responsible for reductions to the tensile strength in 3D woven composites. Kamiya et al. [25] suggested that yarns are damaged by the shedding operation during weaving process. Rudov-Clark et al. [35] investigated the fibre damage during the 3D weaving process of orthogonally woven fibreglass fabric. They found that yarn breakage reduces the tensile failures stress of the yarns. They further explained that the sliding and abrasion of yarns against each other during the 3D weaving process lowers the tensile failure stress, although the Young's modulus is not reduced significantly. Lee et al. [33] conducted tension tests on woven carbon-epoxy composites to quantify the fibre damage during weaving process. They observed that the tensile properties of carbon fibre composites were reduced due to the large amount of fibre damage caused by the weaving process. Lee et al. [34] systematically studied the effect of weaving damage to E-glass yarn on the tensile properties of 3D woven composites. They have found progressive reduction to the tensile strength of the warp yarn. Weaving process caused overall 30% reduction in strength of the dry load-bearing yarn in 3D glass preforms.

2.2 3D woven composite: delamination resistance

Various methods have been developed to increase the delamination resistance of composites, such as rubber toughening of the polymer matrix phase, fibre adhesion treatment to increase the bonding to the matrix, nanoparticle toughening of the matrix, and carbon nanotube treatment of the fibres [39-42]. Another approach which is commonly used is the reinforcement of the composite in the through-thickness direction using fibrous yarns, rods or pins [9, 24, 43]. 3D reinforced composites have increased delamination toughness and impact resistant properties. 3D woven fabric preforms are effective for improving the delamination toughness and impact damage tolerance of composites used in aircraft structures such as wing panel joints, flanges and turbine rotors [24]. Large improvements to these properties are achieved with a relatively small volume fraction of z-binder yarns in 3D woven composites [46, 65].

2.2.1 Fracture resistance of 3D reinforced composite structures

Three techniques are used to experimentally measure the mode I (tensile crack opening), mode II (shear crack sliding) and mode III (tearing) interlaminar fracture toughness properties of laminated composite materials; namely the Double Cantilever Beam (DCB), End Notch Flexure (ENF) and Edge Cracked Torsion (ECT) tests, respectively. The three modes of fracture are illustrated in Fig. 2.6 [44, 45]. Many numerical and experimental studies have been published on the modes I and II loading interlaminar fracture toughness properties on composite materials with through-thickness fibre reinforcement [46-58] . The delamination properties of 3D woven composites under the mode III interlaminar loading condition have not been performed due to difficulties in performing reliable fracture toughness tests, for example, it is possible that small rotations of the specimen within the test fixture can cause compressive stresses to be transmitted across the crack surfaces of the specimen, thereby affecting the measured toughness.

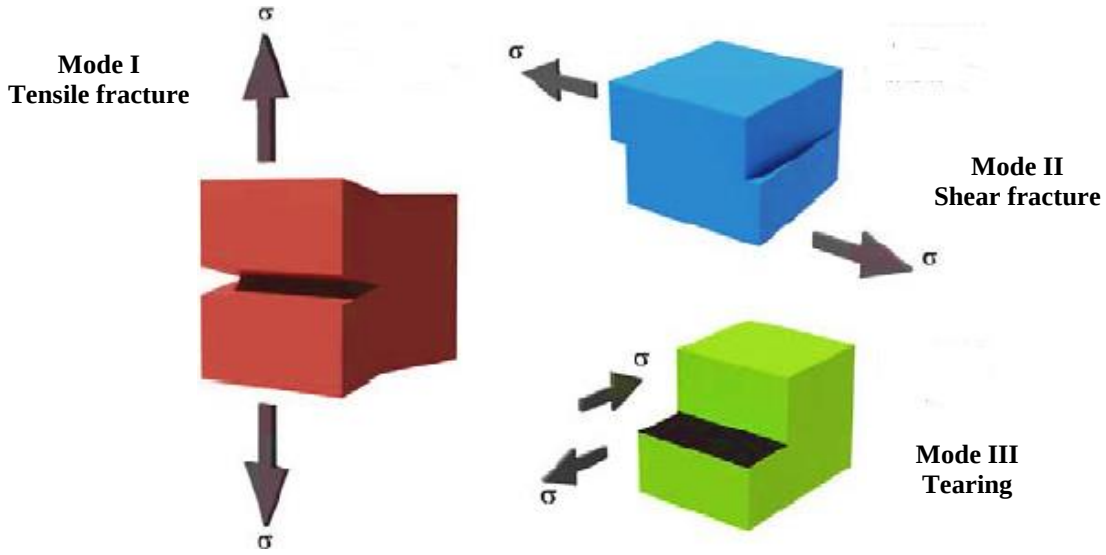

Fig. 2.6: *Fracture modes: mode I (tensile fracture), mode II (shear fracture), and mode III (tearing shear).*

3D woven composites have higher damage tolerance and interlaminar fracture toughness than 2D woven laminates. The delamination resistance of 3D woven composites is dependent on various parameters such as volume content, tensile strength, diameter, Young's modulus and interfacial shear strength of the woven z-binders as well as the thickness of the 3D woven composite material and the delamination crack length [30].

The mode I and mode II fracture toughness values of 3D composites increases with the delamination crack length up to the steady-state toughness value [53, 59-62]. The improvement in the interlaminar fracture toughness is largely due to the formation of a large-scale extrinsic bridging zone, including the number and type of z-binders bridging the delamination crack. The stiffness and strength of the z-binder are important properties for improving the delamination toughness, as is the embedded length of the z-binder which increases with the thickness of the composite material, and the interfacial shear failure stress between the z-binder and the composite. Continuous z-binders such as in 3D woven and stitched composites can provide larger improvements to the interlaminar fracture toughness than discrete z-binders such as z-pins. Continuous z-binders tend to be more resistant to failure by pull-out due to the high-end restraint imposed by the surface segment, thereby resulting in a higher interlaminar toughening effect. Mouritz et al. [46] measured the mode I interlaminar fracture toughness properties for lightly and heavily stitched fibreglass composites, and the G_{Ic} values were respectively 2.2 and 2.8 times higher than the 2D

composite. Arendts et al. [50] investigated the effect of increasing the z-binder content on the mode I fracture toughness properties, and at the highest content studied (8%) the mode I interlaminar fracture toughness properties of the 3D woven composite was 20 times higher than a 2D laminate. As another example, Pingkarawat et al. [63] investigated the effect of z-binder density on the mode I delamination toughness of a carbon-epoxy composite material reinforced with thermoplastic filament stitches. They found that the steady-state fracture toughness value increased rapidly with the stitch density, as shown in Fig. 2.7, and at highest stitch content (4 stitches/cm^2) the toughness was increased about 700%. It was concluded that the improvement to the delamination toughness increases with the stitch density due to a larger number of bridging stitches along the delamination crack.

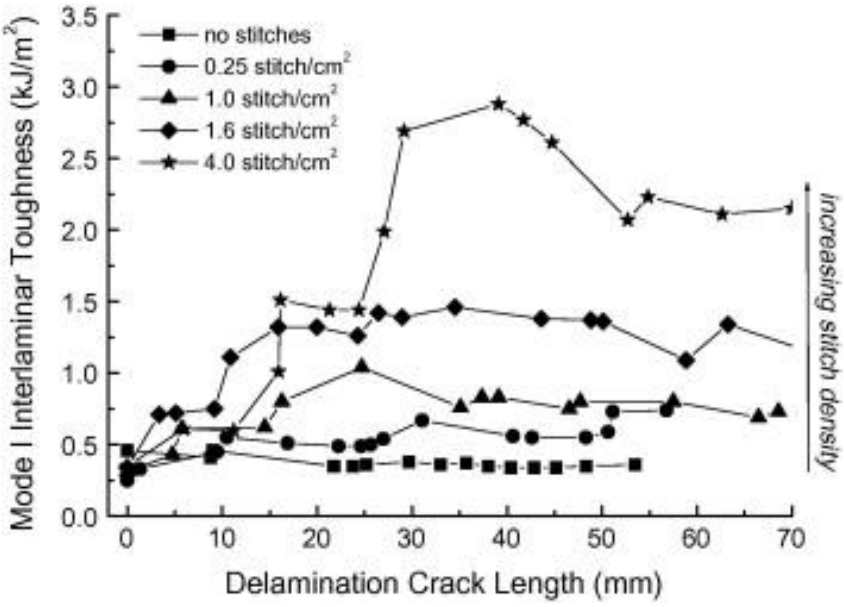

Fig. 2.7: *Mode I R-curve for carbon-epoxy composite reinforced with different densities of thermoplastic stitches [63].*

The amount of interlaminar toughening is also dependent on the geometry of the z-binders; with orthogonal z-binders aligned in the through-thickness direction providing high delamination toughness under mode I interlaminar loading whereas z-binders inclined at an angle of 45° against the direction of crack growth providing the highest mode II delamination toughness. Stegschuster et al. [64] studied the interlaminar fracture toughness properties of 3D woven carbon-epoxy composites containing different volume fractions of z-binders. The fracture toughness of 3D woven composites increased at a quasi-linear rate with increasing

the volume content of z-binders as shown in Fig. 2.8. It was also found in this study that the inclined z-binders were still effective in creating large bridging zone, which is the main reason for the enhanced interlaminar fracture toughness.

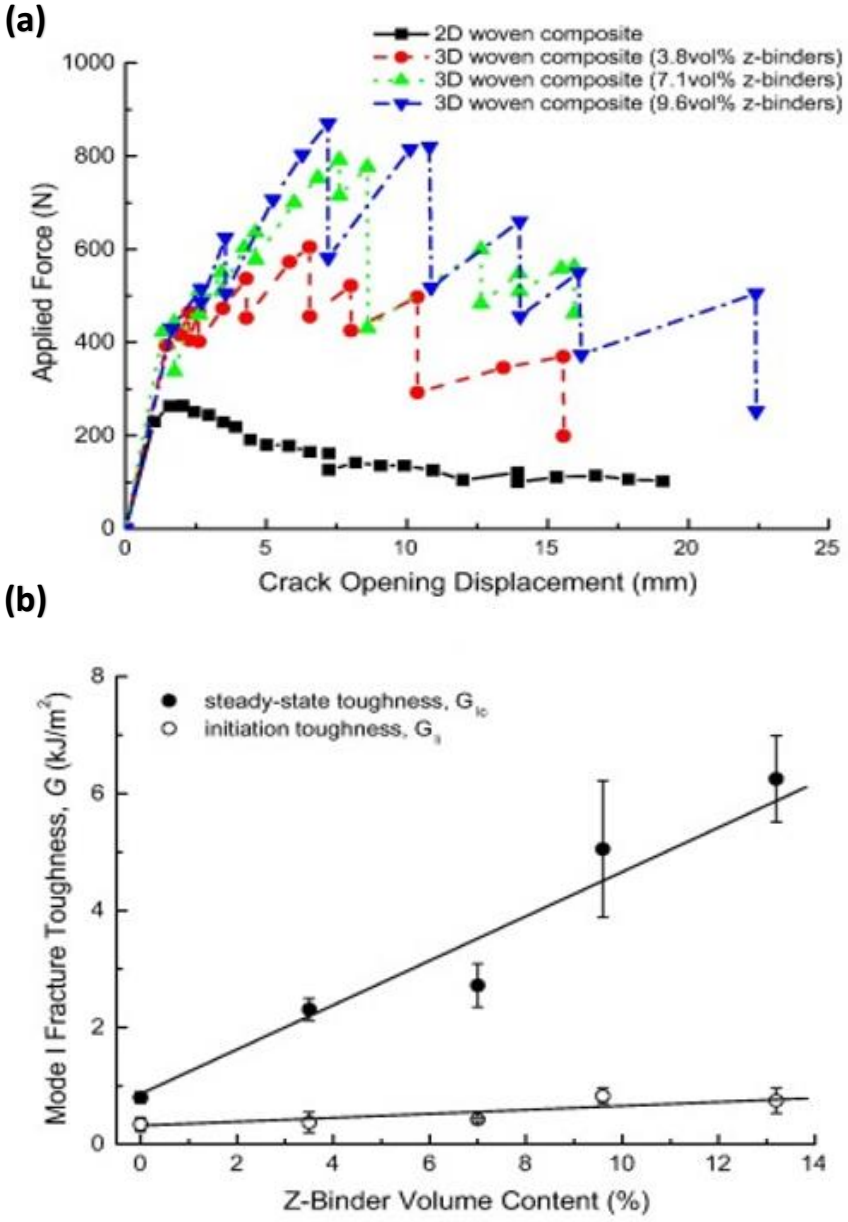

Fig. 2.8: *Effect of z-binder yarn content on the (a) mode I load–displacement curves and the (b) initiation and steady-state mode I interlaminar fracture toughness values for 3D woven carbon-epoxy composites [64].*

Ladani et al. [65] recently investigated a novel 3D woven fibre-polymer composite material that has the combination of properties to both resist delamination crack growth and to self-heal the cracks. The composites contained z-binders made of carbon fibre yarn and/or thermoplastic filament (EMAA). The results show in the Fig. 2.9 that the hybrid 3D reinforcements substantially improved the mode I interlaminar fracture toughness (~1200%).

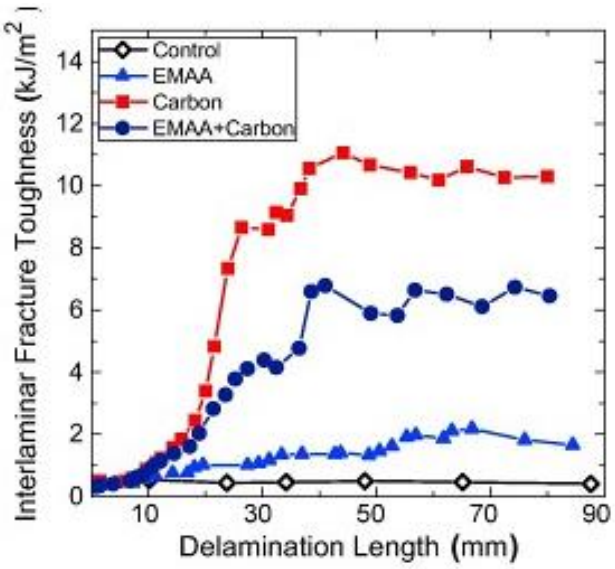

Fig. 2.9: *Mode I crack growth resistance (R) curves for 3D woven composites containing z-binders made of thermoplastic (EMAA), carbon fibres, or combination of EMAA and carbon fibres [65].*

The high interlaminar fracture toughness of 3D woven composites is often due to pull-out of the bridging z-binders after they have fractured. This pull-out action generates friction traction stresses which add to the interlaminar toughening effect. However, z-binders may also rupture at the delamination crack plane without experiencing significant pull-out, and in this case the toughening effect is provided mostly by deformation of the z-binders prior to fracture. Tensile rupture is the common type of failure for continuous z-binders with end restraint i.e. z-binders within 3D woven composites.

Under mode II interlaminar loading different toughening mechanisms are active to those that occur under mode I loading. The z-binders experience elastic deformation at small

crack sliding displacements and then often experience pull-out or shear rupture at large crack sliding displacements, as shown for example in Fig. 2.10. In addition, the mode II delamination toughness is increased by snubbing of the z-binders at large crack sliding displacements. Snubbing is a discipline-specific scientific team used by researchers to describe a interlaminar toughening process in which the z-binder is pressed laterally into the surrounding composite material under high shear strain deformation. The composite material reacts against the snubbing force and thereby resists deformation of the z-binder, and consequently the mode II delamination toughness is increased. The z-binders under mode II interlaminar loading eventually fail at high crack sliding displacements by pull-out or transverse shear rupture.

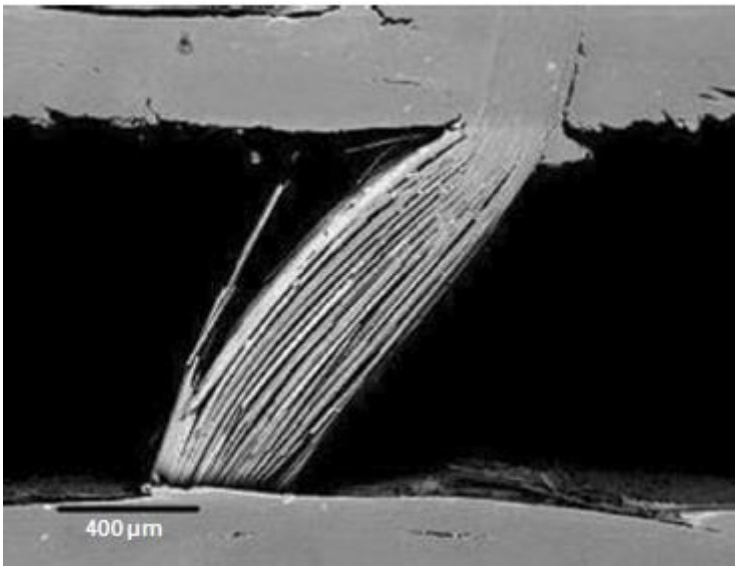

Fig. 2.10: *SEM image showing delamination crack bridging and failure of a z-pin under mode II interlaminar loading of a carbon-epoxy laminate [30].*

The mode II interlaminar fracture properties of three types of 3D woven carbon fibre composites (orthogonal, layer-to-layer interlock, angle interlock) has been investigated using end loaded splits (ELS) and end notched flexure (ENF) specimens [58]. There was no significant difference between the different types of 3D woven composites to initiate mode II interlaminar crack growth. However, the mode II steady-state interlaminar fracture toughness (G_{IIc}) value for the 3D woven composite with the toughened layer-to-layer weave pattern was greater than the standard layer-to-layer. The 3D woven composite containing 3%

z-binder in orthogonal weave showed a moderate reduction in G_{IIc} compared to the 6% z-binder material, as shown in Fig. 2.11. It have been concluded that there is a relatively no or less role for the weave architecture on the mode II propagation values [58].

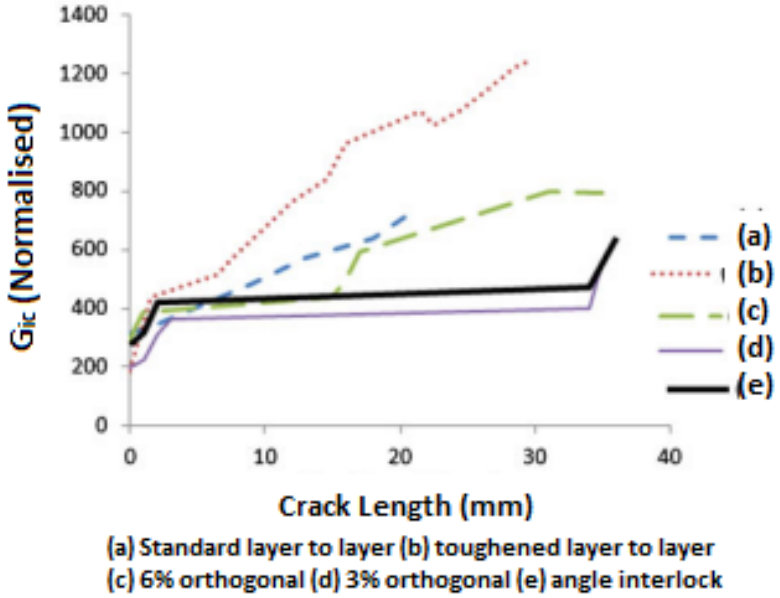

Fig. 2.11: *Comparison of mode II R curves for 3D woven composites with different weave architectures [58].*

Ladani et al. [66] investigated the mode II fracture toughness properties of 3D woven composites reinforced with carbon, poly[ethylene-co-(methacrylic acid)] (EMAA-thermoplastic) and combination of both (carbon + EMAA) z-binders. The results presented in Fig. 2.12 shows that the mode II fracture toughness of the 3D composite reinforced with carbon z-binder showed the highest value, which was ~150% higher than the 2D laminate. The carbon and EMAA z-binders provided a moderate improvement (~75%) whereas the EMAA z-binders increased the toughness by only ~20%. The improvement in mode II fracture toughness is due to the carbon z-binder forming a large-scale bridging zone behind the crack front. The healing of 3D woven composites was also investigated in this study; EMAA z-binders showed good self-repair of mode II delamination cracks.

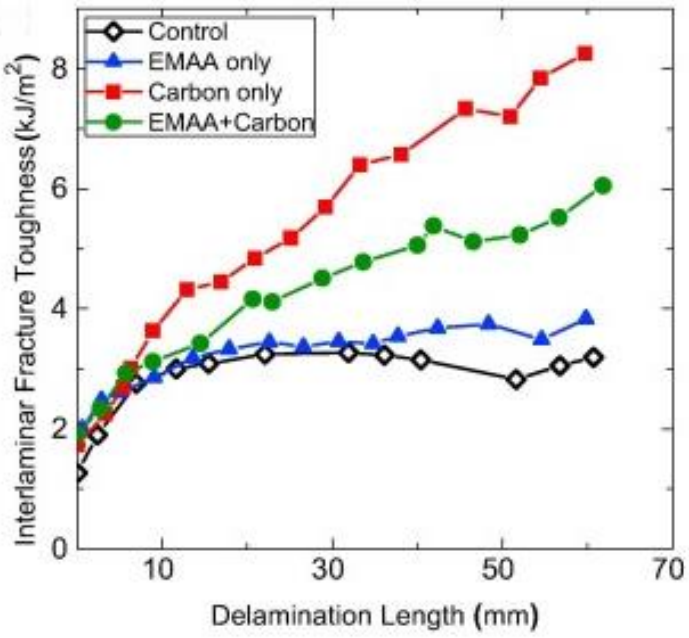

Fig. 2.12: *Mode II R-curves for 3D woven composites reinforced with carbon, EMAA and combination of both (carbon + EMAA) z-binders [66].*

2.2.2 Fatigue resistance of 3D reinforced composite structures

The application of composites in many structural applications requires in-depth knowledge of their fatigue performance under cyclic stress loading conditions. Stress-induced fatigue may be defined as the deterioration to the mechanical, physical or other properties of a material due to damage caused by cyclic or fluctuating loads. Textile composites may also be subjected to fatigue loading in several ways, such as acoustic fatigue and thermal fatigue. Cyclic stress is the most common type of fatigue, and it arises from repeated elastic loading of the material. Several parameters affect the fatigue response of composite materials, such as fibre and matrix material, volume content of z-binder (if present), environmental conditions (temperature, moisture absorption, etc.) and loading conditions (average stress, maximum stress, stress state, *R*-ratio, frequency, etc.).

Wilkinson et al. [67] compared the cyclic tension-tension fatigue behaviour of a non-crimp 3D orthogonal weave composite and 2D laminate at elevated temperature (329°C). They concluded that the 2D laminate offers overall better fatigue performance than the 3D woven composite, especially at higher cyclic stress levels as shown in Fig. 2.13. The fatigue

strength of the 3D woven composite was reduced by the z-binders, which reduced the ultimate tensile stress due to microstructural defects caused by insertion of the z-binders (e.g. fibre waviness).

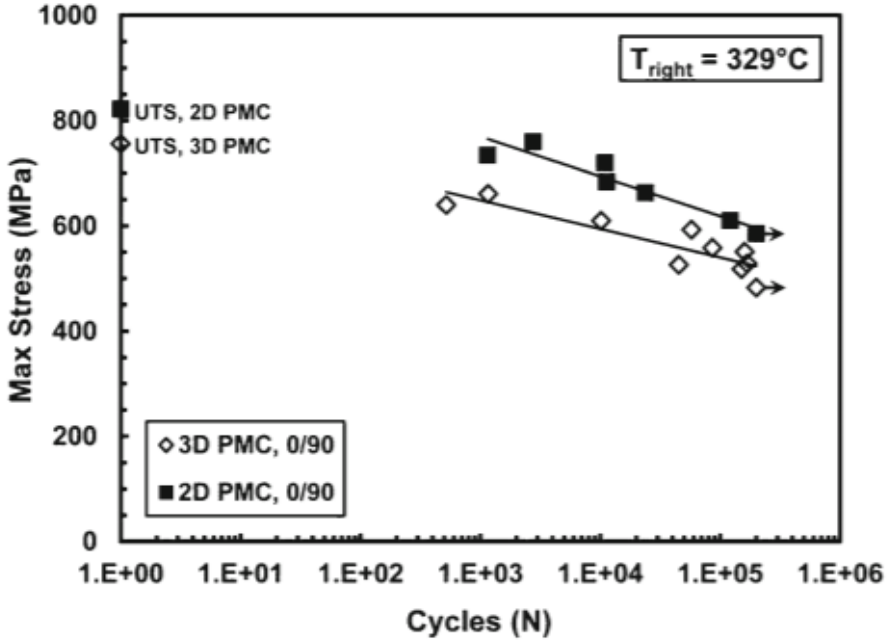

Fig. 2.13: *Fatigue life (S-N) curves for 2D laminate and 3D woven composite at elevated temperature [67].*

Carvelli et al. [68] performed a comparative experimental study into the tensile fatigue properties of a non-crimp 3D orthogonal woven fibreglass composite and equivalent thickness of 2D woven E-glass laminate. Fig. 2.14 shows that the 2D laminate and 3D woven composite had similar fatigue properties, although the fatigue resistance was slightly lower in the warp direction of the 3D composite. They concluded that tensile fatigue resistance of the 3D woven composite was slightly dependent on the loading direction.

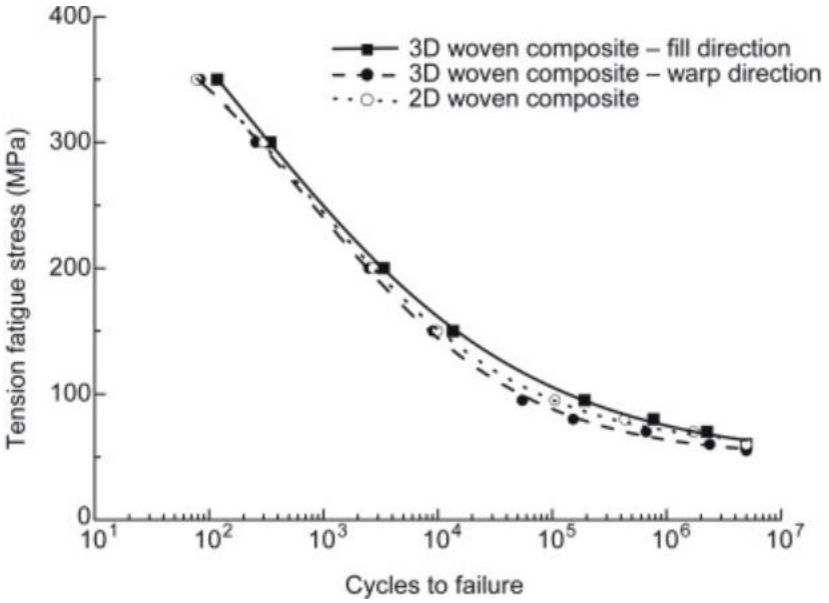

Fig. 2.14: *Tension-tension fatigue life (S-N) curves for non-crimp 3D orthogonal woven composite in warp and fill direction compared with 2D laminate [68].*

Judawisastra et al. [69] experimentally investigated the fatigue behaviour and damage development during cyclic bending loading of 3D woven sandwich composites. They evaluated four types of fibre glass-epoxy panels: two without foam and two PUR foamed panels. They found that the 3D woven glass fabric epoxy panels with polyurethane foam show excellent fatigue behaviour. Very long lifetimes and low stiffness degradation were measured, particularly in the 10 mm thick PUR foamed panel which showed the best results: stiffness degradation lower than 6% at 80% three-point bending ultimate load loading fatigue life higher than 10^6 cycles at 80% three-point bending ultimate load, as shown in Fig. 2.15.

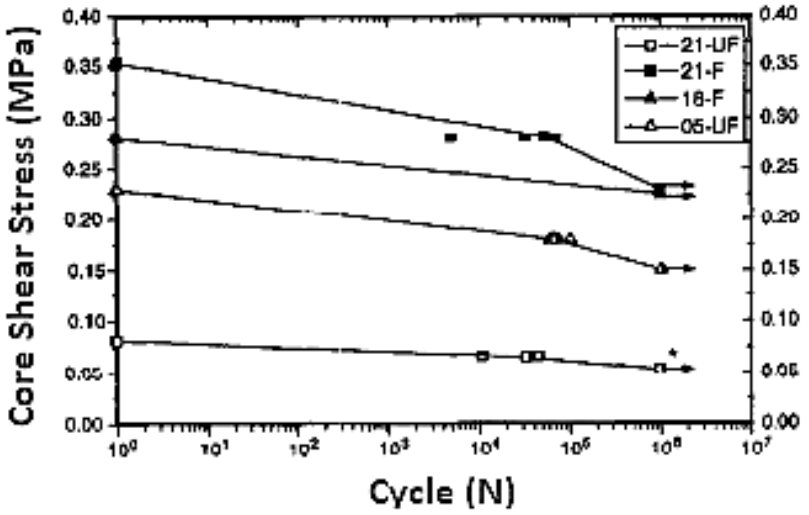

Fig. 2.15: *Stress vs load cycles (S-N) curves of 3D woven panels [69].*

Ladani et al. [70] investigated the mode I and mode II interlaminar fatigue properties of 3D textile composites containing hybrid z-binder materials. Shown in Fig. 2.16 are the Paris curves for a 2D laminate and 3D woven composites containing z-binders made of carbon fibre, thermoplastic (EMMA) or a combination of both materials. The 3D woven composites showed higher fatigue resistance than the 2D laminate. The 3D woven composites showed increases in the threshold strain energy release rate range to initiate fatigue cracking by ~800% and ~200% under mode I and mode II, respectively.

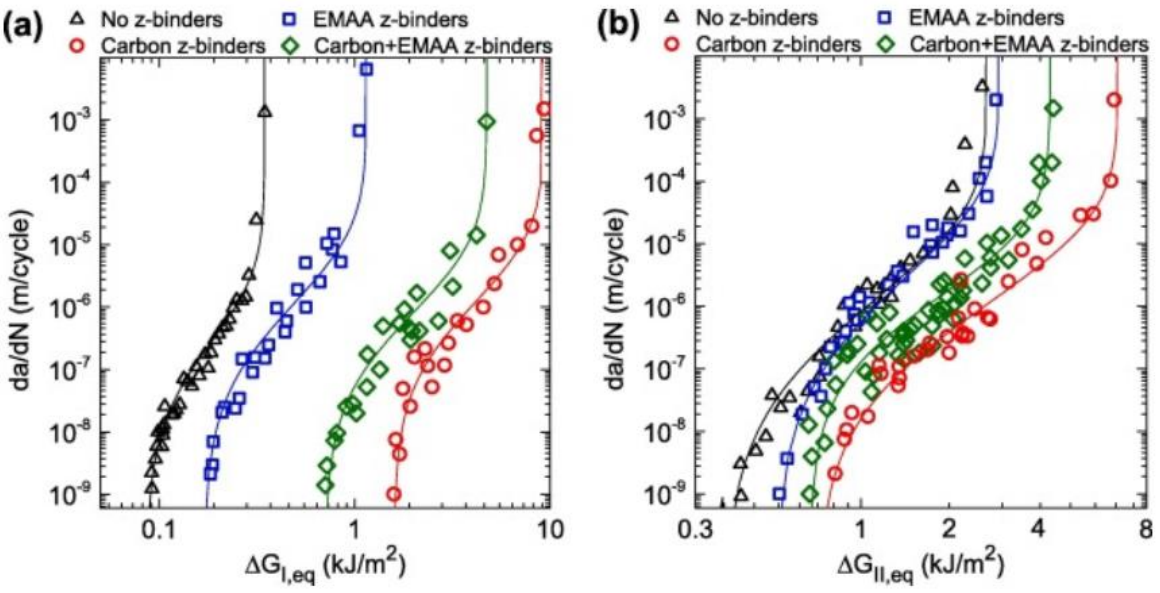

Fig. 2.16: *Paris curves measured for the 2D laminate and 3D woven composites subjected to (a) mode I and (b) mode II interlaminar cyclic loading [70].*

Ladani et al. [70] further investigated the healing of fatigue-induced delamination cracks using EMAA z-binders. The results presented in Fig. 2.17 show partial recovery of the mode I interlaminar fatigue properties of the 3D woven composite after healing. That is, the mode I fatigue crack growth rate curve for the 3D woven composite after healing is further to the left compared to its original condition; that is, the rate of fatigue-induced delamination crack growth after healing is higher than the original composite. However, under mode II fatigue resistance, the healed material was inferior to the 2D laminate.

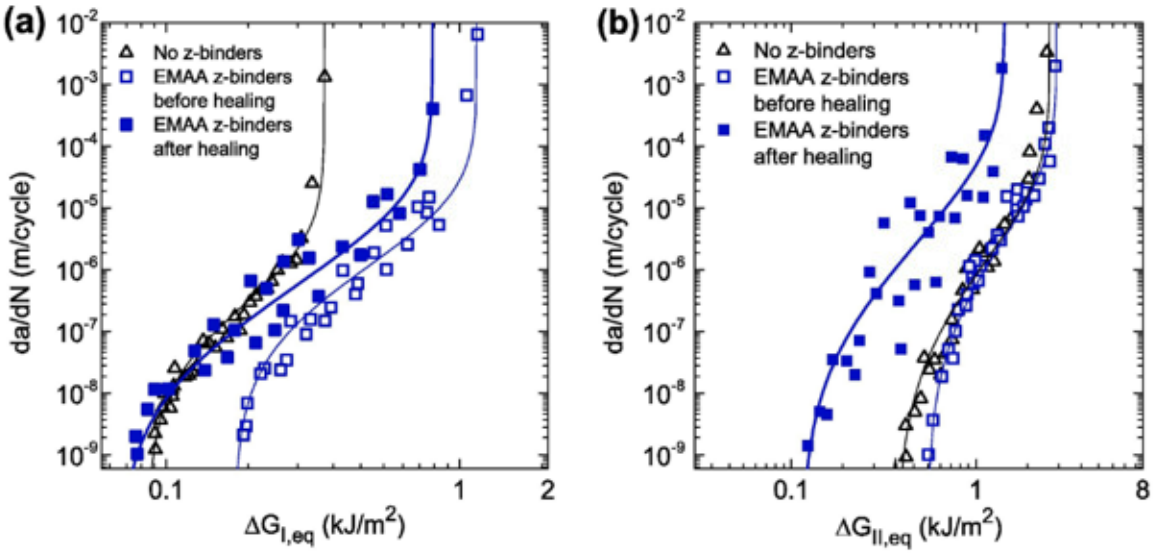

Fig. 2.17: *Paris curves showing the effect of the applied cyclic strain energy release rate range on the delamination crack growth rate for the 3D textile composites before and after healing: (a) EMAA z-binders under mode I, (b) EMAA z-binders under mode II [70].*

Mouritz et al. [71] compared the mode I interlaminar fracture toughness properties of 3D woven composites with composites reinforced with z-pins. They found that the z-pinned composites had higher delamination fatigue resistance than the 3D woven composites for the amount of through-thickness reinforcement used, as shown in Fig. 2.18. Mouritz and colleagues attributed this to the orientation of the z-reinforcement. They explained that the z-pins are aligned nearly orthogonal to the delamination crack, and therefore the z-pins generated a higher bridging traction load under mode I fatigue loading. In comparison, the z-binders in the 3D woven composites were inclined at a steep angle, and this reduced their

mode I bridging traction efficiency and therefore the traction load was lower compared with z-pins.

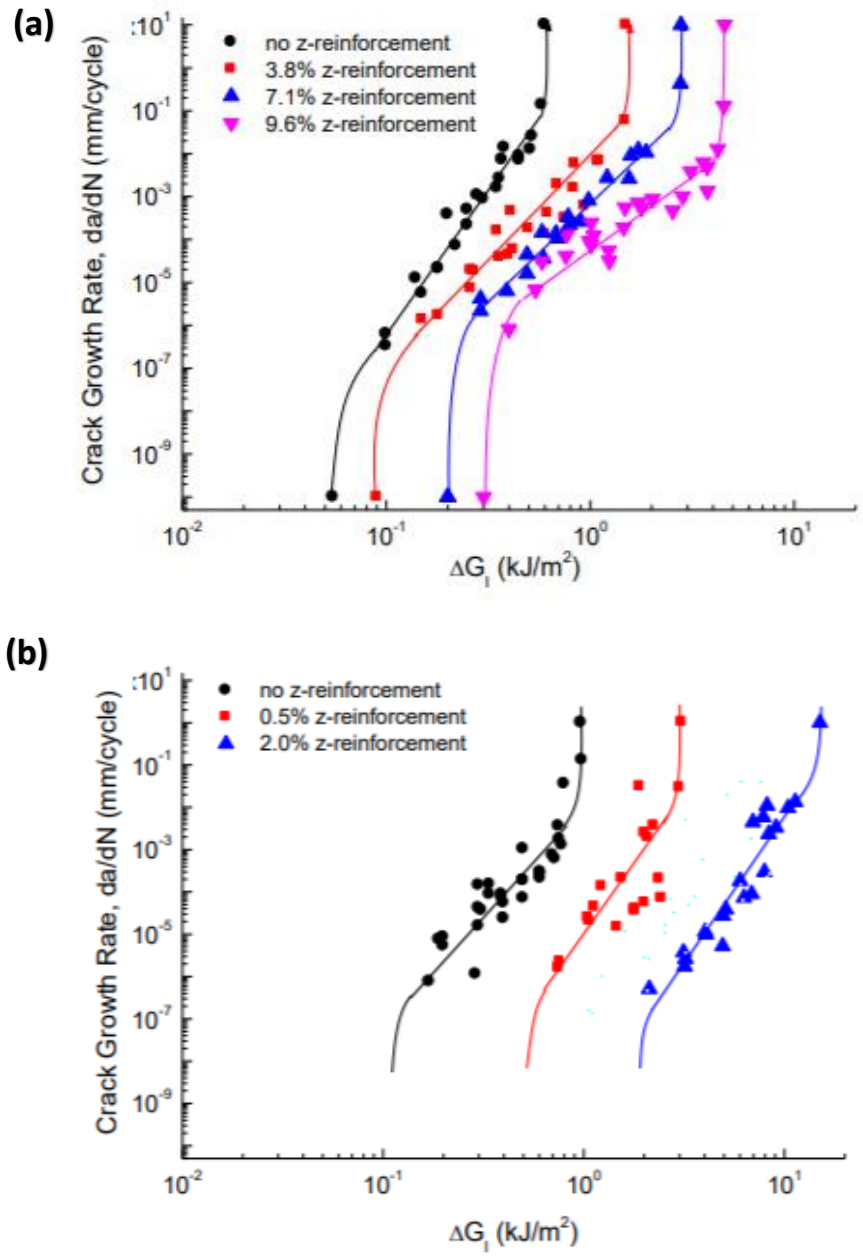

Fig. 2.18: *Paris curves showing the effect of increasing volume content of z-reinforcement on the mode I interlaminar fatigue properties of the (a) 3D woven composites and (b) z-pinned composites [71].*

2.3 Impact damage tolerance of 3D reinforced composite structures

Fibre-polymer composite materials have relatively low interlaminar fracture toughness properties and therefore are prone to delamination cracking when subjected to impact loading. The impact damage resistance and, in some cases, the post-impact mechanical properties of composites can be increased by through-thickness fibre reinforcement. The high impact damage resistance of 3D woven composites is due to their high level of delamination resistance [24]. However, there is very little published research on the impact resistant properties of 3D woven composites. Brandt et al. [72] investigated the impact damage tolerant properties of different types of composite materials i.e. 2D, 3D and knitted. Fig. 2.19 shows the impact force-time response for a 2D laminate and 3D woven composite during drop-weight impact testing. Under comparable test conditions, the 3D material absorbs approximately 2.5 times more energy than the 2D laminate.

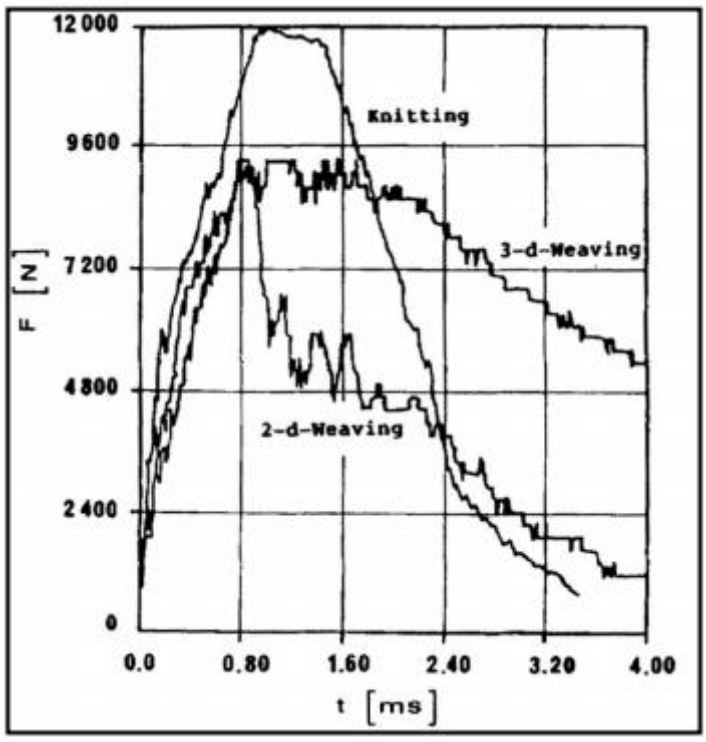

Fig. 2.19: *Impact energy-times curves measured for different types of textile composites [72].*

The amount of impact damage caused to 3D woven composites is often less than an equivalent 2D laminate with the same fibre volume content. For example, Fig. 2.20 shows the effect of increasing impact energy on the amount of delamination damage experienced by 3D

carbon-epoxy composites reinforced with an orthogonal or interlocked woven structure. The amount of impact damage sustained by the two types of 3D woven composite is lower than the 2D laminate. The superior damage resistance of 3D woven composites is due to their high delamination resistance caused by their higher interlaminar fracture toughness properties. The impact damage resistance of 3D woven composites increases with the volume content of z-binder, the use of finer diameter z-binders, the use of high stiffness and strength z-binders, fabric architecture, and high interfacial shear strength between the z-binders and composite material [30].

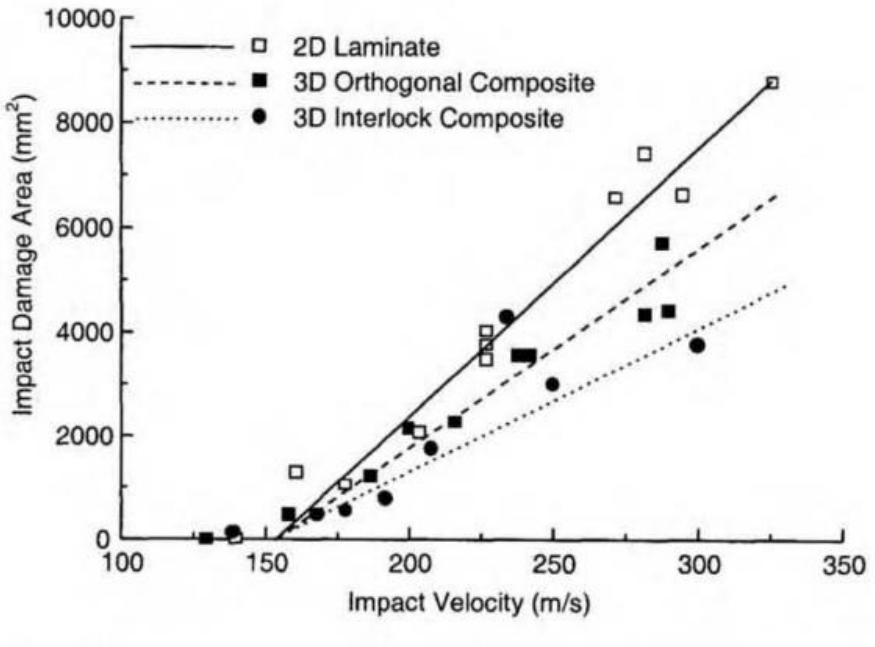

Fig. 2.20: *Effect of impact velocity on the amount of delamination damage to 2D and 3D woven composites [30].*

Ko et al. [73] investigated the impact responses of 3D orthogonally woven and 2D biaxial woven composites. They have found that the impact resistance of composites showed good improvement in impact damage area and damage initiation as well as propagation energy. It was also found that 3D woven composites required higher force to initiate the damage compared with 2D woven composites, as shown in Fig. 2.21.

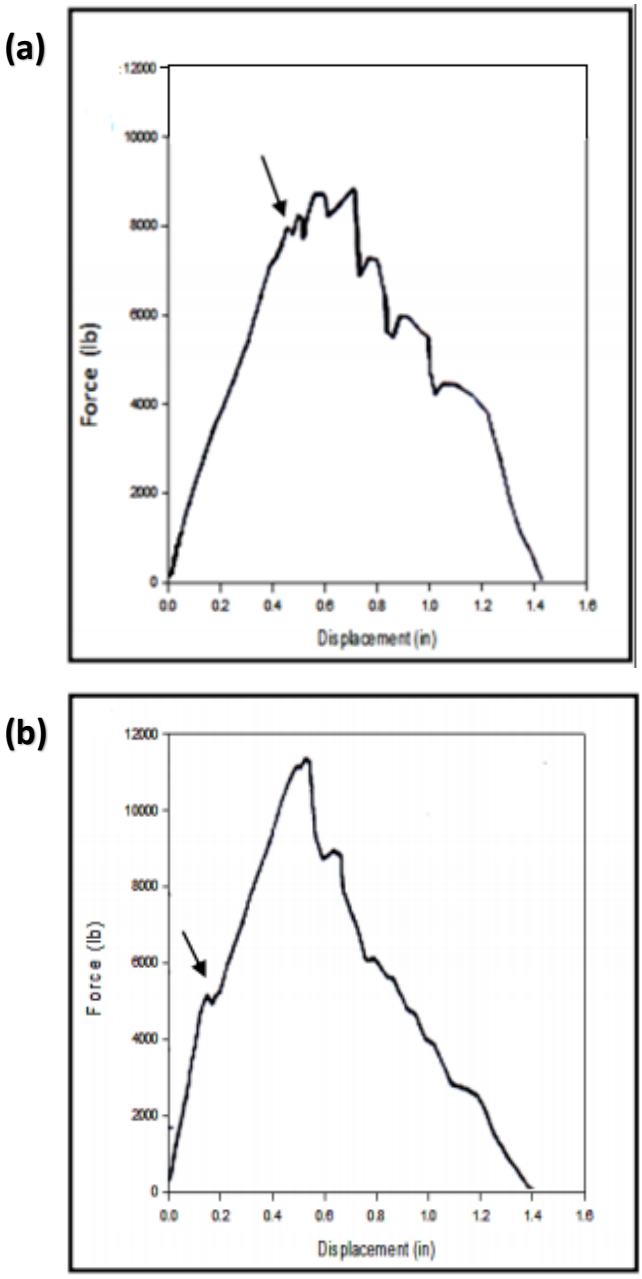

Fig. 2.21: *Impact response of 3D and 2D woven composites: (a) 3D orthogonally woven (b) 2D plain woven. The arrows represent the incipient damage points [73].*

Barndt et al. [74] observed that under comparable impact test conditions, a 3D woven composite suppresses delamination cracking and absorbs significantly more impact energy than 2D woven laminates. The reduction to the amount of impact damage led to an improvement in the residual compression-after-impact strength of the 3D woven composite. The z-binders slow the crack propagation, although (as already discussed) the in-plane fibre damage during weaving process may reduce the strength and fracture resistance of the 3D

composite [75]. Baucom et al. [76, 77] investigated the effect of fabric architecture (2D and 3D orthogonal woven composites) on damage progression and perforation failure. They observed delamination between the plies and fibre damage on both (rear and front) surfaces on both types of material. However, cracking in the 3D woven composites was much less compared to the 2D composite.

Luo [78] and Lv [79] tested a 3D orthogonal hybrid woven composite when transversely loaded at different rates using hemispherical-ended and flat-ended steel rods. Both the energy absorption and damage mechanism were dependent on the loading rate of the rods. Under low rate loading, the 3D composite failed due to excessive tensile and compressive stresses created by the bending moment. At higher loading rate the damage occurred in the forms of matrix cracking and fibre breakage. It was observed that the z-binders prevented delamination. Walter et al. [80] found that during high velocity ballistic loading, delamination was the dominant failure mode accompanied by fibre breakage and matrix failure. Although z-binders resist the delamination during the initial penetration, the effect of z-binder was negligible at much higher velocities.

King et al. [81] and Gerlach et al. [82] investigated the influences of the volume content and locations of z-binders during the impact loading of 3D woven carbon fibre composites. As expected, the amount of impact damage decreased with increasing z-binder content. Also, the damage when impacted near the edge of a z-binder was deeper than when impacted in the centre of the z-binder. Hence, they concluded that z-binder location under the impactor had a direct influence on impact depth [81]. Chen et al. [83] compared the impact response of 3D woven composites with unidirectional laminates and 2D non-crimp laminates. They have found that the impact damage resistance and damage tolerance properties of the 3D woven composites were superior due to the z-binders resisting delamination crack growth [83].

Potluri et al. [84] compared the impact resistance of 3D woven composites at different impact energy levels with 2D woven and cross-ply laminates. The 3D woven composites sustained less damage over the range of impact energies studied, as shown Fig. 2.22. They

also found that the damage was more localised in the 3D woven composites. Furthermore, the amount of damage sustained by the four types of 3D woven composites was similar.

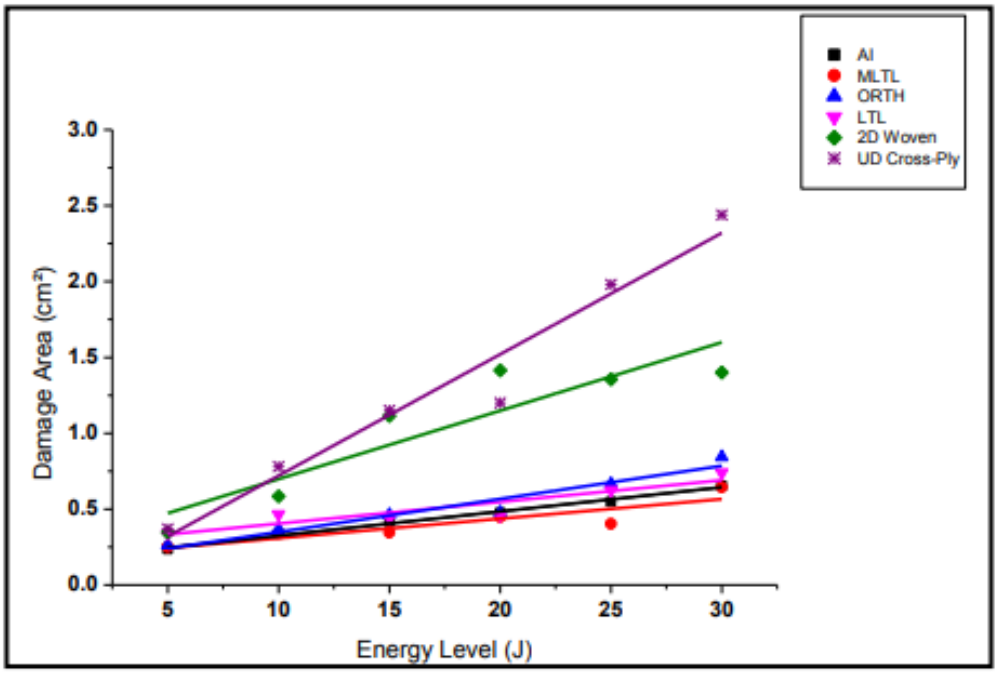

Fig. 2.22: *Damage area vs impact energy curves for angle interlock (AI), modified layer-to-layer (MLTL), orthogonal (ORTH), layer-to-layer (LTL), unidirectional cross-ply (UD cross-ply) and 2D composites [84].*

2.4 In-plane Mechanical Properties of 3D Woven Composites

2.4.1 Tensile properties

The in-plane tensile properties of various types of 3D woven composites have been experimentally investigated, including non-crimped orthogonal, layer interlock and other 3D woven architectures using carbon, glass or Kevlar fibres. Dai et al. [31] compared the tensile properties on six types of 3D woven composite materials, and they concluded that the tensile properties were sensitive to the amount of the waviness to the load-bearing fibres caused by the z-binders. Composites containing orthogonal or angle interlock woven fabrics generally had higher tensile modulus and tensile strength values due to less crimping of the warp yarns by the z-binders. Behera et al. [85] also measured the mechanical properties of various 3D woven composites, and found they were lower than 2D woven and unidirectional laminates, as shown in Fig. 2.23 for the tensile-displacement response measured in the warp and weft directions**.** The tensile properties of 3D woven composites are often lower than the 2D

laminate, as shown for example in Fig. 2.24 [24]. The tensile modulus of 3D woven composites is typically anywhere from 10% to 35% lower than an equivalent 2D laminate [18, 33, 86]. However, some studies report a slightly higher tensile modulus for 3D woven composites [50, 83].

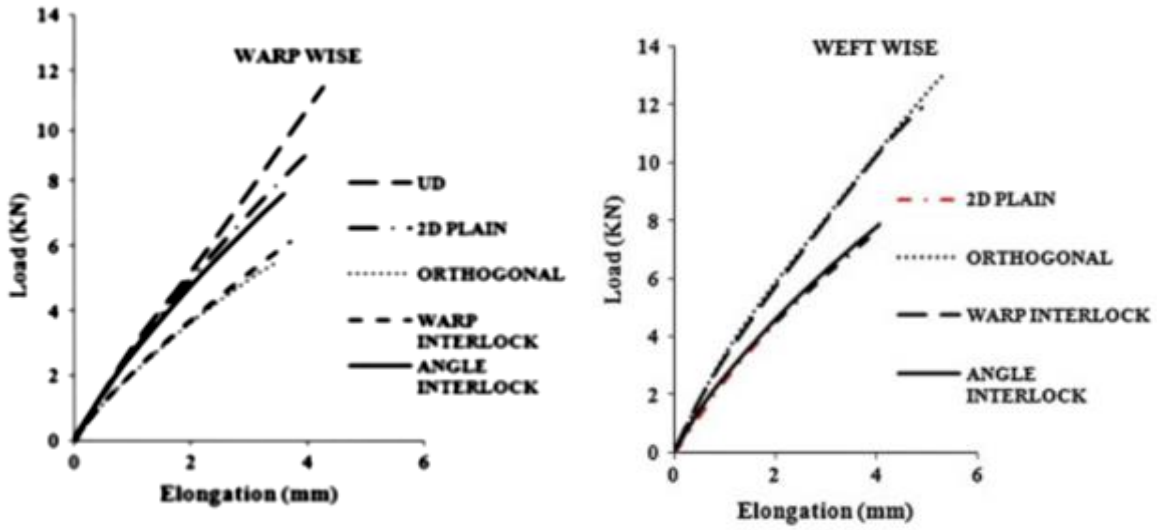

Fig. 2.23: *Effect of weave architecture on tensile load-displacement curves of 2D and three types of 3D woven composites measured in the warp and weft directions [85].*

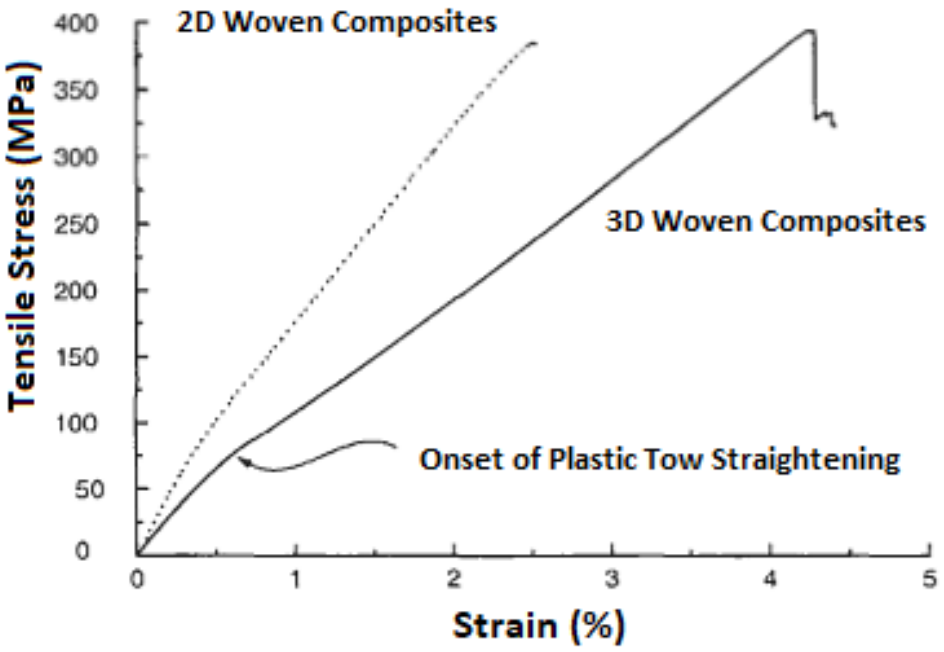

Fig. 2.24: *Tensile stress-strain curves for a 2D and 3D woven composites [24].*

Saleh et al. [87] investigated the effect of different 3D woven fabric architectures on tensile properties. They found that the tensile stiffness and tensile strength were mainly dependent on the fibre volume content of warp and weft yarns, regardless of the fabric architecture. They also found that 3D orthogonal woven composites exhibited the highest tensile strength under off-axis loading due to the interlocked structure provided by the z-binder resisting shear deformation. The reduction in the tensile strength of 3D woven composites is mainly due to damage and waviness of the load-bearing fibres caused by the z-binder during the weaving process. As the z-binders are woven into the fabric the in-plane fibres are damaged and broken as shown in Fig. 2.25. As reported earlier, crimp caused by the z-binders is a contributing factor for the reduction in the tensile strength of 3D woven composites. Lee et al. [34] investigated the fibre damage that occurs during the 3D weaving process on the tensile properties of 3D woven composites. As mentioned earlier, they found that abrasion and breakage of the fibres occurred due to sliding of the yarns against components of the weaving loom, and this reduced the yarn strength. For example, the 3D weaving process caused a ~30% reduction to the tensile failure stress of glass yarns during the fabrication of an orthogonal fabric preform.

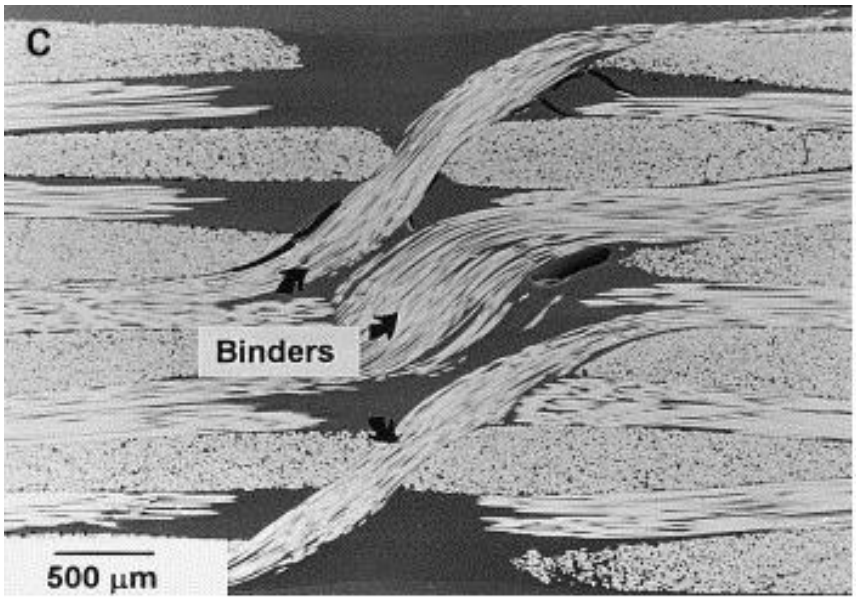

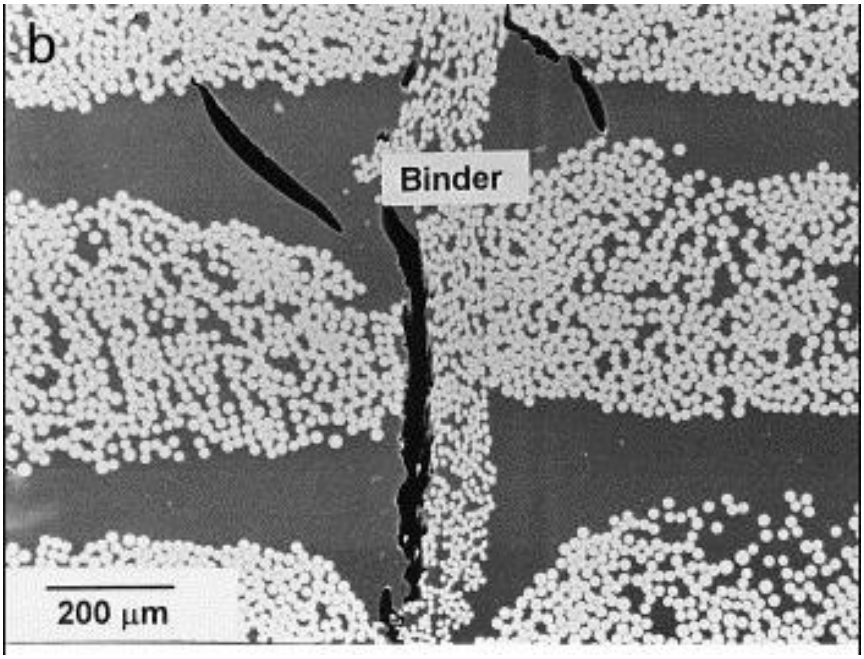

Fig. 2.25: *SEM image showing in-plane fibres damage due to the z-binder [37] .*

2.4.2 Compressive properties

Most studies have found that the compressive modulus of 3D woven composites is lower than the equivalent 2D laminate with the same fibre volume content [24], and this is due to crimping and waviness of the load-bearing fibres caused during the insertion of z-binders. The effects of z-binder content and architecture on the compressive strength of 3D woven composites are complex because both improvements and reductions can occur. For example, Fig. 2.26 shows normalised compressive strength results for three types of 3D woven composites with different z-binder contents. The normalised compressive strength is defined as the compressive strength of the 3D woven composite divided by the strength of 2D woven laminate with nominally the same in-plane fibre content. The results show no clear trend; with the compressive strength being higher, lower or similar to the 2D laminate. However, the compressive strength of 3D woven composites is usually improved or degraded by less than ~20%.

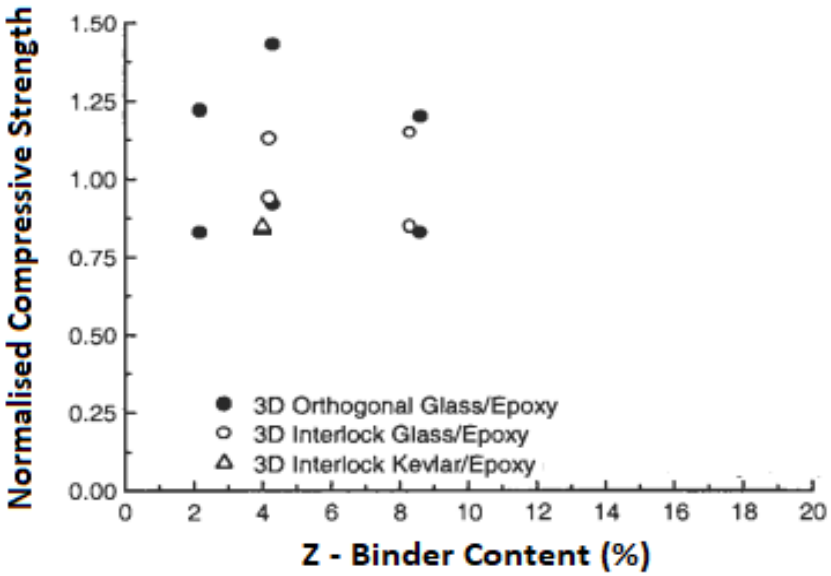

Fig. 2.26: *Plot of compressive strength against z-binder content for 3D orthogonal glass-epoxy, 3D interlock glass-epoxy and 3D interlock Kevlar-epoxy composites [24] .*

Cox et al. [36] observed that 3D woven composites fail under axial compression loading via kinking of the load-bearing tows. Kinking is defined as the failure process that initiates at regions with a low resistance to plastic shear deformation, such as material defects (e.g. void, crack) or where fibres are misaligned from the load direction. The kink bands in 3D woven composites first initiate in the tows which have experienced the greatest amount of crimping/waviness by the z-binder. Therefore, reducing the amount of tow crimping increases the kinking stress and consequently the compressive strength of 3D woven composites. Cox et al. [36] further compared the compression properties of a unidirectional carbon/epoxy laminate against a 3D woven composite, and measured a large reduction to the failure strength but a large increase to the failure strain due to the z-binders, as shown in Fig. 2.27.

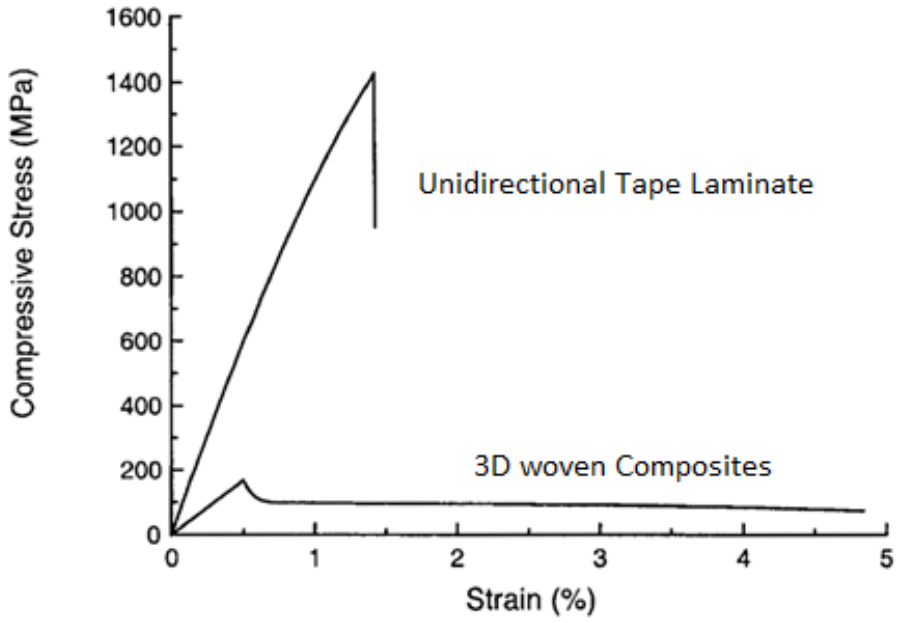

Fig. 2.27: *Compression stress-strain curves for a unidirectional tape laminate and a 3D woven composites [36] .*

Potluri et al. [84] studied the compression properties for different 3D weaving patterns and validated a model based on an energy-minimization technique using their experimental data. Mahadik et al. [27] conducted compression tests on 3D woven angle interlock composite specimens moulded at different degrees of compaction. They observed that the compression strength and failure mechanism were dependent on the highly crimped region (mainly near the z-binder region). Higher crimp lead to larger reductions in the compressive properties of the 3D woven composites. Behera et al. [85] compared the compression properties of different architectures of 3D woven composites, and found that the angle interlock architecture provided the composite with a higher failure stress than warp interlock and orthogonal architectures. However, all three types of 3D woven composites have lower compressive properties than 2D woven and unidirectional laminates. As discussed, the lower compression properties of the 3D woven composites are often due mostly to the breakage, crimping and waviness of load-bearing fibres by the z-binders.

2.4.3 Flexural properties

Similar to tensile and compression properties, the flexural properties are affected by the z-binders in 3D woven composites. The effect of z-binder yarn on the flexural properties

has been investigated by several researchers [15, 36, 52, 80, 88], and they are usually lower than 2D laminates with an equivalent fraction of in-plane fibres.

Umer et al. [89] compared the flexural properties of composites with different 3D woven architectures. They have found that the angle interlock architecture had higher flexural properties in the warp direction compared with orthogonal and layer-to-layer woven architectures, as shown in Fig. 2.28. It was also found that bending-induced damage initiated at the resin-rich areas around the z-binders, and then propagated along the warp yarn in orthogonal and angle interlock woven composites.

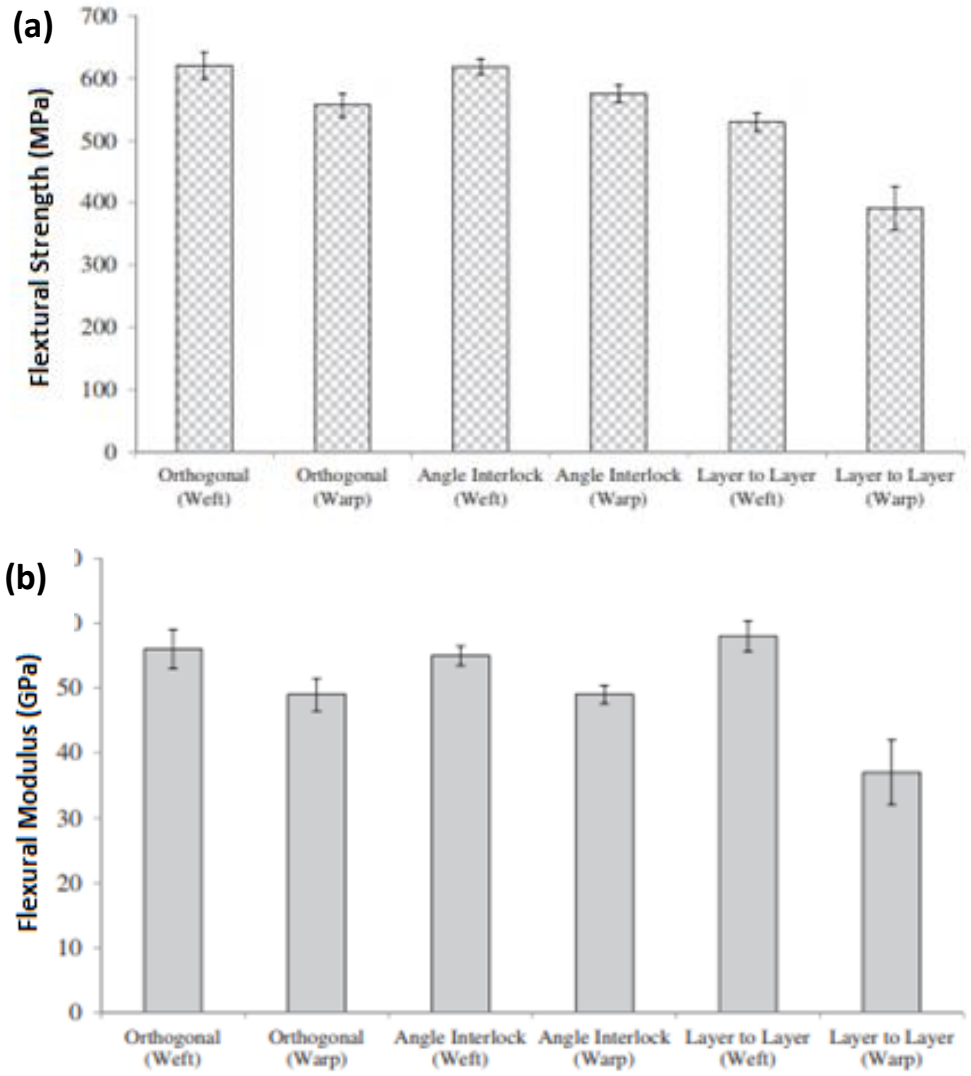

Fig. 2.28: *Comparison of the flexural properties of different types of 3D woven composites: (a) strength and (b) modulus [89].*

Sun et al. [90] investigated the effect of z-binder content on the flexural properties of non-woven 3D orthogonal composites. As mentioned, the non-woven technique reduces the damage and crimping of in-plane warp yarns. It was found that the flexural strength increased with the z-binder content. However, the flexural modulus was dependent on thickness of the z-binder. Sun and colleagues concluded that the flexural properties depend on multiple properties of the weave, including the diameter and volume content of z-binders as well as the amount of crimping, waviness and damage to the load-bearing fibres.

2.5 Other Properties of 3D Reinforced Composites

Besides the interlaminar fracture toughness, fatigue, impact and in-plane mechanical properties, other properties such as thermal conductivity of 3D woven composites have been investigated.

2.5.1 Thermal properties

Conventional 2D laminates have low thermal conductivity, particularly in the through-thickness direction, because of the poor heat transfer properties of the polymer matrix and fibre-matrix interfaces. As a result, laminates lack the capacity to rapidly dissipate heat when used in elevated temperature applications [91] .

The thermal conductivity of composite materials can be increased by the insertion of through-thickness fibres which act as the heat transfer pathway. Schuster et al. [92] investigated the thermal conductivity of a 3D woven carbon composite reinforced with z-binders made of carbon pitch fibres or copper filament. The results are presented in Fig. 2.29. shows that the increasing the volume content of copper z-binder about 6% increases the out-of-plane thermal conductivity by a factor of eight compared with traditional uniaxial or biaxial composites [92] . Gowayed et al. [93] found a similar effect.

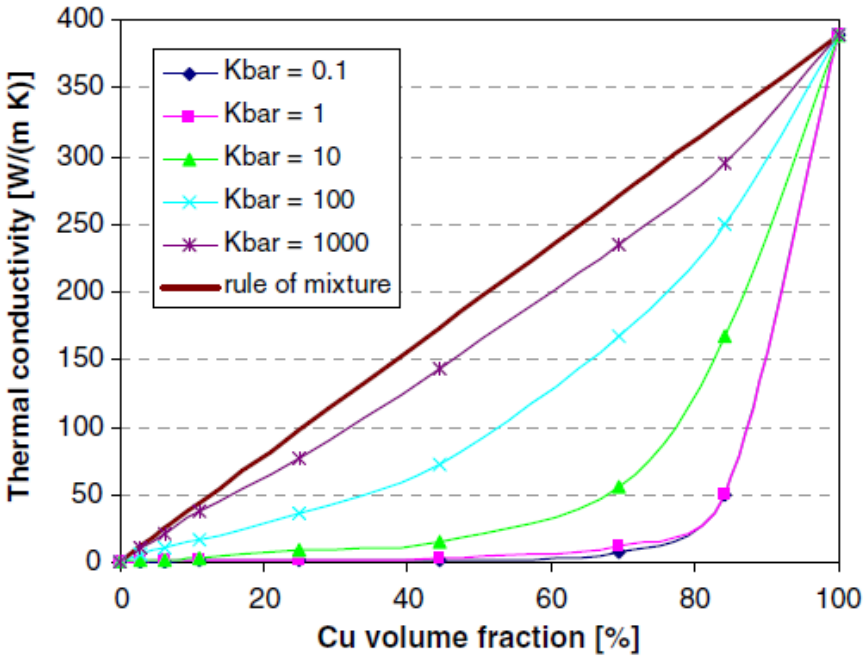

Fig. 2.29: *Thermal conductivity of 3D woven composites reinforced with different volume content of copper fibres [92].*

Schuster et al. [94] investigated thermal conductivity of copper fibre composites by varying the thermal conductivity of the meter bar, designated by the symbol *k*, between 0.1 to 1000 W/(m K), as shown in Fig. 2.29. Schuster et al. demonstrated that the copper z-binders in 3D woven composites can increase greatly the through-thickness thermal conductivity. It was found that inserting z-binders made of thin copper wire or carbon yarn into an 3D orthogonal woven composite increased the through-thickness heat conduction properties. The improvement to the through-thickness conductivity was controlled by the volume fraction and thermal conductivity of the z-binders, as shown in Fig. 2.30. Other parameters also affect the through-thickness conductivity, including the thickness of the composite and the thermal isotropy of the z-binder.

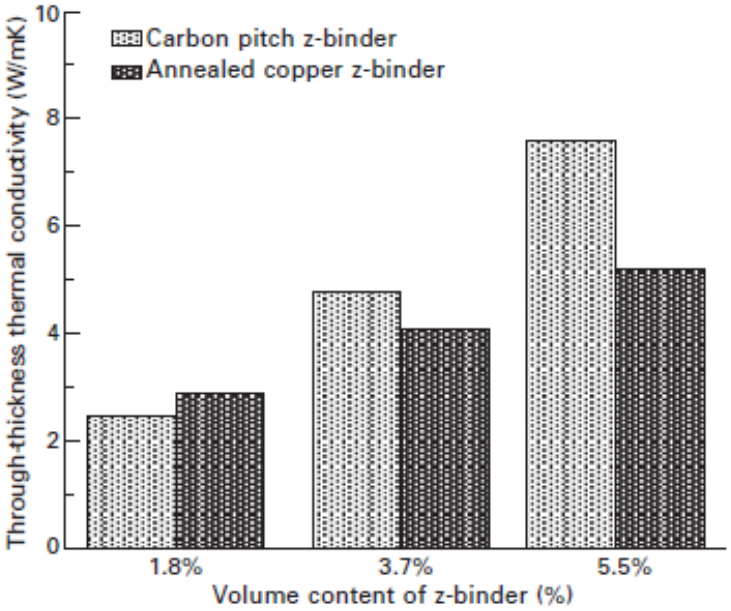

Fig. 2.30: *Effect of type and volume fraction of z-binder on the through thickness thermal conductivity of 3D woven carbon/epoxy [94].*

2.6 Research gap analysis

This literature review has presented numerous studies that proves woven z-binders in composite materials increase the mode I and mode II delamination fracture toughness, mode I and mode II delamination fatigue resistance, and impact tolerance of 3D woven composites. However, there are very few published studies on the mode II delamination fracture toughness and impact properties. Also, there is little published research into the electrical and other properties of 3D woven composites, and these properties are explored in the following research chapters. Chapters 3 and 4 present research into the interlaminar fracture and fatigue behaviour of 3D woven composites reinforced with metal and carbon z-binder. Chapter 5 presents research into the electrical conductivity properties of 3D woven composites. Damage detection properties are also very important in 3D woven composites, the techniques adopted to detect the damage in the 3D composite is investigated in Chapter 6. Very little published research is found in impact properties of 3D woven composites, Chapter 7 is briefly describing the impact and compression after impact properties. No any published research were found on 3D woven T-joints, these joints are widely used in aerospace structures. Chapter 8 is focused on structural properties of 3D woven T-joints. In last Chapter 9 is describing the in-plane properties of 3D woven composites.

Chapter 3: Mode I and Mode II Delamination Fracture Properties of 3D Woven Composites Containing Metal or Carbon Z-binders

Abstract

This chapter presents an experimental investigation into the mode I and mode II interlaminar fracture toughness properties of 3D composite materials reinforced by through-thickness weaving of z-binders. The z-binders were made of copper, steel or carbon fibre. The mode I and II interlaminar fracture properties were measured using the double cantilever beam (DCB) and end notch flexure (ENF) tests, respectively. The steel and carbon z-binders were more effective at improving the mode I and mode II delamination toughness and at resisting the growth of delamination cracks, whereas copper was less effective. The fracture toughness properties were improved by the z-binders forming a large-scale extrinsic bridging zone along the delamination crack. The results further reveal that the improvement in fracture toughness properties was also dependent on the volume content of z-binders. The influence of the material properties of the z-binder on their delamination strengthening capacity and failure mode are experimentally determined.

3.1 INTRODUCTION

Carbon fibre-polymer composites are susceptible to delamination and matrix cracking from service-induced stresses due to through-thickness (interlaminar) static and fatigue loads, edges stresses, environmental degradation and foreign object impact damage (e.g. hail stone, bird strike), as reported earlier. Three-dimensional (3D) fibre composites have superior delamination resistance and damage tolerant properties [29]. 3D fibre composites have high resistance to delamination cracking [46, 49, 58, 64, 95, 96] and barely visible impact damage [82, 84, 97] . Due to these properties, there is interest in the use of 3D woven composites in light-weight aircraft structures and engine components (e.g. inlet fan blades) as well as turbine blades for power generation [29].

The delamination fracture toughness properties of 3D woven composites under mode I and mode II loads have been investigated by other researchers [49, 58, 95]. The z-binders increase the interlaminar fracture toughness by forming a large-scale crack bridging process zone along delamination cracks. For example, Tamuzs et al. [96] examined the effect of z-binder volume content (2-5%) on the mode I fracture toughness properties, and reported that the toughness of the 3D woven composite was up to 10 times higher compared with a 2D laminate without z-binders. As another example, Kerber et al. [98] measured the mode II interlaminar fracture toughness of 3D woven composites containing different volume contents of z-binders, and found that increasing the z-binder content improved the toughness by up to 3 times. Fishpool et al. [58] also found that z-binders in 3D orthogonal or interlock composites improve the mode II fracture toughness by 2-3 times compared with a 2D laminate.

The delamination toughening effect of z-binder is dependent on many factors such as volume content, areal density, spacing, diameter, loading mode etc. To date, all published studies on the delamination toughness properties have been performed on 3D woven composites reinforced with z-binders consisting of carbon or glass tows. However, there is no reported work on the interlaminar fracture properties of 3D composites containing metal z-binders.

This chapter presents an investigation into the delamination resistant properties of carbon-epoxy composite materials reinforced in the through-thickness direction with woven metal z-binders. The z-binders used were copper and stainless steel, and were selected as z-binder materials because they are representative of low and high strength metals, respectively. The metal z-binders were woven in an orthogonal pattern into the dry carbon fabric preform to the composite material. For comparison, the delamination resistance of a composite material with z-binders made of continuous carbon fibre tows were studied. The modes I and II interlaminar fracture toughness properties of the 3D woven composites were measured experimentally, and compared against a control laminate without any through-thickness reinforcement. The study also aims to identify the delamination toughening mechanisms induced by the metal z-binders, and how these mechanisms are different to fibre-based z-binders conventionally used in 3D woven composites.

3.2 MATERIALS AND EXPERIMENTAL METHODOLOGY

3.2.1 Composite Materials

Composite materials with and without z-binders were fabricated using 198 gsm plain woven carbon fabric and low-temperature cure epoxy resin. The single ply fabric consisted of T300 3K carbon tows (AC220127 supplied by Colan Ltd.) woven with a balanced (50:50) proportion of warp and weft yarns. Thirty-two layers of the dry carbon fabric were stacked with the warp tows aligned in the same direction to create a cross-ply fibre pattern for the composite preform. The fabric preform was manually woven in an orthogonal (through-thickness) pattern using one of three types of z-binder material: copper, stainless steel and carbon tows. The orthogonal weave of the pattern of the z-binders in the fabric perform is shown in Fig. 3.1.

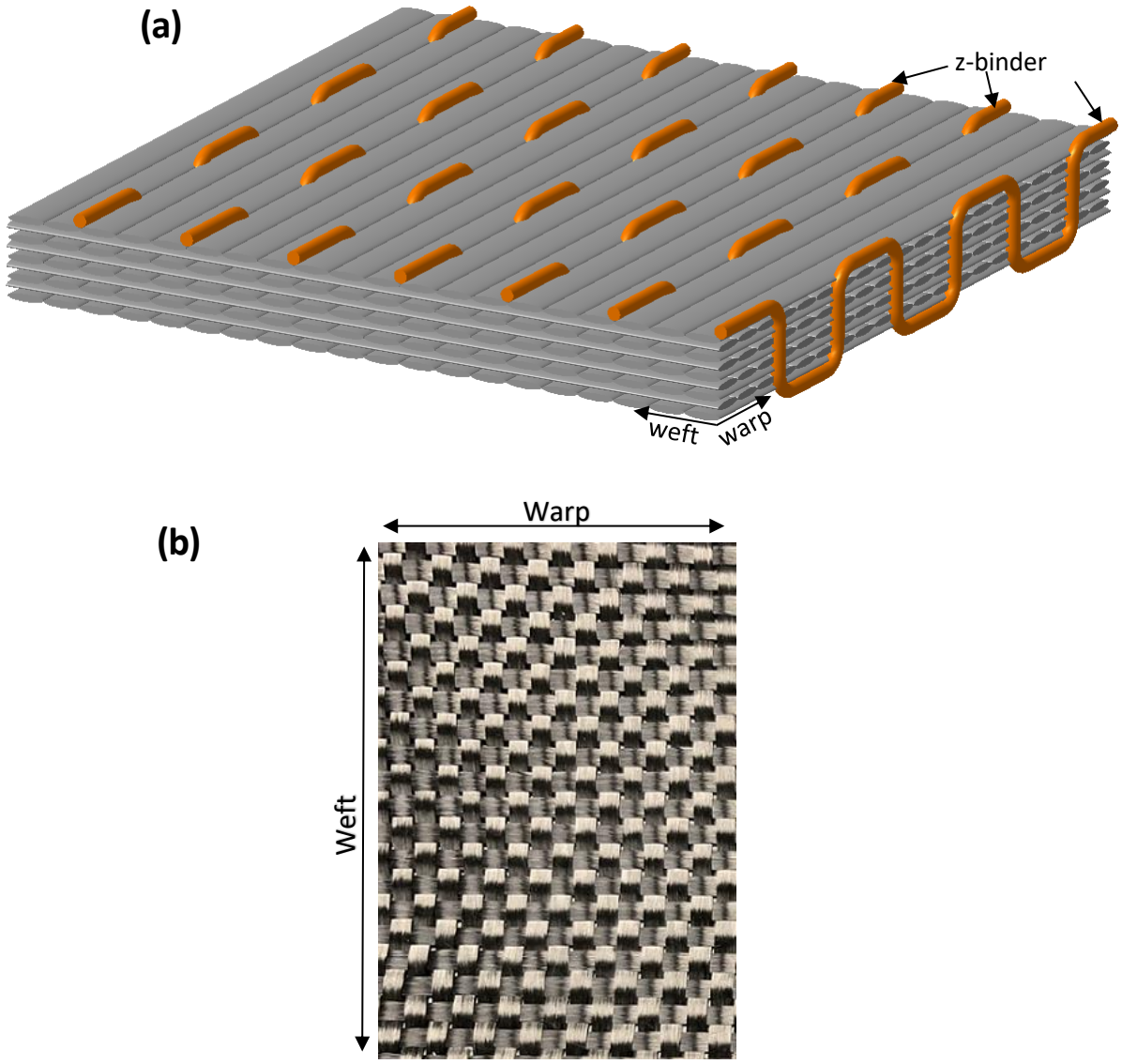

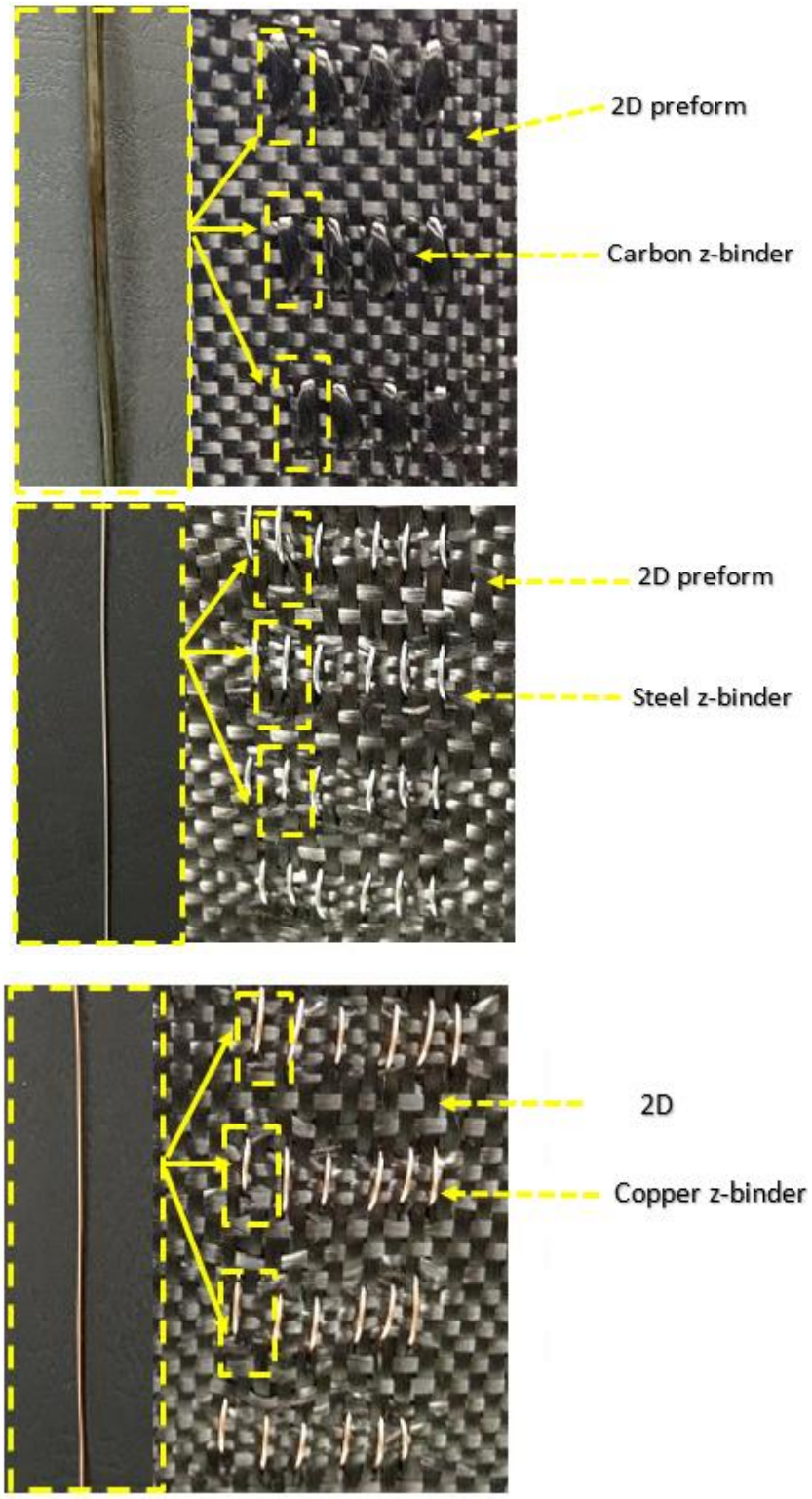

Fig. 3.1: *(a) Schematic showing the orthogonal weave pattern of the z-binders in a 3D woven carbon fabric. (b) Top surface views of 2D and 3D woven fabrics reinforced with carbon, steel and copper (right-hand side) and images of the z-binder filaments before insertion (left-hand side).*

Copper and stainless steel were selected for the metal z-binders because they represent low and high strength metals, respectively, and their mechanical properties are given in Table 3.1. The copper was high purity (99.9% Cu) with a low concentration of trace elements. The stainless steel (316L) had the alloy composition of 16-18% Cr, 10-14% Ni, 2-3% Mo and 2% (max) Mn. Carbon tows (Tenax® HTS40) were selected because they are commonly used as z-binders in 3D orthogonally woven composites.

The copper and steel z-binders had a diameter of 0.51 mm (24 gauge), and were cleaned and degreased before being orthogonally woven into the dry carbon fabric preform stacks. The carbon z-binder was an 800 tex (12K) tow with nominal diameter of ~0.75 mm, which is thicker than the metal z-binders. The fibre packing density in the carbon tow was about 66%, and therefore the equivalent load-bearing diameter of the fibres (when the void spaces are ignored) was about 0.5 mm, which is very close to the metal z-binders.

The copper, steel and carbon z-binders were orthogonally woven into the fabric preform in straight, parallel rows along the warp fibre direction (as illustrated in Fig. 3.1b). The volume content of metal or carbon z-binders is given in Table 3.2. In this thesis the volume contents are referred as low and high. The volume content of z-binder was controlled by the spacing and pitch of the orthogonal weave architecture. It is worth noting that these z-binder contents are very low compared to other interlaminar fracture studies on 3D woven composites, which are typically in the range of 2-10 vol% [46, 64]. Low z-binder contents were used to minimise any adverse impact on the in-plane mechanical properties of the materials, which are described later in this PhD thesis.

Before starting the weaving process, the stack of single ply carbon fabrics were stapled around the edges to avoid slippage using insertion of the woven z-binder. A ruler was placed along both sides of the stack to make sure equal spacing of stich is weave on both sides, as shown in Fig. 3.2 (a). The z-binders were manually woven into the stack of single ply carbon fabric in an orthogonal pattern using a steel sewing needle. The needle used for weaving the z-binder were ~55 mm long and ~1.5 mm thick as shown in Fig. 3.2 (b).

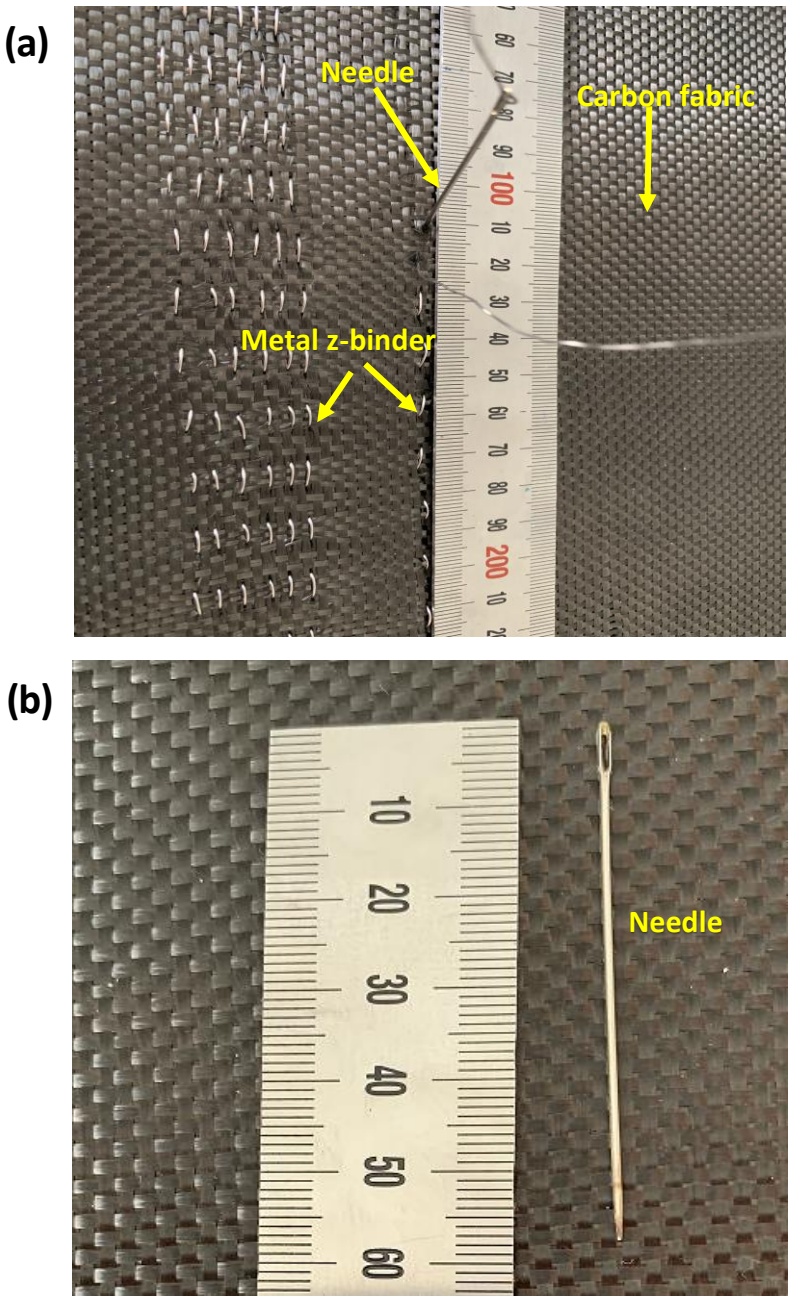

Fig. 3.2: *(a) Manual 3D weaving process, (b) Needle used in weaving process.*

Table 3-1: *Mechanical properties of z-binder materials.*

Z-binder	Young's Modulus (GPa)	Yield Stress (MPa)	Tensile Failure Stress (MPa)	Failure Strain
Carbon	240	-	4400	1.8%
Copper	117	70	62	4.7%
Stainless steel	200	170	485	~60%

Table 3.2. *Volume fraction of in-plane fibres and the z-filament weave contents in the 2D laminate and 3D woven composites.*

Z-Binder			
Type	**Weave density (binders/cm^2)**	**Z-binder areal content (%)**	**Z-binder volume content (%)**
None	-	-	-
Carbon	0.8	0.35	0.70 (i.e. low)
	1.6	0.70	1.30 (i.e. high)
Copper	1.6	0.33	0.65 ((i.e. low)
	3.2	0.66	1.13 (i.e. high)
Steel	1.6	0.33	0.65 (i.e. low)
	3.2	0.66	1.13 (i.e. high)

After weaving, two additional carbon fabric plies were placed on both the top and bottom surfaces of the preform, which was then infused with epoxy resin. The fabrics were infused using the vacuum bag resin infusion process, as shown in Fig. 3.3, with an epoxy consisting of diglycidyl ether of biphenol A (Sicomin SR8100) and diamine hardener (Sicomin SD 8824) at the ratio of 100:22. The resin-infused fabrics were cured at room temperature for 24 hours and then post-cured at 60°C for 8 hours. In addition, a laminate sample without any z-binder, but the same number (36) of carbon fabric plies, was manufactured as the control composite material. The final thickness of the control laminate and different types of 3D woven composite was the same at 9.5 mm. The volume fraction of in-plane carbon fibres in the different materials is given in Table 3.3. The insertion of the z-binders reduces the fibre content by several percent. The insertion of z-binders are responsible to reduce the fibre content.

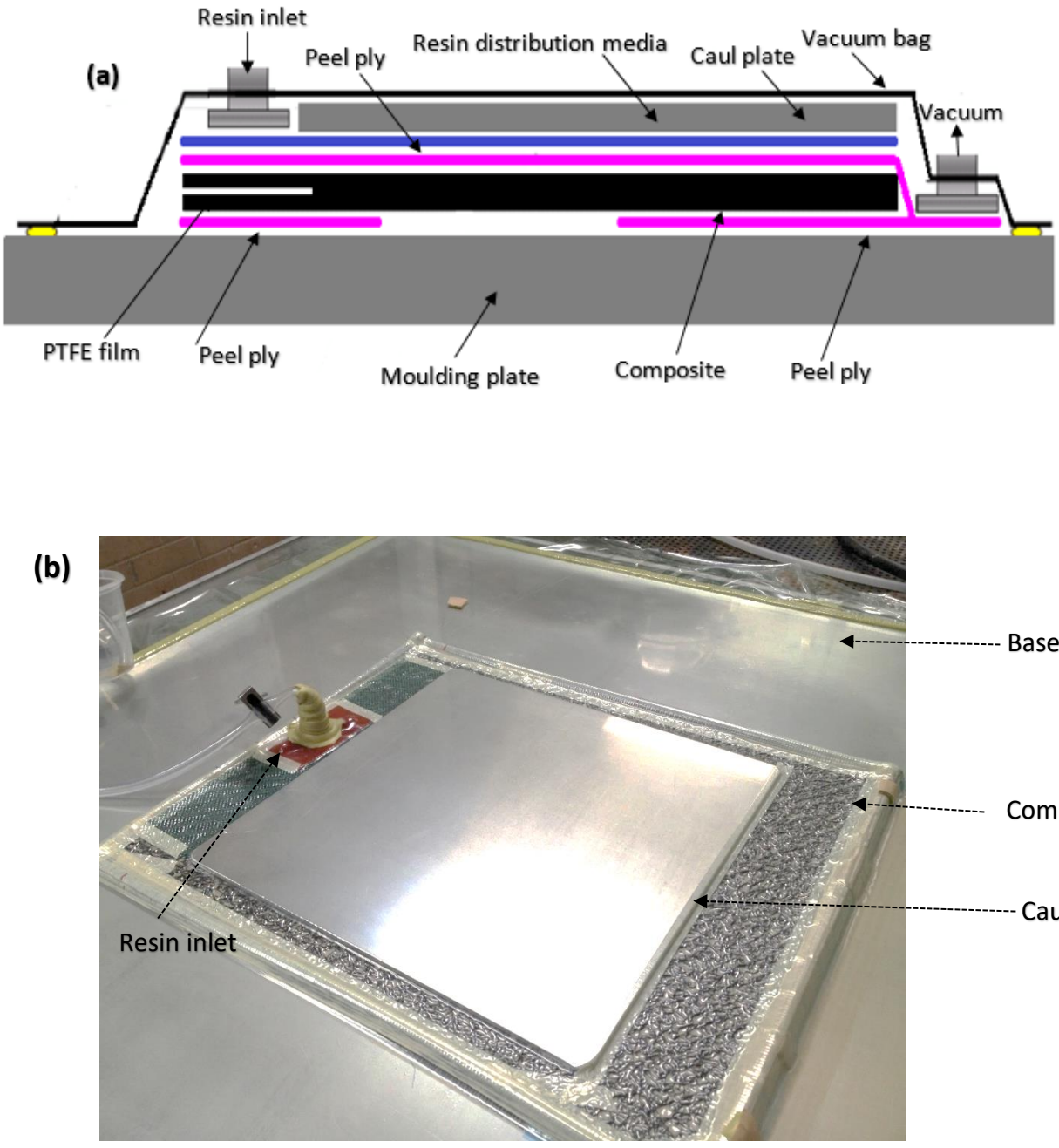

Fig. 3.3: *(a) Schematic of vacuum bagging resin infusion process. (b) Vacuum bagging resin infusion process*

Table 3-3: *Volume fraction of in-plane carbon fibres in the 2D laminate and 3D woven composites.*

Z-binder	Fibre Volume Fraction
None	0.39
Carbon 0.70 vol% 1.30 vol%	 0.38 0.34
Copper 0.65 vol% 1.13 vol%	 0.36 0.35
Stainless steel 0.65 vol% 1.13 vol%	 0.35 0.33

3.2.2 Mode I Interlaminar Fracture Toughness Test

The mode I interlaminar fracture toughness properties of the control laminate and the 3D woven composites were measured using the double cantilever beam (DCB) test. The DCB specimens were 200 mm long and 25 mm wide (Fig. 3.4a). The end of the DCB samples that was subjected to crack opening loading contained a 70 mm long mid-plane pre-crack created using 25 µm thick polytetrafluoroethylene (PTFE) film, and this was used to initiate the delamination. Due to the very high fracture toughness induced by the z-binders, it was necessary to reinforce the entire length of the DCB specimens with 2.6 mm thick unidirectional carbon-epoxy laminate tabs. The tabs were externally bonded to the DCB specimens using an epoxy-paste adhesive (Araldite 420, Huntsman). Without these tabs, the composite specimens would have broken in the sub-laminate arms rather than via delamination crack growth.

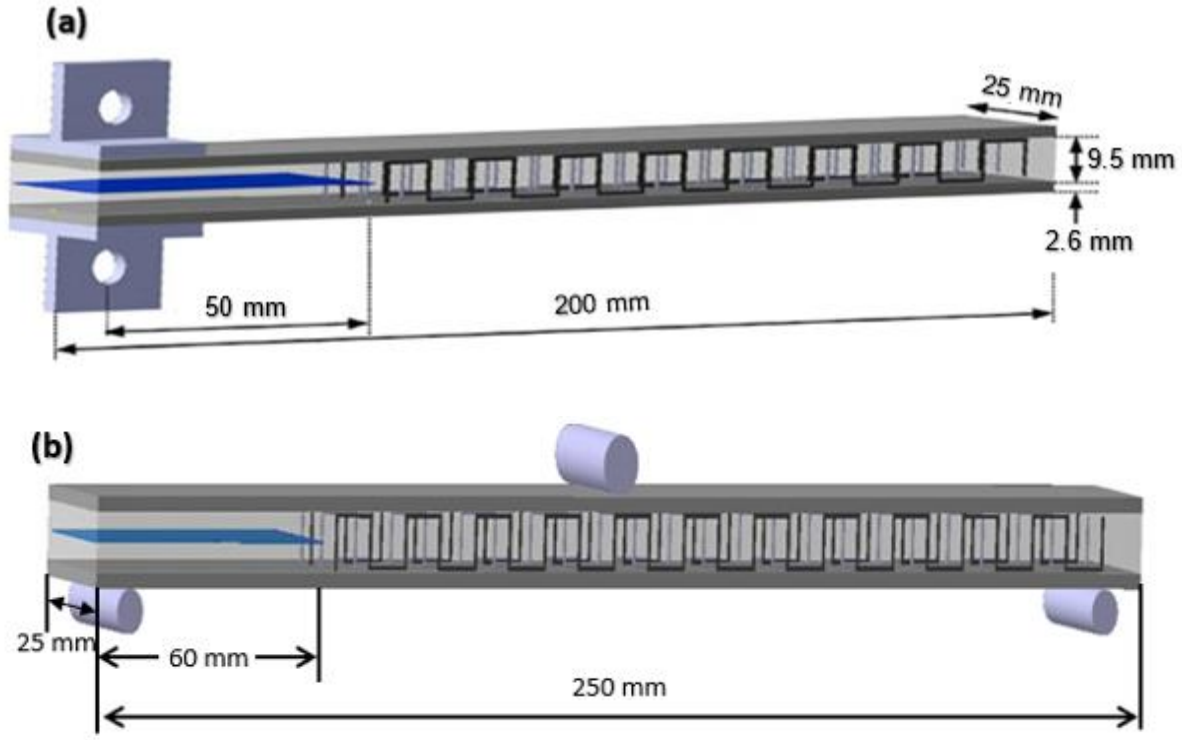

Fig. 3.4: *(a) DCB specimen and (b) ENF specimen. The architecture of the orthogonally woven z-binders is shown.*

Mode I fracture toughness testing was conducted in displacement control using a 10 kN Instron machine as shown in Fig. 3.5. The test involved increasing the crack opening displacement at the pre-cracked end of the DCB sample at a constant rate of 2 mm/min in accordance with ASTM D5528 specifications. As the delamination propagated along the specimen mid-plane, its length was measured using a travelling optical microscope. The mode I interlaminar fracture toughness was calculated using:

$$G_I = \frac{3P\delta}{2b\,(a+|\Delta|)} \qquad (1)$$

where P denotes the applied force, δ is the crack opening displacement, a is the total crack length, b is the width of the DCB specimen, and Δ is a correction factor. Three samples of each type of composite material were tested under identical conditions.

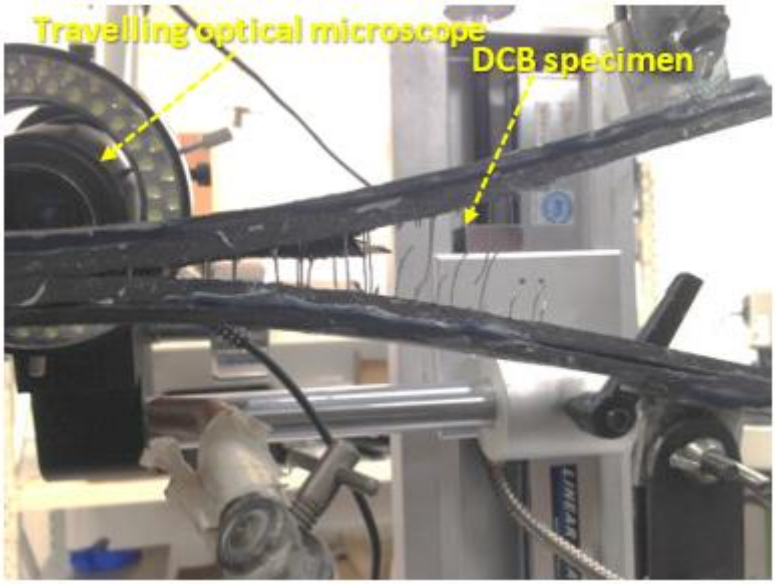

Fig. 3.5: *DCB test for measuring the mode I interlaminar fracture toughness properties.*

3.2.3 Mode II Interlaminar Fracture Toughness Test

The mode II interlaminar fracture toughness properties of the composite materials were measured using the end notch flexure (ENF) test. The ENF specimen was 250 mm long and 25 mm wide (Fig. 3.4b), and contained a 60 mm long mid-plane pre-crack at one end formed using 25 µm thick PTFE film. Like the DCB specimens, the ENF samples were strengthen with carbon-epoxy tabs to avoid transverse fracture and ensure delamination fracture. The ENF samples were loaded in three-point bending at a thickness-to-support span ratio of nearly 1-to-20. The test was performed by applying a monotonically increasing bending displacement to the mid-span point of the ENF specimen at the rate of 0.5 mm/min to force delamination crack growth, as shown in Fig. 3.6.

The mode II interlaminar fracture toughness (G_{II}) was calculated using:

$$G_{II} = \frac{9a^2 Pc^{\delta}max}{2b(2L^3 + a^3)} \quad (2)$$

where P is the applied bending force, b is the specimen width, and L is the support span length. As with the DCB test, three samples for each type of material were used to measure the mode II interlaminar fracture toughness properties.

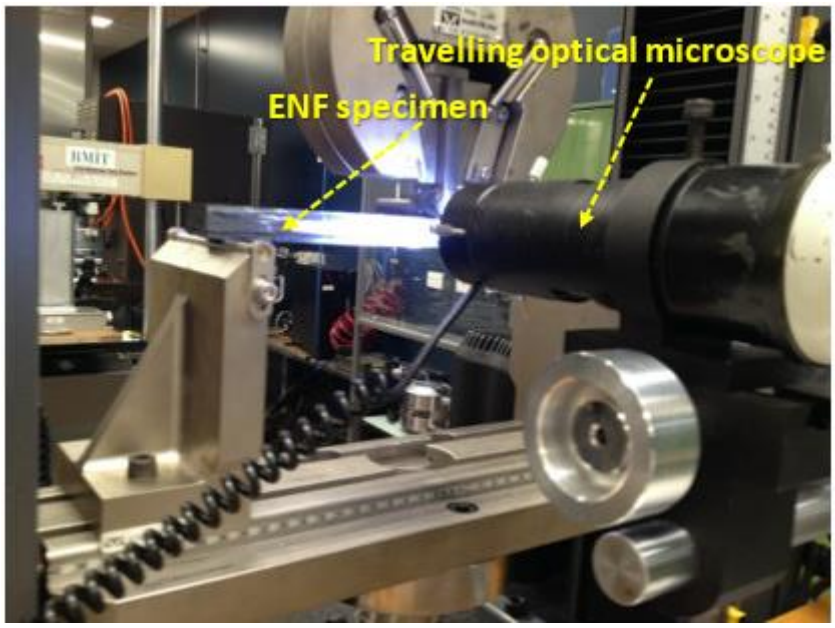

Fig. 3.6: *ENF test for measuring the mode II interlaminar fracture toughness properties.*

3.2.4 Crack Bridging Traction Load Tests

The modes I and II crack bridging traction laws for the woven z-binders were measured using through-thickness tension (crack opening) and transverse shear (crack sliding) tests, respectively. Such tests are often used to measure the bridging traction load generated by z-binders, z-pins and other types of through-thickness reinforcing fibres under mode I and mode II interlaminar loads [e.g. [99, 100]. The test specimens were manufactured with the same carbon fibre–epoxy laminate used in the DCB and ENF specimens. The specimens were 30 mm long and 25 mm wide, and consisted of two halves of the carbon-epoxy material separated at the mid-plane by thin PTFE film. The specimens contained a 4 x 4 array of woven z-binders made of copper, stainless steel or carbon. The modes I and II cracking bridging traction laws were measured by applying a crack opening or crack sliding force to the specimen at a constant rate of 1 mm/min until all the z-binders had failed, as shown in Fig. 3.7 and Fig. 3.8. The applied force was divided by the number of z-binders to determine the average bridging traction load per z-binder. Two samples of each type of 3D composite material were tested under identical conditions.

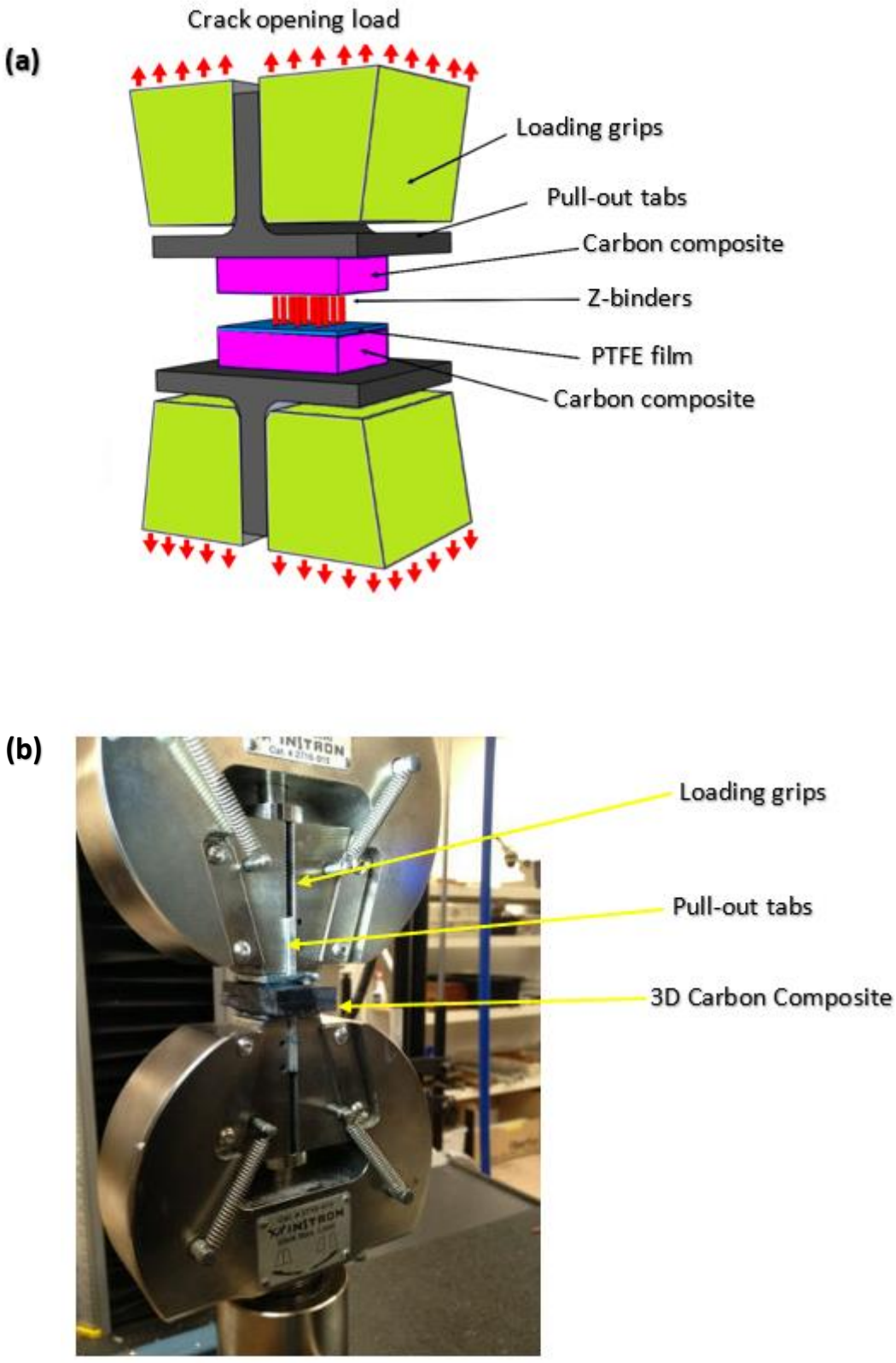

Fig. 3.7: *(a) Schematic and (b) photograph of mode I z-binder traction load test.*

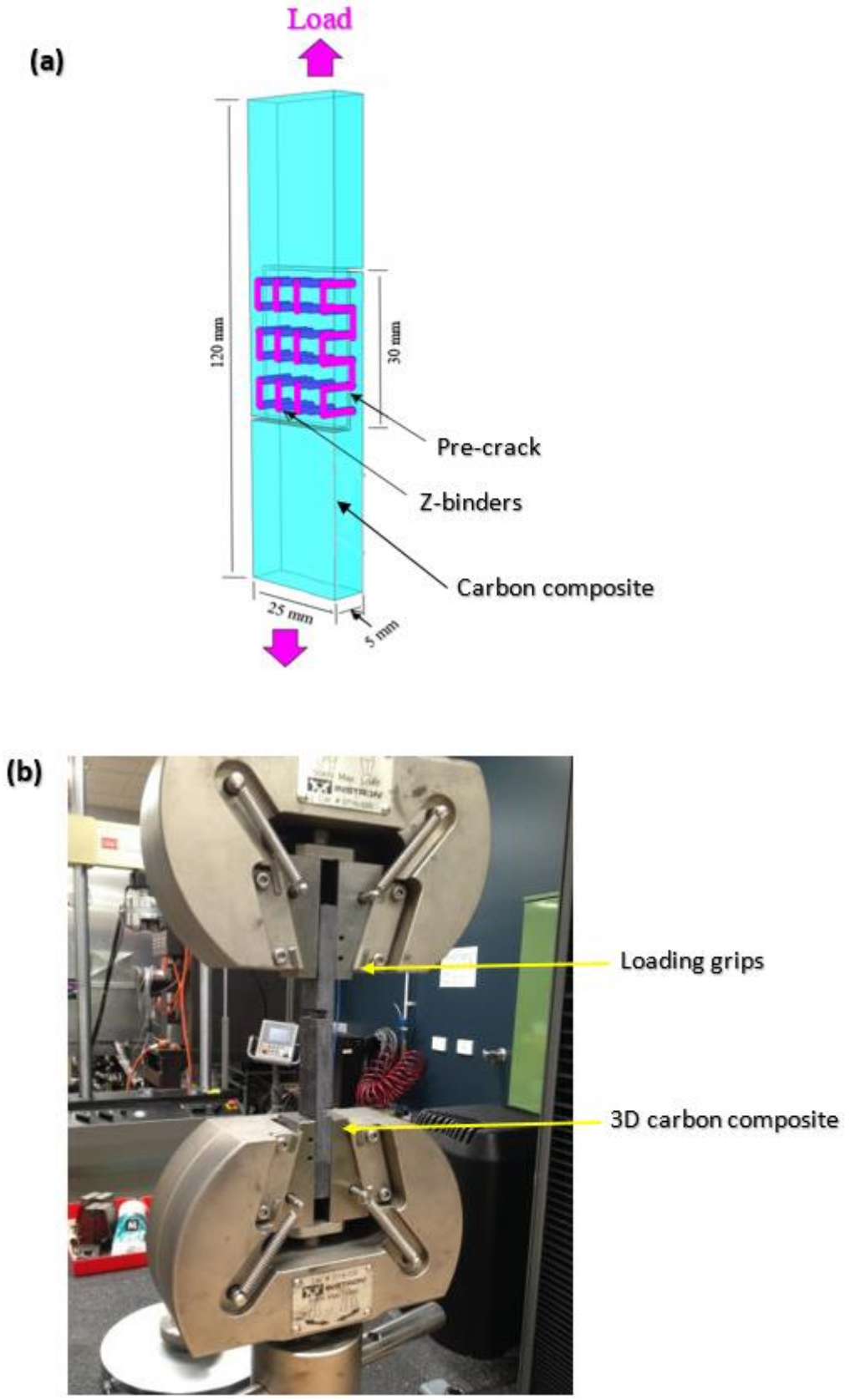

Fig. 3.8: *(a) Schematic and (b) photograph of mode II z-binder traction load test.*

3.2.5 X-ray computed tomography

The mode I and mode II specimens were inspected using an X-ray micro-computed tomography machine (μ-CT, DE Phoenix v/tome/xS), which is shown in Fig. 3.9. The X-ray images were taken using the machine operation settings of 280 μA current and 60 kV voltage. During inspection the DCB and ENF specimens were rotated through the X-ray beam in increments of 0.2° for an average exposure time of 333 ms and a voxel size of 19 μm. After the scan, all the images were post-processed by using volume analysis tool (VG Studio Max software).

Fig. 3.9: *Micro-computed x-ray (CT) imaging machine (DE Phoenix v/tome/xS).*

3.3 RESULTS AND DISCUSSION

3.3.1 Mode I Interlaminar Fracture Toughness

Applied load-crack opening displacement curves are presented in Fig. 3.10 for the 2D laminate (control) and the 3D woven composites. The volume fraction of z-binder in the 3D composites is the same (high) and curves with the same profiles were measured at the lower z-binder content. There was good repeatability in the load-crack opening displacement results when repeated measurements were performed, as shown for example for the 3D woven composite containing carbon z-binders. The curves initially increase linearly with displacement, and during this phase there is no delamination crack growth from the pre-crack in the DCB specimen. The onset of non-linearity in the curves corresponds to the initiation of delamination crack growth, and then the load decreases with increasing displacement as the delamination propagates along the mid-plane of the DCB specimen. The z-binders increase

the load required to force delamination crack growth, with the magnitude increasing in the order: copper, carbon and steel.

The mode I crack growth resistance (R-) curves for the 2D laminate and 3D woven composites are presented in Fig. 3.10(b). The curves for the 3D composite had the high z-binder content. The curves show the effect of increasing delamination crack length (Δa), defined by the distance between the delamination crack tip (a) and pre-crack tip (a_o), on the mode I interlaminar fracture toughness (G_I). The effect of increasing z-binder content on the steady-state fracture toughness (G_{Ic}) values is shown in Fig. 3.10(c). The mode I toughness values for the 2D laminate are relatively low over the entire length of delamination crack growth. The experimental results show that the z-binders increase the toughness. However, the magnitude of the toughening is dependent on the z-binder material, with copper being the less effective. Table 3.4 shows G_{Ic} values for other types of 3D composites compared with the materials used in this study. The values show greater improvement in steady-state fracture toughness values for steel z-binder. Whereas, carbon z-binder shows moderate improvement, and copper shows the least improvement in G_{Ic} values.

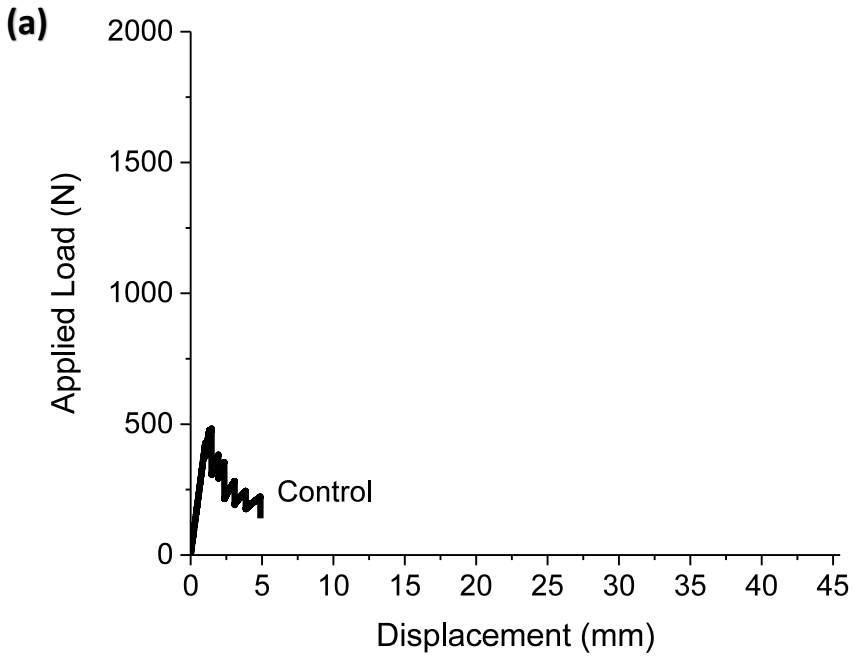

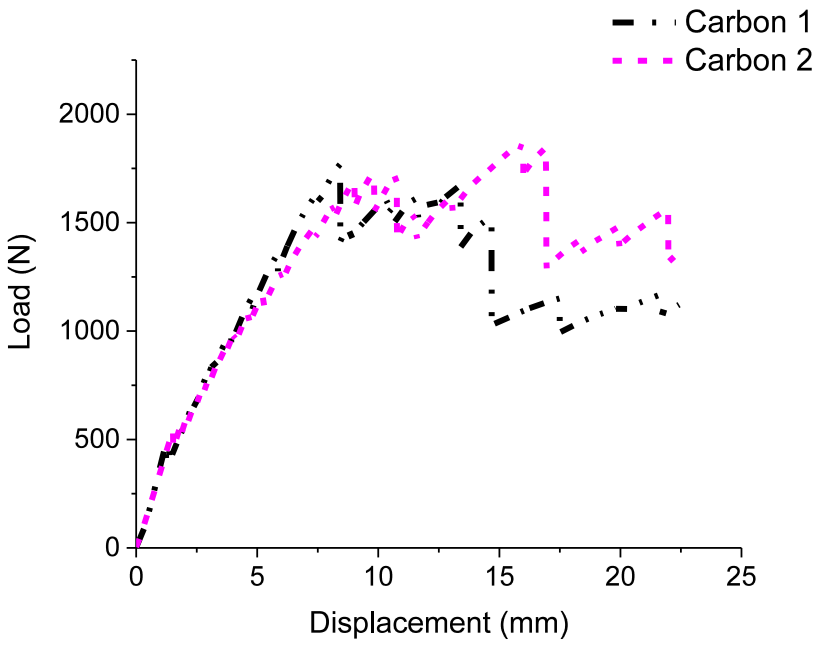
Carbon 1
Carbon 2
Load (N)
2000
1500
1000
500
0
0
5
10
15
20
25
Displacement (mm)

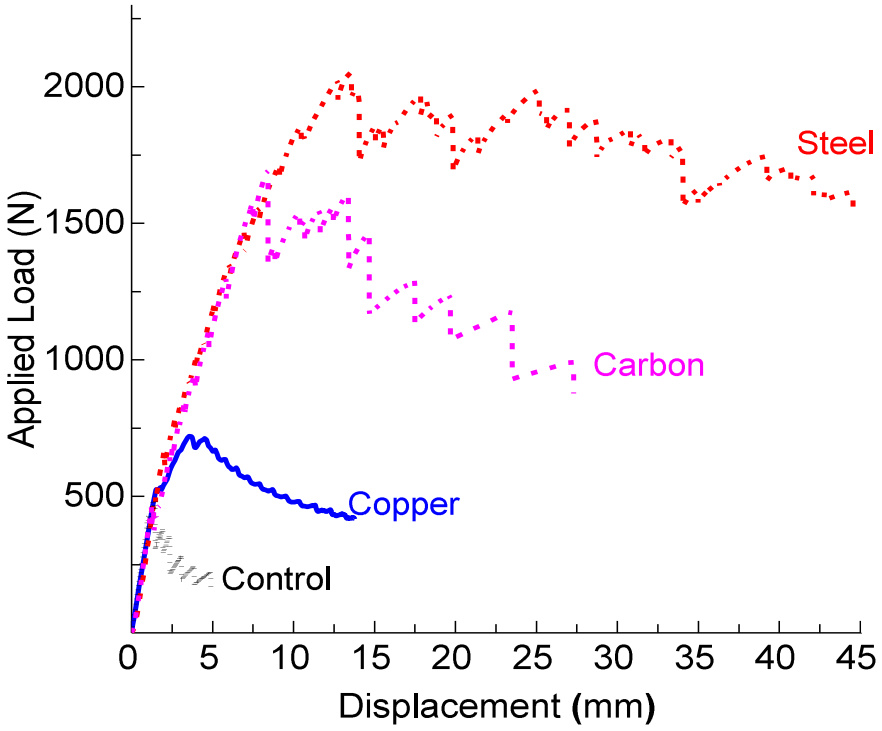
Applied Load (N)
2000
1500
1000
500
Steel
Carbon
Copper
Control
0
5
10
15
20
25
30
35
40
45
Displacement (mm)

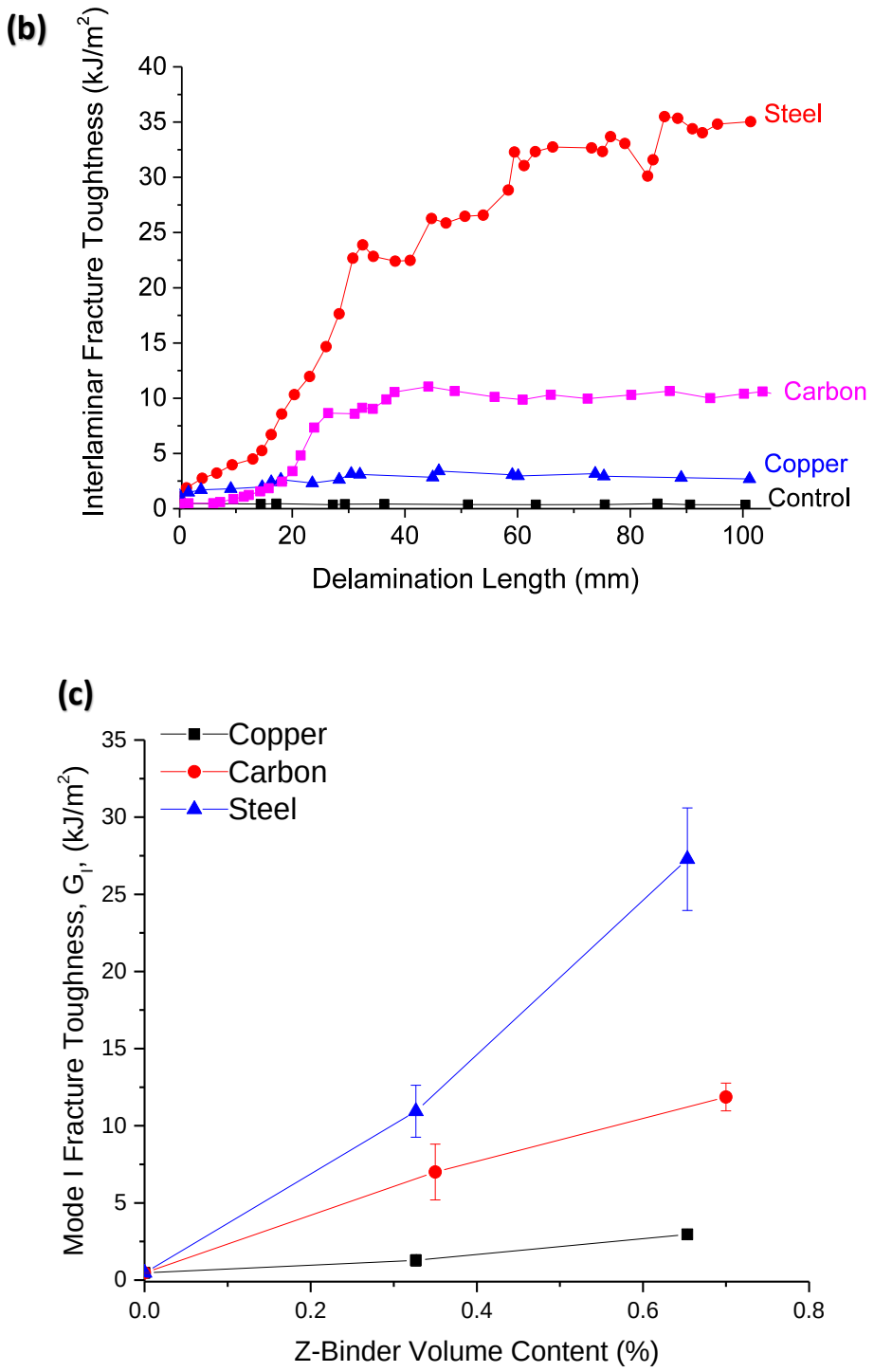

Fig. 3.10: *(a) Examples of mode I traction load-crack opening displacement curves. Shown are curves for the 2D (control) laminate and 3D woven composite containing carbon z-binders. (b) Mode I R-curves for the 2D laminate and 3D woven composites. (c) Effect of z-binder content on mode I steady-state fraction toughness. The z-binder content to the 3D woven composites in (a) and (b) is high.*

Table 3-4: *G_{Ic} values compared with other types of 3D woven composites.*

Composite	Z-binder type	Weave pattern	Z-binder volume content	G_{Ic} (kJ/m^2)	G_{Ic} percentage increase	Reference
Fibreglass vinyl-ester composite	Glass	Orthogonal	2.3 binder/cm^2	~1.4	~40	[46]
Fibreglass vinyl-ester composite	Glass	Layer-interlock	4.6 binder/cm^2	~1.2	~20	[46]
Carbon-epoxy composite	Carbon	Orthogonal	13.2%	~6.8	~580	[64]
Carbon-epoxy composite	Carbon	Hybrid (Orthogonal interlocked)	13 binder/cm^2	~2.6	~160	[49]
Carbon-epoxy composite	Carbon	Orthogonal	0.7%	~10.5	~650	[65]
Carbon-epoxy composite	Steel Copper Carbon	Orthogonal	1.13% 1.13% 1.3%	~28 ~2.5 ~10.5	~6900 ~525 ~2525	This study

The copper z-binder increases the mode I interlaminar fracture toughness by forming a short-length bridging zone along the delamination crack in the 3D woven composite, as shown in Fig. 3.11. This figure presents the cross-sectional view of a DCB specimen made of the 3D woven composite containing copper z-binders, a schematic image of the copper z-binder bridging zone (based on experimental observation), and a fractured copper z-binder on the delamination crack surface observed after DCB testing. The copper z-binder exerts mode I bridging stresses across the delamination crack which increases the fracture toughness, as shown by the traction load-crack opening displacement curve in Fig. 3.12. (The curve was measured using the mode I crack bridging traction load test, Fig. 3.7). Fig. 3.12 (a-c) for copper, carbon and steel z-binders respectively show good repeatability in traction load results. The copper z-binders bridging the delamination crack initially deform elastically before reaching a peak traction stress. Beyond this point the traction stress drops rapidly due to plastic deformation and necking of the copper z-binders leading to their fracture. The traction stresses generated by the copper z-binders are much lower than those generated by the steel and carbon, and this accounts in part for copper having a lower mode I toughening effect. Fig. 3.11(b) shows schematically the copper z-binders bridging the delamination

undergo a series of physical changes with increasing crack opening: elastic deformation (immediately behind the crack tip), plastic deformation and necking, and finally tensile rupture at the bridging zone length of ~10 mm. The copper z-binders fracture at the delamination plane and do not experience pull-out (Fig. 3.11c).

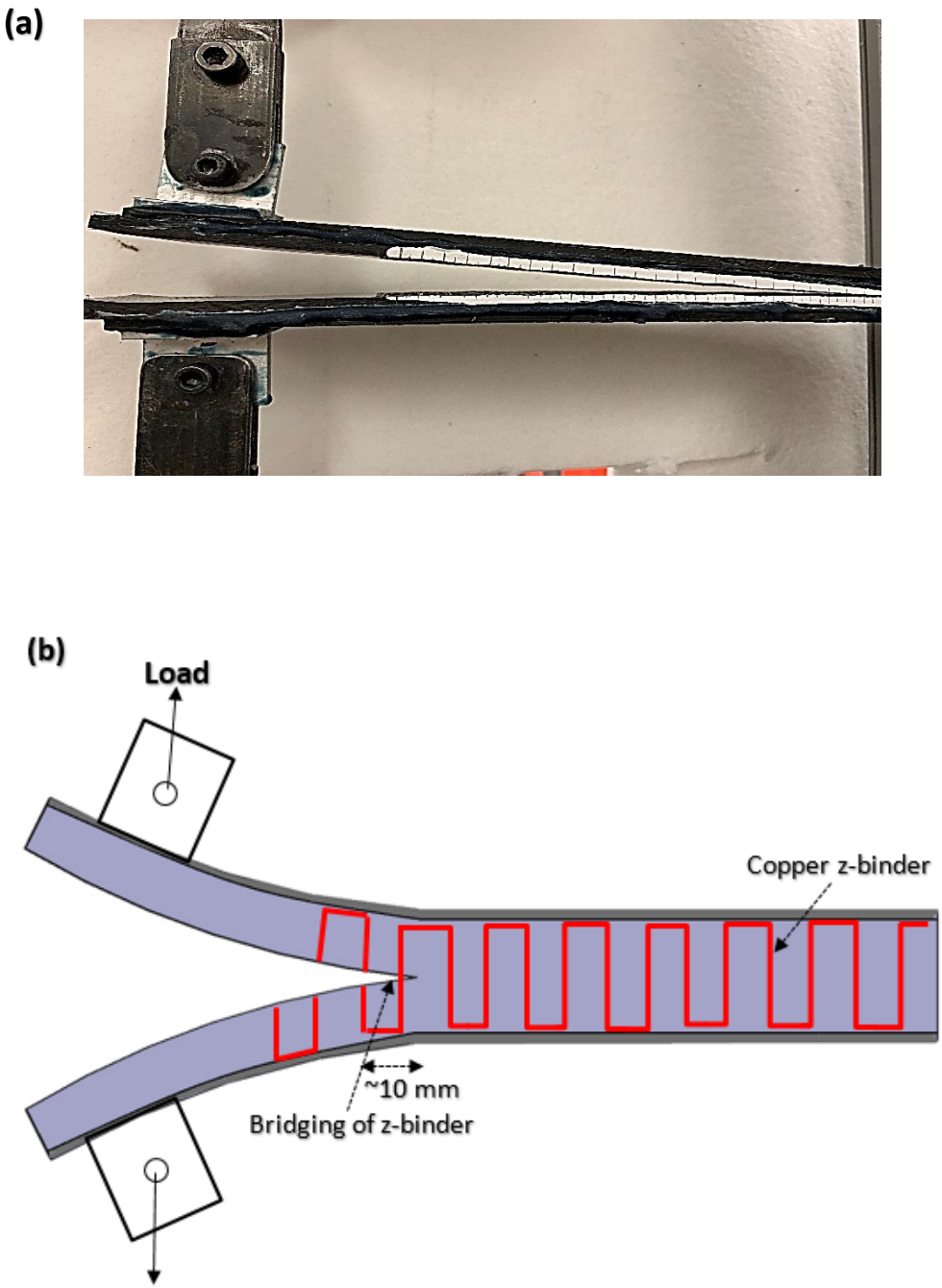

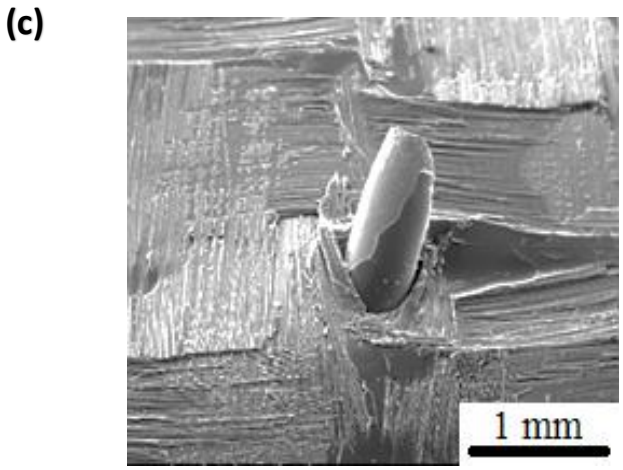

Fig. 3.11: *Mode I delamination fracture of the 3D woven composite with copper z-binders. (a) Side-view of DCB specimen. Note the visible absence of bridging z-binders. (b) Schematic of crack bridging mechanism. (c) Fractured z-binder on delamination crack surface. The direction of crack growth in (a) and (b) is left to right.*

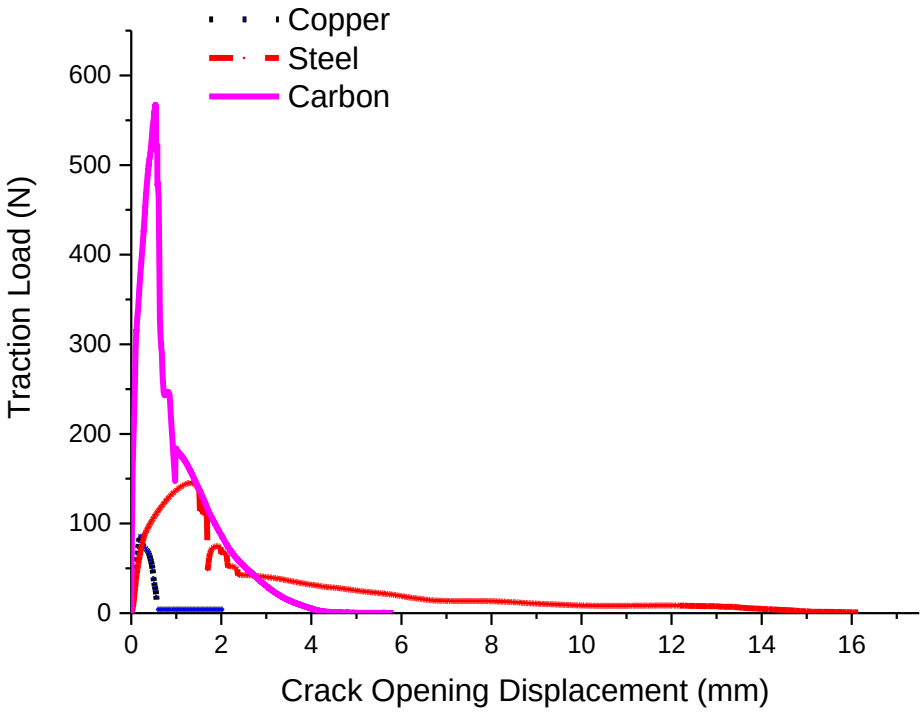

Fig. 3.12: *Mode I crack bridging traction load-displacement curves for the z-binders (a) copper, (b) carbon and (c) steel. In each case two curves are shown, and (d) traction load-displacement curves for all z-binders.*

The carbon z-binders, which have an intermediate toughening effect compared to the copper and steel, also increase the mode I fracture toughness by forming a large-scale bridging zone, as shown in Fig. 3.13. Shown is a DCB specimen of the 3D woven composite containing carbon z-binders, a schematic illustration of the bridging mechanism of these z-binders, and a fractured z-binder that experienced pull-out failure. The crack bridging traction stresses and mechanisms induced by the carbon z-binders are different to the copper, and this accounts for its stronger mode I interlaminar toughening effect. The z-binder pull-out traction tests reveal that the carbon generated a peak mode I traction stress that was much higher (~3x) than the copper (Fig. 3.12). This is because the tensile stress limit of the carbon tows is higher than the copper z-binder (see Table 3.1). Also, the carbon generates higher traction forces beyond the peak stress leading to larger crack opening displacement values than the copper. The carbon z-binders do not fracture at the delamination crack plane, but instead break at the bend radius where they are forced to bend sharply from the in-plane to through-thickness direction. It is believed failure occurs because of localised damage to fibres in the carbon tow during the 3D weaving process. Fibrous z-binders are damaged during the bending actions required to insert them in the through-thickness direction of 3D woven fabrics [34]. Morales [101] measured a 75% reduction to the tensile failure stress of carbon tows due to bending and other actions applied during through-thickness stitching. Therefore, it is believed the carbon z-binders are most damaged and weaken at the bend radius that causes failure here rather than at the delamination crack plane. After breaking at the bend radius, the fractured carbon ligament is pulled from the composite under increasing crack opening, and this process generates high frictional traction stresses which did not occur with the copper. Due to these processes, the carbon z-binder creates a bridging traction zone along the delamination crack in the DCB specimen which is 20-30 mm long, and therefore longer than the copper (only ~10 mm). The longer bridging zone length combined with the higher bridging stresses results in the carbon z-binder increasing the mode I interlaminar toughness more than copper.

(a)

(b)

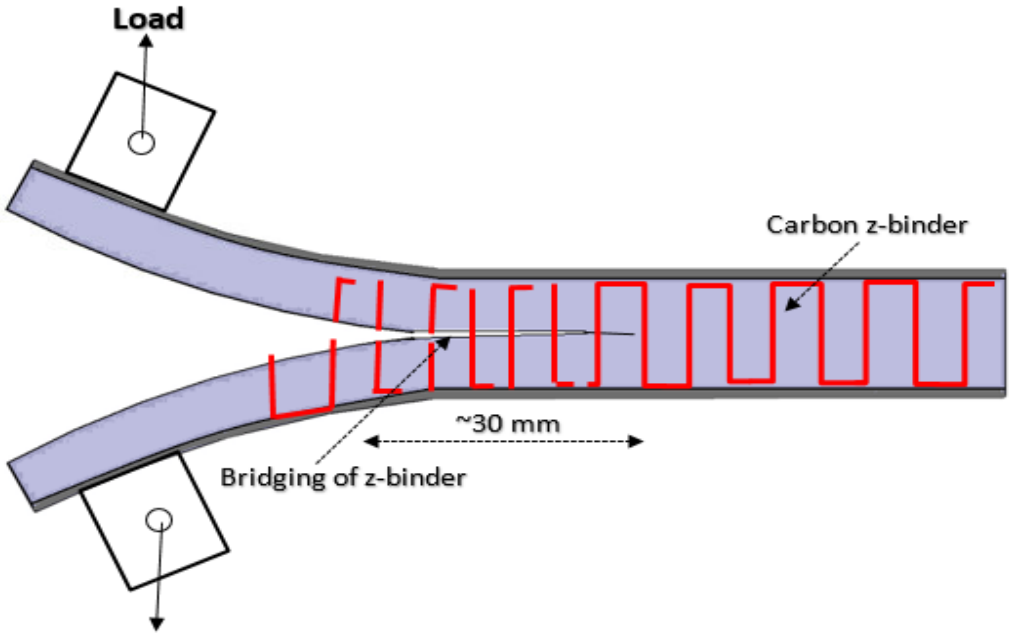

(c)

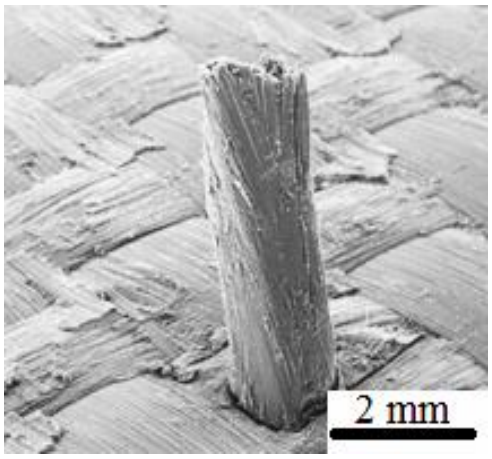

Fig. 3.13: *Mode I delamination fracture of the 3D woven composite with carbon z-binders. (a) Side-view of DCB specimen. (b) Schematic of crack bridging mechanism. (c) Fractured z-binder on delamination crack surface. The direction of crack growth in (a) and (b) is left to right.*

The steel z-binder has an extraordinary strong mode I toughening effect, with the steady-state toughness value being ~28 kJ/m^2 for the highest content (which was only 0.13 vol%). This toughness value is much higher than that reported for composites toughened using other techniques, such as carbon nanoparticles (typically under 3-4 kJ/m^2) e.g. [60, 102], oxide nanoparticles (less than ~0.6 kJ/m^2) e.g. [103], rubber particles (below ~1.5 kJ/m^2) e.g., [104, 105] interleaves (under ~1.5-3 kJ/m^2) e.g., [106-108] short fibres (below ~1-2 kJ/m^2) e.g., [109, 110] stitches (under 5-10 kJ/m^2) e.g. [111] and z-pins (less than 10-15 kJ/m^2) e.g. [112-114]. It is also much higher than previous reported mode I interlaminar toughness values for other types of 3D woven composites containing fibre-based z-binders [46, 58, 64, 95, 96]. To the author's knowledge, the mode I toughness of ~28 kJ/m^2 is the highest value ever reported for a toughened composite material.

The high toughening effect of the steel z-binder is due to its capacity to generate and maintain high bridging traction stresses to very large crack opening displacement, as shown in Fig. 3.14. The steel z-binder generated a bridging zone along the delamination crack in the DCB specimen which is much longer (up to ~60 mm) than the zones created by the copper (~10 mm) and carbon (~20-30 mm), and this is due to the very high failure strain limit of the steel (~60% as reported in Table 3.1). Therefore, even though the peak mode I traction stress

generated by the steel z-binder is only ~50% of that for the carbon (see Fig. 3.12), the capacity of the steel to generate a longer bridging traction zone containing a higher number of z-binders contributes significantly to the very high interlaminar toughness. Furthermore, the bridging steel z-binders break inside the 3D woven composite at a location well away from the delamination crack. The broken ligaments of the steel z-binder are pulled-out together under increasing crack opening, thereby doubling the pull-out traction stress compared to just one ligament pulled-out (which is the case for carbon). In summary, therefore, the exceptionally high mode I toughness induced by the steel z-binder is due to several key mechanisms: (i) high peak traction stress, (ii) high failure strain which enables a very long crack bridging zone to develop, and (iii) concurrent pull-out of the two broken ligaments of the z-binder.

(a)

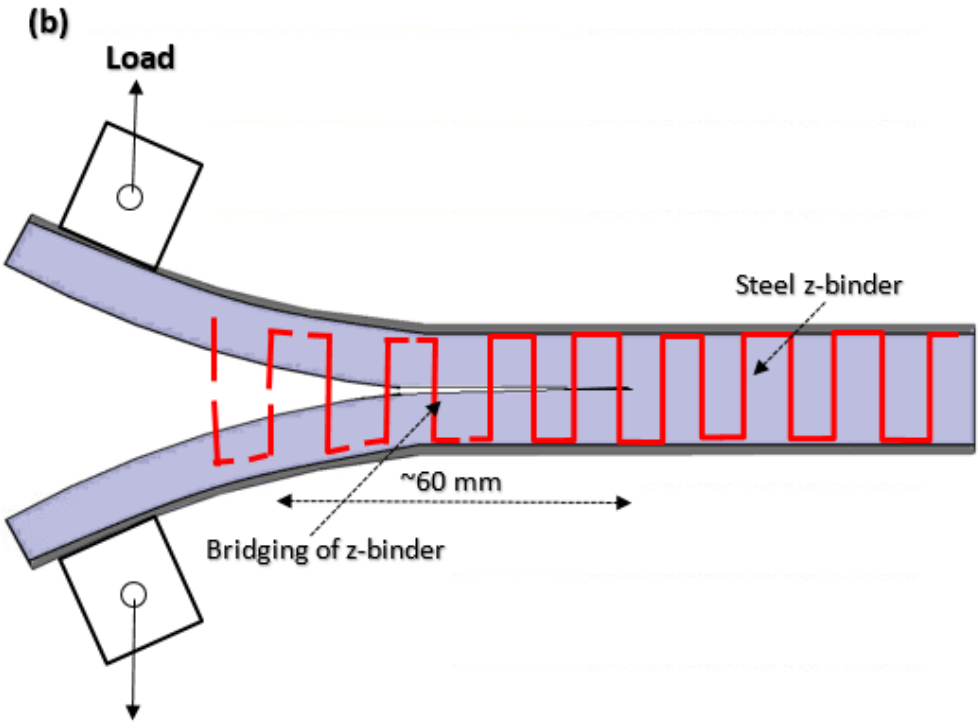

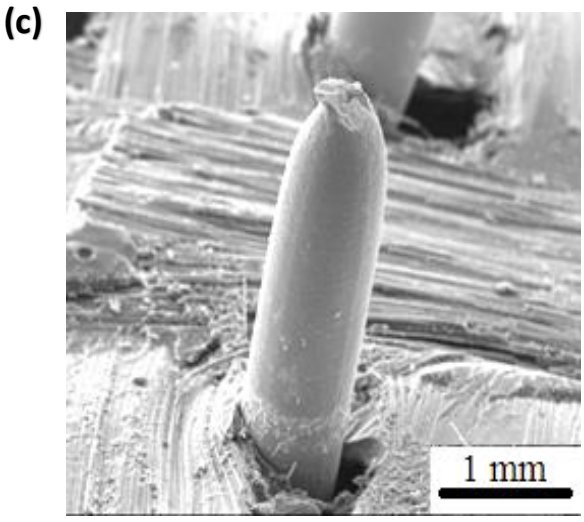

Fig. 3.14: *Mode I delamination fracture of the 3D woven composite with steel z-binders. (a) Side-view of DCB specimen. (b) Schematic of crack bridging mechanism. (c) Fractured z-binder on delamination crack surface. The direction of crack growth in (a) and (b) is left to right.*

3.3.2 Mode II Interlaminar Fracture Toughness

The measured bending load-deflection curves for the 2D laminate and 3D woven ENF specimens are shown in Fig. 3.15. The bending load-deflection curves in Fig. 3.15(a) show good repeatability. Similar to the mode I curves (Fig. 3.9), the mode II curves show an initial

elastic response when no crack growth occurs then a peak stress which corresponds with the onset of delamination propagation from the pre-crack tip, and finally a reduction to the load caused by crack extension along the mid-plane of the ENF specimens. The z-binders increase the applied bending loads to force crack growth, although the magnitude of the increases are much less than for mode I.

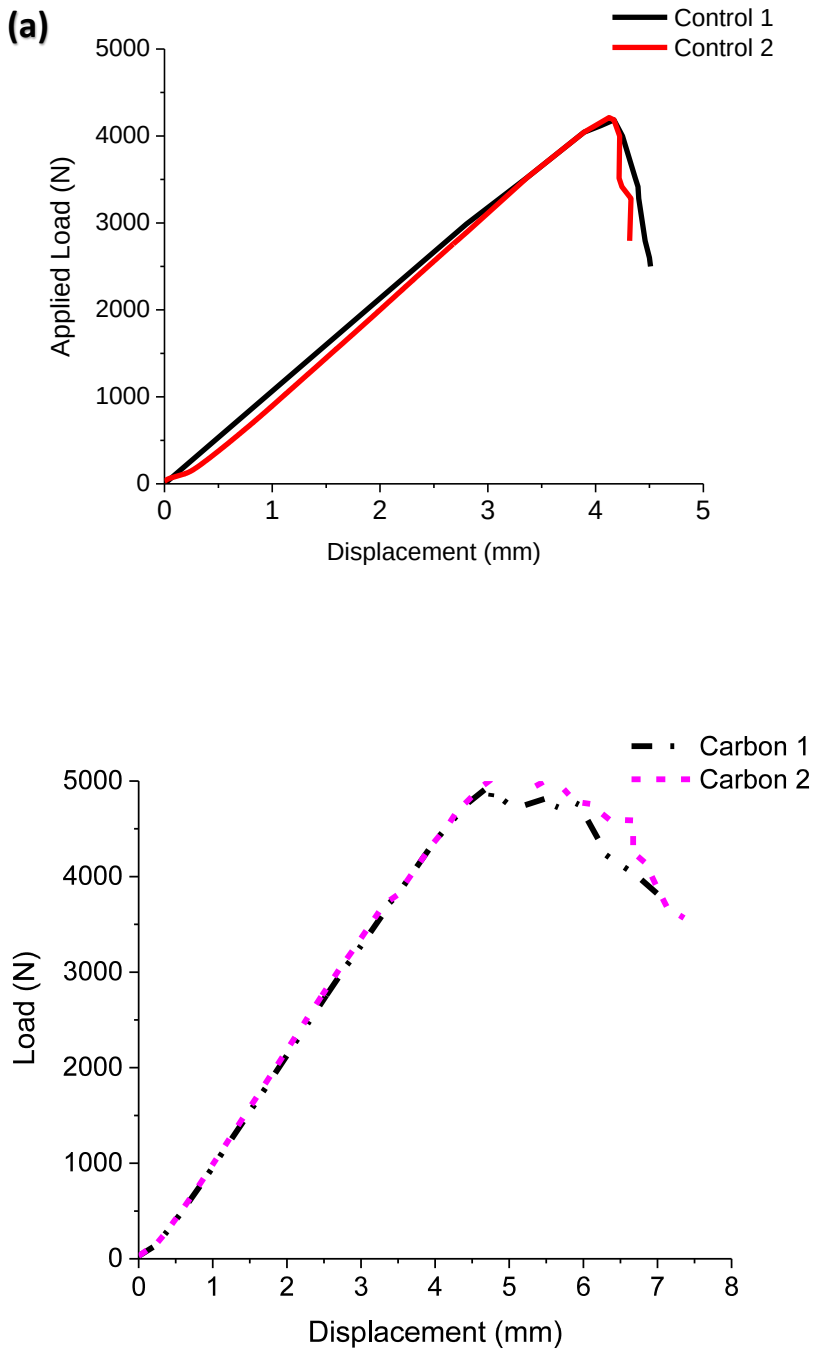

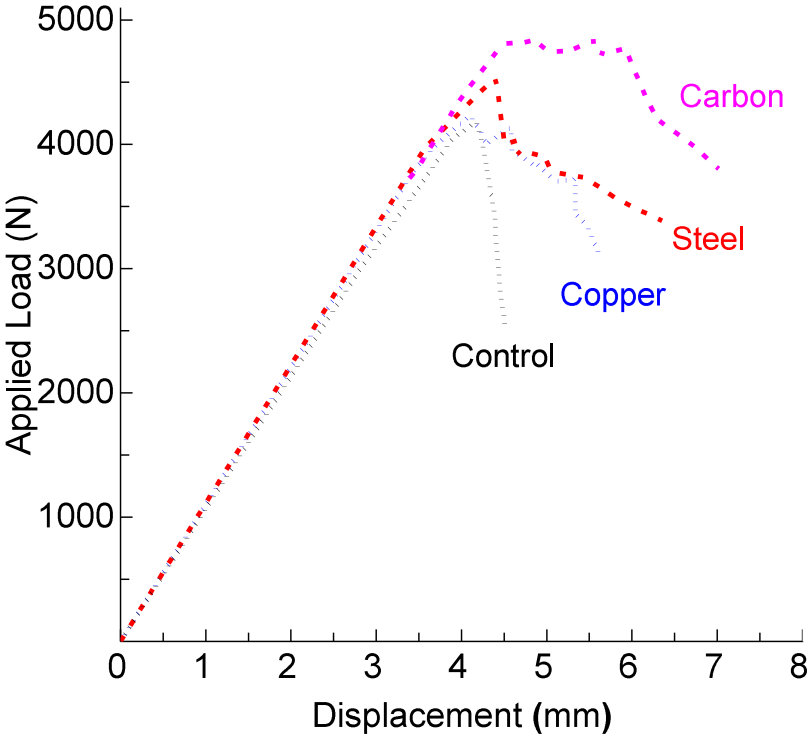
Applied Load (N)
5000
4000
3000
2000
1000
0
1
2
3
4
5
6
7
8
Displacement (mm)
Carbon
Steel
Copper
Control

(b)

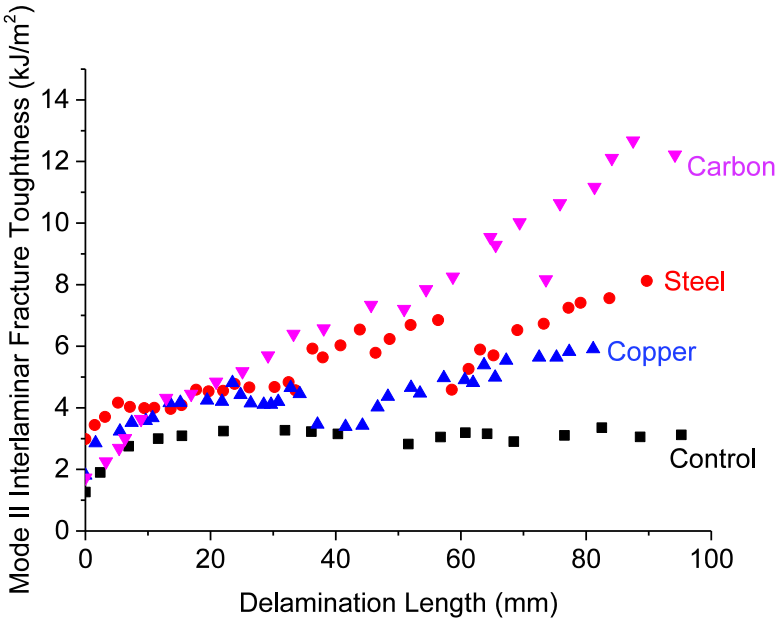
Mode II Interlaminar Fracture Toughness (kJ/m²)
14
12
10
8
6
4
2
0
0
20
40
60
80
100
Delamination Length (mm)
Carbon
Steel
Copper
Control

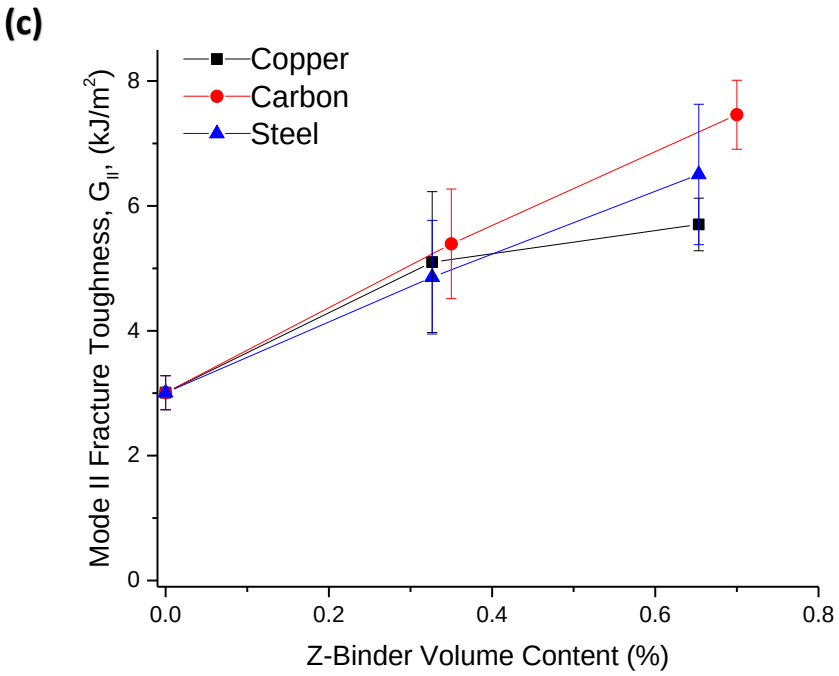

Fig. 3.15: *(a) Examples of mode II traction load-crack opening displacement curves. Shown are curves for the 2D (control) laminate and 3D woven composite containing carbon z-binders. (b) Mode II R-curves for the 2D laminate and 3D woven composites. (c) Effect of z-binder content on mode II steady-state fraction toughness. The z-binder content to the 3D woven composites in (a) and (b) is high.*

The mode II interlaminar fracture toughness properties of the composite materials were measured using the end notch flexure (ENF) test. The mode II R-curves are presented in Fig. 3.15b, for the 2D laminate (control) and the 3D woven composites. The R-curve for the 2D laminate increases over the initial ~10 mm of delamination growth and then reaches a steady-state value. The initial rise in the R-curve is due to increasing sliding resistance between the opposing surfaces of the growing delamination crack. The woven carbon fabric in the laminate causes a wavy crack path along the mid-plane of the ENF specimen. The asperities on the opposing crack surfaces interlock when sliding in opposite directions, and this increases the mode II toughness. The length over which the asperities interlock behind the crack front is ~10 mm, and this accounts for the initial increase to the mode II toughness. Fig. 3.15(b) also shows that all three types of z-binder increase the mode II interlaminar toughness, although the toughening induced by the steel is only slightly higher than copper

and both these metals are less effective than carbon. The effect of increasing volume content of z-binder on the mode II steady-state interlaminar fracture toughness is shown in Fig. 3.15(c). Within the bounds of experimental scatter, the 3D woven composites have the same toughness at the lower z-binder content. At the higher content, the toughening effect of steel and carbon were similar and only slightly higher than the copper. The results reveal that the improvements to the fracture toughness properties are much less sensitive to the material properties of the z-binder material under mode II than mode I interlaminar loading conditions.

The improvements to the mode II delamination resistance of the 3D composites was due to the z-binders forming a long crack bridging zone. Fig. 3.16-3.18 show the mode II interlaminar toughening processes induced by the different z-binders, and Fig. 3.20 shows their mode II bridging traction curves. Fig. 3.20(a,b,c) show good repeatability in mode II sliding traction curves for copper, steel and carbon z-binders, respectively. The copper and steel z-binders are elastically close to the crack front and plastically deformed in shear along the delamination crack plane, but did not fracture. The sliding displacements of the crack surfaces during ENF testing are much lower (typically less than 0.7 mm) than the crack openings during mode I DCB testing, as shown in Fig. 3.19. Consequently, the bridging metal z-binders are subject to much lower strains during the growth of a mode II delamination crack and do not reach the shear failure strain. This also accounts for the mode II R-curves rising continuously as shown in Fig. 3.15b, because the bridging zone created by the z-binders does not reach a fully developed condition. Furthermore, the absence of large strain plastic deformation and pull-out of the steel z-binders (which occurs under mode I interlaminar loading) is the reason for its lower toughening effect under mode II loading. The mode II bridging process of the carbon z-binder is different to the metals, and involved elastic deformation close to the crack front followed by rupture near the bend radius, although pull-out did not occur.

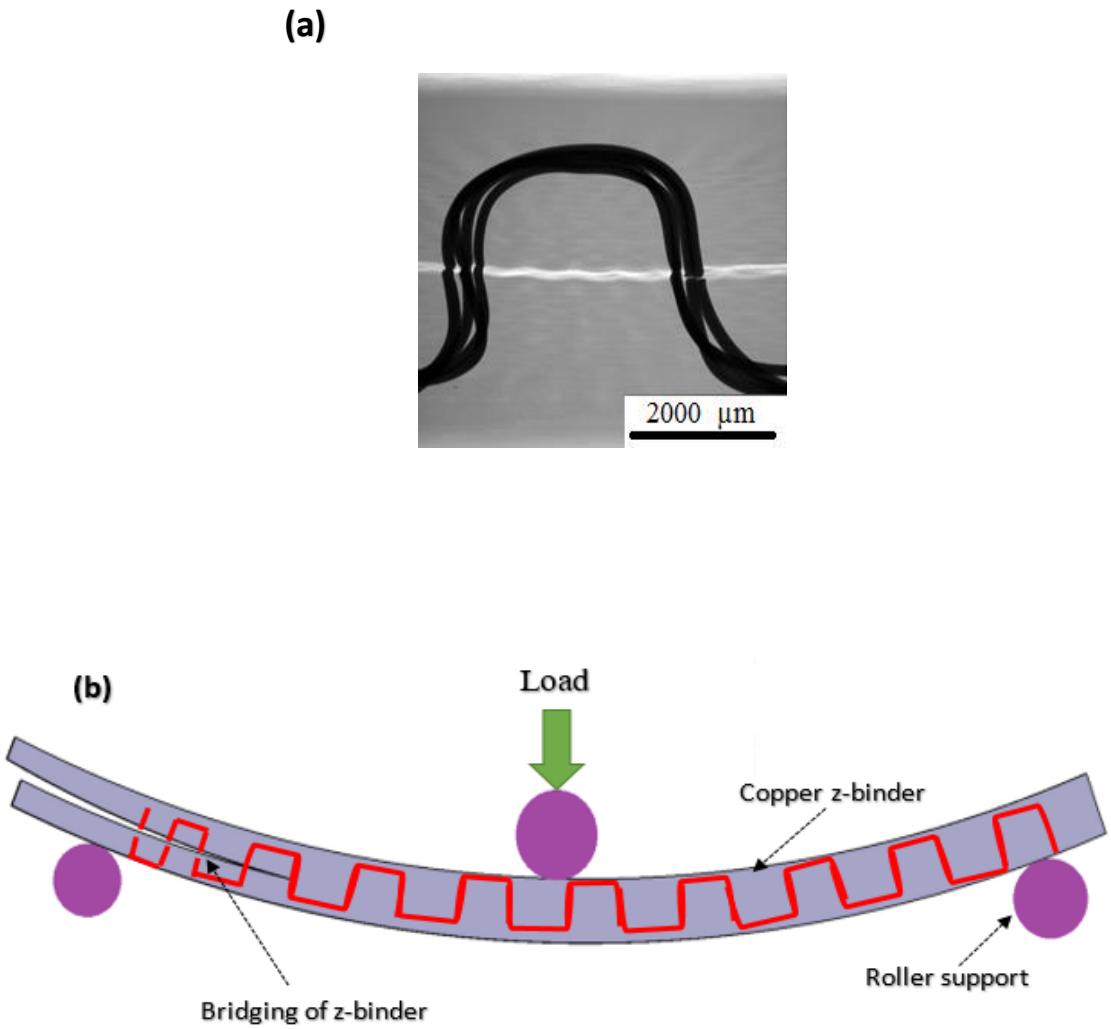

Fig. 3.16: *Mode II delamination fracture of the 3D woven composite with copper or steel z-binders. (a) Side-view of ENF specimen taken using X-ray computed microtomography showing localised plastic shear deformation of metal z-binders at the mode II delamination crack plane. (b) Schematic of crack bridging mechanism.*

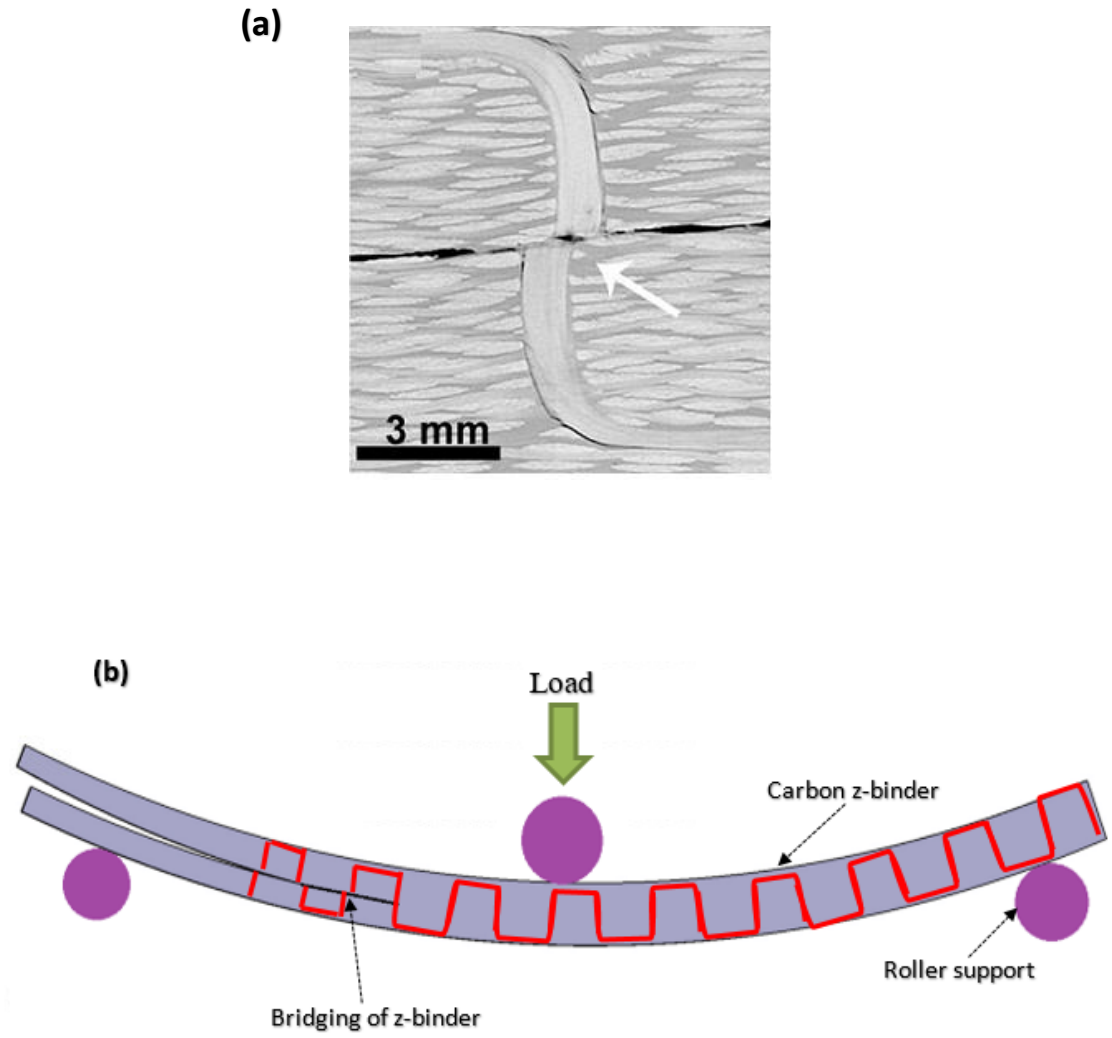

Fig. 3.17: *Mode II delamination fracture of the 3D woven composite with carbon z-binders. (a) Side-view of ENF specimen taken using X-ray computed microtomography showing localised shear fracture of a carbon z-binder at the mode II delamination crack plane.* (b) Schematic of crack bridging mechanism.

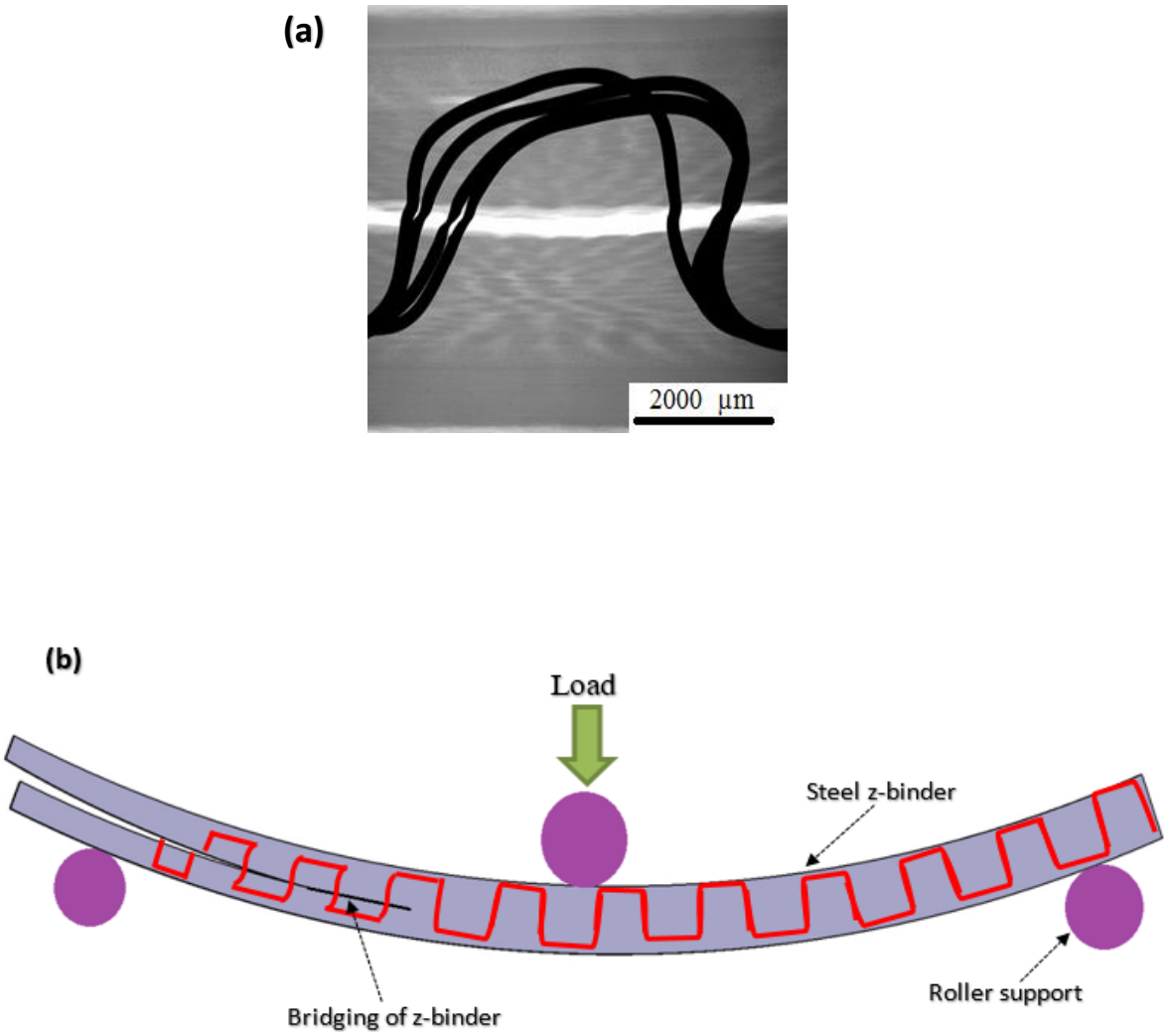

Fig. 3.18: *Mode II delamination fracture of the 3D woven composite with steel z-binders. (a) Side-view of ENF specimen taken using X-ray computed microtomography. (b) Schematic of crack bridging mechanism.*

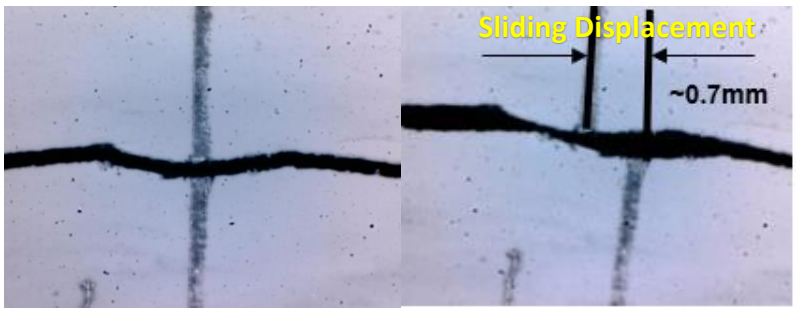

Fig. 3.19: *The sliding displacement of the crack surfaces during ENF testing.*

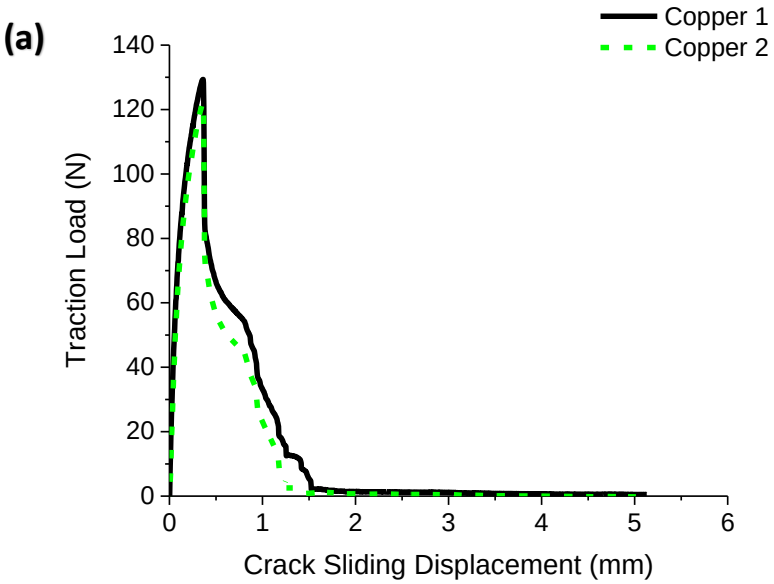
(a)
Copper 1
Copper 2
Traction Load (N)
Crack Sliding Displacement (mm)
0
20
40
60
80
100
120
140
0
1
2
3
4
5
6

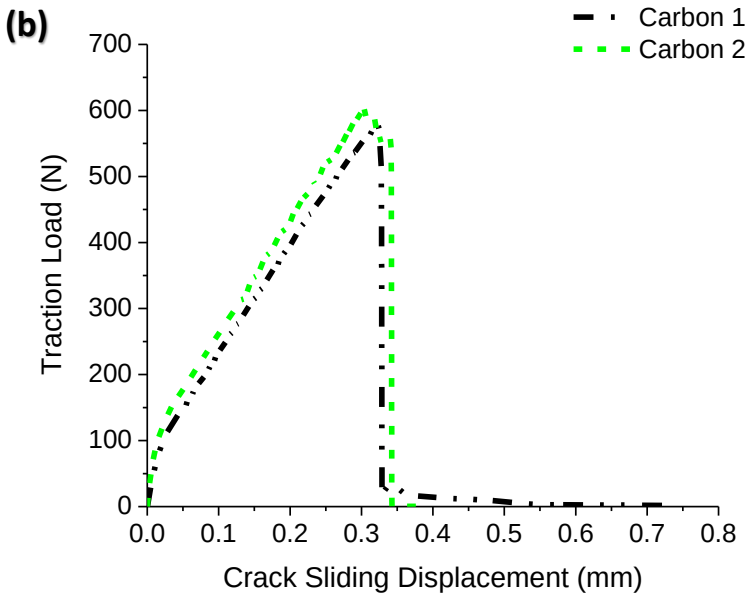
(b)
Carbon 1
Carbon 2
Traction Load (N)
Crack Sliding Displacement (mm)
0
100
200
300
400
500
600
700
0.0
0.1
0.2
0.3
0.4
0.5
0.6
0.7
0.8

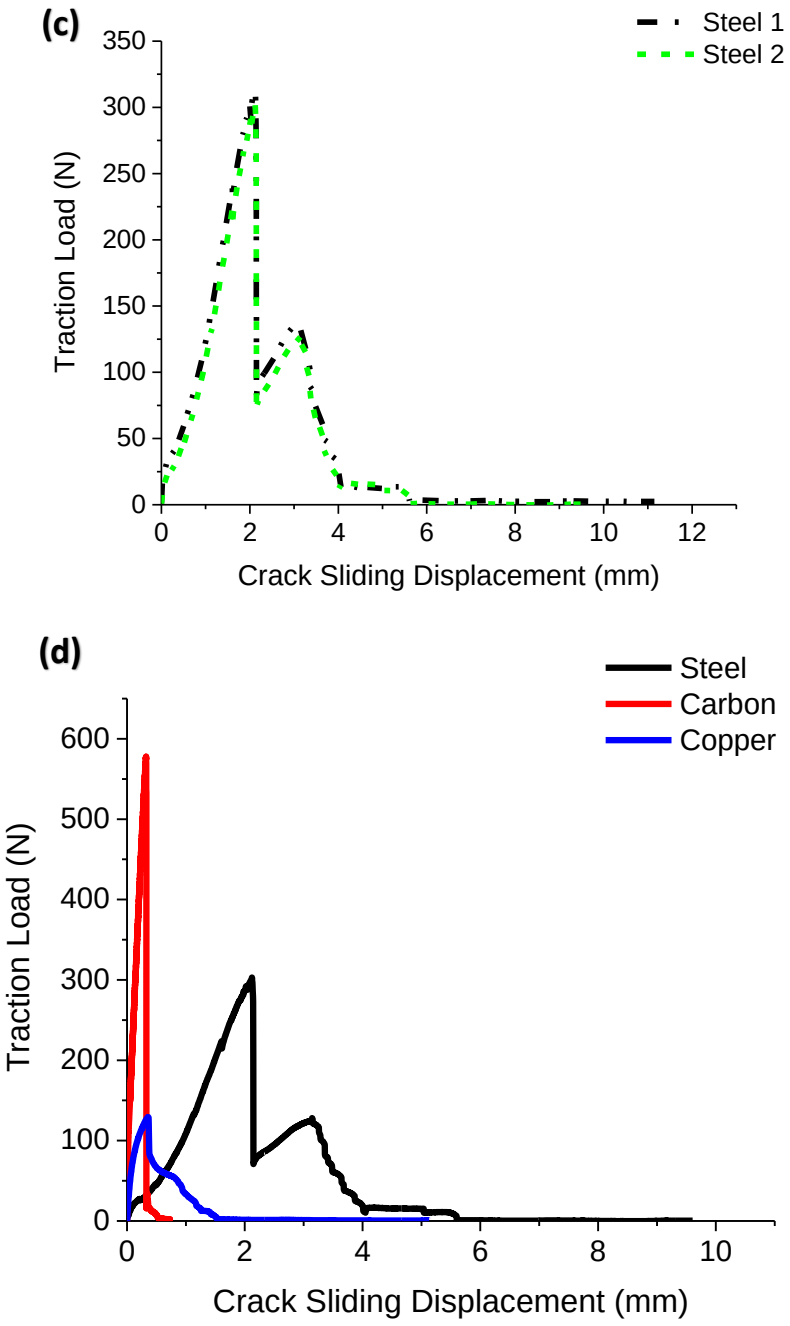

Fig. 3.20: *Mode II crack bridging traction load-displacement curves for the z-binders (a) copper (b) carbon (c) steel and (d) traction load-displacement curves for all z-binders.*

3.4 CONCLUSIONS

It is well known that through-the-thickness reinforcement using woven fibre-based z-binders is an effective way to increase the delamination resistance of composite materials [46, 58, 64, 65, 95, 96]. This study has demonstrated for the first time that woven z-binders made of a

high strength, ductile metal such as steel can improve the mode I interlaminar fracture toughness even more than carbon z-binders. The 3D woven material containing steel z-binders has an exceptionally high mode I toughness (~28 kJ/m^2), which is the highest interlaminar toughness value yet reported for a toughened composite. The high toughness is due to a multitude of toughening mechanisms induced by the steel z-binder under large crack opening displacement. These mechanisms include the formation of a very long crack bridging traction zone, which is the result of the high failure stress and ductility of the steel together with the fracture of the bridging z-binders occurring within the composite (and not at the delamination crack plane) resulting in the pull-out of the broken ligaments. However, relatively soft metals such as copper are less effective than carbon for the mode I delamination toughening of 3D woven composites.

The mode II interlaminar toughness properties are similar for the 3D woven composites containing z-binders made of carbon or metal. While the metal z-binders increase the mode II delamination resistance, the exceptionally high mode I toughening effect of the steel is not replicated under mode II delamination crack growth conditions. Both the carbon and metal z-binders increase the mode II interlaminar toughness via large-scale crack bridging, although the amount of shear sliding displacement is less than the amount of crack opening displacement under mode I and consequently the delamination toughening induced by the z-binders is less.

Chapter 4: Mode I and Mode II Delamination Fatigue Properties of 3D Woven Composites Containing Metal Z-binders

Abstract

This chapter presents an experimental investigation into the improvement to the mode I and mode II delamination fatigue properties of 3D composites reinforced with through-thickness woven z-binders. Three types of z-binders were used in this study - copper, stainless steel or carbon - are the same materials used in the previous chapter. The mode I and mode II fatigue properties were measured under cyclic displacement control conditions using Double Cantilever Beam (DCB) and End Notch Flexure (ENF) test specimens. All the z-binders were effective in resisting the initiation and growth of delamination cracking under mode I and mode II interlaminar fatigue loads, although the fatigue strengthening effect was greater for mode I. The mode I and mode II fatigue properties were increased due to the z-binders forming a large-scale extrinsic bridging zone along the fatigue crack. The mode I and mode II fatigue properties were also improved by increasing the volume content for all types of z-binder.

4.1 INTRODUCTION

Delamination cracking is a long-standing problem in fibre reinforced polymer composites. As already mentioned in previous chapter, delamination damage can result from high interlaminar loads, impact (e.g. hail stone, bid strike), edge stresses, or environmental degradation of the composite [115-117]. After the delamination crack develops, it can grow rapidly under relatively low cyclic interlaminar stresses caused by out-of-plane fatigue loading [113]. This fatigue crack growth behaviour is a concern in safety-critical composite structures. For example, composite aircraft structures must be designed to avoid delamination growth for a specific operational period involving variable fatigue loads. The delamination crack growth rate depends on many factors, which include the cyclic stress range, fatigue stress ratio (R-ratio), and the type of fatigue loading (e.g. mode I, mode II). Many techniques have been used to improve the resistance to delamination cracking induced by cyclic fatigue stress

loading, including using z-pins, stitches, z-anchors and three-dimensional weaving [43, 118-127]. These studies have proven that reinforcing composites in the through-thickness direction with fibres having high fatigue strength can increase the resistance against fatigue-induced delamination cracking. Of these techniques, z-pinning and 3D weaving show the most promising improvements to the delamination fatigue resistance. For example, Pegorin et al. [128] increased the fatigue resistance of a carbon-epoxy composite using z-pins. They reported that increasing the volume content of z-pins can increase the threshold stress intensity to initiate fatigue cracking by about 17 times and 8 times for mode I and mode II interlaminar fatigue loading, respectively. Zhang et al. [129] examined the effect of mode I cyclic loading on the crack bridging traction force generated by z-pins. It was found that the z-pin traction load decreased with an increasing the number of loading cycles.

Very little research has been performed on the interlaminar fatigue properties of 3D woven composites. Stegschuster et al. [64] studied the mode I and mode II interlaminar fatigue properties and fatigue strengthening mechanisms of a 3D woven composite reinforced with carbon z-binders. The z-binders promoted large improvements to the fatigue properties via large-scale crack bridging. Apart from this study, there is little published research on 3D woven composites.

This chapter presents an experimental investigation into the influence of the z-binder material and volume content on the mode I and mode II interlaminar fatigue properties of 3D woven composites. Composite materials containing different types of z-binders (steel, copper or carbon) in an orthogonal weave pattern was studied. The mode I and mode II interlaminar fatigue properties were measured over a wide range of cyclic stress intensity values ranging from the threshold condition to initiate slow crack growth up to the condition needed to cause fast, unstable fatigue crack growth. The failure behaviour of z-binders and the fatigue toughening mechanism were examined using scanning electron microscopy and X-ray computed tomography (CT).

4.2 MATERIALS AND EXPERIMENTAL METHODOLOGY

4.2.1 Composite materials and reinforcement process

The carbon fabric used in this study was the same as that used in the study reported in *Chapter 3*. Carbon-epoxy composites reinforced with copper, steel or carbon z-binders were manufactured as described in the previous chapter. The z-binders were manually inserted into 32 plies of the carbon fabric along the warp direction in straight, parallel rows with a repeating orthogonal pattern. The z-binder materials and weaving process were the same as in the previous chapter. The epoxy resin (diglycidyl ether of biphenol A (Sicomin SR8100)) and diamine hardener (Sicomin SD 8824) was used for the polymer matrix. A 2D (control with no z-binder) laminate and the 3D woven composites were manufactured using the vacuum bagging resin infusion process.

4.2.2 Mode I and mode II interlaminar fatigue testing

The 2D (no z-binder) and 3D woven composite materials were manufactured into double cantilever beam (DCB) and end notch flexure (ENF) test specimens for mode I and mode II interlaminar fatigue testing. The dimensions of the DCB and ENF samples are given in *Chapter 3* (Fig. 3.3). The specimens were initially subjected to interlaminar loading to sharpen the crack tip by growing the delamination up to ~5 mm. Both mode I and mode II fatigue testing was performed in the displacement control condition, and the fatigue crack were grown by increasing the number of load cycles under a constant cyclic strain energy release rate. A 10 Hz loading frequency was applied to the pre-cracked end of the DCB and ENF samples. The R-ratio, which is defined as the ratio of the minimum to maximum opening/bending displacements of the sample in one load cycle, and was set at 0.1. A E3000 Instron with a 3 kN load cell and MTS 100 kN machines were used for mode I and mode II fatigue testing, respectively. A travelling optical microscope was used to measure the fatigue crack length.

The DCB and ENF specimens were subjected to mode I and mode II fatigue loading over a range of equivalent cyclic interlaminar strain energy release rates, which is defined by [130, 131]:

$$\Delta G_{eq} = \left(\sqrt{G_{max}} - \sqrt{G_{min}}\right)^2 \quad (1)$$

where G_{max} and G_{min} are the maximum and minimum strain energy release rate values applied in one cycle. These values are calculated using:

$$G_{Imax} = \frac{3P_{max}\delta_{max}}{2b(a+|\Delta|)} \quad (2)$$

$$G_{Imin} = \frac{3P_{min}\delta_{min}}{2b(a+|\Delta|)} \quad (3)$$

where a is the total length of the crack, b is the sample width, and Δ is a correction factor.

The maximum and minimum mode II interlaminar strain energy release rate values, G_{II}, were calculated using:

$$G_{IImax} = \frac{9a^2P_{max}\delta_{max}}{2b(2L^3+3a^3)} \quad (4)$$

$$G_{IImin} = \frac{9a^2P_{min}\delta_{min}}{2b(2L^3+3a^3)} \quad (5)$$

where L is the support span length, a is the total crack length, and b is a sample width.

The mode II fatigue equivalent energy release rate ($\Delta G_{II,\,eq}$) is then determined using:

$$\Delta G_{II,eq} = \left(\sqrt{G_{IImax}} - \sqrt{G_{IImin}}\right)^2 \quad (6)$$

The Paris curves show a log-log linear region which can be described by:

$$\frac{da}{dN} = C\Delta^m \quad (7)$$

where C is a material constant and m defines the gradient of the curve. Values for m for the mode I and mode II fatigue conditions are discussed later.

The samples were subjected to a range of applied strain energy release rates by changing the displacement range, and the resulting crack growth rate (ASTM D6115). Paris curves were generated by plotting the fatigue crack growth rate against the cyclic strain energy release rate, ΔG_{eq}, for the 2D and 3D composites. The fatigue curve can be divided into three regions (as shown in Fig 4.1).

- Region I is a fast fracture zone where the crack growth rates accelerate rapidly. This region is above the growth rate of ~10^{-2} mm/cycle.

- Region II refers to a steady-state region and it is approximately linear. This region is typically between growth rates of ~10^{-5} and ~10^{-2} mm/cycle.
- Region III is a threshold region where the crack growth rate is very slow and typically starts from below ~10^{-5} mm/cycle.

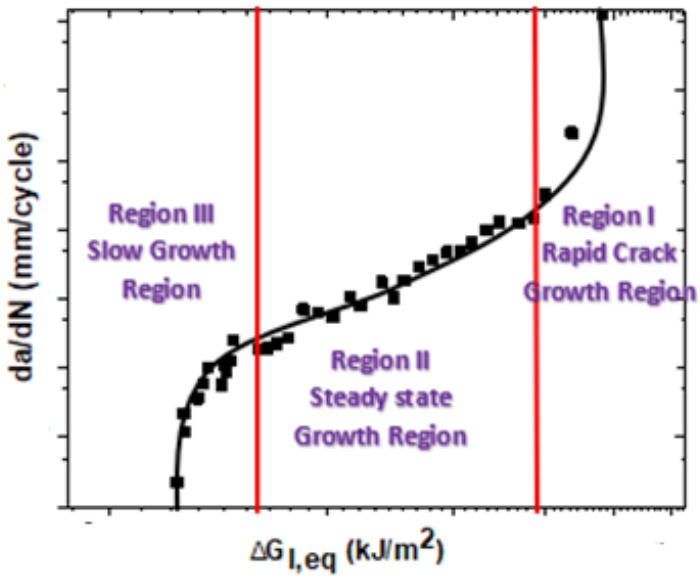

Fig. 4.1: *Typical fatigue crack growth curve (Paris curve) showing the three fatigue regions.*

4.3 RESULTS AND DISCUSSION

4.3.1 Mode I interlaminar fatigue properties

Paris curves of mode I cyclic stress intensity factor ($\Delta G_{I,eq}$) plotted against the delamination crack growth rate (da/dN) for the 2D (control) laminate and the 3D woven composites are shown in Fig. 4.2. Through-thickness weaving increased substantially the delamination fatigue resistance. The improvement in mode I fatigue crack growth resistance of the 3D woven composites was due to the large-scale bridging zone generated by the z-binders. The traction loads generated by the bridging z-binders slow the fatigue crack growth rate. This fatigue strengthening mechanism is common in 3D woven composites [49, 64, 70, 119]. The carbon and steel z-binders showed the greatest improvements in the mode I fatigue resistance, whereas the copper z-binder showed the least improvement (Fig. 4.2).

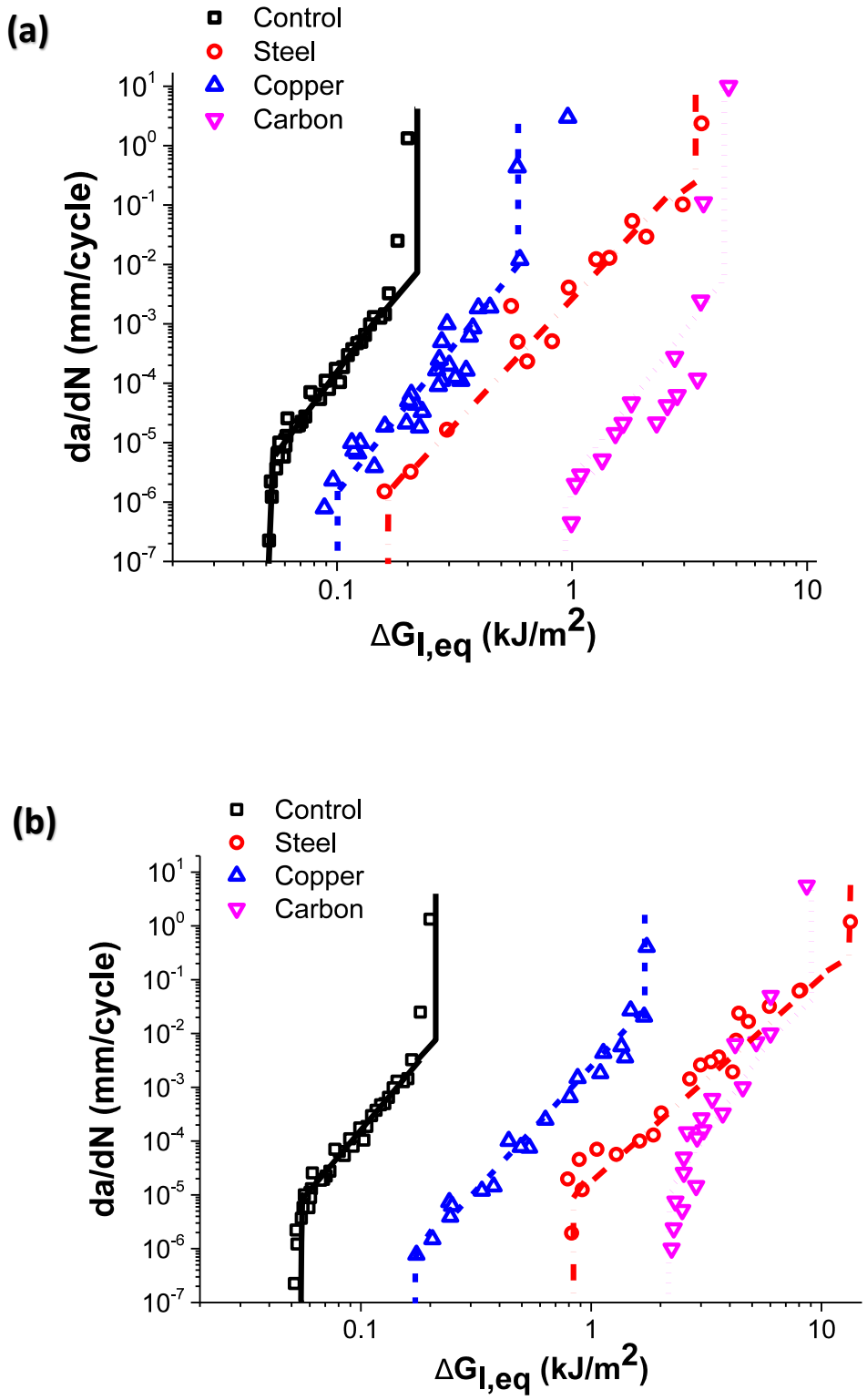

Fig. 4.2: *Mode I Paris curves for the 2D and 3D composites reinforced with steel, copper or carbon z-binders with (a) low and (b) high volume contents.*

There is a significant scatter in the fatigue crack growth rate data for the 3D composites compared with 2D laminate. The scatter in the crack growth rates is due to the unstable slip (crack extension)-stick (crack arrest) phenomenon. It was observed during the fatigue test that when the z-binders failed at the rear of the bridging zone (where the crack opening is highest), there was a sudden acceleration in the crack growth rate. On the other hand, when the fatigue crack front reached the z-binders at the front of the bridging zone, there was a slow-down in the growth rate. The acceleration and deceleration in the mode I crack growth rate causes the scatter in the crack growth rates for the 3D composites. The scatter in the crack growth rate data is also reported for other types of 3D composite with through-thickness reinforcement [64, 113, 114].

The effect of z-binder volume content on the mode I delamination fatigue resistance of the 3D woven composites is also shown in Fig. 4.2. The 3D composites show improved resistance to mode I fatigue crack growth for the low and high contents, although the fatigue resistance increased with the z-binder volume content. Mouritz et al. [71] reported that using a relatively modest amount (3.8%) of z-binder increased the mode I fatigue strength of a 3D woven composite, and increasing the z-binder content up to 9.6% showed further improvement. The increase in mode I fatigue properties is due to a greater number of z-binders bridging the fatigue crack which slowed the crack growth rate.

The effect of z-binder volume content on the improvement in threshold strain energy release rate value ($\Delta G_{eq,th}$) to initiate mode I fatigue crack growth is shown in Fig. 4.3. The improvement in the threshold strain energy release rate for the low and high contents is due to the generation of higher crack bridging traction load and energy under mode I cyclic loading.

The gradient of the Paris curve (m) defines the sensitivity of a material to variations in the cyclic stress intensity range. The m values for the 3D woven composites containing steel or copper z-binders are slightly lower than the 2D laminate. However, the difference in gradient values may not be statistically significant due to the high amount of scatter in the

crack growth rate data. It is hard to conclude whether the z-binder has any significant effect on the *m* value.

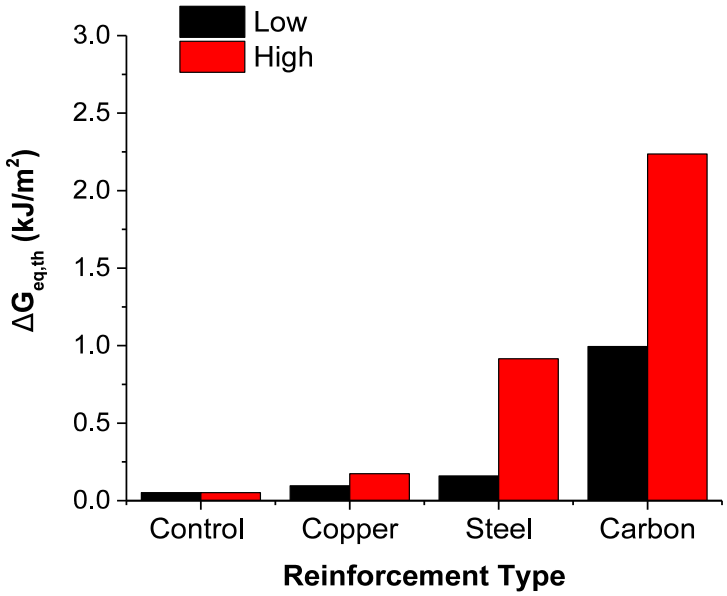

Fig. 4.3: *Effect of z-binder material on mode I ΔGeq,th value to initiate fatigue crack growth for the 2D laminate and 3D woven composites.*

Table 4-1: *Mode I delamination m values of the 2D and 3D composites.*

Z-binder material	**Z-binder volume content**	***m***
Control (no z-binder)	0%	5.35
Copper	Low	4.88
	High	4.27
Steel	Low	3.80
	High	3.68
Carbon	Low	5.58
	High	8.23

The mode I fatigue strengthening mechanism is dependent on z-binder material properties. The strengthening mechanisms under mode I fatigue loading for the copper z-binder is shown in Fig. 4.4 (a, b). During the mode I cyclic fatigue growth the copper z-binders bridging the delamination failed at the crack plane by tensile fatigue cracking. Fig. 4.4 (c) shows the fracture surface of the copper z-binders. The fracture surface show beach mark-like striations, which is indicative of fatigue cracking. The spacing between the beach marks

increased with the cyclic strain intensity range value applied to the 3D composite reinforced with metal z-binders. The radiating pattern of the striations from the single point at the surface of the metal z-binder reveal that fatigue cracking initiated at the surface stress concentration, such as small scratch. The fatigue crack grows with the increasing number of load cycles until ultimately the metal z-binders failed.

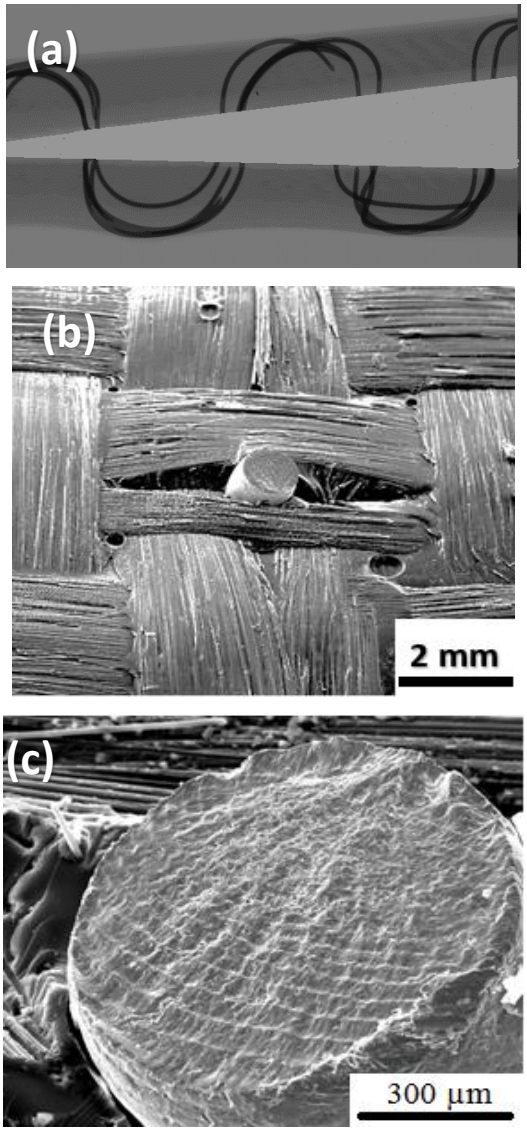

Fig. 4.4: *(a) X-ray computed tomography image showing side-view of DCB specimen of 3D composite containing copper z-binders when subjected to mode I interlaminar cyclic loading. The direction of crack growth from right from left. (b) Fracture surface of 3D composite reinforced with copper z-binders. (c) Mode I fatigue induced beach mark striations on a failed copper z-binder.*

The delamination fatigue properties of the 3D composites reinforced with steel z-binder were improved by the z-binders creating a large-scale extrinsic bridging zone along the mode I fatigue crack, as shown in Fig. 4.5 (a, b). The steel z-binders did not fail along the delamination fracture plane, and instead they broke in fatigue inside the composite and then were partially pulled-out with increasing cyclic loading. The steel z-binders generated a longer bridging traction zone containing a higher number of z-binders than the copper, and this contributed significantly to the higher mode I fatigue properties. Furthermore, the steel z-binders broke inside the 3D woven composite at a location well away from the delamination crack. The two broken ligaments of the steel z-binder were pulled-out together under increasing crack opening, thereby doubling the pull-out traction stress than had just one ligament pulled-out. Therefore, the steel z-binder showed greater improvement under mode I fatigue loading compared to the copper z-binder due to the friction traction stress generated by this pull-out process. Fig. 4.5 (c) shows the fracture surface of a steel z-binder, and it shows similar beach mark-like striations observed in copper z-binders. The spacing of striations increased with the cyclic strain intensity range.

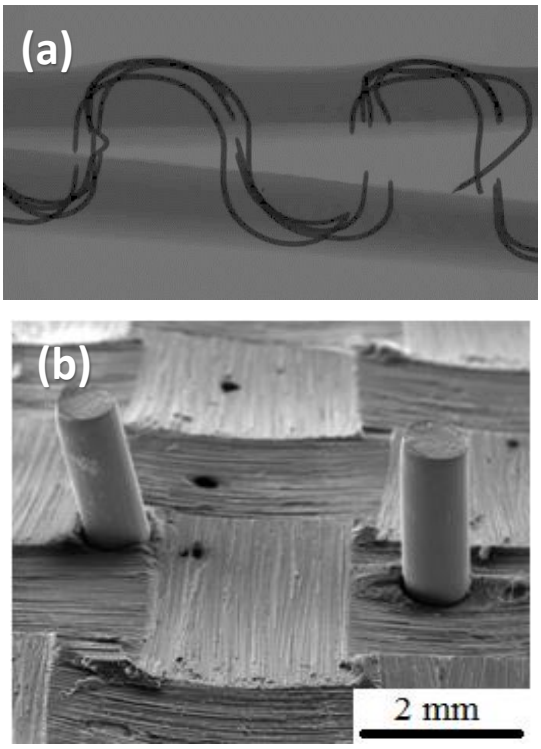

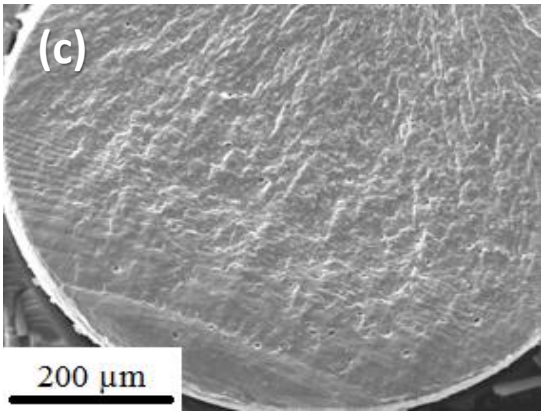

Fig. 4.5: *(a) X-ray computed tomography image showing side-view of DCB specimen of 3D composite containing steel z-binders when subjected to mode I interlaminar cyclic loading. The direction of crack growth is from right to left. (b) Fracture surface of 3D composite reinforced with steel z-binders. (c) Mode I fatigue induced beach mark striations until the failure of steel z-binder.*

The carbon z-binders were progressviely debonded and pulled-out under the mode I cyclic crack opening loads, as shown in Fig. 4.6 (a, b). The mode I traction loads generated by the carbon z-binders bridging the delamination shielded the crack tip, thereby slowing the fatigue crack growth rate. Fig. 4.6 (b) shows a broken carbon z-binder protuding from the surface of the delamination fatigue crack. Like the steel, the carbon generates high traction forces beyond the peak stress with increasing cyclic loading. The carbon z-binders do not fracture at the delamination crack plane, but instead break at the bend radius where they are forced to bend sharply from the in-plane to through-thickness direction.

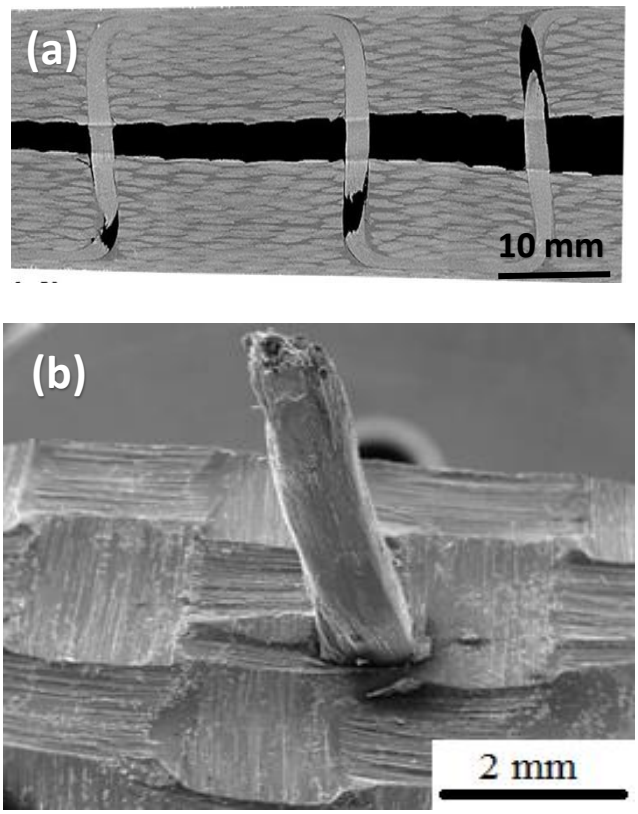

Fig. 4.6: *(a) X-ray computed tomography image showing side-view of DCB specimen of 3D composite containing carbon z-binders when subjected to mode I interlaminar cyclic loading. The direction of crack growth is from right to left. (b) Fracture surface of 3D composite reinforced with carbon z-binders.*

Fig. 4.7 shows tensile fatigue life (S–N) curves measured for materials similar to the z-binders used in the 3D woven composites [113]. The curves show the fatigue strength increases in the order: copper, steel, carbon – and this correlates with the improvement to the mode I interlaminar fatigue properties (Fig. 4.2).

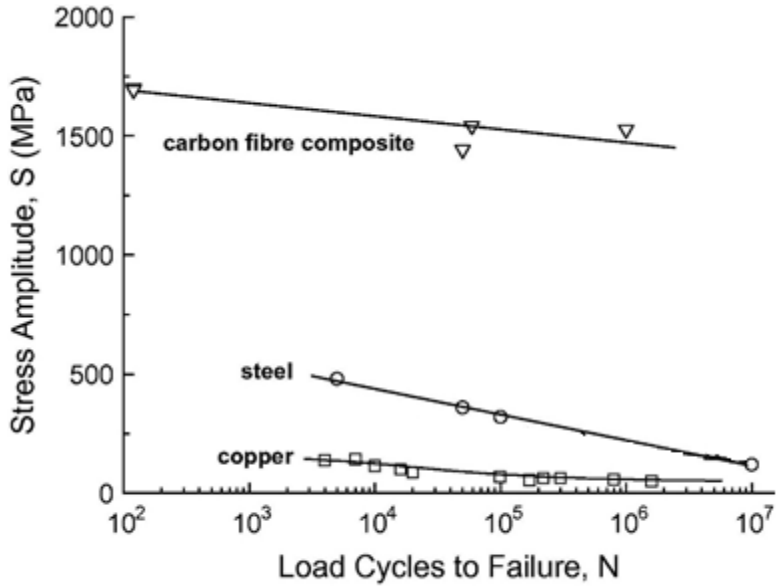

Fig. 4.7: *Fatigue life curves for copper, steel and carbon fibre composite[113]* .

4.3.2 Mode II interlaminar fatigue properties

Paris curves of mode II cyclic stress intensity factor ($\Delta G_{II,eq}$) plotted against the delamination crack growth rate (da/dN) for the 2D laminate and 3D woven composites are shown in Fig. 4.8. The mode II delamination fatigue resistance was increased by the z-binders. The bridging of z-binders shielded the crack tip, and hence slowing the mode II fatigue crack growth rate. Similar to mode I, scatter in mode II delamination growth rates was caused by the stick-slip nature of the fatigue crack growth process.

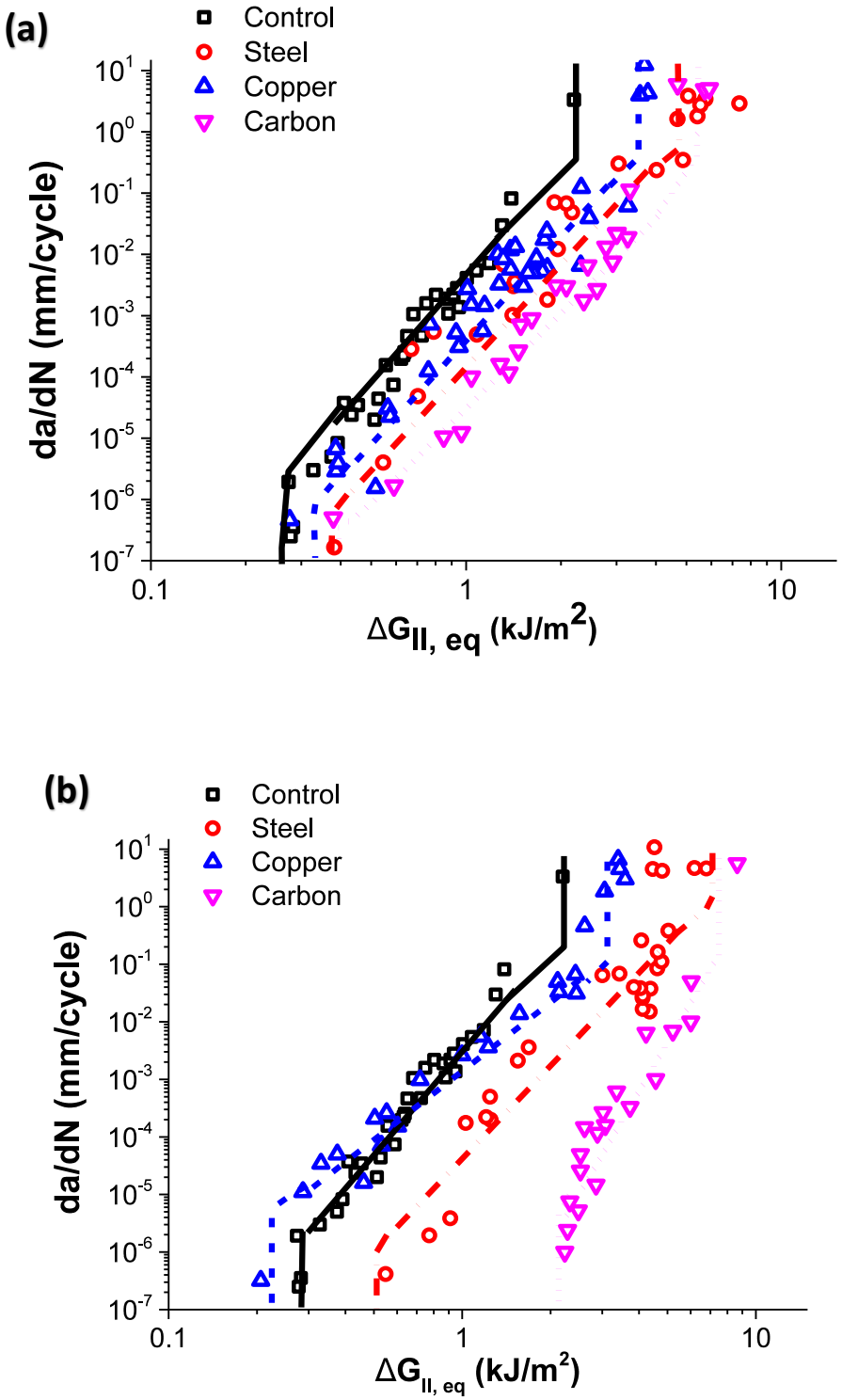

Fig. 4.8: *Mode II Paris curves for the 2D and 3D composites reinforced with steel, copper or carbon z-binders with (a) low and (b) high contents.*

Under mode II interlaminar cyclic fatigue loading, all the z-binder materials improved the fatigue properties. Compared to mode I, however, the z-binders were less effective at increasing the mode II fatigue resistance. Other researchers [71, 132, 133] also report the same behaviour in that the through-thickness reinforcement was more effective at interlaminar fatigue strengthening under mode I compared to the mode II loading. The carbon and steel z-binders were effective at increasing the mode II fatigue resistance by generating a large-scale bridging zone along the mode II delamination fatigue crack. Due to the higher stiffness, strength and fatigue resistance of the carbon z-binders, they effectively resist cyclic shear loading which results in the largest increases to the interlaminar fatigue strength. On the other hand, the copper z-binder has the lowest stiffness and fatigue strength which results in the weakest strengthening effect under mode II cyclic loading. The gradient values (*m*) are shown in Table 4.2, and for mode II fatigue-induced delamination growth they show no obvious trend with increasing volume content of z-binders.

Table 4-2: *Mode II m values of the 2D laminate and 3D woven composites.*

Z-binder material	**Z-binder volume content**	***m***
Control (no z-binder)	0%	5.92
Copper	Low	5.36
	High	4.77
Steel	Low	4.34
	High	2.00
Carbon	Low	6.79
	High	9.18

The effect of z-binders on the improvement to the threshold strain energy release rate value ($\Delta G_{eq,th}$) to initiate mode II fatigue crack growth is shown in Fig. 4.9. All three types of z-binder increase the mode II interlaminar fatigue properties with increasing volume content. Although the mode II fatigue strengthening effect is lower using the metal z-binders compared to the carbon.

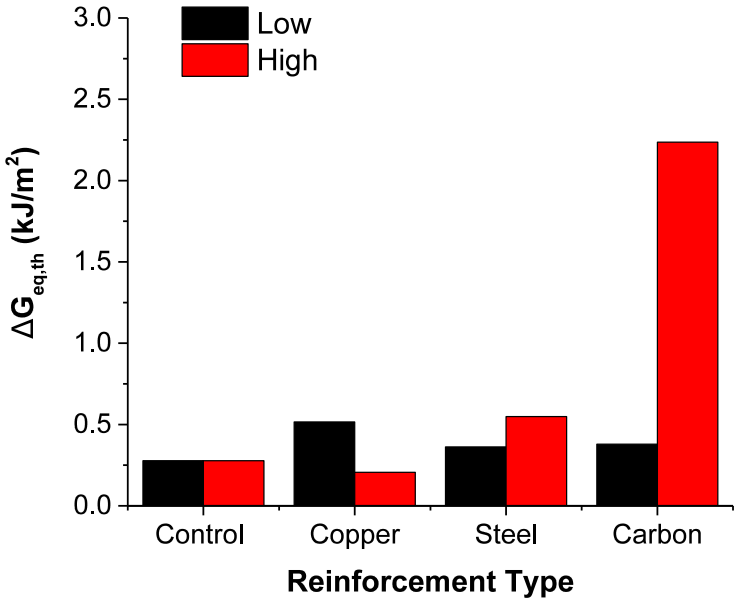

Fig. 4.9: *Effect of z-binder material on mode II $\Delta G_{eq,th}$ value to initiate fatigue crack growth for 2D and 3D composites reinforced with steel, copper or carbon z-binders.*

The improvement in mode I fatigue resistance using the binders is much greater than compared with mode II fatigue resistance, and is due to the difference in the mode I and mode II fatigue strengthening mechanism of the z-binder bridging zone. Under mode I, all types of z-binders generated higher crack bridging traction loads and energies than under mode II [133]. The strengthening mechanism of copper and steel z-binders under mode II fatigue loading are shown in Fig. 4.10 (a, b) and Fig. 4.11 (a, b). The fatigue strengthening mechanism is dependent on z-binder material properties. The metal z-binders behaved differently to the carbon z-binders. The copper and steel z-binders bridged the delamination crack plane and experienced cyclic plastic shear deformation.

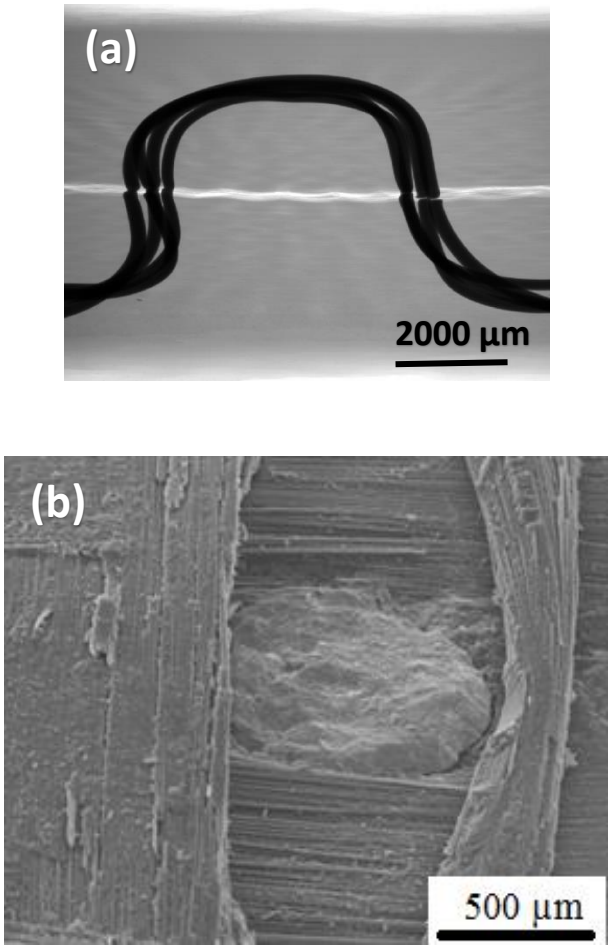

Fig. 4.10: *(a) X-ray computed tomography image showing side-view of ENF specimen of 3D composite containing copper z-binders when subjected to mode II interlaminar cyclic loading. Note: Direction of fatigue crack growth is right to left. (b) Fracture surface of 3D composite reinforced with copper z-binders.*

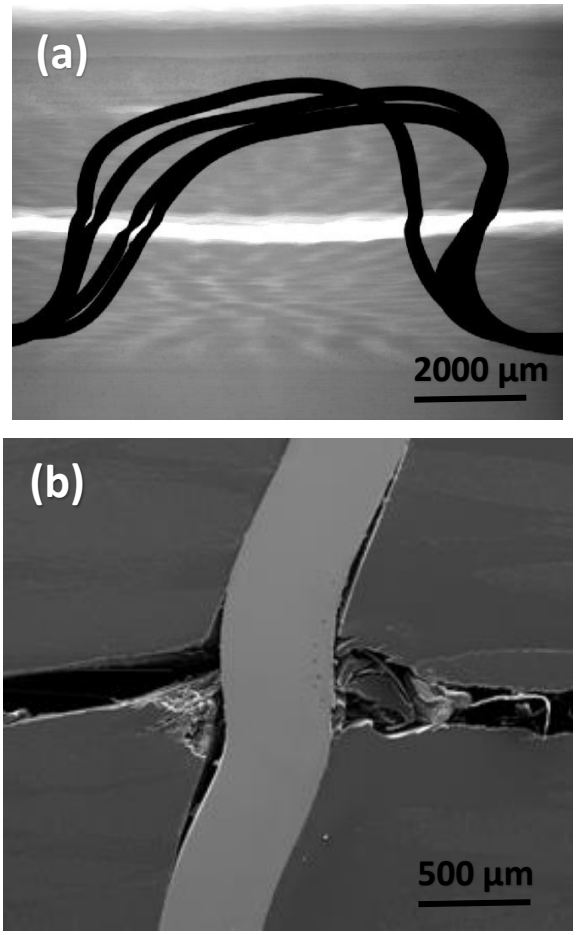

Fig. 4.11: *(a) X-ray computed tomography image showing side-view of ENF specimen of 3D composite containing steel z-binders when subjected to mode II interlaminar cyclic loading. Note: Direction of fatigue crack growth is right to left. (b) Side-view of 3D composite reinforced with steel z-binder during mode II fatigue loading.*

The carbon z-binders show more improvement than copper and steel z-binders under mode II fatigue loading. Fig. 4.12 shows the carbon z-binder was deformed and fractured in shear along the fatigue crack plane. At lower cyclic sliding displacements between the delamination crack surfaces, the carbon z-binders began to debond due to fatigue cycling and bridged the crack without being damaged as shown in Fig. 4.12 (a). At higher cyclic strain energy release rate values, when the sliding displacement was greater, the carbon z-binders began to break as shown in Fig. 4.12 (b). The fractured carbon z-binders do not pull-out and consequently the traction energy was lower resulting in a smaller improvement to the mode II fatigue properties compared to mode I. The crack bridging mechanism generated by the

debonding and failure of carbon z-binders disspipated the energy caused the improvement to the mode II fatigue resistance of the 3D woven composites.

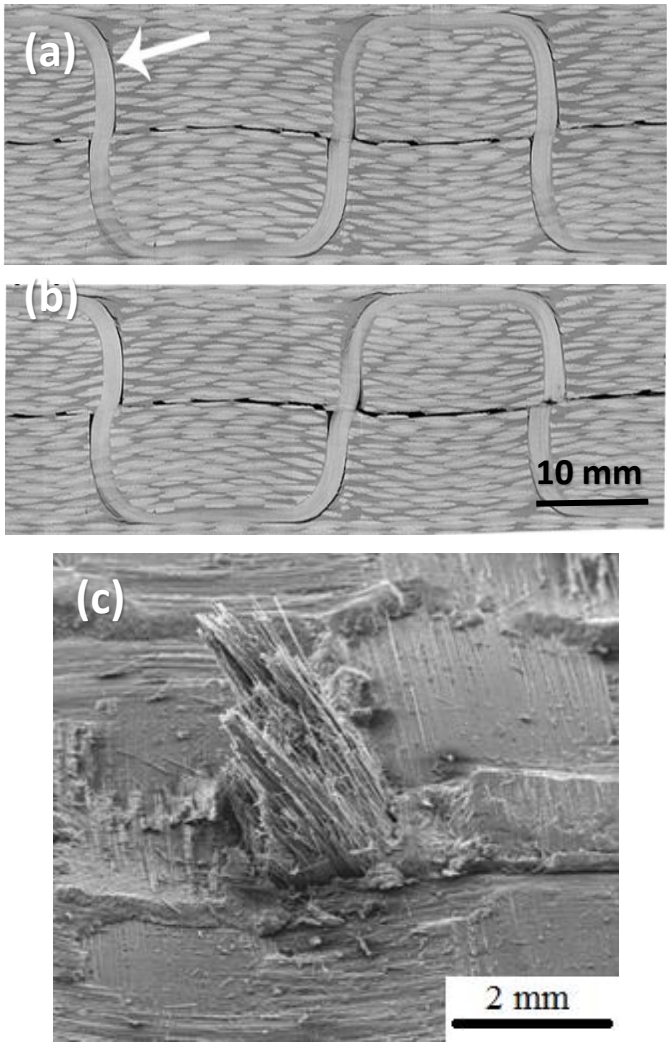

Fig. 4.12: *(a, b) X-ray computed tomography image showing side-view of ENF specimen of 3D composite containing carbon z-binders when subjected to mode II interlaminar cyclic loading (a) at low and (b) at high applied strain energy release rate range. Note: Direction of fatigue crack growth is right to left. The arrow in (a) indicates the location where the carbon z-binders have debonded from the laminate. (c) Fracture surface of 3D composite reinforced with carbon z-binders.*

4.4 CONCLUSIONS

The results presented in this chapter prove that the mode I and mode II interlaminar fatigue resistance properties of 3D woven composites are improved by woven z-binders. The z-binders bridge the delamination fatigue crack and resist crack extension under cyclic loading. The z-binders are more resistant to mode I than mode II fatigue crack growth; thereby resulting in a greater mode I fatigue strengthening effect. Damage and failure of the z-binders within the bridging zone is different for mode I and mode II fatigue loading. Copper z-binder provided the least improvement, whereas steel showed more improvement due to the partial pull-out of z-binder and carbon z-binders failed progressively by interfacial debonding and pull-out under mode I cyclic loading.

Through-thickness reinforcement using steel, copper and carbon z-binder improves the resistance of the 3D textile composite against the initiation and growth of delamination cracks when subjected to cyclic II interlaminar loading. Metal z-binders provided less improvement than carbon z-binders due to generation of much lower strain energy during the growth of mode II delamination cracks and do not reach the shear failure strain.

Chapter 5: Electrical Conductivity of 3D Composite Woven with Metal or Carbon Z-binders

Abstract

This chapter presents an original experimental study into the effects of the volume content and electrical properties of z-binders on the through-thickness and in-plane electrical conductivity of 3D woven composites. The 3D composites were orthogonally woven with z-binders made of carbon tow, stainless steel or copper, which have different electrical properties. It was found that the copper increased the through-thickness conductivity by about 5700x, whereas the stainless steel and carbon increased the conductivity by approximately 150x and 12x respectively. However, varying the volume content or electrical properties of the z-binders did not change significantly the in-plane conductivity of the laminates. A simple model based on rule-of-mixture can predict the electrical conductivity properties of 3D woven composites.

5.1 INTRODUCTION

A limiting property of many fibre reinforced polymer composite materials is low electrical conductivity. Consequently, composites used in aircraft surfaces and other applications at risk of lightning strike must contain a highly conductive material (e.g. copper mesh) to rapidly dissipate the electrical charge in order to minimise damage. The high resistivity of composites also limits their application in electrical/electronic devices and other components requiring high conductivity. Composites have low electrical conductivity in both the in-plane and (in particular) through-thickness directions. For example, the in-plane and through-thickness conductivity values for unmodified continuous carbon/epoxy laminate (fibre content ~50 vol %) is typically about ~10^3–10^4 S/m S/m and ~10-10^2 S/m, respectively.

Many techniques have been developed to increase the electrical conductivity of composite materials, which include doping of the polymer matrix with highly conductive carbon-based nanoparticles (e.g. carbon nanofibres, carbon nanotubes, graphene) [134-136],

metal particles (e.g. copper) [137], polyaniline [138] or milled carbon particles [139, 140]; carbon nanoparticles grown directly onto the carbon fibres [42, 141]; or carbon with or without additives such as copper chloride or chopped carbon fibres [142].

A recently developed technique is the insertion of highly conductive thin rods in the through-thickness (or z-) direction of composite materials during manufacture to create a low resistivity pathway for current flow. Pegorin et al. [143] reported that z-pins inserted in the through-thickness direction of carbon-epoxy laminates are highly effective at increasing the electrical conductivity. The improvement to the through-thickness conductivity can be controlled by the type and volume content of the z-pins, with improvements of up to ~10^6. More recently, Grigoriou et al. [144] discovered that z-pins can also be used to increase the through-thickness electrical conductivity of sandwich materials with a thick core of polymer foam or balsa wood. However, a limitation of the z-pin technique is that it cannot increase the in-plane electrical conductivity due to its discrete design [143, 144]. Z-pins are not physically connected to each other, and therefore do not form the continuous pathway for current flow required to increase the in-plane conductivity of composite materials. A potential solution is the insertion of electrically conductive continuous z-binders into composites which increase both the in-plane and through-thickness electrical conductivity values. However, such an approach has not been explored.

Many studies have demonstrated that continuous z-binders can be inserted in both the in-plane and through-thickness directions of composite materials using orthogonal or layer interlock weaving [26, 42, 141]. 3D woven composites display outstanding damage tolerant properties, including high interlaminar fracture toughness (as reported in Chapter 3) [24, 142], interlaminar fatigue resistance (Chapter 4) [49] and impact damage resistance (Chapter 7) [46] of composites. Sharp et al. [94] demonstrated that metal z-binders woven into carbon-epoxy composite material can increase greatly the through-thickness thermal conductivity. However, the use of metal and other highly conductive z-binder materials to controllably increase the electrical conductivity of 3D woven composite materials has not been evaluated.

We present the new approach of using three-dimensional woven z-binders to increase the electrical conductivity properties of fibre-polymer composite materials. The electrical properties of carbon-epoxy laminates containing orthogonally woven continuous z-binders made of thin metal wire (e.g. copper, stainless steel) or carbon tows were studied. The volume fraction of the z-binders was kept relatively low to minimise any adverse impact on the mechanical properties of the composite materials (which are investigated later in this PhD thesis). The effect of the material type and volume fraction of the z-binders on the in-plane and through-thickness electrical properties of a carbon-epoxy composite was studied experimentally and analytically. The research reveals that the improvement to the electrical properties of composites is substantial (orders of magnitude) and that the properties can be tailored via the judicious design and selection of the woven z-binders.

5.2 MATERIALS AND EXPERIMENTAL METHODOLOGY

5.2.1 Manufacturing and Microstructure of Composite Materials

The composite materials used in this study were fabricated using a plain woven T300 carbon fabric (AC220127 supplied by Colan Ltd.) and epoxy polymer. The fabric specification and weaving pattern was the same as used in previous chapters. Copper, stainless steel and carbon tows were used as a z-binder material. These materials were selected for the z-binders because they cover a wide range of electrical conductivity values (over three orders of magnitude) increasing in the order: carbon tow, stainless steel and copper. The electrical conductivity values of the three types of z-binder materials are given in Table 5.1.

The carbon, stainless steel and copper were orthogonally woven in straight, parallel rows along the warp fibre direction to the stacked carbon fabric, as illustrated in Fig. 5.1. The volume content of the z-binder was the same as in previous studies, and the values are given in Table 5.1. A 2D woven laminate without any z-binder, but with the same number of carbon fabric plies, was used as the control material to benchmark the electrical properties of the 3D woven composites.

***Table 5-1**: Properties of the z-binder weave architecture in the 3D woven composites.*

Material	Axial Electrical Conductivity (S/m)	Weave density (binders/cm^2)	Areal content (%)	Volume content (%)	Weight content (%)
Carbon	6.3 x 10^4	0.8	0.35	0.07	0.09
		1.6	0.70	0.14	0.17
Copper	6.0 x 10^7	1.6	0.33	0.065	0.39
		3.2	0.66	0.13	0.68
Steel	1.4 x 10^6	1.6	0.33	0.065	0.35
		3.2	0.66	0.13	0.60

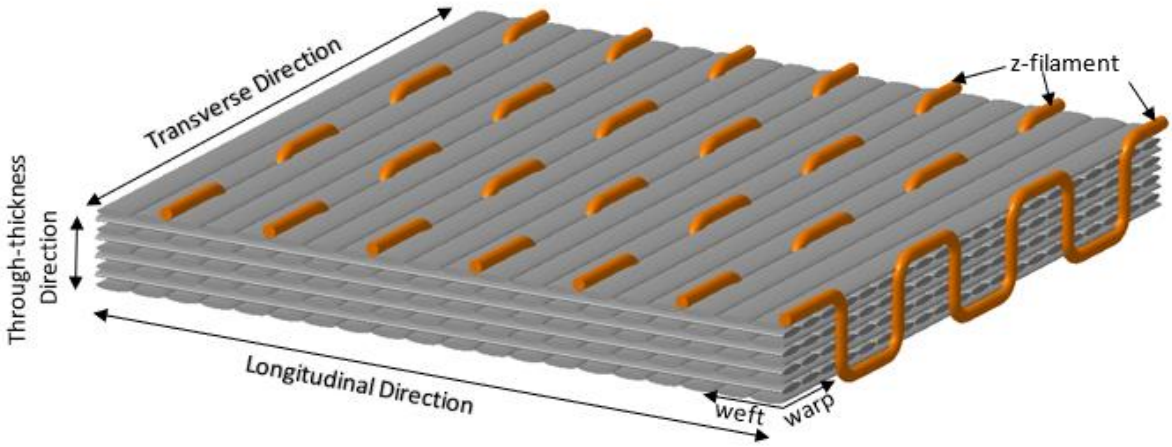

***Fig. 5.1:** CAD image of the 3D fabric showing the orthogonal architecture of the z-binders.*

The 2D and 3D fabrics were infused with liquid epoxy resin using the vacuum bag resin infusion (VBRI) process. The epoxy, hardener and VBRI process used in this study was the same as used in previous chapters. The final thickness of the different composites was the same at 9.5 mm.

5.2.2 Electrical Measurements

The in-plane and through-thickness electrical conductivity values of the 2D and 3D woven composites were measured at room temperature using the test method illustrated in Fig. 5.2, which is adapted from ASTM D4496 and ASTM D257. The sample dimensions were 27 mm wide, 40 mm long and 9.5 mm thick, and contained a sufficient number of z-binder to provide the bulk conductivity values of the composite material.

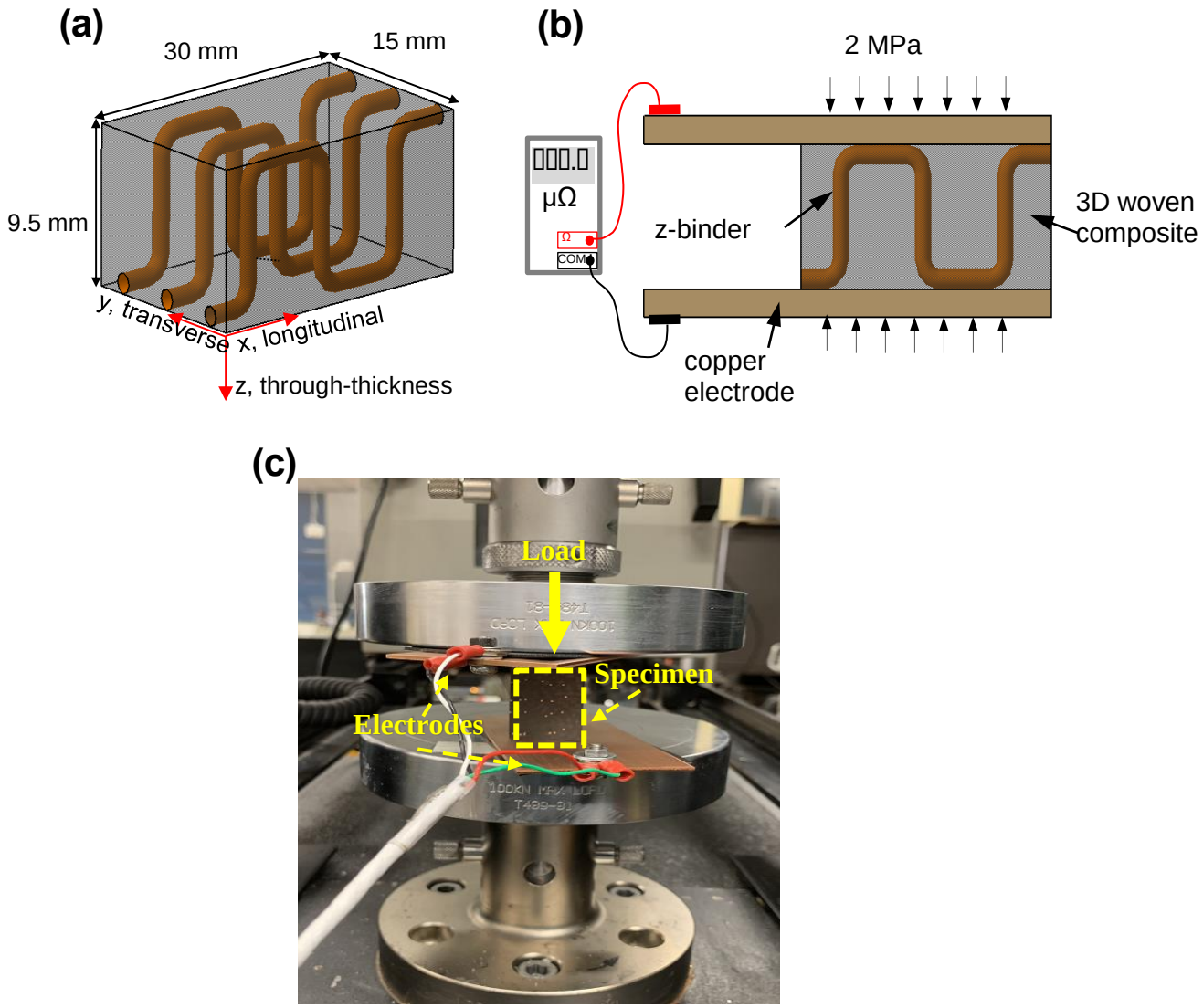

Fig. 5.2: *Schematics of (a) electrical conductivity sample, (b) through-thickness conductivity test method, and (c) test setup for measuring electrical conductivity.*

Before testing, the sample surfaces were machined flat and then polished to expose surface segments of the z-binder to the electrodes. Copper strips (1.5 mm thick) were used as electrodes, and these were attached to the opposing surfaces of the sample to measure the conductivity values in the through-thickness, longitudinal and transverse directions. A conductive silver paste (supplied by Structure Prob Inc.) was used to bond the copper electrodes to the samples. A relatively low compressive force (~1 MPa) was applied to ensure good contact between the copper electrodes and composite sample during the electrical measurement, which were performed using the 4-wires method with a Keysight micro-Ohm meter (type 3442OA).

5.3 RESULTS AND DISCUSSION

The effects of the material and volume content of the woven z-binder on the electrical conductivity of the 3D composite measured experimentally in the through-thickness, longitudinal and transverse directions is shown in Fig. 5.3-5.5. In these figures the data points and curves show the measured and calculated conductivity values, respectively. The results show that orthogonal weaving of z-binders is an effective method for increasing the through-thickness electrical conductivity of the composite; with large improvements gained using a relatively low volume content of z-binder.

The electrical conductivity of the 3D woven composites in each of the three directions can be calculated using rule-of-mixtures (ROM) analysis, and these are shown by the curves in Fig. 5.3-5.5. ROM analysis can be applied when it is assumed that the z-binders and carbon-epoxy host material act independently in the flow of current. The electrical conductivity in the through-thickness (z-direction) can be defined from the first principle for resistors acting in parallel by:

$$\mathrm{K}_{cz} = (\mathrm{K}_z \cdot V_z) + \mathrm{K}_{oz} \cdot (1 - V_z) \quad \textbf{(1)}$$

where V_z and K_z are the volume content and electrical conductivity of the z-binders in the through-thickness direction, respectively. K_{oz} is the through-thickness conductivity of the host composite material (i.e. 2D laminate).

The conductivity of the 3D woven composites in the longitudinal (x-direction) is given by:

$$\mathrm{K}_{cx} = \frac{l_o}{b\ t\ R_{cx}} \quad \textbf{(2)}$$

where l_o, b and t are the length, width and thickness, respectively. R_{cx} is the electrical resistance along the longitudinal direction, which can be defined from the principle for the resistors acting in parallel by:

$$\frac{1}{R_{cx}} = \frac{1}{R_x} + \frac{1}{R_{ox}} = \frac{n_r \cdot (\mathrm{K}_x \frac{\pi d^2}{4})}{l} + \frac{\mathrm{K}_{ox} \cdot (bt - \frac{\pi d^2}{4} n_r)}{l_o} \quad \textbf{(3)}$$

where, K_x and K_{ox} are the electrical conductivity values of the z-binder and control composite (2D laminate) in the longitudinal direction, respectively. n_r, d and l are the number of rows,

diameter and length of the z-binders, respectively. For the 3D woven materials investigated in this study, the distance travelled by the current within z-binders, l is much longer than that in the composite, l_0; due to the orthogonal weave pattern. Now substituting R_{cx} from Eqn (3) into (2) and rearranging the terms gives:

$$\mathrm{K}_{cx} = \frac{l_0}{l}\,\mathrm{K}_x \cdot \left(\frac{\pi d^2 n_r}{4\,b\,t}\right) + \mathrm{K}_{ox} \cdot \left(1 - \frac{\pi d^2 n_r}{4\,b\,t}\right) \quad \textbf{(4)}$$

Thus, the ROM for the longitudinal conductivity of the 3D woven composite is given by:

$$\mathrm{K}_{cx} = \frac{l_0}{l}(\mathrm{K}_x \cdot V_x) + \mathrm{K}_{ox}(1 - V_x) \quad \textbf{(5)}$$

where V_x is the volume content of the z-binders in the longitudinal direction.

The conductivity of the 3D woven composites in the transverse (y-)direction is given by:

$$\mathrm{K}_{cy} = \frac{b}{t\,l_o\,R_{cy}} \quad \textbf{(6)}$$

R_{cy} is the electrical resistance in the transverse direction. The z-binders increase the conductivity of the section of the 3D composite material having a width, *d* being equal to the diameter of the z-binders. From ROM analysis, the conductivity of this section is given by:

$$\mathrm{K}'_y = \left(\mathrm{K}_y \cdot V_y\right) + \mathrm{K}_{oy} \cdot \left(1 - V_y\right) \quad (7)$$

where V_y is the volume content of the z-binders within the 3D woven composite. K_y and K_{oy} are the transverse conductivity of the z-binders and the control composite (2D laminate), respectively. The z-binders do not form a continuous network in the transverse direction, and therefore current flow between the neighbouring parallel rows of z-binders is disrupted by the more resistive carbon-epoxy material. Thus, the electrical conductivity of 3D composite in the transverse direction can be derived by assuming a series of alternating resistors whose conductivities are given by K'_y and K_{oy}. Then the transverse electrical resistance of the resulting unit cell of the 3D composite material is given by:

$$R_{cy} = R_y + R_{oy} = \frac{b - n_r d}{l\,t\,\mathrm{K}_{oy}} + \frac{n_r d}{l\,t\,\mathrm{K}'_y} \quad \textbf{(8)}$$

Now substituting R_{cy} from Eqn (8) into (6) and rearranging the terms gives:

$$\mathrm{K}_{cy} = \frac{\mathrm{K}_{oy}}{1 - n_r \frac{d}{b}\left(1 - \frac{\mathrm{K}_{oy}}{\mathrm{K}'_y}\right)} \quad \textbf{(9)}$$

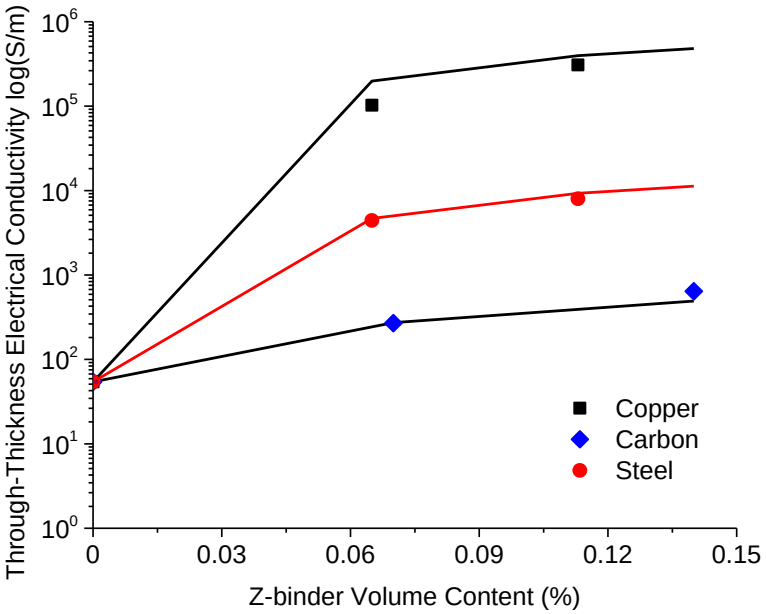

Fig. 5.3: *Effects of material type and volume content of z-binder on the through-thickness electrical conductivity of the 3D woven composites. The data points and curves were measured experimentally and calculated (Eqn (1)), respectively. The data points represent experimental values and the solid lines represent calculated values.*

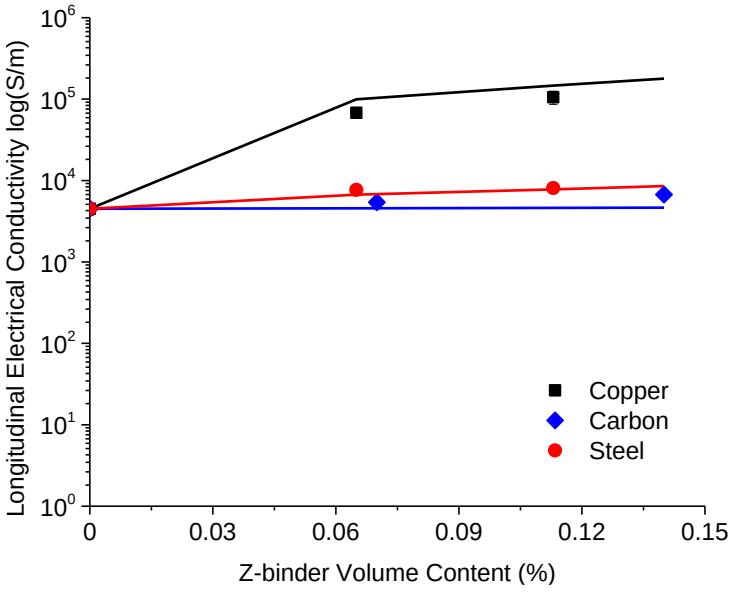

Fig. 5.4: *Effects of material type and volume content of z-binder on the longitudinal electrical conductivity of the 3D woven composites. The data points and curves were measured experimentally and calculated (Eqn (5)), respectively. The data points represent experimental values and the solid lines represent calculated values.*

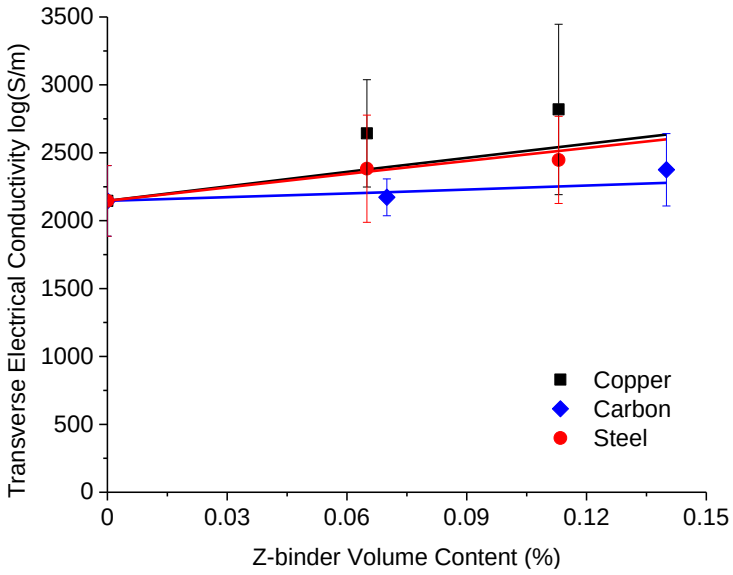

Fig. 5.5: *Effects of material type and volume content of z-binder on the transverse electrical conductivity of the 3D woven composites. The data points and curves were measured experimentally and calculated (Eqn (9)), respectively. The data points represent experimental values and the solid lines represent calculated values.*

The through-thickness conductivity increased linearly with both the electrical conductivity and volume content of the z-binder material, with copper being the most effective. At the highest volume content studied (0.13%), the copper increased the through-thickness conductivity by about 5700x, whereas the stainless steel and carbon increased the conductivity by ~150x and ~12x respectively. The z-binder increased the through-thickness conductivity by creating a continuous pathway for current flow between the electrodes attached to the surfaces of the composite material. The z-binders behave like resistors in parallel within the 3D woven composite, thereby providing a low resistance path for current flow while the surrounding carbon-epoxy material remains much more resistive, as shown schematically in Fig. 5.6 (a).

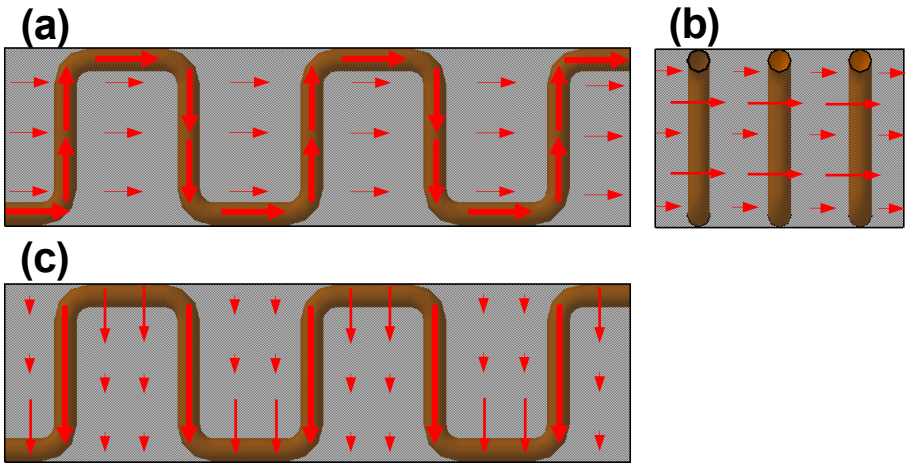

Fig. 5.6: *Schematic representation of the current flow in the (a) longitudinal, (b) transverse and (c) through-thickness directions.*

The improvements to the longitudinal conductivity values were significantly less than in the through-thickness direction. The carbon tow and steel wire induced only modest increases to the longitudinal conductivity (3% and 70%, respectively) at the highest z-binder content. The copper z-binder was more effective (31-fold increase), but again the improvement was significantly less than in the through-thickness direction. The lower improvement to the longitudinal conductivity was due to the increased resistivity of the z-binder caused by the orthogonal weave pattern. Similar to the through-thickness direction, the z-binders in the longitudinal act like resistors in parallel which aids the flow of electrical current between the electrodes (Fig. 5.6b). In the longitudinal direction, however, the z-binders create a continuous pathway for current flow between the surfaces of the composite material samples which is ~2x longer. This results in a two-fold increase in the resistance to current flow, resulting in lower improvements to the longitudinal conductivity of the 3D woven composites. However, the absolute conductivity values are similar or higher in the longitudinal compared to the through-thickness direction. This is because the host composite material provides a much greater contribution to the longitudinal conductivity. The measured conductivity values of the laminate without z-binders in the through-thickness and longitudinal directions are ~55 and 4500 S/m. The carbon fibres within the composite material contribute much more to the conductivity in the longitudinal direction, and therefore the

apparent percentage improvement gained by the z-binder is less than in the through-thickness direction.

The z-binders had little or no significant effect on the electrical conductivity in the transverse direction, as shown in Fig 5.5. The carbon z-binder did not increase the transverse conductivity whereas the stainless steel and copper promoted relatively small improvements (of only about 15% and 35% respectively for the highest volume content). The improvement was significantly lower than the through-thickness and longitudinal conductivities because the z-binders do not form a continuous network in the transverse direction. Therefore, current flow between the neighbouring parallel rows of z-binders is disrupted by the more resistive carbon-epoxy material between the rows. While not studied experimentally here, this problem can be overcome by weaving the z-binders along both the longitudinal and transverse directions of the composite to create a 0/90 pattern, as illustrated in Fig. 5.7

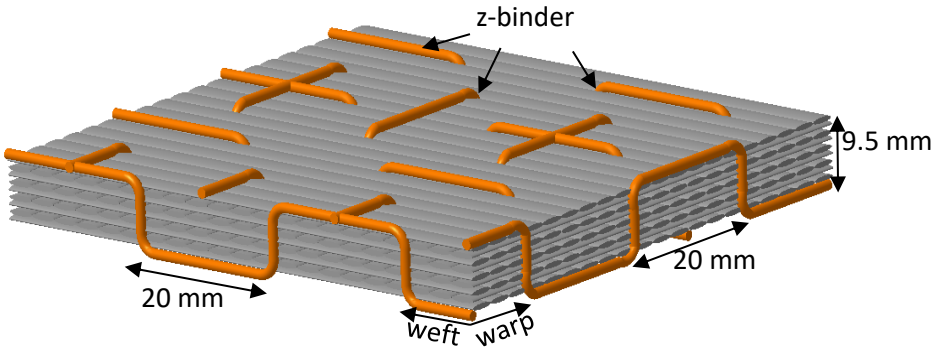

Fig. 5.7. *3D fabric showing balanced orthogonal architecture of the z-filaments in longitudinal and transverse directions.*

The improvements to the electrical properties were gained with relatively weight penalty to the 3D woven composite materials. Figure 5.8 shows plots of the bulk density of the materials with increasing volume fractions of the different z-binders. The carbon z-binders had virtually no effect on the density whereas the metals increased the density. This reveals that large increases to through-thickness and longitudinal conductivities were achieved with relatively modest increases to the weight of the 3D composite materials.

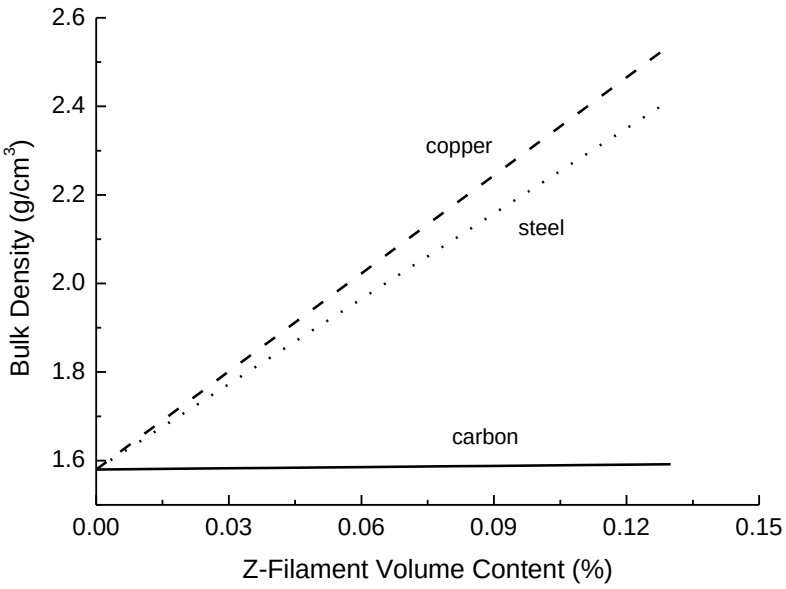

Fig. 5.8: *Effects of the volume fraction and type of z-binder on the density of the 3D woven composites.*

These models given by Eqn. (2), (5) and (9) were applied to the 3D woven composites, and the curves in Fig. 5.3-5.5 show the calculated electrical conductivity values and its comparison to the experimentally measured conductivities. The through-thickness, longitudinal and transverse conductivities calculated using Eqns (2), (3) and (5), respectively, and the experimentally measured conductivity values are in close agreement for the 3D composites with different z-binders. The agreement indicates that the measured increases to the conductivity values is due to an additive effect (i.e. rule-of-mixtures) of the electrical conductivities of the z-binder and the host composite, and both materials act independently like resistors in parallel for the through-thickness and longitudinal directions and like resistors in series in the transverse direction (Fig. 5.5). This shows that the model presented here can be used to effectively design 3D woven composite with tailored conductivity properties in the three directions using electrically conductive z-binders. Table 5.2 shows electrical conductivity values for other types of conductive materials compared with the z-binder materials used in this PhD project. The values show greater improvement in electrical conductivity values for copper z-binder. Whereas, steel z-binder shows moderate improvement and carbon shows the least improvement in electrical conductivity values.

Table 5-2: *Electrical conductivity values compared with other types of conductive materials.*

Composite	Conductive material	Electrical conductivity	Electrical conductivity percentage increase	Reference
CNTs-Polyepoxy Composites	Carbon nanotubes	1.3×10^{-2} S/m	~5.5	[135]
Carbon-fibre-reinforced polypropylene composites	Short carbon-fibre	10^{-4} S/cm	~1E+12	[138]
Unidirectional glass-fibre-reinforced polyethylene composites	Carbon black (10 %)	2.5×10^{-2} S/m	~25	[139]
Unidirectional glass-fibre-reinforced polyethylene composites	Carbon fibre (20 %)	2×10^{-2} S/m	~20	[139]
Carbon-epoxy composites	Milled carbon fibres and CNTs (6 %)	6.34 S/cm	~50	[140]
Carbon fibre/epoxy (CF/EP) composite	nano-scale carbon black (3 %)	6.1×10^{-2} S/m	~20	[142]
Carbon-epoxy composites	Carbon z-pins 0.25 % 1.43 % 2.34 % 4.00 %	 71 S/m 460 S/m 770 S/m 1200 S/m	 ~8700 ~57000 ~96000 ~150000	[143]
Carbon-epoxy composites	Copper z-pins 0.20 % 0.41 % 0.82 % 1.02 % 1.23 % 1.84 %	 97034 S/m 204238 S/m 378043 S/m 484982 S/m 623472 S/m 905747 S/m	 ~12 mill ~25 mill ~47 mill ~60 mill ~77 mill ~113 mill	[143]
Carbon-epoxy composites	Steel z-pins 0.20 % 0.41 % 1.02 % 1.23 %	 2650 S/m 5074 S/m 12113 S/m 15419 S/m	 ~330000 ~630000 ~150000 ~190000	[143]
Carbon-epoxy composites	Titanium z-pins 0.20 % 0.41 % 1.02 % 1.23 %	 3432 S/m 6292 S/m 13350 S/m 19892 S/m	 ~420000 ~780000 ~1600000 ~2400000	[143]

5.4 CONCLUSIONS

The electrical conductivity of composite materials, which usually have high resistivity, can be improved greatly by continuous z-binders made of a conductive material woven in the through-thickness and in-plane directions. Orthogonal weaving of z-binders made of thin metal wire or carbon fibre roving into the dry fabric preforms of composite materials before resin infusion is a viable method for controllably increasing the electrical conductivity. The through-thickness conductivity is increased greatly by the z-binders, with the magnitude of the improvement controlled by the material type and volume content of the z-binder. The z-binders create a continuous conductive pathway for current flow in the through-thickness direction, thereby greatly increasing the electrical conductivity in this direction. The z-binders also increase the longitudinal conductivity of the composite material, although the improvement is less than for the through-thickness conductivity. The increase to the in-plane conductivity relies upon the z-binders forming a continuous orthogonal weave pattern which provides the pathway for current flow along the composite material. The improvements to the electrical properties can be accurately predicted using ROM analysis. ROM modelling can be used to design 3D woven composites with tailored electrical properties based on the judicious choice of the volume content and material of the z-binder.

Chapter 6: Detecting Delamination Damage in 3D Woven Composite using Electrical Resistivity

Abstract

The *in-situ*, real-time detection of delamination cracks in 3D composites woven with copper, steel or carbon z-binders is presented in this chapter. 3D woven composites were reinforced in the through-thickness direction with low and high volume contents of z-binder made of different material (i.e. copper, steel, carbon). The z-binders increase the electrical conductivity of the 3D woven composite materials, as reported in the previous chapter. Mode I interlaminar fracture tests reveal that the increased electrical conductivity due to the z-binders can be used to detect the growth of delamination cracks via large, measurable changes to the electrical resistivity. The woven z-binders can be used for the *in-situ* detection and monitoring of mode I delamination growth within 3D woven composite materials, which is not possible without z-binders.

6.1 INTRODUCTION

A critical structural integrity issue in the use of carbon fibre reinforced polymer laminates in light-weight structures is the reliable detection of damage, including delamination cracks. The initial inspection of a damaged composite is often performed using visual and, in some cases, tap testing techniques. However, delamination cracks are not visible in carbon fibre laminates and can be very hard to detect using tap testing when the damage is small or buried deep below the surface [145]. Delamination cracks can be detected using non-destructive evaluation (NDE) techniques such as ultrasonics, thermography, X-ray computed tomography and laser shearography. However, it is often necessary to take the composite part out-of-service to perform the non-destructive inspection. Several structural health monitoring (SHM) techniques are capable of the real-time and *in-situ* detection and monitoring of delamination damage in composite structures, including acoustic emission, ultrasonics, Bragg grating optical fibres and comparative vacuum monitoring. The detection of the delamination cracking via changes to the electrical resistivity to the carbon fibre composite is another approach.

Several studies have demonstrated that damage to composite materials can be detected using electrical resistance methods [146-149]. For example, damage can be monitored by passing a direct electric current through the material using the electrical resistance change (ERC) technique [150-153]. However, the electrical conductivity properties of carbon fibre laminates are very low, particularly in the through-thickness direction, as reported in the previous chapter. Therefore, it is necessary to increase substantially the electrical conductivity of the laminate for ERC techniques to be reliable. Highly conductive fillers, such as nanoparticles, nanofibers or graphene [154-157], can be used to increase the electrical conductivity of composite laminates. For example, Boger et al. [155] reported that the addition of a low concentration of conductive carbon nanoparticles to the epoxy matrix of a glass fibre composite reduced the electrical resistivity to a low enough level that damage could be detected, including small damage (i.e. fibre cracking), via changes to the electrical resistivity. Ladani et al. [157] recently proved that a small quantity of nanoparticles in the epoxy matrix to carbon fibre composite joints increases the electrical conductivity such that the size and location of delamination damage can be detected via measured changes to the electrical resistivity.

Z-pins have also been used to detect delamination cracking within laminates via measurable changes to the electrical resistivity. Z-pins can increase the through-thickness electrical conductivity of composites to a sufficiently high level that it is possible to use electrical resistivity methods to detect damage. Zhang et al. [158] reinforced laminates with carbon fibre z-pins which were connected in series and parallel to an array of electrodes. The z-pins protruded above the composite surface to allow connection to the wire electrodes. The z-pins were pulled out during mode I delamination growth in the laminate, and this disrupted the flow of electric current between the electrodes via the pins. Zhang and colleagues found that this technique could detect the size and location of delamination cracks. Pegorin et al. [159] also demonstrated that z-pins can be used to detect mode I delamination cracks. In this study the z-pins did not need to protrude from the surfaces, and instead a single positive/negative electrode pair was used to measure the resistivity changes of the z-pinned laminate caused by delamination crack growth. Pegorin and colleagues showed that the electrical resistance method was sensitive to the volume content and material of the z-pins.

This research chapter presents an experimental investigation into the *in-situ*, real-time detection of mode I delamination cracks in 3D woven composites via changes to the electrical resistivity. The effects of volume content and material type of the woven z-binders (metal and composite) on their capacity to detect delamination cracks are determined. This chapter also presents an analytical model to predict the increase to the electrical resistivity of 3D woven composites caused by delamination cracking, and the modelled results are compared to experimental measurements.

6.2 MATERIALS AND EXPERIMENTAL METHODOLOGY

6.2.1 Composite Materials

The composite materials used in this study were fabricated using a plain woven T300 carbon fabric (AC220127 supplied by Colan Ltd.) and epoxy polymer. The materials are identical to those investigated in the previous research chapters.

6.2.2 Damage Detection Measurements

Mode I interlaminar fracture toughness tests were performed on the 2D laminate and 3D woven composite materials to determine whether the z-binders can be used to detect delamination cracking via measurable changes to the electrical conductivity. Double cantilever beam (DCB) specimens made of the different materials were used, as shown schematically in Fig. 6.1. The DCB coupons were 240 mm long, 25 mm wide and 9.5 mm thick, and the z-binders extended along the specimen length in parallel rows. Each coupon contained a 50 mm long pre-crack created using 25 μm thick PTFE film at the end which was subjected to crack opening loading. Due to the high delamination resistance of the 3D composite coupons containing z-binders, it was necessary to reinforce the entire length of the DCB specimens (including the 2D laminate) with unidirectional carbon-epoxy laminate tabs (each 2.65 mm thick), as described in *Chapter 3*.

Copper electrodes were bonded using silver-based conductive paste to the upper and lower surfaces of DCB specimen (see Fig. 6.1). The electrode patches covered an area of 10 mm × 25 mm, and were attached near the end of the DCB specimen that was subjected to crack opening loading. The delamination crack was forced to grow by loading the pre-cracked end of the DCB coupon at a constant crack opening displacement rate of 2 mm/min using a

50 kN load capacity Instron machine. The crack opening displacement (δ) was measured using the cross-head separation in accordance with ASTM D5528. The crack was forced to propagate at short intervals (typically less than 5 mm) along the mid-plane of the DCB coupon, and at each interval the test was interrupted to measure both the crack length (*a*) and the electrical resistance (*R*). The resistivity was measured between the two electrodes, which involved the current flowing from the negative electrode across the crack via the bridging z-binders as well as the current flowing around the crack tip to the positive electrode (as indicated by the red arrows in Figure 6.1). Three DCB samples of each type of material were tested to measure the change to the electrical resistivity with increasing mode I delamination crack length. The current flow was measured in micro ohm (μΩ).

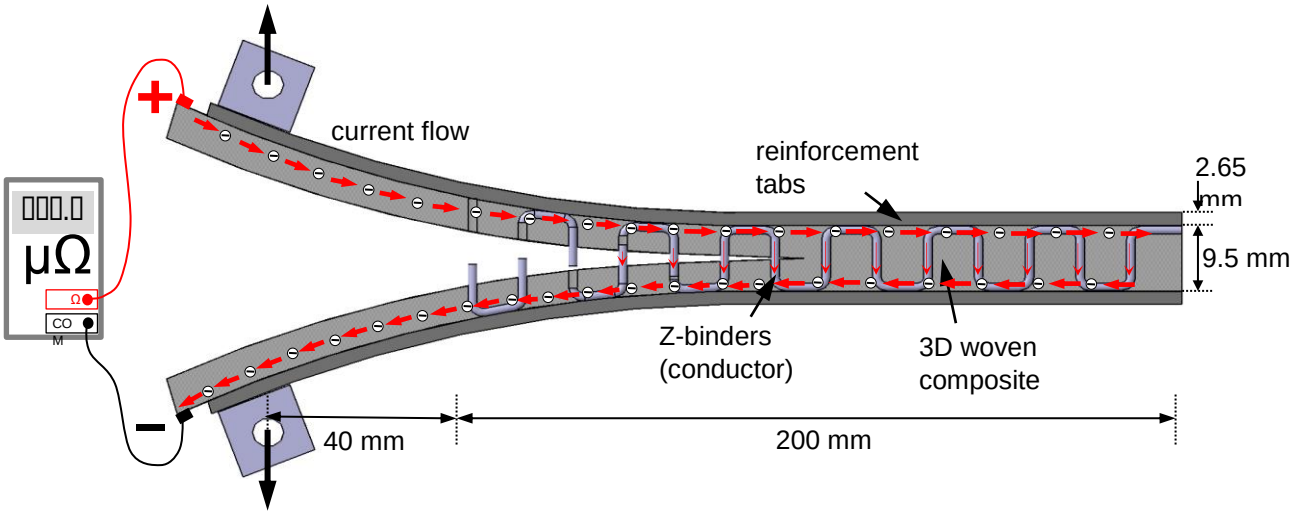

***Fig. 6.1**: Schematic of the delamination detection test on a DCB specimen of the 3D woven composite. The direction of electric current flow between the electrodes is indicated by the red arrows.*

6.3 RESULTS AND DISCUSSION

6.3.1 Electrical-Based Detection of Delamination Cracking in 3D Textile Composites

The measured change to the electrical resistivity of the DCB coupons for the 2D laminate and 3D woven composites with increasing delamination crack length is shown in Fig. 6.2 The percentage change to the electrical resistivity of a DCB specimen is defined by:

$$\frac{\Delta R}{R_o} = \left(\frac{R_d - R_o}{R_o}\right).100 \qquad (1)$$

where R_d and R_o are the measured resistivity values in the delaminated and original (i.e. no crack growth) conditions, respectively. The electrical resistivity of the 2D control laminate increased slowly with increasing delamination length, and at the longest crack length (~140 mm) was increased by only ~5 %. The relatively small increase in resistivity was due to the increased path length for current flow between the electrodes. The current flows from the negatively charged electrode along the delaminated ligament of the DCB coupon. The current then flows around the crack tip and along the opposing delaminated ligament to the positive electrode. When the crack increases in length, the distance over which the current must flow also increases thereby increasing the electrical resistivity of the 2D control laminate. This effect also occurs for the 3D woven composites, although the percentage increase to the electrical resistivity caused by delamination growth is much larger. The three types of z-binder materials studied – carbon fibre, stainless steel and copper – and the two volume contents studied induced large, measurable changes to the electrical resistivity during delamination crack growth. This was due to the z-binders decreasing significantly the original resistivity of the composite material (as described in the previous chapter), and thereby increasing the sensitivity to the detection of delamination growth. During delamination propagation in the 3D woven composites the current flow occurred around the main crack front as well as along the bridging z-binders until they failed by fracture and pull-out when a short-circuit was induced. The experimental data plotted in Fig. 6.2 show that the increase in resistivity of the 3D woven composites often occurred as abrupt step changes, and this was due to the breakage of the z-binders at the rear of the bridging zone and the resulting localised short-circuit.

It is also shown in Fig. 6.2 that the effect of the z-binder material on the sensitivity to detect delamination growth via an increase to the electrical resistivity was not the same, and increased in the order: copper (least effective), carbon fibre and stainless steel (most effective). While copper was the most effective at increasing the electrical conductivity of the composite material (as reported in chapter 5), it was the least effective for delamination crack detection. This was because copper z-binders generated the shortest bridging zone length during delamination crack growth (typically under ~10 mm) before the z-binders fractured due to their relatively low failure stress (as described in *Chapter 3*). In comparison, the z-

binders made of carbon fibre and (in particular) stainless steel formed much longer crack bridging zones (~20 mm and 40-50 mm, respectively) (also explained in *Chapter 3*). When the length of the bridging zone increased the z-binders made an increasingly important contribution to increasing the sensitivity of the 3D woven composites to changes in the electrical resistivity during delamination growth. The longer the crack bridging zone, the greater the sensitivity to changes to the electrical resistivity and consequently the more effective the z-binders were at monitoring the growth of delamination cracks.

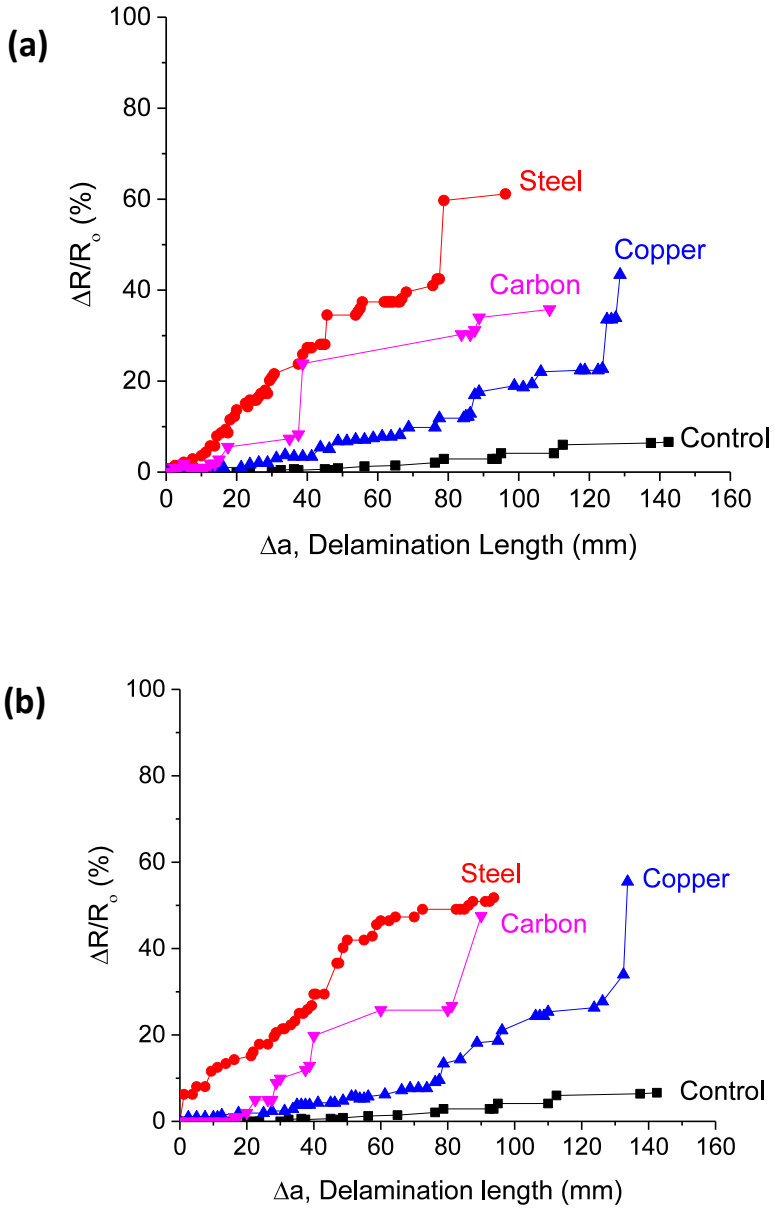

Fig. 6.2: *Effect of increasing delamination length on the percentage change to the electrical resistivity of the composite materials containing (a) low, (b) high volume content of z-binders.*

6.4 CONCLUSIONS

This study has proven that due to the increased electrical conductivity, the z-binders can be used to monitor the growth of mode I delamination cracks in 3D woven composite materials via changes to the resistivity. Electrical-based crack growth detection methods often lack sufficent sensitivity to detect delamination growth. The effect of the z-binder material on the sensitivity to detect delamination growth was increased in the order: copper (least effective), carbon fibre and stainless steel (most effective). While copper was the most effective at increasing the electrical conductivity of the composite material (as reported in chapter 5), it was the least effective for delamination crack detection due to the small bridging zone generated during the damage detection process which significantly affected the electrical resistivity of the DCB specimen. However, the insertion of woven z-binders increases the sensitivity to reliably detect the initiation and propagation of delamination cracks in 3D woven composites. The z-binders also provide the additional benefit of increasing the mode I interlaminar fracture toughness and fatigue strength, electrical conductivity, impact damage resistance and joint strength of composite materials, as reported in the other chapters.

Chapter 7: Impact Damage Tolerance of 3D Woven Composites Using Metal Z-binders

Abstract

This chapter presents an experimental investigation into the low-velocity impact damage resistance and the compression-after-impact (CAI) properties of 3D woven composites. The effects of z-binder material and volume content on the amount of impact damage and the residual compressive properties of 3D composites are investigated, and compared to a 2D (control) laminate without z-binder reinforcement. Impact testing was conducted at two energy levels: 25 J and 50 J. Non-destructive evaluation revealed that the impacted 3D woven composites sustained delamination and matrix cracking, including back-face damage, although the amount of damage was less than the 2D laminate. The improved damage resistance was due to the z-binders creating a bridging zone along the impact-induced delamination cracks. The compression-after-impact (CAI) strength properties of the 3D woven composites were reduced less than for the 2D laminate due to the smaller amount of impact damage.

7.1 INTRODUCTION

3D composites have proven capability to provide high impact damage resistance. As reported in *Chapter 2*, 3D composites reduce the amount of delamination damage caused by high ballistic impact, low velocity impact and large hailstones [77, 161-163]. It has been proven by various researchers that the impact resistance, post-impact strength, and delamination toughness are improved by insertion of z-binders [24, 97, 164-168].

Several researchers [162, 169-171] have extensively studied the mechanism of high damage tolerance for 3D composites. It is found that the amount of impact damage caused to 3D woven composites is less than 2D laminates with the same fibre volume content. The higher damage resistance of 3D woven composites is due to their high interlaminar fracture toughness properties. Naik et al. [172] studied the damage resistance of glass reinforced 3D woven structures which were subjected to different impact energies. The delamination damage increased linearly with the impact energy, except at higher energies when perforation becomes an increasingly dominant mechanism. Chiu et al [173] investigated the

impact and compression-after-impact (CAI) properties of angle interlock 3D carbon woven composites. It was concluded that the impact damage tolerance was superior to 2D composite.

Apart from the studies by Naik et al. [172] and Chiu et al [173], the impact damage resistance and tolerance of 3D woven composites has not been studied. Specifically, there are no published studies into the impact resistance of 3D woven composites containing metal z-binders. This chapter presents an experimental investigation into the impact damage resistance and CAI properties of 3D woven composites reinforced with different z-binder material (steel, copper or carbon) at two volume contents which are termed 'low content' and 'high content' in this thesis. The impact performance of these 3D woven composites is compared to a near-equivalent 2D laminate, which is used as the control material. The 3D woven composites were subjected to barely visible impact loading using the drop-weight method. The damage was characterised and quantified using visible inspection and X-ray computed tomography. The CAI properties of 3D woven composites were also measured.

7.2 MATERIALS AND EXPERIMENTAL METHODOLOGY

7.2.1 Composite Materials

The 3D woven composite specimens were manufactured using a 198 gsm plain woven T300 carbon fabric (AC220127 supplied by Colan Ltd.) (see *Chapter 3*). The specimens consisted of 20 stacked plies of the carbon fabric, which was manually woven in an orthogonal (through-thickness) pattern using carbon fibre tows, copper wire or stainless steel wire. The weaving process and pattern is described in *Chapter 3*. The z-binders were woven in a 100 mm x 100 mm sized region in the centre of the specimens, which were 150 mm long x 100 mm wide (Fig. 7.1). The warp tows to the carbon fabric and the weave direction of the z-binders were both in the lengthwise direction of the specimens. The fabrics were infused using the same epoxy polymer as used in the previous research chapters using the VBRI process.

7.2.2 Impact Tests

The impact tests were conducted on a 2D (control) laminate and 3D woven composites with the dimensions of 100 mm wide x 150 mm long (Fig. 7.1). Drop weight impact tests were

performed on the composites using the impact rig shown in Fig. 7.2. The samples were clamped along the edges. All impact tests were performed according to ASTM D713 specifications using a 12 mm hemispherical hardened steel impactor weighing 2.9 kg. The impactor was dropped from 0.88 m and 1.75 m heights onto the centre of the sample (Fig. 7.1). The impactor was instrumented with a dynamic force transducer to measure the impulse force-time response during contact with the sample. The impulse force was measured at a sampling rate of 19.2 kHz. Two incident impact energies 25 J and 50 J were selected for the impact test. Five samples for each of material type and impact energy were tested.

7.2.3 Compression-After-Impact (CAI) Test

The post-impact compressive properties of the composites were measured using the method specified in ASTM D7137. Three samples of each type of composite material were axially compressed along the warp (0°) fibre direction at an end-shortening rate of 0.5 mm/min until failure. The ends of the sample were clamped whereas the sides were laterally supported using anti-buckling guides, as shown in Fig. 7.3. Digital Image Correlation (DIC) was used to determine the strains on the sample surface during the CAI test. Before testing, the surface of the specimens was sprayed in white colour, and then a high contrast random speckle pattern was created by non-uniformly spraying black dots on the white surface. To confirm the suitability of the size and density of the speckle pattern on the accuracy of the DIC measurements, the specimen was fixed in the compression fixture, and one test image of the sample was taken as shown in Fig. 7.4. A digital camera was positioned a short distance from the specimen to record the DIC images during testing. The images were taken at the rate of 1 ms/image. Post-processing of the images to extract the strain values was performed in MATLAB using the procedure described by Jones [174], and this was used to determine the compressive modulus and surface strain maps.

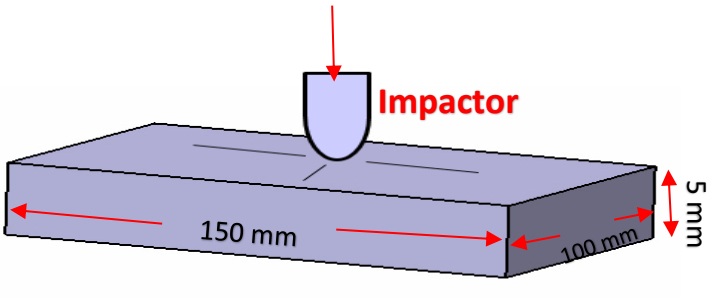

Fig. 7.1: *Schematic representation of the impact test.*

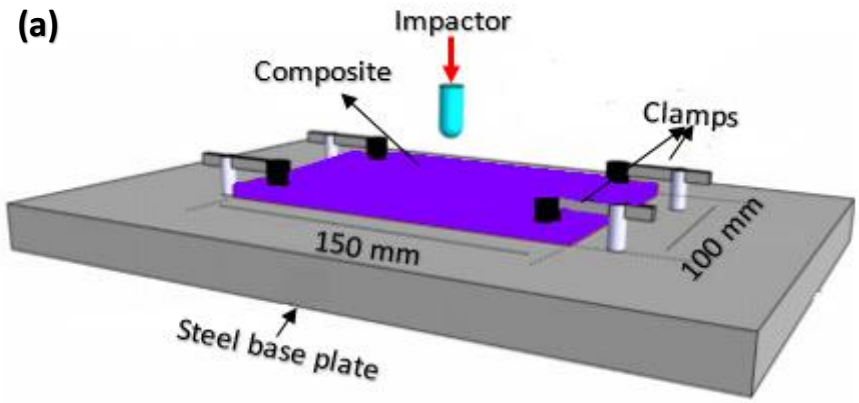

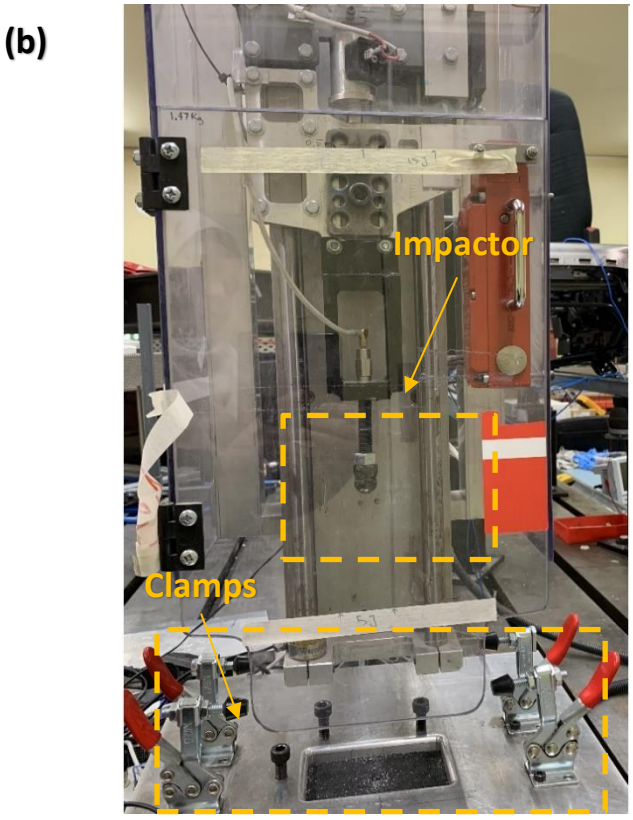

Fig. 7.2: *(a) Schematic of Drop weight impact testing setup, (b) Drop weight impact testing machine.*

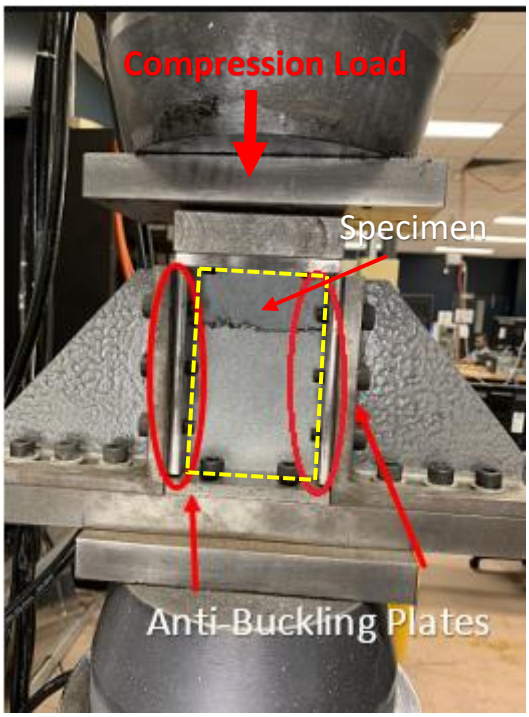

Fig. 7.3: *Compression test fixture with anti-buckling guides.*

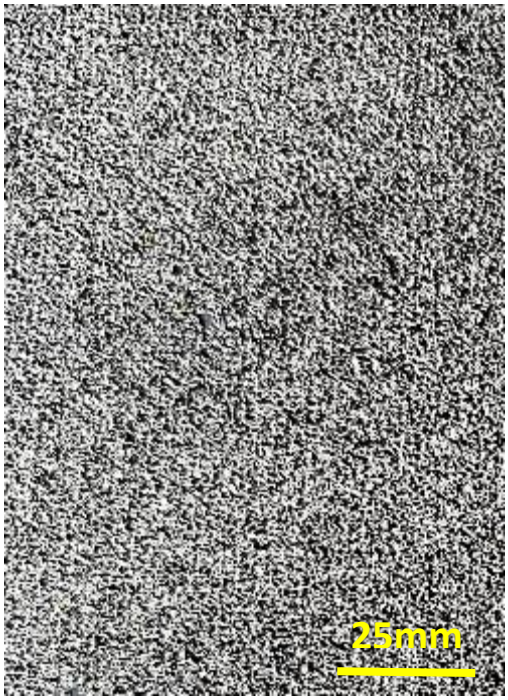

Fig. 7.4: *Random speckle pattern on a composite sample for digital image correlation (DIC).*

7.3 RESULTS AND DISCUSSION

7.3.1 Impact response

The impulse force-time curves measured for the 2D laminate at the incident impact energies of 25 J and 50 J are shown in Fig. 7.5. The results show good repeatability for all five impact tests performed on the laminate. At both energy levels, the impact force initially increases linearly and then experiences a load drop before reaching the peak load. The first load drop is due to the onset of impact damage, which can occur as delaminations, fibre breakages and/or matrix cracking [175]. The load drop is higher at the higher impact energy, which is indicative of more damage (which is expected). Fig. 7.6 presents multiple impact force-time curves for the 3D woven composite containing the steel z-binder, and again at both incident energy levels that confirms a good repeatability in the test results. Similar repeatability was found for the 3D composites with copper or carbon fibre z-binders.

Impact load-time curves for the 2D laminate and different types of 3D woven composites are presented in Fig. 7.7. There is no significant difference between the curves measured for the different materials at the low impact energy, except that the small load drop is more apparent for the 2D laminate. At the higher impact energy, the curves were also similar for the different materials, although the peak load and post-peak load values are slightly lower for the 2D laminate.

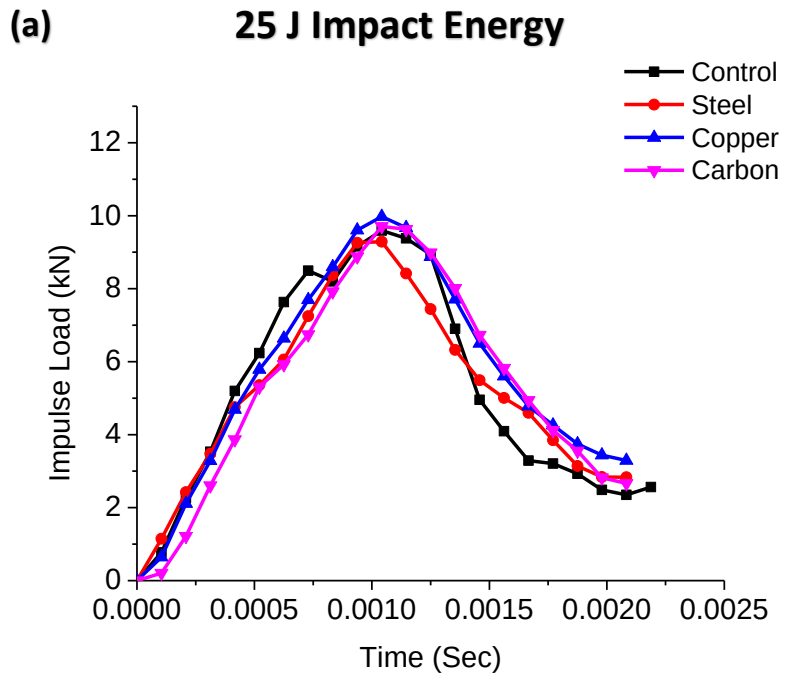

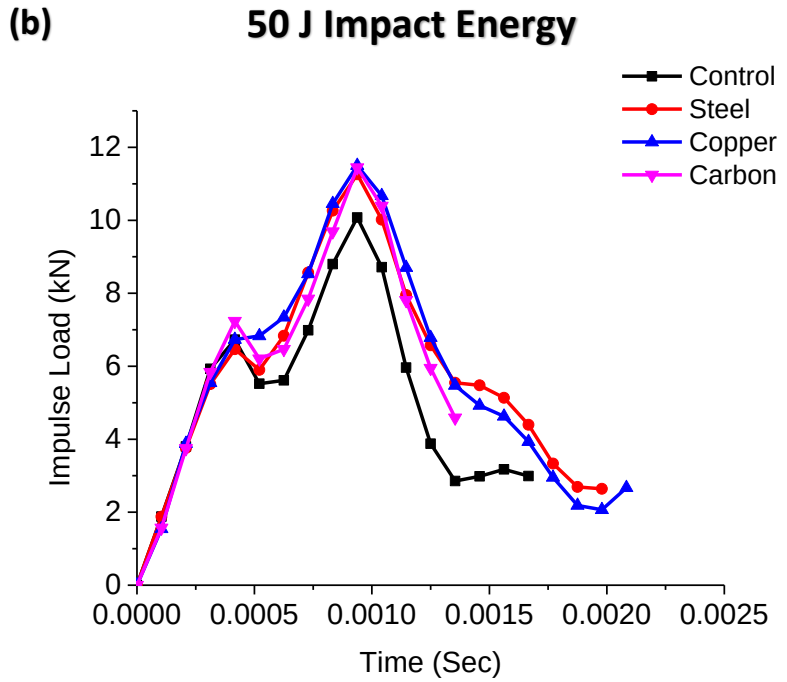

Fig. 7.5: *Impact load-time curves for the 2D laminates and 3D woven composites at the incident impact energies of (a) 25 J and (b) 50 J.*

Following impact testing, the 2D and 3D woven composites were non-destructively inspected using X-ray computed tomography (CT). The impacted surface of all the test samples had a shallow indentation, which was caused by the impactor locally crushing the surface. Splitting cracks orientated in the 0^o and 90^o fibre directions were also observed on the impacted surface. The back-face surface also sustained longitudinal splitting cracks, as shown in Fig. 7.8. These damage modes were observed in all types of composite material (i.e. 2D and 3D), and was not affected significantly by the type or volume content of z-binder reinforcement. The bending deflection of the composite specimens caused by the impact event generates interlaminar shear and through-thickness tensile stresses which caused the formation of splitting cracks. These cracks are much longer at the back than the front surface, and this is due to higher tensile strains generated at the back surface during impact.

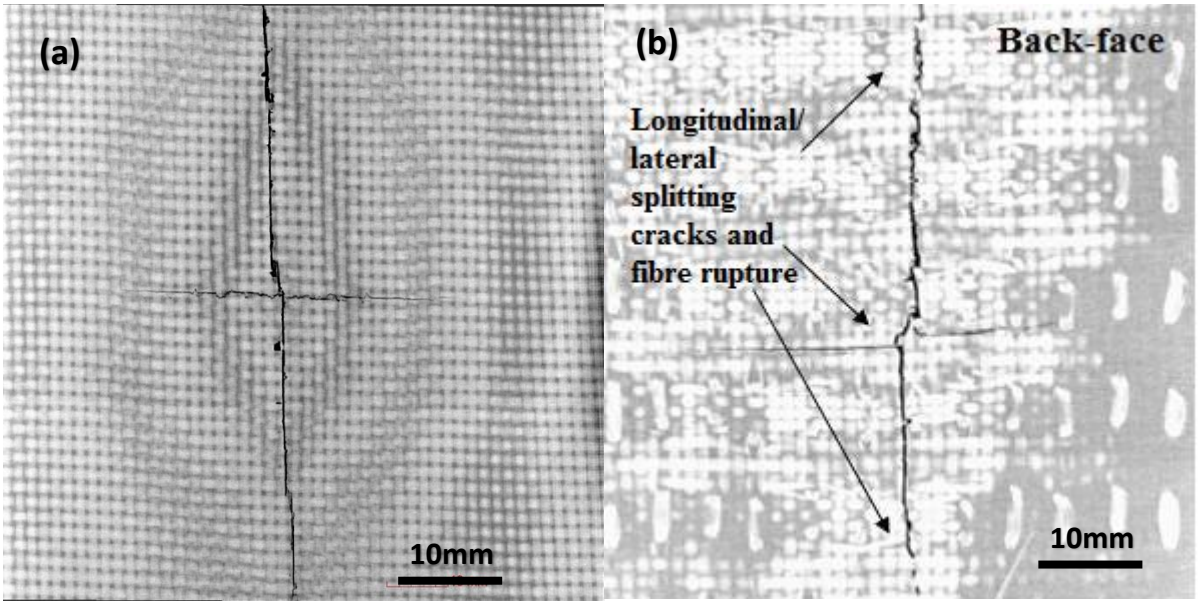

Fig. 7.6: *X-ray CT images of back-face damage to the (a) 2D and (b) 3D woven composites. The composite in (b) contained carbon z-binders.*

Cross-sectional X-ray CT images in Fig. 7.9 show the internal damage to the 2D laminate and a 3D woven composite (reinforced with carbon z-binders) impacted at the two energy levels. The two most obvious types of damage were delamination cracking and ply rupture. The length of delamination cracks between the plies in the 2D laminate was higher at the higher impact energy level. All 3D composites sustained a large through-thickness crack

along the interface between the z-binder and composite material. Compared with the 2D laminate, all of the 3D woven composites experienced less delamination damage. The X-ray CT images for steel and copper 3D woven composites were not taken due to the charging caused by the large difference in the metal and carbon densities. Due to the large difference in the X-ray absorption coefficient of the metal z-binders and carbon-epoxy laminate material, it was not possible to obtain high quality X-ray CT images of the 3D woven composites containing steel or copper.

(a)

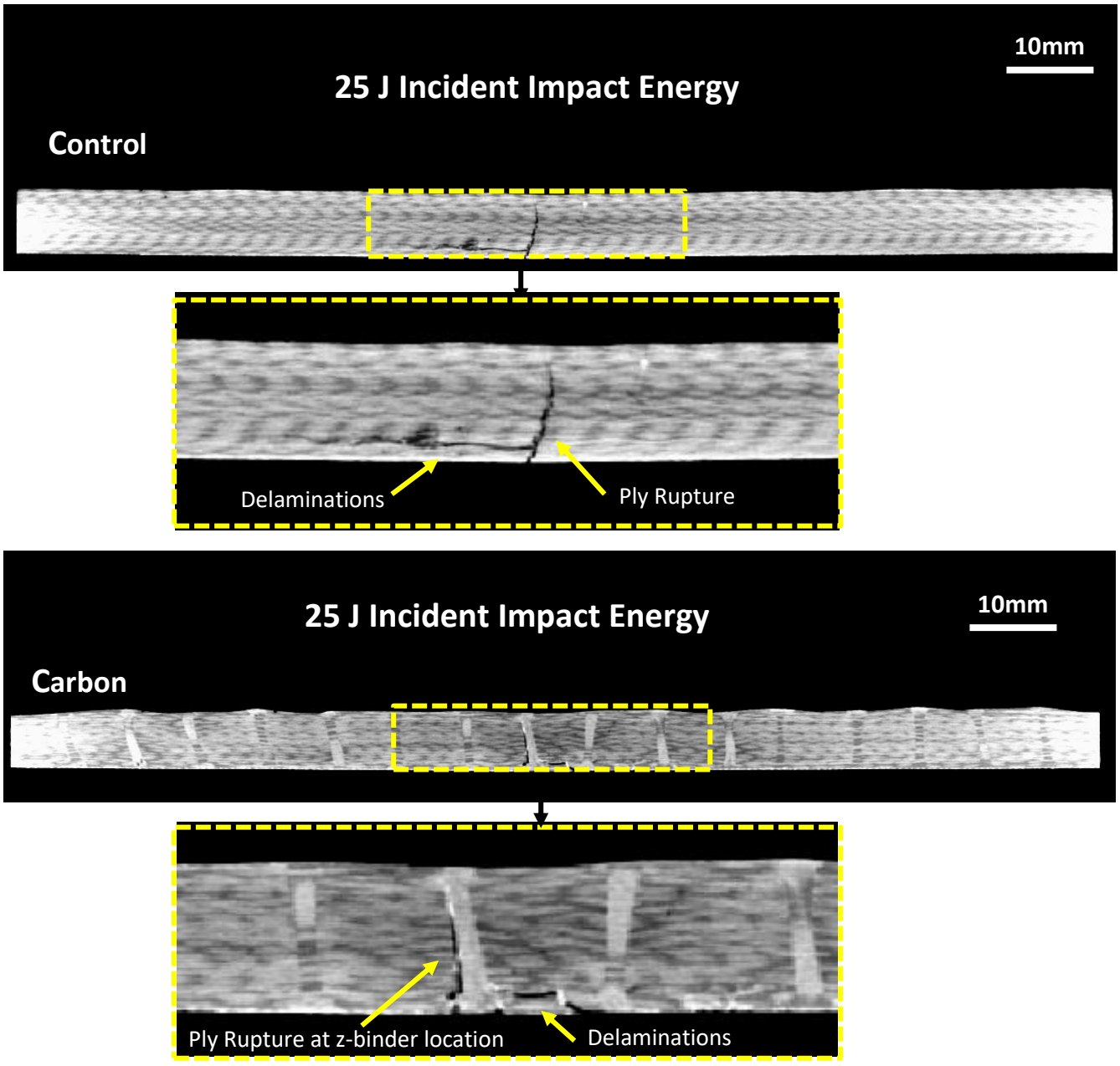

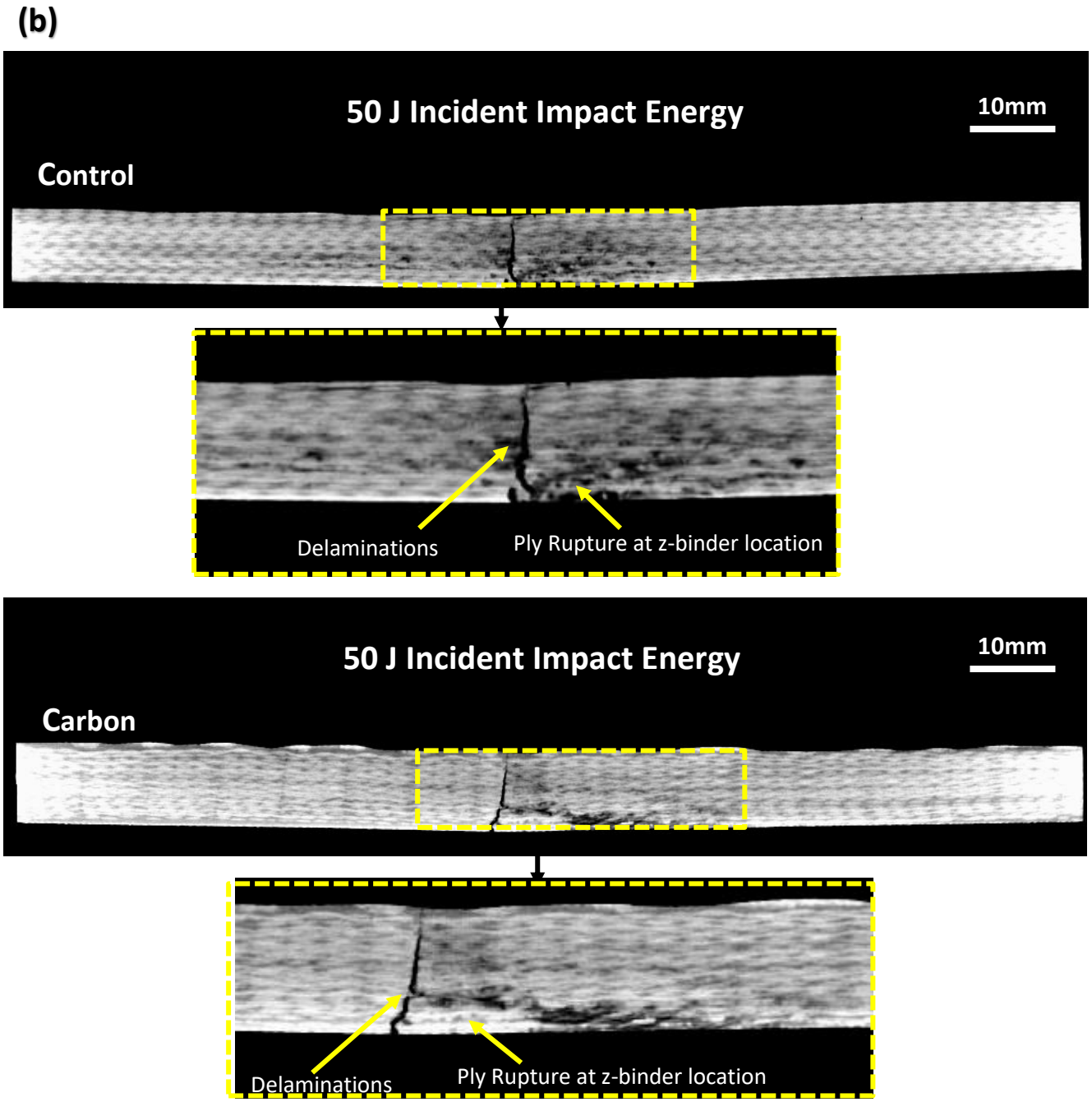

Fig. 7.7: *Cross-sectional X-ray CT images showing the effect of impact energy (a) low (25 J) and (b) high (50 J) on the 2D laminate and the 3D woven composite containing carbon z-binders.*

The X-ray CT imaging revealed that the projected delamination area in the x-y plane of the impacted specimens was approximately rhomboid (i.e. diamond) shaped, as shown for example in Fig. 7.10 (a). Assuming this shape, the back-face delamination damage area (A_{dmg})

was simply calculated using:

$$A_{dmg} = \frac{1}{2} W_{lat} \times L_{long}$$

where W_{lat} and L_{long} are the lateral and longitudinal lengths of the splitting cracks at the back-face. Using this analysis, Fig. 7.10 (b) shows the effect of incident impact energy on the back-surface delamination damage area for the 2D laminate and 3D woven composites. The z-binders reduced the average area of the delamination damage, with the different z-binders causing similar reductions. The reduction to the delamination damage area was due to a large-scale bridging zone created by the z-binders which increases the modes I and II interlaminar fracture toughness values (as reported in *Chapter 3*). Under the impact test conditions used here, the delamination damage is caused mostly by interlaminar shear stresses concentrated to the region immediately below and surrounding the impact point. The interlaminar fracture toughness testing (*Chapter 3*) revealed that the mode II delamination toughness was improved by the z-binders, although the magnitude of the toughening effect was not influenced greatly by the type of z-binder. That is, the mode II interlaminar fracture toughness properties of the 3D woven composites with copper, carbon and steel were similar (unlike the mode I toughness properties where copper was the less effective and steel the most effective). For this reason, the different type of 3D woven composite shows similar reductions in the amount of impact-induced delamination damage, and is not influenced significant by the type of z-binder material.

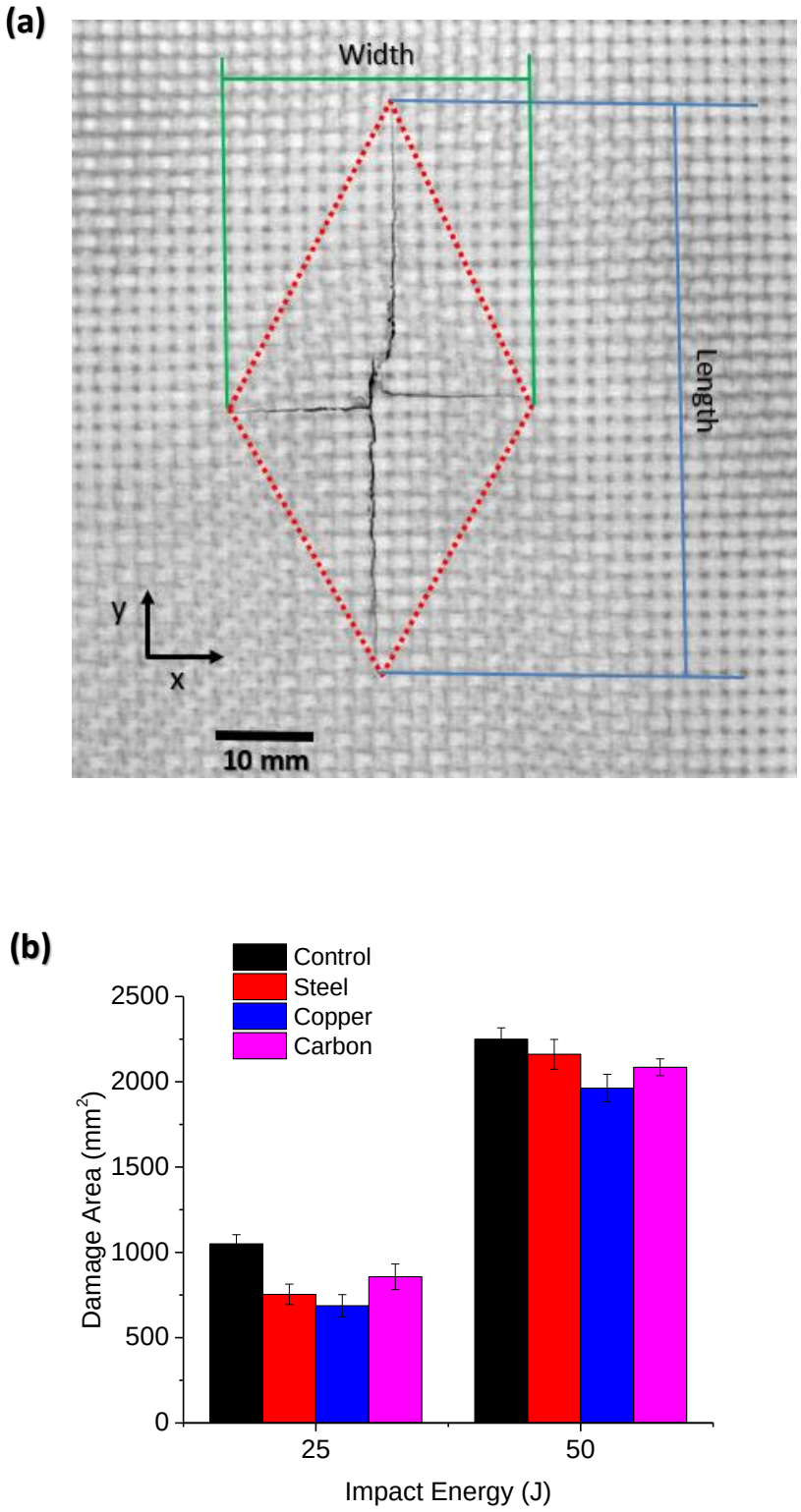

Fig. 7.8: *(a) Example X-ray CT image used for measuring impact damage area. (b) Effect of impact energy on the back surface delamination damage area for the 2D and 3D woven composites.*

7.4. In-plane compressive properties of 2D and 3D composites.

7.4.1 Pre and post impact compressive properties of 2D and 3D composites

Following impact testing, the residual compression properties of the composites were measured. Compressive stress-strain curves measured for the 2D laminate and 3D woven composites without impact damage (pre-impact) are presented in Fig. 7.11. The failure stress of the 3D woven composites was much lower than the 2D laminate, and the mechanisms responsible for this are investigated in *Chapter 9*. In all materials, failure occurred by micro-buckling/kinking of the load-bearing tows, which was aided by the z-binders.

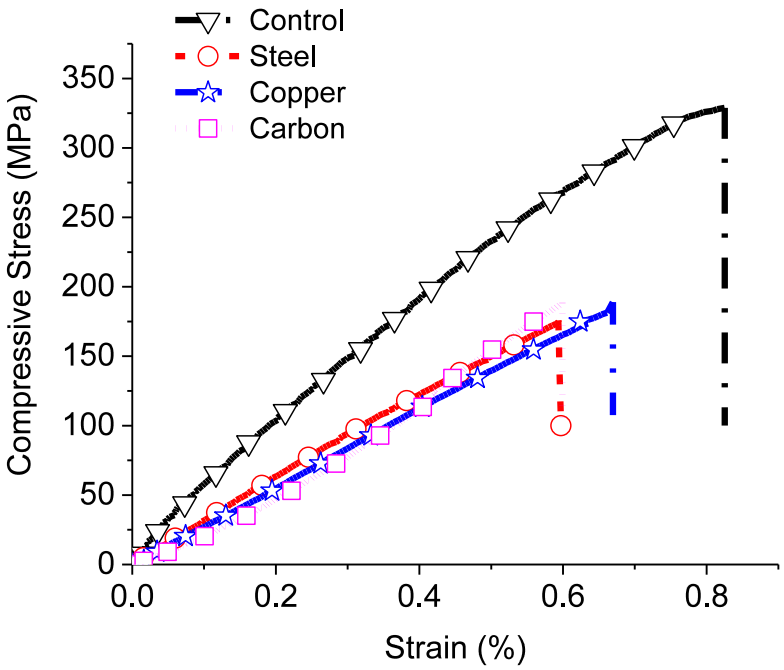

Fig. 7.9: *Compressive stress-strain curves for the 2D laminate and 3D woven composites before impact loading.*

Compressive stress-strain curves measured for the 2D laminate and 3D woven composites with impact damage are presented in Fig. 7.12. The curves show the applied load increased linearly with the strain until failure of the specimen. Similar to the pre-impacted composites, the impacted specimens failed by kinking of the load-bearing tows with failure initiating in the impact damaged region. The impacted specimen for all materials for low and high incident energy shows no reduction in compressive response as shown in Fig. 7.12**.**

Whereas, the impacted specimens for high incident energy shows improvement in the copper and carbon z-binder composites but shows reduction in the steel z-binder composite, which may have been caused by more damage to the load-bearing (in-plane) fibres from the weaving of steel z-binder compared with copper and carbon z-binders, as shown in Fig. 7.12. It is worth noting that manual weaving of the fibre preforms with the steel z-binder was very challenging due to its higher stiffness compared to the carbon and copper z-binders. Thus, weaving with steel z-binders is likely to cause greater damage to the load-bearing fibres.

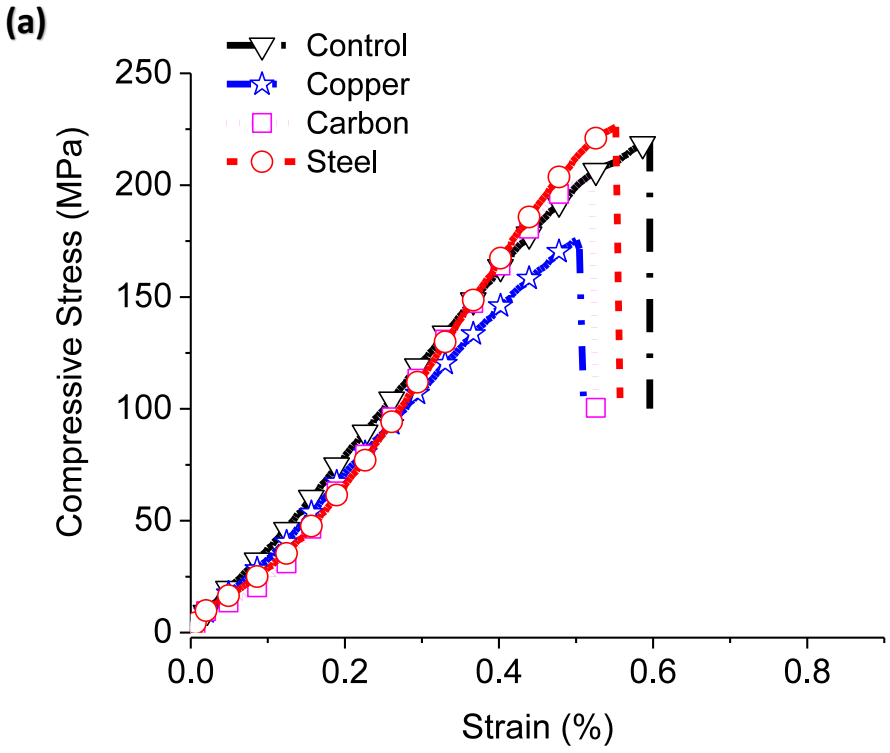

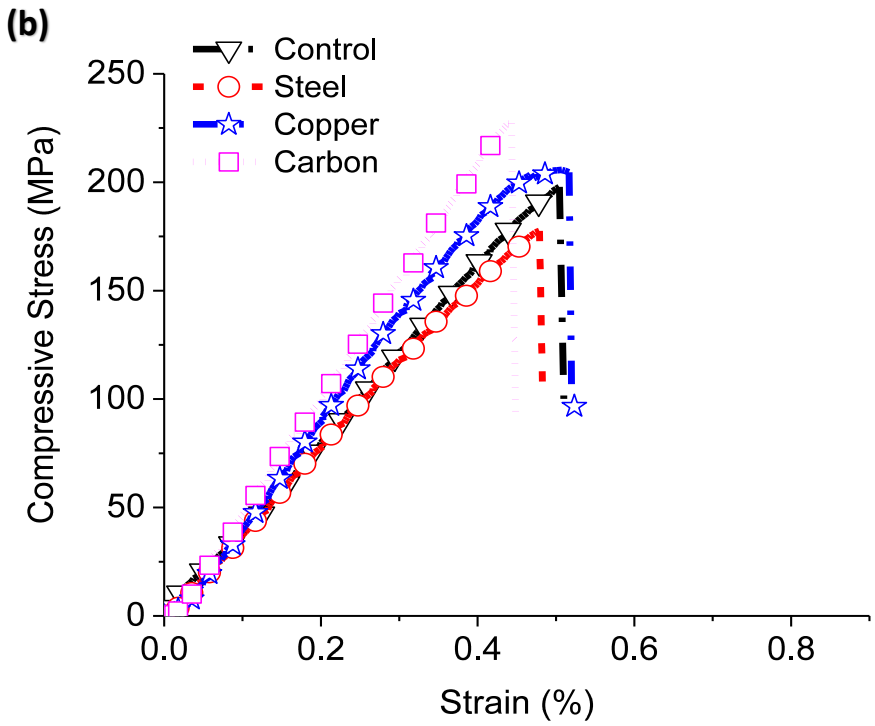

Fig. 7.10: *Compressive stress-strain curves for the 2D laminate and 3D woven composites impacted at (a) 25 J and (b) 50 J.*

The compression strain (ε_{yy}) response of the 2D and 3D laminates for low and high incident energies is presented in Fig. 7.13. The DIC generated strain images were taken at 30%, 50% and just before final failure (100%). The 2D laminate shows a relatively uniform strain field concentration over the surface until the final failure. On the other hand, all the 3D laminates show high strain concentrations in the locations of the z-binders for both volume content, and the crack propagation initiated at the location of the impact. With increasing stress levels, the strain at the location of the damage increased significantly, which was followed by the fracture of the specimen at the ultimate failure strain, as shown in Fig. 7.13 (a,b).

(a)

% of failure strength	30%	50%	100%
Control	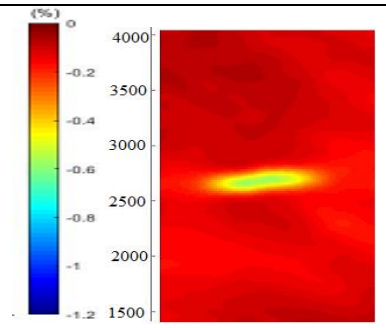	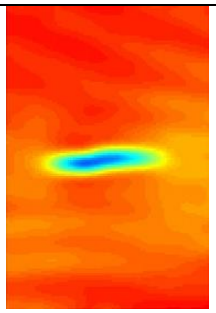	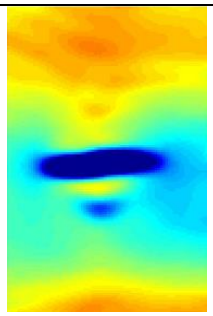
Steel (High)	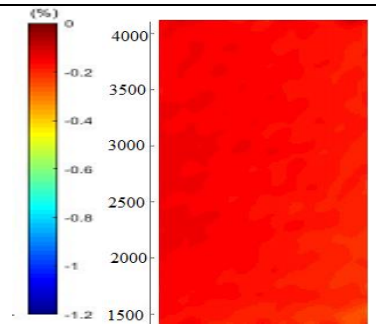	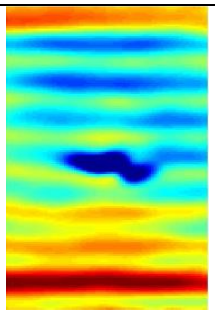	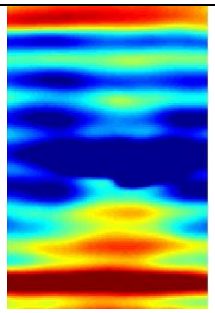
Carbon (High)	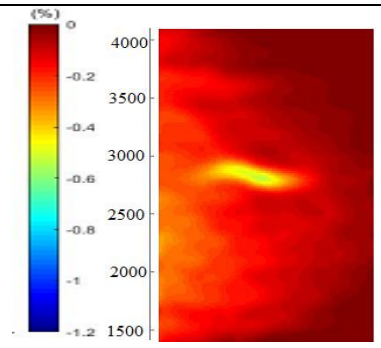	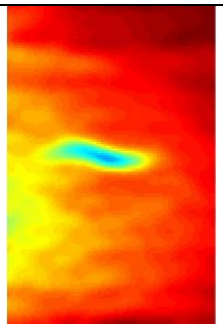	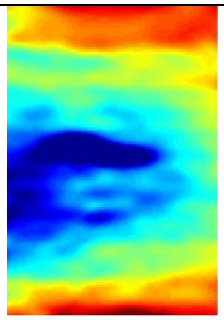
Copper (High)	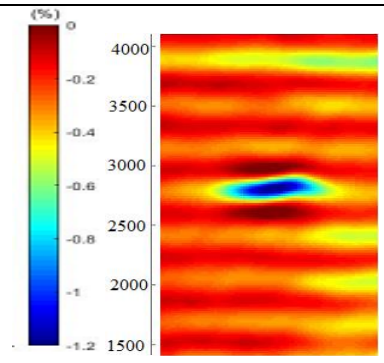	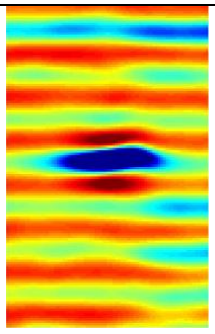	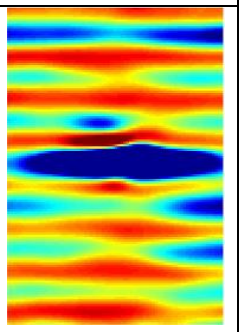

(b)

% of failure strength	30%	50%	100%
Control	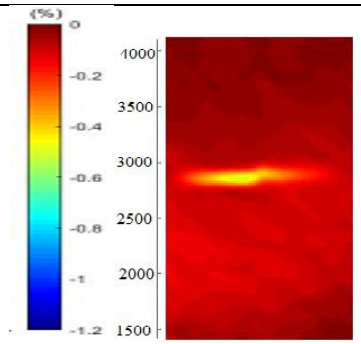	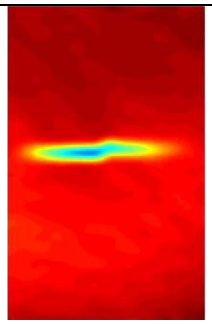	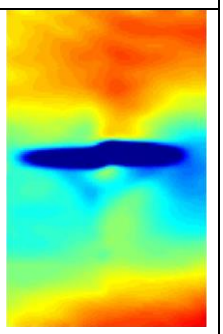
Steel (High)	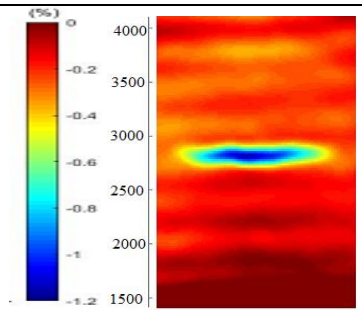	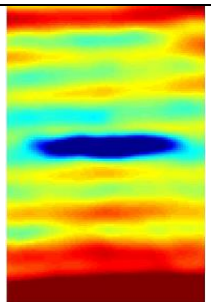	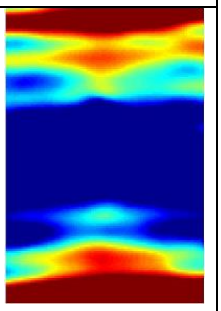
Carbon (High)	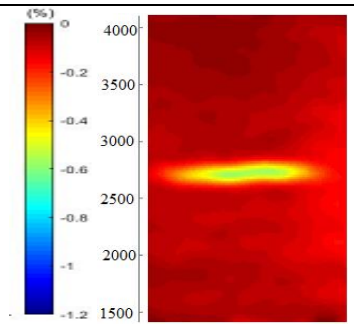	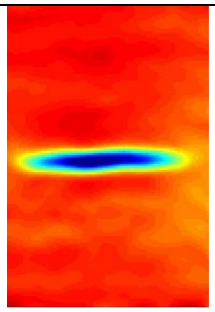	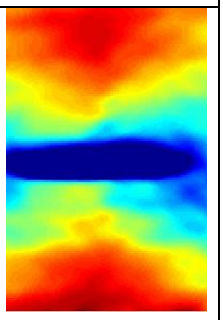
Copper (High)	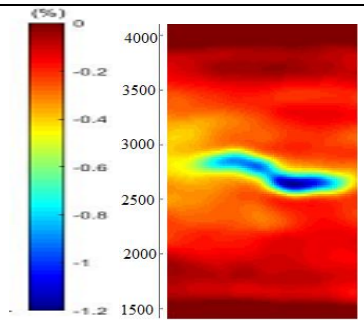	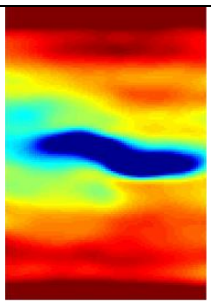	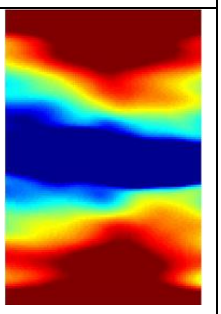

Fig. 7.11: *Compression strain (Ɛyy) images measured at 30%, 50% and just prior to 100% of the failure stress for the 2D (control) laminate and the 3D woven composites subjected to (a) low (25 J) and (b) high (50 J) impact energies.*

The compression properties for the materials before and after impact loading at the low and high incident energies are shown in Fig. 7.14. The reduction in compression modulus of the pre-impacted specimens is dependent on several factors, including the fibre waviness and fibre volume content of the load-bearing fibres. The major cause of the reduction in compression modulus in the 3D woven composites is attributed to the damage occurred due to the impact energies (25 J and 50 J). Another cause of this reduction is the fibre waviness around the z-binders. The compression modulus of impacted specimens shows no major reduction for all types of z-binder material.

The pre-impact compressive strength and compression-after-impact (CAI) strength values of the 2D laminate and different types of 3D composites are shown in Fig. 7.15. The average compressive failure stress of pre-impact specimens for all the z-binder material is lower than the 2D composite. The compressive properties of 3D composites can be reduced [31, 32, 176] due to in-plane fibre waviness and out-of-plane fibre crimping caused by the z-binders [31, 177, 178]. Furthermore, finite element analysis and experimental results show that fibre waviness and crimping lowers the compressive stress needed to initiate kinking of the load-bearing fibres in 3D woven composites [24, 30, 31]. On the other hand, all the compression modulus results are in the bounds of experimental scatter, so the compressive modulus of impacted specimens for both low and high incident energies and for all z-binder material shows no major reduction for all types of z-binder material.

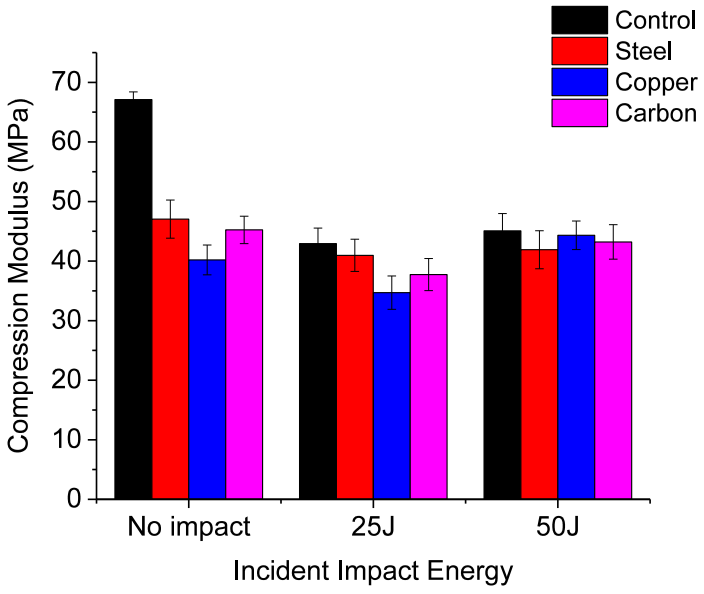

Fig. 7.12: *Effect of z-binder on compression modulus of different z-binders.*

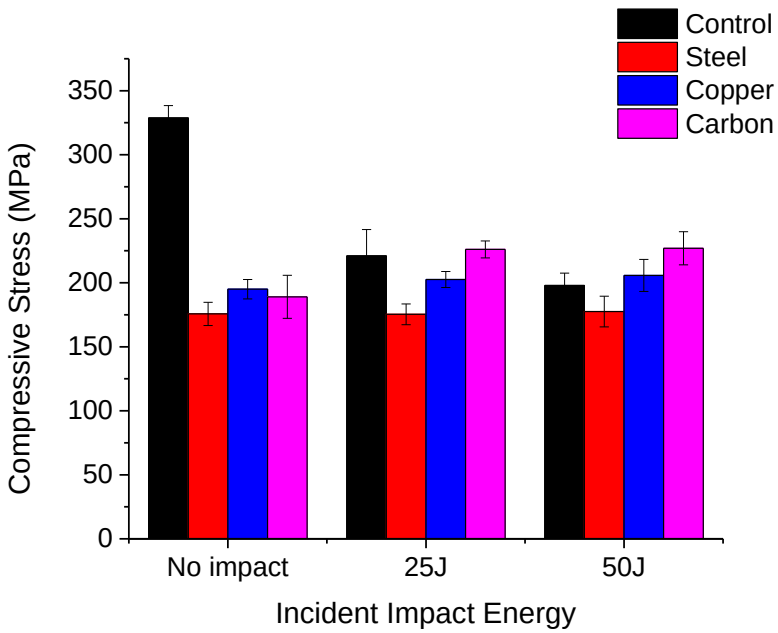

Fig. 7.13: *Effect of z-binder on compression stress of different z-binders.*

Fig. 7.16 and 7.17 shows the failure modes of the 2D laminate and the 3D composite woven with carbon z-binder. The failure mechanism was not affected significantly by z-binders, with both materials failing by kinking and microbuckling of the 0° tows. The CAI strength of the 3D composites was dependent on the type of z-binder material. The results show that the CAI strength were higher for copper and carbon z-binder composites, whereas steel z-binder composite shows reduction compared with 2D and other 3D composites.

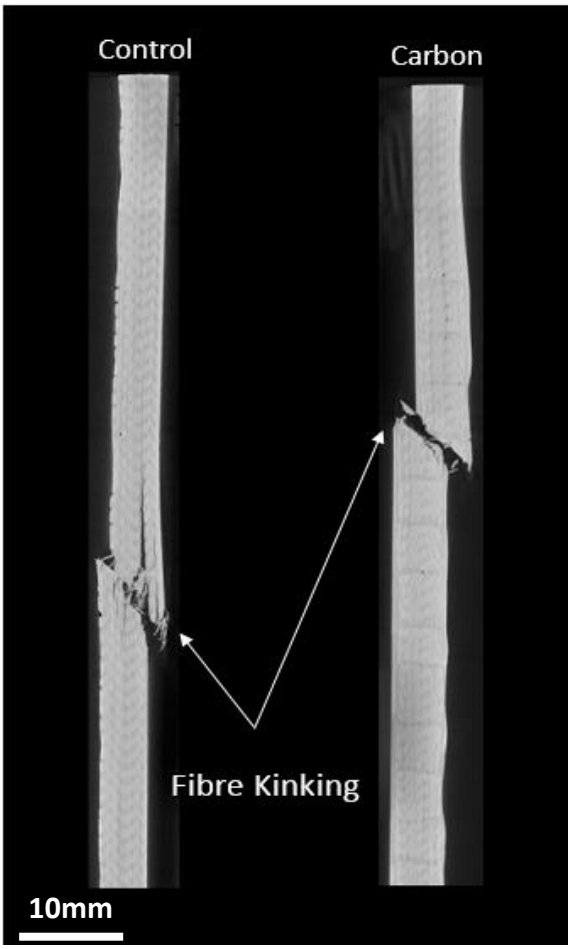

Fig. 7.14: *X-ray images showing compressive failure of the control (no z-binder) and carbon 3D composites.*

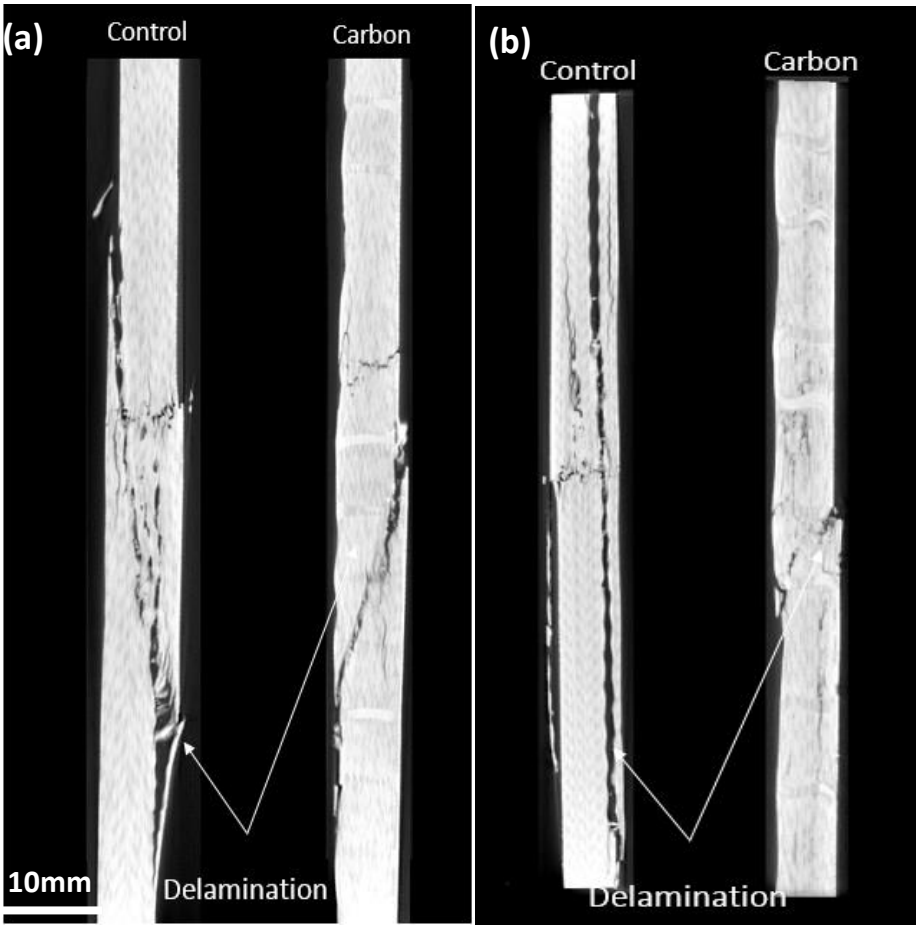

Fig. 7.15*: X-ray images showing compressive failure in (a) 25 J and (b) 50 J.*

7.5 CONCLUSION

The results presented in this chapter have shown that the presence of z-binders can reduce the amount impact damage and the reduction to the compression-after-impact properties of the 3D composites is also decreased. The effect of material type and volume content of z-binder were investigated in this chapter. It was found that the z-binder showed reduction in compressive properties of the 2D and 3D composites. The impact damage area for the 3D composites was lower than the 2D laminate. 3D composites showed no reduction in the compression-after-impact strength and compressive modulus for all the z-binder materials. Both impact energies (25 J and 50 J) showed reduction to the impact damage area, however high impact energy (50 J) showed more improvement than low energy (25 J). This is due to the development of the large-scale bridging zone. The CAI results shows reduction in compression modulus this is due to the damage of in-plane fibres due to the insertion of z-binder.

Chapter 8: Structural properties of 3D composite T-joints woven with metal or carbon z-binders

Abstract

An experimental investigation is presented into improvements to the maximum load limit and other structural properties of T-shaped laminate joints reinforced with thin woven metal filaments. The skin/flange section of carbon-epoxy T-joints contained metal filaments made of copper or steel woven in the through-thickness (z-) direction. A T-joint containing woven z-binders of carbon yarn was also evaluated. Stiffener pull-off tests performed on the T-joints demonstrated the woven z-binders promote large improvements to the maximum load and absorbed energy capacity (up to ~2-fold and ~3-fold, respectively). The strengthening effect of the z-binders is controlled by their volume fraction and material type, with steel being more effective than copper or carbon. The z-binders resist large-scale cracking in the skin/flange region, and the strengthening mechanisms are described in this chapter. This study demonstrates that through-thickness woven metal z-binders are highly effective at strengthening and toughening T-joints made of laminated composite material.

8.1 INTRODUCTION

T-shaped joints are used to transmit loads between orthogonal structural components used in aircraft, ships, civil infrastructure, automobiles and many other applications. As examples, T-joints are commonly used for stiffening thin-walled panels such as wing skin and fuselage barrel sections on aircraft and for strengthening pressure vessels. However, T-joints made of fibre reinforced polymer laminate can be damaged by high out-of-plane loads and high energy impact events. The main components to T-joints – stiffener, skin and flanges/webs – are usually joined using a polymer via adhesive bonding and/or co-curing. Under high external loads, the bonded sections are susceptible to fracture, and this can compromise the physical and mechanical integrity of the T-joint; allow the leakage of water, gas and other medium; and cause other problems.

Various techniques and materials are used to improve the structural properties and damage resistance of bonded joints made of laminated composite materials. This includes the use of toughened adhesive [179], which is the most common method, nanoparticle toughened polymers in the adhesive and/or laminate [131, 180-183], interleaving of thermoplastic film or woven tows [184, 185], optimisation of the ply stacking sequence [186, 187], geometric design changes to the fillet region [188], and through-thickness fibre reinforcement using tufting [189], z-pinning [189-197], stitching [197-202] or 3D braiding [203, 204]. Of these techniques, through-thickness reinforcement is generally the most effective at increasing the ultimate failure stress and failure strain limit of joints. For example, Cartié et al. [189] doubled the ultimate failure load of a carbon-epoxy T-joint by tufting using S-glass threads. As another example, Koh et al. [191] measured improvements to the ultimate failure load of T-joints of up to ~75% using z-pins.

3D weaving is another through-thickness reinforcement method that can improve the structural properties of composite joints. 3D weaving is a versatile process that can produce a variety of textile preform shapes for different types of composite joints, including T-shaped joints [205-208]. The versatility allows joint preforms to be woven using many types of fibrous materials, with carbon and glass yarns being most commonly used. Experimental testing and finite element modelling demonstrates that T-joints made of 3D woven fabric composite have superior structural properties compared to T-joints made of bonded laminate [209-214]. For example, Soden et al. [209] experimentally measured the structural properties of 3D woven T-joints when loaded in axial tension along the skin section. While the load required to initiate first cracking in the 3D woven T-joints was similar to a laminated T-joint, both the peak load limit and fracture energy were higher. Soden and colleagues found that the structural properties of 3D woven T-joints increased with the density of through-thickness filaments, reaching the maximum improvement of nearly six-fold in ultimate load and five-fold in fracture energy. As another example, Yan et al. [211] measured a three-fold higher peak load limit for a 3D woven T-joint compared to a laminated T-joint when subjected to stiffener pull-off loading. The z-binders increased the interlaminar fracture resistance and damage tolerance of the 3D woven joints, and thereby improved structural properties such as maximum load and fracture energy. The improvements to the structural properties of other

types of 3D woven joints, such as π-shaped connections for I-beams, has also been investigated [215, 216].

To date, the 3D woven joints that have been studied contain fibrous yarns for the through-thickness reinforcement (glass or carbon). However, significant damage is caused to the through-thickness yarns during the 3D weaving process [33-35]. For example, Rudov-Clark et al. [35] measured a ~50% reduction to the tensile failure stress of z-binders made of E-glass yarns during the weaving of 3D orthogonal fibreglass fabric. The z-binder yarns are forced to bend through tight curvatures and slide against the weaving machinery, and these actions abrade and break some of the fibres and thereby weaken the yarns, as described in *Chapter 2*. It is feasible that this damage can be overcome by substituting z-binders made of fibrous yarns with thin metal wire. Metal z-binders are plastically deformed in the weaving process, however they are not weakened and do not break. For example, Sharp et al. [94] produced a 3D woven fabric containing thin copper wires for the z-binders as a means to increase the thermal conductivity. However, little is known about the properties of 3D woven composite materials and their structures when reinforced in the through-thickness direction with metal filaments.

The aim of the study presented in this chapter is to investigate the efficacy of woven metal z-binders for increasing the structural properties of laminated T-joints. The skin-flange sections to a carbon-epoxy T-joint are reinforced in the through-thickness direction with woven z-binders made of thin copper or steel wire. For comparison, the T-joint containing woven z-binders made of fibrous carbon yarns is evaluated. The study determines the improvements to the structural properties of the T-joint under the stiffener pull-off loading condition to confirm whether metal z-binders are as effective as z-binders made of carbon fibre yarn, which is commonly used. The effects of z-binder material and z-binder content on the structural properties of the T-joint is determined, including stiffness, load-to-first failure, ultimate load limit and energy absorption capacity. The strengthening mechanisms by which the metal z-binders increase the T-joint properties are identified. The work in this chapter also aims to compare the strengthening efficacy of woven metal z-binders against other methods used to increase the properties of T-joints, such as stitching and z-pinning. This study aims to demonstrate the through-thickness weaving with metal z-binders is a simple and effective method to increase the structural properties of laminated T-joints.

8.2 T-JOINTS AND EXPERIMENTAL METHODOLOGY

8.2.1 T-joint Specimens

Four types of T-joint specimen were studied to evaluate the strengthening effect of woven metal z-binders: (i) control T-joint without z-binder, (ii) T-joint with copper z-binders, (iii) T-joint with steel z-binders and (iv) T-joint with carbon z-binders. The basic design and dimensions of the T-joint specimen is shown in Fig. 8.1. The only significant difference between the different joints was the thickness of the skin-flange section, with the values given in Table 8.1. This section was thicker for T-joints containing z-binders made of carbon fibre or steel.

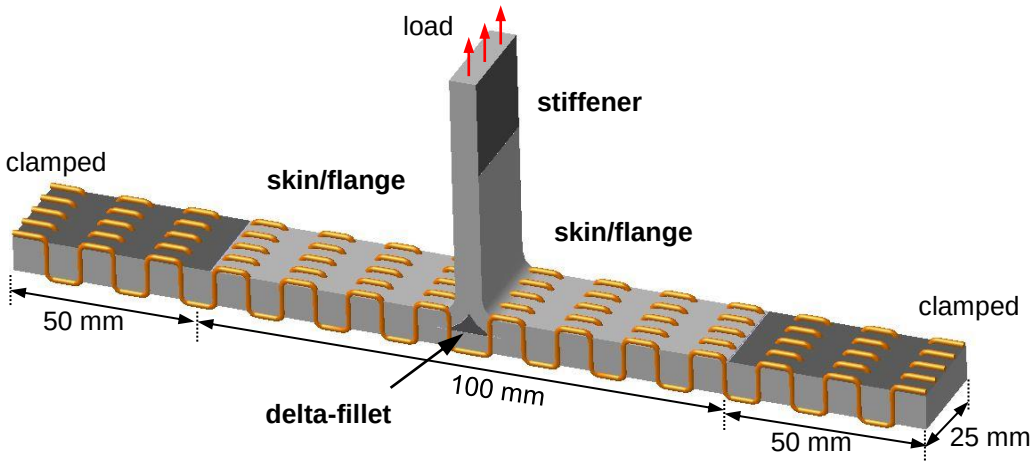

Fig. 8.1: *Schematic of T-joint specimen reinforced with woven z-binders.*

Table 8-1: *Thickness and in-plane carbon fibre content of the skin-flange section of the T-joint specimens.*

T-Joint	Skin-Flange Thickness (mm)	Skin-Flange Fibre Content (vol %)
No z-binders	5.07 ± 0.08	0.39
Copper z-binders		
Low content	5.08 ± 0.10	0.36
High content	5.13 ± 0.10	0.35
Carbon z-binders		
Low content	5.23 ± 0.19	0.38
High content	6.00 ± 0.08	0.34
Steel z-binders		
Low content	7.39 ± 0.16	0.35
High content	7.58 ± 0.10	0.33

The T-joint specimens were manufactured using a 198 gsm plain woven T300 carbon fabric (AC220127 supplied by Colan Ltd.). The specimens consisted of a flat skin panel and two L-shaped sections, which when placed back-to-back formed the stiffener and flanges. The skin contained 10 plies of the carbon fabric with the warp yarns all aligned in the lengthwise direction. The two L-shaped sections also contained 10 plies of fabric aligned in the lengthwise direction. Where the fabrics to the flanges and the skin connect they were manually woven in an orthogonal (through-thickness) pattern using thin filaments of copper, steel or carbon fibre yarn (as indicated in Fig. 8.1). The orthogonal weave pattern is shown in Fig. 8.2. The z-binders were woven in straight parallel rows along the length of the skin-flange sections, as shown in Fig. 8.1. Neither the delta-fillet region nor the stiffener contained z-binders.

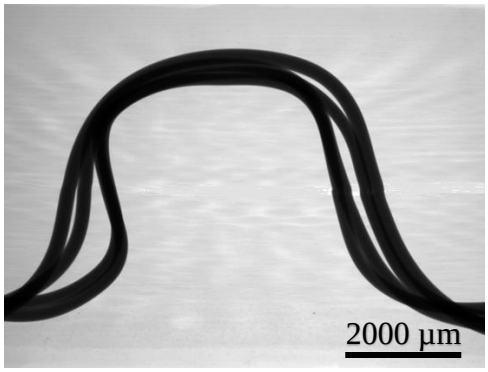

Fig. 8.2: *X-ray computed tomography image of the orthogonal weave pattern to a metal z-binder.*

Copper and steel were chosen for the metal z-binders to reinforce the T-joint because they represent relatively low and high strength materials, respectively. Carbon yarn was also used as a z-binder material. These are the same z-binder materials used in the previous research chapters. The mechanical properties of the metals before being woven into the fabric preforms to the T-joints are given in Chapter 3.

The skin/flange sections of the carbon fabric preform to the T-joint were reinforced with woven z-binders at areal fractions in the through-thickness directions of ~0.35 % and 0.7 %, which are termed 'low content' and 'high content' in this work. The corresponding z-binder volume content in the T-joint were ~0.6 % and 1.0 %. The areal fraction was adjusted by varying the pitch of the orthogonal weave pattern along each row, and the spacing between the rows. For the low z-binder content the pitch and row spacing were ~10 mm and 6 mm respectively, and for the high z-binder content they were ~7.5 mm and 4 mm.

The T-joint fabric preforms were infused with liquid epoxy resin using the vacuum bag resin infusion technique as shown in Fig. 8.3. The epoxy was a diglycidyl ether of bisphenol A resin (SR8100) and diamine hardener (SD8824) supplied by Sicomin®, with a weight mix ratio of 100 (resin)-to-22 (hardener). The delta-fillet region at the base of the stiffener was filled with the epoxy during the infusion process. After infusion, the T-joints were cured inside the vacuum bag for 24 h at room temperature, and then post-cured at 60°C for 8 hours inside an oven while still under pressure applied by the vacuum bag. T-joint specimens were cut into the dimensions shown in Fig. 8.1 using a diamond tip bench-top saw. The skin, flange and stiffener laminates dimensions are given in table 8.1. The width of joint was ~25 mm. The

total length of the T-joint was ~200 mm. The T-joint specimen containing woven z-binder is shown in Fig. 8.4.

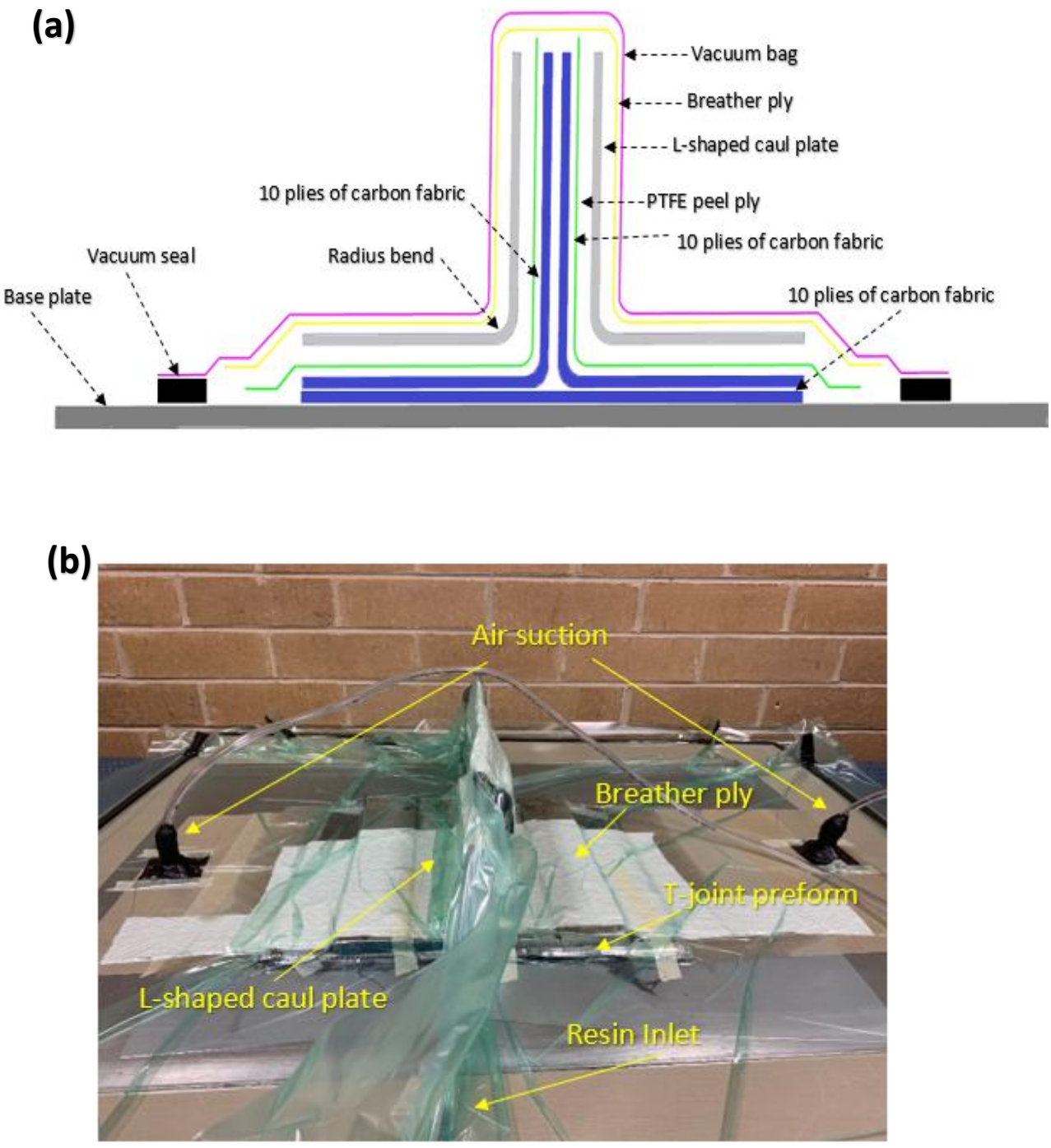

Fig. 8.3: *Vacuum bagging resin infusion process of T-joint.*

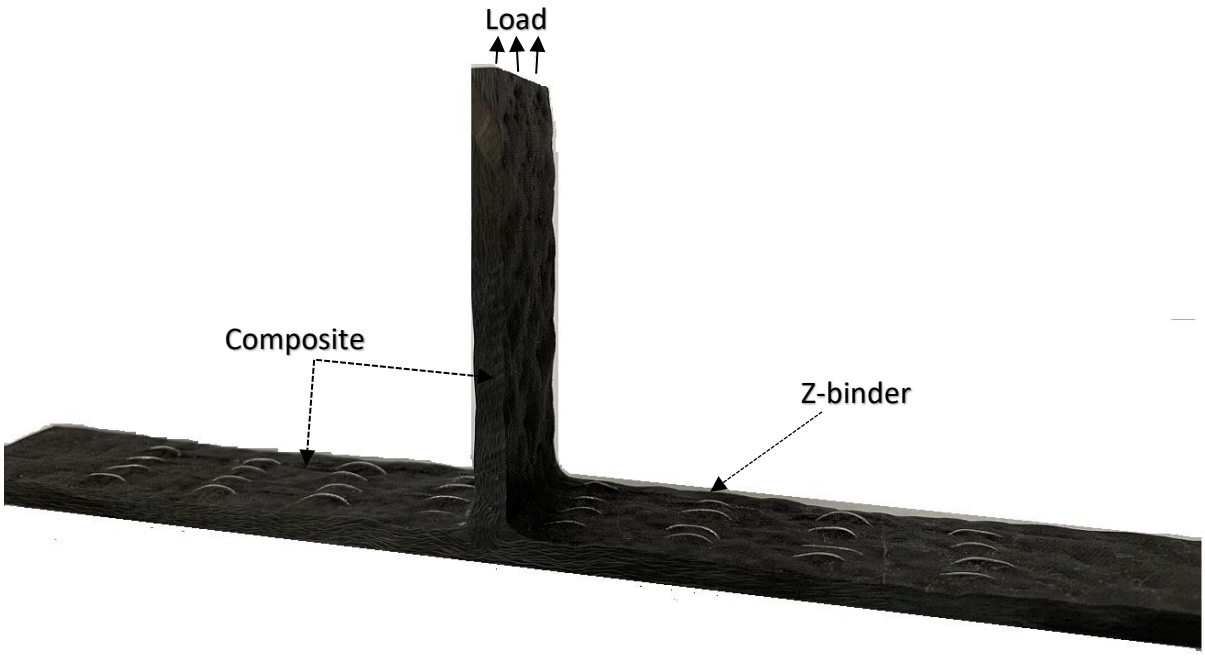

Fig. 8.4: *Photograph of cross-sectional views of a T-joint specimen containing woven z-binders.*

8.2.2 T-joint Structural Test

The structural properties of the T-joint specimens were determined by applying a pull-off (tensile) force to the stiffener (as indicated in Fig. 8.1). Before loading, the end of the stiffener was clamped to a 50 kN load capacity Instron machine while the two ends of skin/flange section were clamped to a rigid base plate, as shown in Fig. 8.5. The pull-off load was applied to the stiffener at the constant displacement rate of 1 mm/min until failure. A Nikon D3500 DSLR camera was used to capture side-view images of the T-joint specimens at the frame rate of 24 s^{-1} to track the initiation and progression of damage over the duration of each test. Loading of the specimen was stopped when either the damage between the skin and flange reached the clamped ends or the skin laminate ruptured. A minimum of four samples were tested for each type of T-joint specimen.

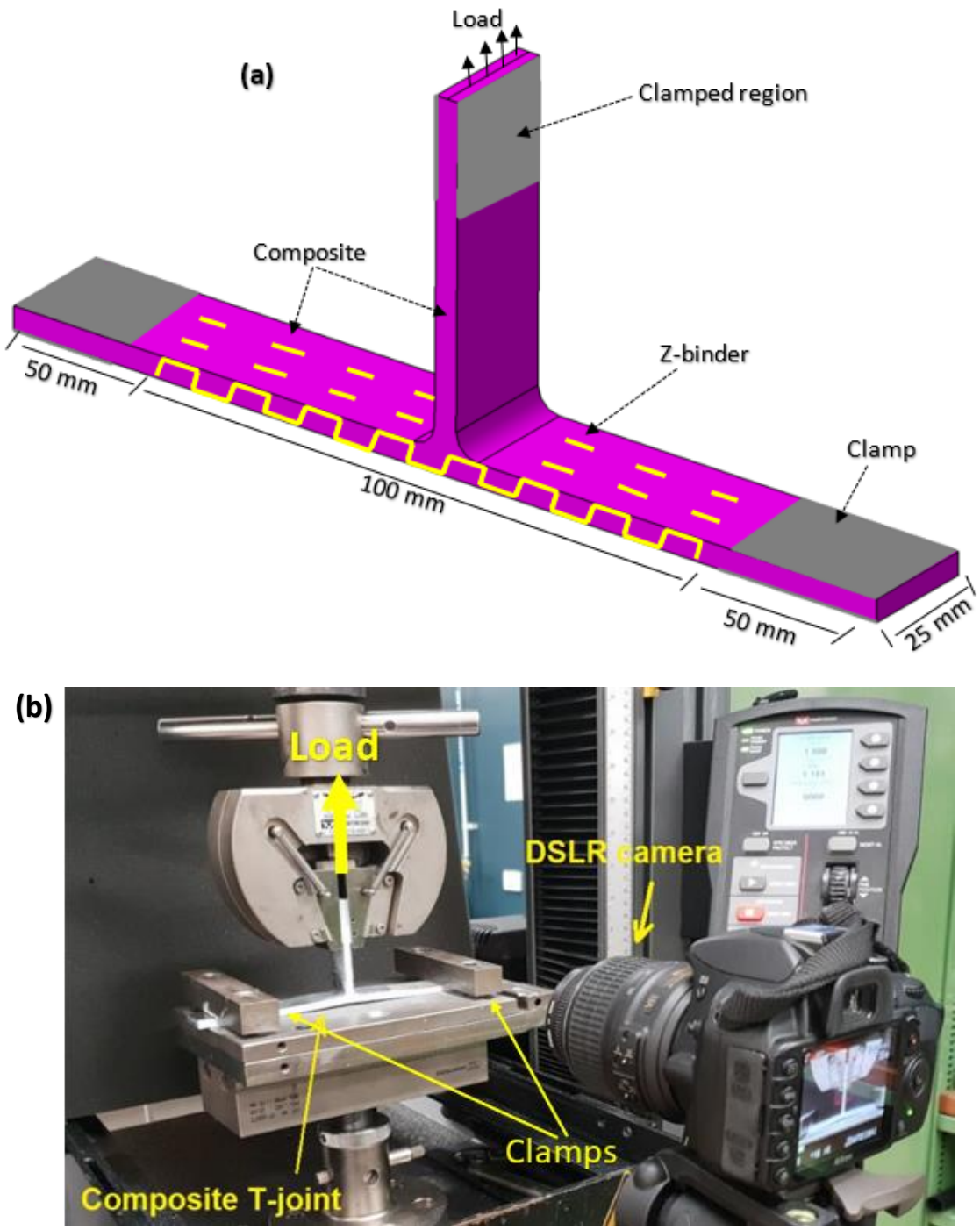

Fig. 8.5: *(a)Stiffener pull-off test sample, (b) Stiffener pull-off test setup .*

The stiffness, load-at-first failure, ultimate load and absorbed energy capacity values were used to determine the structural properties of the T-joints. The load-at-first failure was measured when the first crack appeared in the T-joint. Ultimate load was measured at the maximum load of the T-joint whereas the absorbed energy is defined by the area under the curve up to ultimate load, as shown in Fig. 8.6.

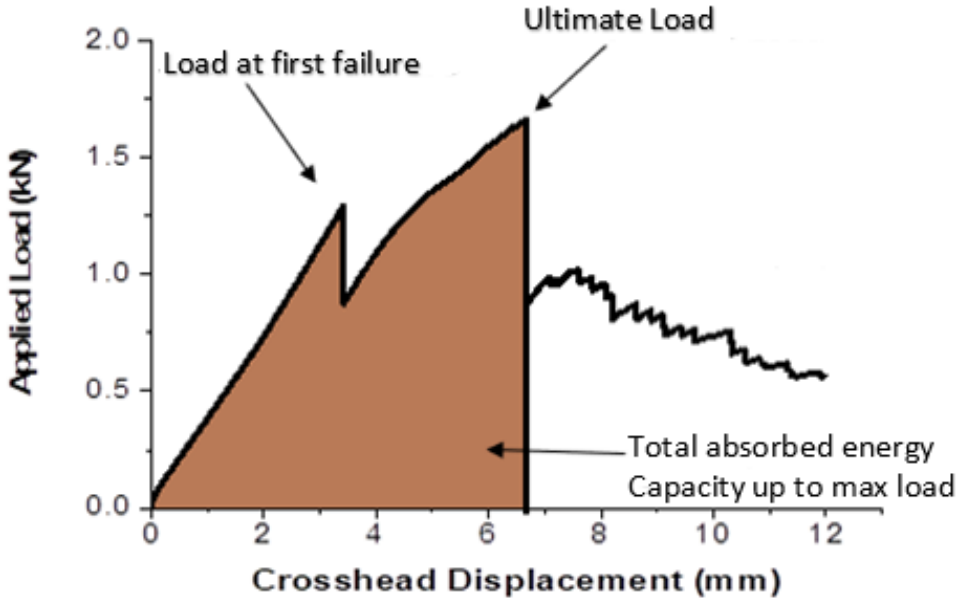

Fig. 8.6: *Schematic of parameters measured for T-joint structural properties.*

8.3 RESULTS AND DISCUSSION

Applied load-displacement curves are presented in Fig. 8.7 for the control T-joint and the joints containing woven z-binders. The curves for all the T-joint types show an initial linear increase up to ~1.3 kN, when a load drop occurs due to the onset of damage, which in all cases involves the initiation of cracks in the delta-fillet region (Fig. 8.8). Damage always initiates as short delamination cracks (typically under 5-6 mm long) in the delta-fillet due to the high geometric stress concentration in this region [186-188]. All the T-joints can continue to carry load beyond the onset of first failure until they reach their ultimate load, which is higher for the T-joints reinforced with z-binders compared to the control joint. Beyond peak load, the residual load-bearing strength of the T-joints containing z-binders is also higher than the control joint.

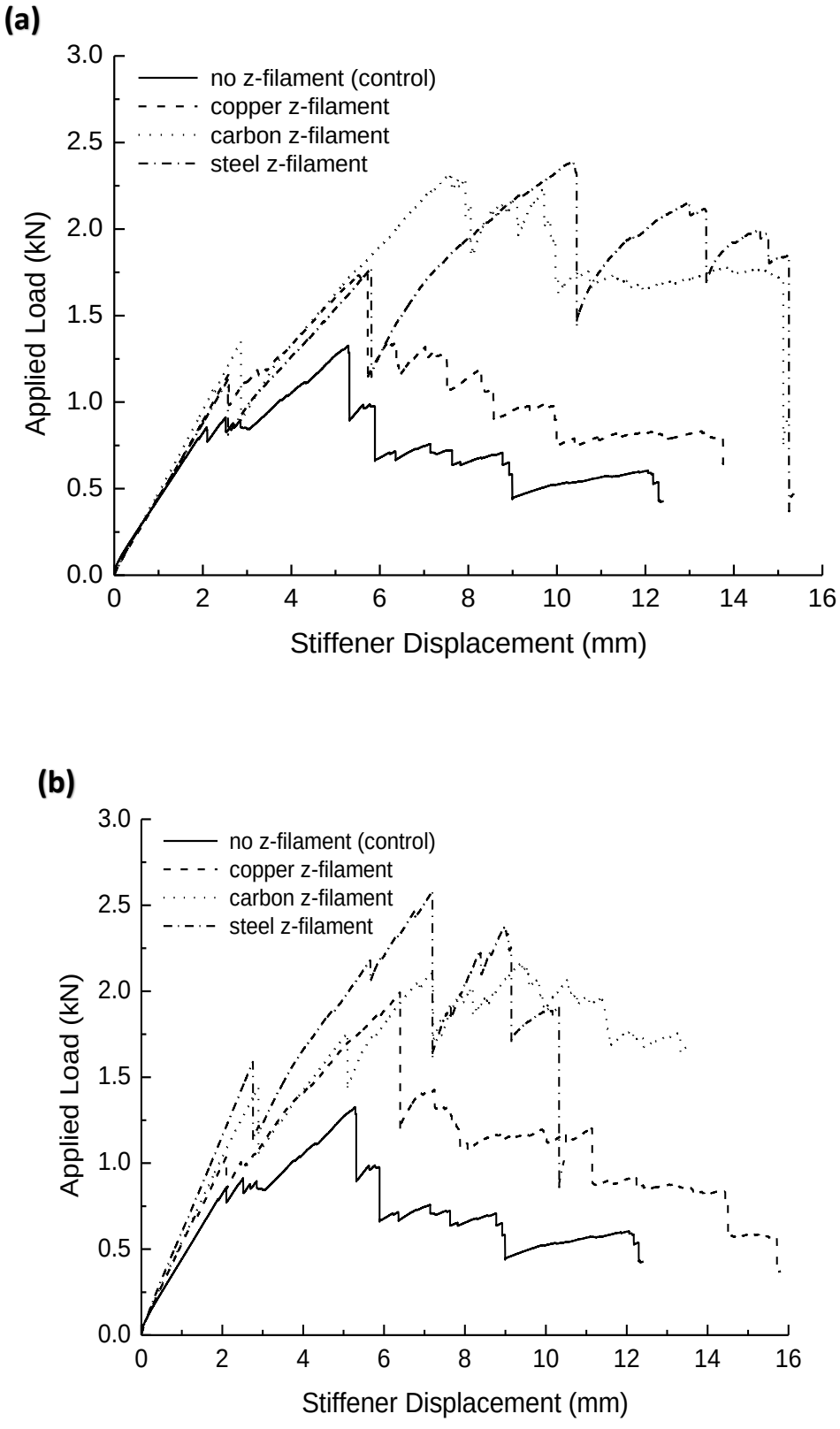

Fig. 8.7: *Applied load-displacement curves for the control T-joint and the T-joints containing woven z-binders at the (a) low and (b) high contents.*

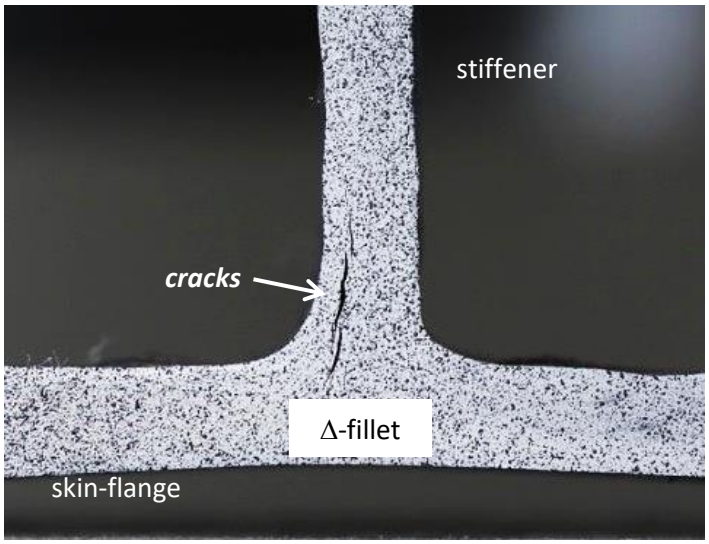

Fig. 8.8: *Cross-section photograph of the delta-fillet region to a T-joint showing damage caused at first failure.*

The elastic stiffness of the T-joint is increased by the woven z-binders, as shown in Fig. 8.9. The stiffness value defines the linear elastic region of the load-displacement curve before the first load drop. The stiffening effect due to the z-binders increases with their content in the T-joint. The increase in stiffness also depends on the z-binder material, with the lowest and largest improvements gained with the copper and steel, respectively. The increase in stiffness is attributed in part to the z-binders increasing the thickness of the skin/flange section of the T-joints (see Table 8.1), which experiences bending during testing, as shown in Fig. 8.10. The bending stiffness of the skin/flange section increases with its thickness, which in turn increases the measured stiffness of the T-joint. The skin/flange thickness increases with the z-binder content, resulting in the increased joint stiffness. The skin/flange thickness also increases in the order: copper, carbon and steel z-binders; which corresponds to the measured increases in joint stiffness.

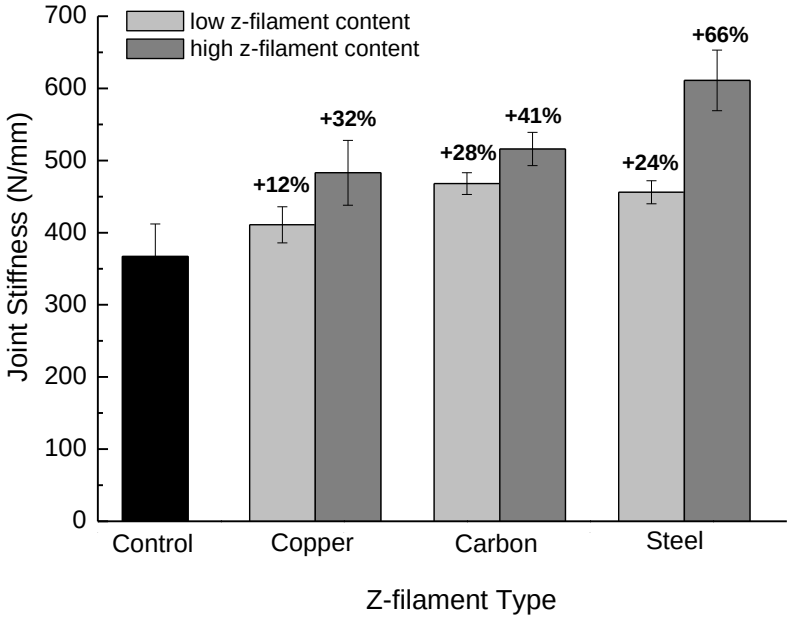

Fig. 8.9: *Stiffness of T-joints with and without woven z-binders. The percentage values give the increase for the T-joints with z-binders compared to the control joint.*

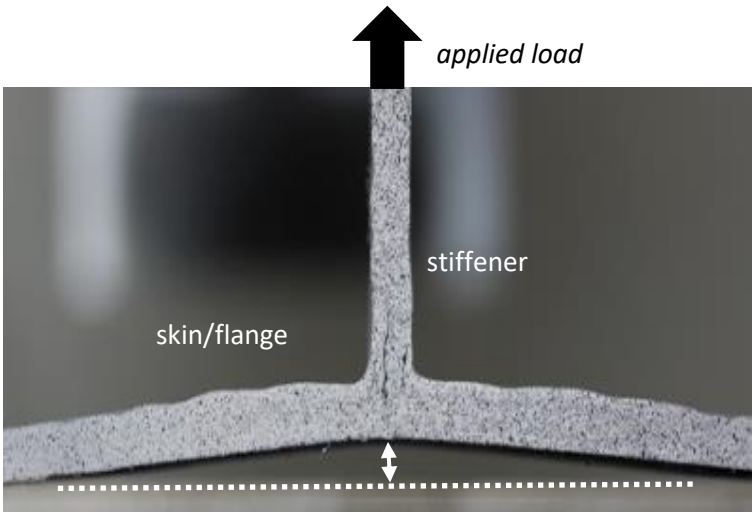

Fig. 8.10: *Deflection of skin/flange section of a T-joint specimen. The horizontal dashed line indicates the original position of the section before loading. The lower arrow indicates the magnitude of the bending deflection.*

The load-at-first failure of the T-joints, defined by the initial drop in the load-displacement curve, has not increased significantly by the woven z-binders. First failure involves the

initiation, growth and then arrest of short cracks in the delta-fillet region (Fig. 8.8). This cracking occurs due to the generation of interlaminar tensile (mode I) and interlaminar shear (mode II) stresses between the plies in the delta-fillet region [186-188]. Interlaminar fracture studies on 3D woven composites report that the strain energy release rate to initiate delamination cracking is not increased greatly by z-binders [46, 58, 64, 96, 217], which was also found in this study (*Chapter 3*). The modes I and II strain energy release rate values for crack initiation in the laminate materials used in the skin/flange regions of the T-joints are given in Table 8.2, and these are from the toughness tests reported in *Chapter 3*. The woven z-binders did increase the crack initiation energy release rate of the laminate material, although the increase was relatively small (under ~350 J/m^2). This is because woven z-binders do not induce substantial toughening until the crack is sufficiently long to establish a bridging zone typically involving 1-2 rows of z-binders, which equates to 10-20 mm in the T-joint specimens with low content of z-binders. Therefore, the initial cracking in the delta-fillet region is arrested before it reaches the length needed for the z-binders in the skin/flange sections to create a large-scale bridging zone, and consequently there is no significant improvement to the load-at-first failure. A similar effect has been reported for T-joints with other types of through-thickness reinforcement in the flange/skin section, such as tufted threads [189] and z-pins [191, 192]. Like the woven z-binders studied here, tufts and z-pins do not increase the load-at-first failure of T-joints subjected to stiffener pull-off loading, and this is also due to cracking initiating in the delta fillet (which does not contain z-direction reinforcement) and due to the cracking being too short to form a large-scale bridging zone in the skin/flange sections.

Table 8-2: *Modes I and II interlaminar fracture toughness for crack initiation and steady-state crack growth for the laminate materials used in the skin/flange sections of the T-joint specimens. Data from Chapter 3.*

Composite Material	**Mode I Interlaminar Toughness (J/m^2)**		**Mode II Interlaminar Toughness (J/m^2)**	
	Initiation (G_{Ii})	Steady-State (G_{Ic})	Initiation (G_{IIi})	Steady-State (G_{IIc})
No z-binders (control)	380	460	1300 ± 110	3276 ± 125
Copper z-binders				
Low content	559 ± 230	1656 ± 437	2766 ± 518	5721 ± 273
High content	738 ± 110	2058 ± 155	2634 ± 730	7518 ± 1096
Carbon z-binders				
Low content	559 ± 60	7716 ± 67	2545 ± 220	8190 ± 794
High content	461 ± 50	10735 ± 1104	1800 ± 250	12361 ± 862
Steel z-binders				
Low content	426 ± 150	11610 ± 2744	1824 ± 550	5878 ± 354
High content	615 ± 250	26500 ± 1963	3375 ± 360	7064 ± 1397

The z-binders increase the ultimate load and absorbed energy capacity of the T-joints, as shown in Fig. 8.11. The absorbed energy is calculated from the area under the load-displacement curve up to ultimate load, and is a measure of the work energy. Both the ultimate load and absorbed energy capacity increase with the z-binder content of the T-joint. These structural properties are also dependent on the z-binder material, and increase in the order: copper (lowest), carbon, steel (highest). The improvement to the T-joint properties is due to the z-binders increasing the interlaminar fracture resistance of the skin/flange sections. Photographs of the control T-joint (without z-binders) and the T-joints containing z-binders immediately following reaching maximum load are presented in Fig. 8.12. At the ultimate load, the control T-joint fails catastrophically by the rapid growth of cracks from the delta-fillet along the skin/flange interface and along the mid-plane of the stiffener (Fig. 8.12a). This fracture mode is common for T-joints made of non-toughened carbon-epoxy laminate subjected to stiffener pull-off loading [186-188]. The T-joint containing the copper z-binders fractures at the maximum load point in the same way as the control joint (Fig. 8.12b). However, during large-scale crack growth from the delta-fillet region along the skin/flange interface the copper z-binders form a bridging zone as shown schematically in Fig. 8.13 (which is based on experimental observation). Crack growth along the skin/flange sections occurs under mixed mode I/II interlaminar stress conditions, although the mode I (peeling)-type interlaminar stress is dominant [186, 187]. This cracking is resisted by the copper z-binders

forming a bridging zone as damage extends from the delta-fillet region to the clamped ends of the skin/flange. The copper z-binders generate bridging traction forces that resist crack growth along the skin/flange interface, and thereby increase the ultimate load and absorbed energy capacity. The steady-state fracture toughness values of the carbon-epoxy laminate materials used in the skin/flange sections to the different types of T-joint are given in Table 8.2. The interlaminar toughening effect of the copper z-binders increases with the volume content, and therefore the structural properties of the T-joints also increase. The bridging copper z-binders are plastically deformed and then break under increasing opening of the skin/flange interfacial crack, thereby allowing fracture to progress towards the clamped ends of the T-joint specimen.

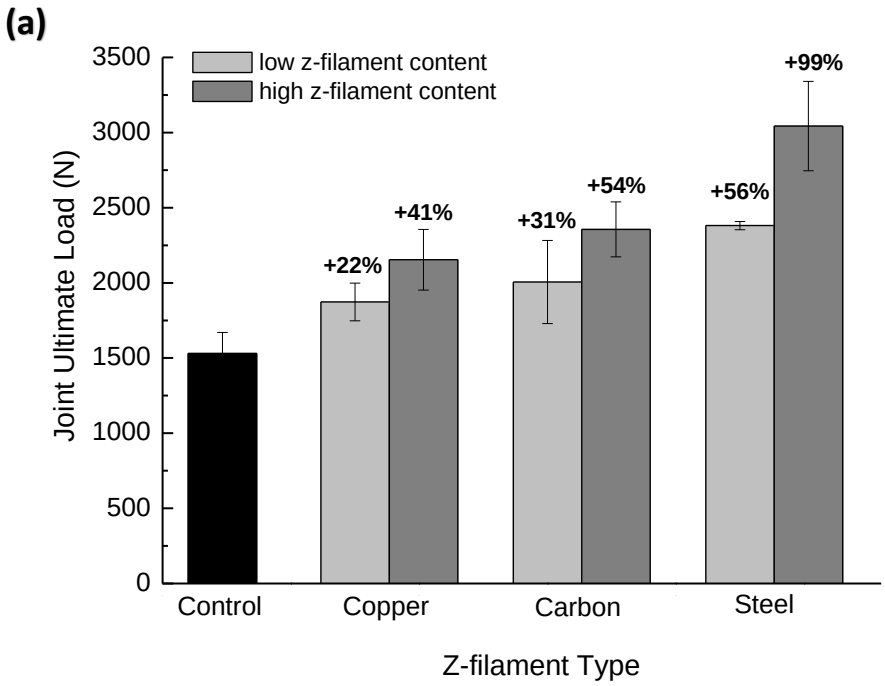

(b)

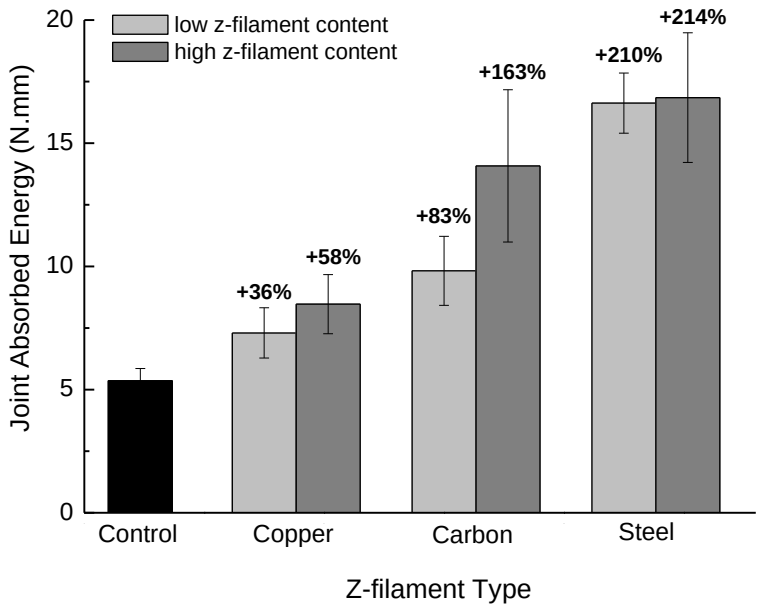

Fig. 8.11: *(a) Ultimate load and (b) absorbed energy capacity of T-joints with and without woven z-binders. The percentage values give the increase to the T-joints with z-binders compared to the control joint.*

The z-binders made of carbon fibre or steel are capable of suppressing crack growth into the skin/flange sections (Figs 8.12c & 8.12d). These z-binders stop the propagation of cracks from the delta-fillet region into the skin/flange sections, although cracking along the stiffener (which does not contain z-binders) does occur. The suppression of cracking in the skin/flange section, and the corresponding increases to the ultimate load limit and absorbed energy capacity, is due to the exceptionally high toughening effect of the carbon and steel z-binders, as shown in Table 8.2. The high toughening effect of these z-binders, which increased with their volume content, results in the large improvements to the ultimate load and absorbed energy capacity of the T-joint. The observation that the z-binders made of carbon and steel suppressed cracking in the skin/flange section, and instead failure occurs by rupture of the skin laminate immediately below the delta-fillet region, is further evidence of their high toughening effect in T-joints. That is, these z-binders increase the fracture resistance of the skin/flange sections to such a high level that it exceeds the rupture stress of the laminate material used for the skin.

While the carbon z-binder promotes high resistance to crack growth along the skin-flange section and thereby increases the ultimate load and absorbed energy capacity, even greater improvements to these properties are achieved using the steel z-binder due to its higher interlaminar toughening effect. This reveals that z-binders made of high strength and toughness metals such as steel can be more effective than fibrous filaments at increasing the structural properties of T-joints. However, z-binders made of relatively low strength metals such as copper result in lesser improvements to the T-joint properties.

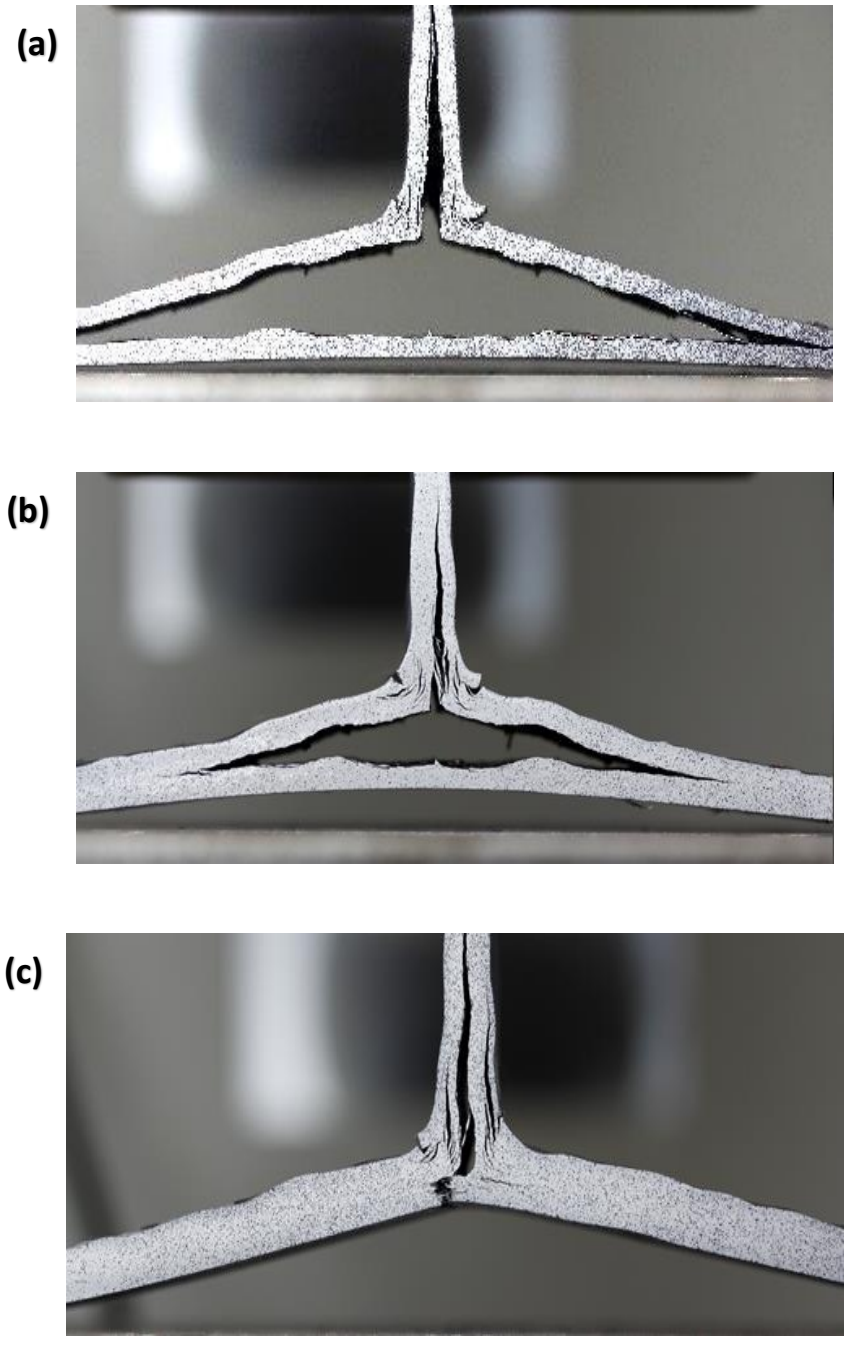

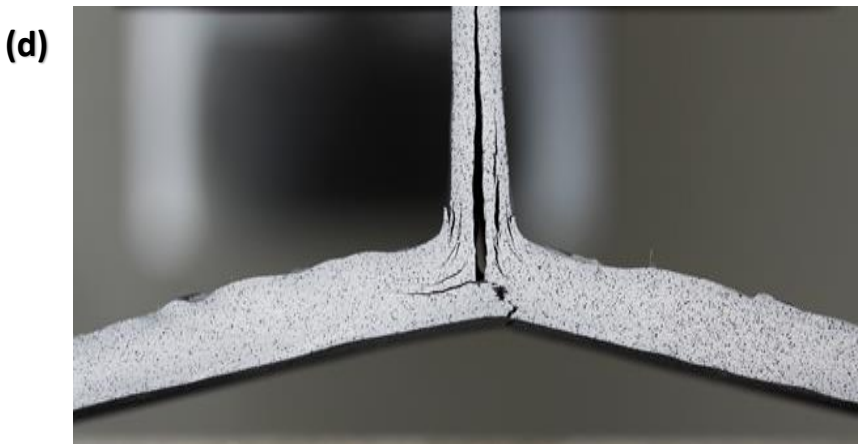

Fig. 8.12: *Photographs of T-joint specimens immediately following fracture at the ultimate load. (a) Control T-joint. T-joints with z-binders of (b) copper, (c) carbon fibre and (d) steel. The joints in (b-d) are reinforced at the high z-binder content.*

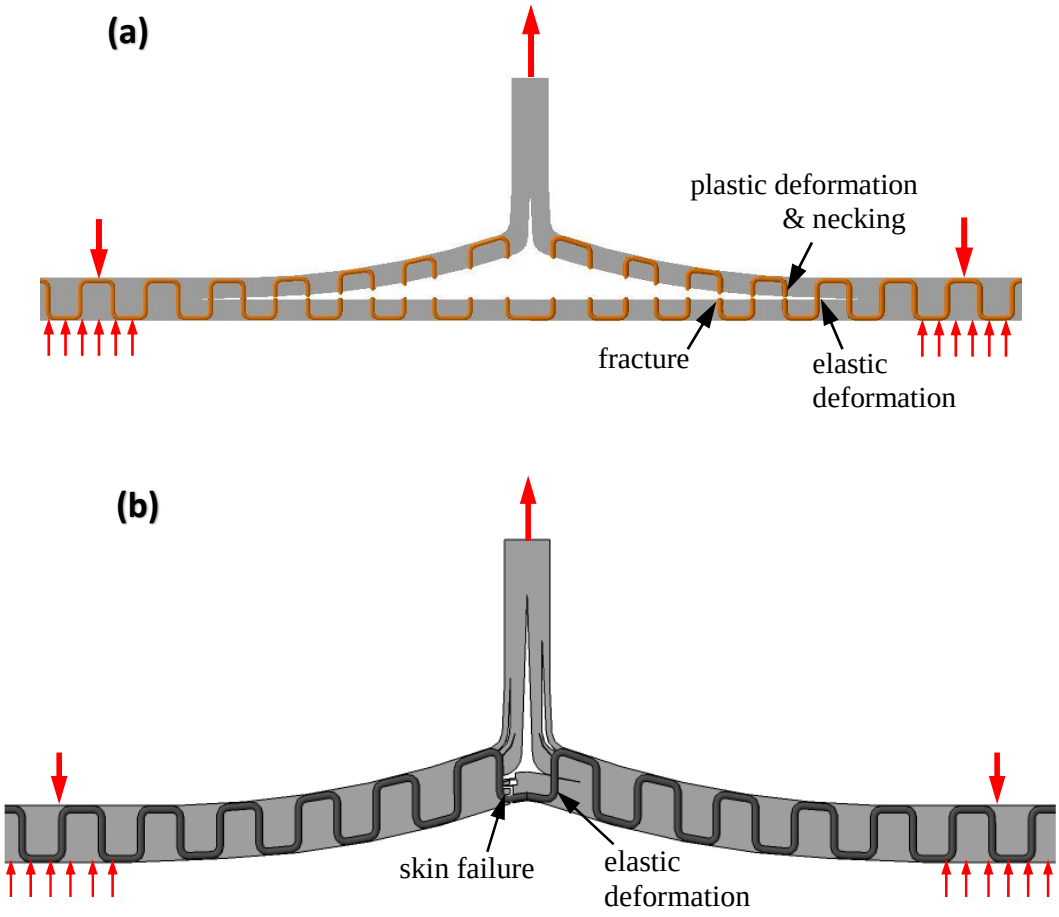

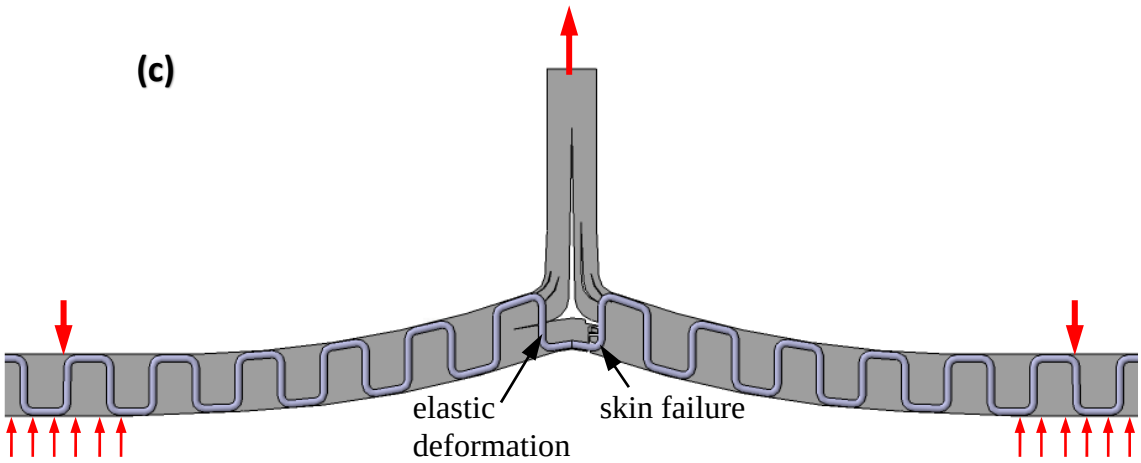

Fig. 8.13: *Schematic of (a) copper, (b) carbon and (c) steel z-binders bridging the crack along the skin-flange section of a T-joint.*

There is a strong correlation between the improvement of the mode I interlaminar fracture toughness of the laminate material used in the skin/flange section by the z-binders and the increase to the ultimate load and absorbed energy capacity of the T-joint. Plots of the normalised mode I toughness of the laminate against the normalised ultimate load and normalised absorbed energy capacity are presented in Fig. 8.14. The toughness value is the mode I steady-state fracture toughness value of the laminate containing z-binders normalised to the toughness value of the control laminate. Similarly, the normalised load and normalised energy are these values for the T-joint with z-binders normalised to the value for the control joint. Strong correlations exist between the mode I fracture toughness and the properties of the T-joint. However, large improvements to the mode I toughness using z-binders must occur to achieve smaller increases to the ultimate load and absorbed energy of the T-joint. For example, the data trend in Fig. 8.14 indicates that the mode I toughness must be increased ~60-fold to double the ultimate load of the joint. Similarly, the toughness must be raised ~20-fold to double the absorbed energy capacity. Such large increases required to the fracture toughness of the laminate material used in the T-joint demonstrate the challenge of strengthening of T-joints. Cracking in the web of the skin in the T-joints increases with the mode I interlaminar fracture toughness of the T-joints.

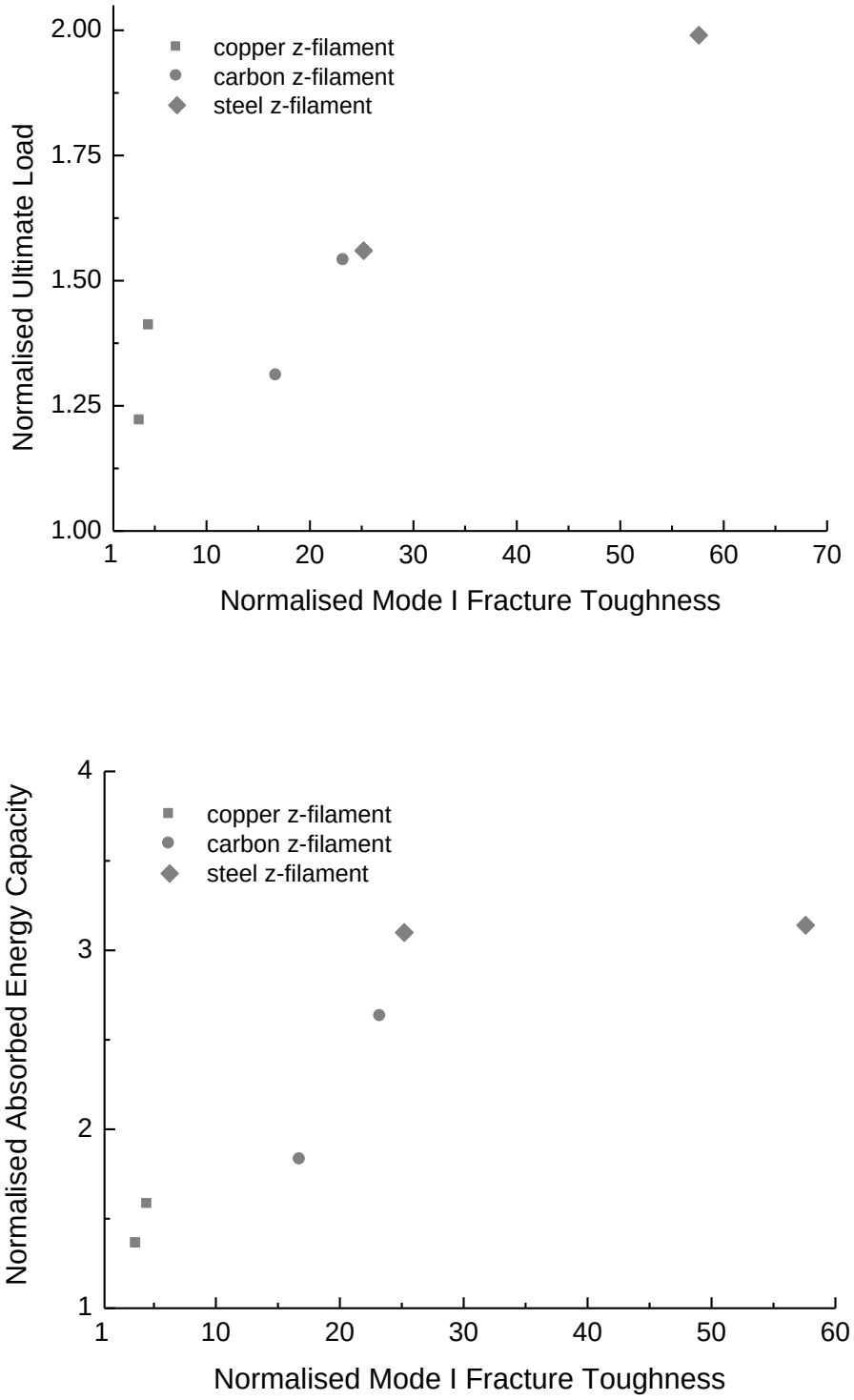

Fig. 8.14: *Plots of normalised mode I fracture toughness against (a) normalised ultimate load and (b) normalised absorbed energy capacity of the T-joints.*

The capacity of the metal z-binders to increase the ultimate load limit of the T-joints is compared in Table 8.3 against published load data for T-joints reinforced with different types of fibrous z-binders (as well as the carbon fibres used in this study). Included in the table is also ultimate load data for T-joints toughened using other methods, including nanoparticles [183], woven inserts [185], ply optimisation [187] and the through-thickness reinforcement techniques of 3D weaving [211], tufting [189], stitching [197, 201, 202], z-pinning [189, 191, 194, 197] or rods [190]. All the ultimate load data in Table 8.3 is for carbon-epoxy T-joints subjected to the stiffener pull-off load condition, and is defined by the percentage change compared to the control joint in the same study. However, differences exist between studies in the type and ply stacking pattern of carbon-epoxy material used in the T-joint specimens. Differences also exist between studies in the geometry and boundary conditions of the T-joint specimens. While the data in Table 8.3 should be used with care as an absolute, quantitative comparative assessment of the different methods for strengthening T-joints, it reveals that the woven steel z-binders are highly effective (on a percentage basis) at increasing the ultimate load. At the highest volume content of steel z-binders used (1.0%), the ultimate load of the T-joint nearly doubled. Only one other T-joint, made using a fully integrated 3D woven fabric, achieved a higher percentage increase to the ultimate load [211]. Even the copper z-binder, which is less effective than the steel, increases the ultimate load of the T-joint to values similar to or (more often) higher than other joint toughening methods.

Table 8-3: *Comparison of percentage increase to the ultimate load of T-joints subjected to stiffener pull-off loading.*

Joint Strengthening Method	Strengthening Conditions	Increase in Ultimate Load Limit	Reference
3D weaving	Steel z-binders (0.6 vol %) Steel z-binders (1.0 vol %)	56 % 99 %	This study
3D weaving	Copper z-binders (0.6 vol %) Copper z-binders (1.0 vol %)	22 % 41 %	This study
3D weaving	Carbon fibre z-binders (0.6 vol %) Carbon fibre z-binders (1.0 vol %)	31 % 54 %	This study
Nanoparticles	Carbon nanotubes (1 wt %) Carbon nanofibres (1 wt %) Graphene nanoplatelets (1 wt %)	17 % 45 % 2.1 %	[183]
Ply Optimisation	Design 1 Design 2 Design 3	18 % 0.6 % 23 %	[187]
Woven interleaves	Series 2 Series 3 Series 4 Series 5	-5.1 % 19 % 29 % 3.4 %	[185]
Stitching	Carbon fibre stitches (0.5 vol %) Carbon fibre stitches (2 vol %)	47 % 41 %	[197]
Tufting	S-glass tufts	65 %	[189]
Z-pinning	Carbon fibre z-pins (0.5 vol %)	12 %	[189]
Z-pinning	Carbon fibre z-pins (0.5 vol %) Carbon fibre z-pins (2 vol %) Carbon fibre z-pins (4 vol %)	35 % 68 % 76 %	[191]
Z-pinning	Carbon fibre z-pins (0.28 mm diameter) Carbon fibre z-pins (0.5 mm diameter) Carbon fibre z-pins (0.7 mm diameter)	48 % 33 % 11 %	[194]
Z-Pinning	Carbon fibre z-pins (0.5 vol %) Carbon fibre z-pins (2 vol %)	1.7 % 35 %	[197]
Rods	Short carbon fibre rods (15 mm) Long carbon fibre rods (45 mm)	83 % 73 %	[190]
3D weaving	Carbon fibre z-binders (Type 1) Carbon fibre z-binders (Type 2)	44 % 206 %	[211]

Using metal z-binder comes at a weight penalty due to their density being higher than the carbon-epoxy laminate material used in the T-joint. The increase in the bulk density of the different T-joint specimens as a function of the z-binder volume content is given in Fig. 8.15. At the highest volume content of steel and copper z-binders used (1.0%), the percentage increases in the bulk density of the T-joints were 4.0% and 4.7%, respectively. For the T-joints

containing steel z-binder, a two-fold increase in the ultimate load to failure is achieved with a modest increase in the bulk density of 4.0%.

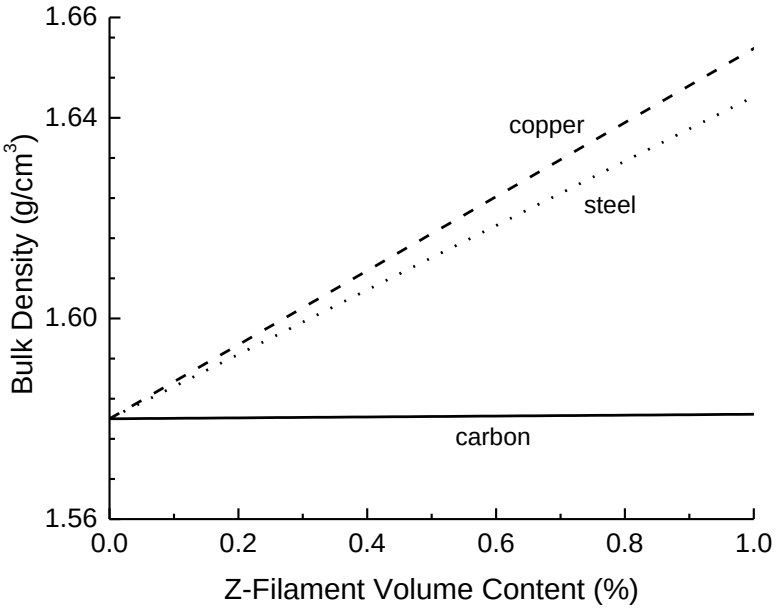

Fig. 8.15: *Effects of the volume fraction and type of z-binder on the bulk density of the T-joints.*

In addition to improving the structural properties of T-joints, using metal z-binders offers the opportunity to improve other properties which is not easily achieved using fibrous z-binders made of carbon or glass. As mentioned, Sharp et al. [94] reports that metal z-binders increase the thermal conductivity of 3D woven composites more than fibrous filaments. For example, Sharp and colleagues measured 12-fold increase to the thermal conductivity of 3D woven composite containing copper z-binders. Therefore, metal z-binders can potentially be used to tailor the thermal properties of T-joints for high temperature applications. Metal z-binders can also increase the electrical conductivity of the laminate material used in T-joints. For example, results presented in Chapter 5 showed large increases to the through-thickness electrical conductivity (up to about three orders of magnitude) and in-plane electrical conductivities of the carbon-epoxy laminate (up to one order of magnitude) using copper z-binders. Steel z-binders also increase significantly the through-thickness and in-plane electrical conductivities of the laminate. Metal z-binders offer the opportunity to controllably increase the electrical conductivity of T-joints (and other joint geometries) via the judicious selection of the material type and volume content. Through-thickness reinforcement using

thin metal pins can be used for the structural health monitoring of composite materials. Recent studies have shown that metals such as copper and steel can be used to monitor the growth of delamination cracks in z-pinned laminates via changes to the electrical conductivity [158, 159, 218]. In Chapter 6 it is proved that the z-binders can detect damage in laminates so, it is feasible that woven metal z-binders can be used for the structural health monitoring of T-joints due to changes to the electrical conductivity caused by cracking and other types of damage. The potential use of metal z-binders for controlling the electrical, thermal, damage sensing and other properties of T-joints is a topic worthy of on-going investigation.

8.4 CONCLUSIONS

Thin metal filaments woven in an orthogonal (through-thickness) pattern into T-shaped carbon-epoxy laminated joints can improve greatly the structural properties. The metal filaments, which are not damaged during the weaving process (unlike fibrous yarns), can be woven into dry fabric preforms to joints prior to resin infusion. Provided the metal filament is thin enough to be flexible (which in this study was 0.51 mm diameter) then it can be woven via localised plastic deformation where it bends between the in-plane to through-thickness directions.

The metal z-binders did not increase significantly the load-at-first failure of the T-joint when subjected to the stiffener pull-off load condition. First damage involves cracking within the delta-fillet section of the T-joint, and this section is not reinforced with z-binders. However, the metal z-binders increase both the ultimate load and absorbed energy capacity via interlaminar toughening of the skin/flange section. When strained beyond ultimate load, the residual load-bearing capacity of the T-joints is also improved using metal z-binders. The improvement to these structural properties increases with the z-binder content due to the higher toughening effect. The property improvements also depend on the z-binder material. Copper wire is less effective than carbon fibre yarn at increasing the joint properties due to its weaker crack bridging traction properties and consequently lower improvements to the interlaminar fracture toughness properties of the laminate material used in the skin/flange sections of the T-joint. Steel promotes a stronger strengthening effect than carbon yarns in the T-joint. The steel z-binder increases the interlaminar fracture toughness and crack

bridging traction properties more than the carbon z-binder, and this results in larger improvements to the ultimate load and energy absorption capacity. Based on comparative analysis of published data, the steel z-binder appears to increase the percentage ultimate load of a T-joint more than other techniques such as nanoparticles, interleaving, stitching, tufting and z-pinning.

Chapter 9: In-plane mechanical properties of 3D woven composites

Abstract

This chapter presents an experimental study into the in-plane tensile, compressive and flexural properties of 3D woven composites reinforced with z-binders made of steel, copper or carbon fibre. The experimental results show that the elastic modulus and failure stress properties of 3D woven composites are reduced by z-binders. The tensile and flexural properties are not significantly affected with increasing z-binder volume content. However, compression properties are decreased with increasing z-binder volume content. The mechanisms responsible for the softening and weakening of the 3D woven composites are identified using acoustic emission monitoring, scanning electron microscopy (SEM) and fractography. The reduction to the compression properties is due to several microstructural defects present in the 3D woven composites, most notably fibre misalignment and reduction to the volume content of load-bearing fibres.

9.1 INTRODUCTION

3D woven composites have combine high mechanical properties and enhanced delamination toughness with impact resistance [9, 24, 64, 219-221], as described in detail in the literature review chapter. However, the z-binder yarns can reduce the in-plane mechanical properties. A large amount of property data has been published on the elastic modulus and strength of 3D woven composites for in-plane tension, compression, flexural and interlaminar shear loads [222-225]. The mechanical properties of 3D composites reinforced with high-strength stitches or rods are reduced due mostly to ply crimping and fibre waviness [43, 226, 227]. Lee et al. [34], Mouritz et al. [228] and Reedy et al. [229] found that the Young's modulus of 3D woven composites is between about ~10% and 35% lower than the equivalent 2D laminate (without z-binders). The lower modulus is due to localised fibre waviness of the load-bearing yarns caused by the z-binder. Based on a review of published property data, Tong et al. [24] concluded that the magnitude of the reduction to the Young's modulus of 3D woven composites is not strongly influenced by the volume content and weave architecture of the z-binders. Tan et al. [165] investigated the tensile

properties of weft yarns and z-direction yarns in orthogonal carbon composite. They observed that the average Young's modulus and tensile strength of z-direction yarn was lower than the weft direction yarn. This reduction was due to the z-binder/matrix interfacial debonding, and the z-binder breakage with slight fibre pull-out.

Based on a comprehensive review of published data, Mouritz and Cox. [228] concluded that the in-plane mechanical properties (stiffness and failure stress) of 3D woven composites can be reduced by the z-binders, but the reduction is usually under 20% when compared with a 2D laminate. They attribute the reductions to microstructural and geometric defects caused by the through-thickness weaving process, such as clusters of broken and damaged fibres, fibre crimp and fibre/ply waviness. Tong et al. [24] and Reedy et al. [229] report that the flexural properties are reduced ~20%-30% due to the crimping and misalignment of in-plane fibres by the z-binders.

All published studies into the mechanical properties have been performed on 3D woven composites containing z-binders made of fibrous yarns (mostly carbon or glass). No studies have yet been published on the properties of 3D woven composites with metal z-binders, and whether the changes are similar or different to fibrous z-binders.

This chapter presents an experimental investigation into the effect of the material type and volume content of z-binders on the tensile, compressive and flexural properties of 3D woven composites. The composites contained steel, copper or carbon z-binders which are the same materials studied in the previous research chapters. The mechanisms responsible for any changes to the mechanical properties of the 3D woven composites are investigated using acoustic emission monitoring and scanning electron microscopy (SEM).

9.2 MATERIALS AND EXPERIMENTAL METHODOLOGY

9.2.1 Composite materials

The in-plane mechanical properties of four types of carbon fibre reinforced composites were studied: (i) 2D control laminate (i.e. without any z-binder), (ii) 3D woven composite containing copper z-binder, (iii) 3D woven composite having stainless steel z-binder and (iv) 3D woven composite reinforced with carbon z-binder. The composite specimens are the same as those materials studied in the previous research chapters. The 2D and 3D woven composites contained 20 plies of the carbon fabric stacked in a cross-ply [0/90]

pattern. The 3D fabrics were manually woven in the same way as described in the previous chapters using copper wire, stainless steel wire or carbon fibre tow. The 3D woven composites were reinforced with z-binders at volume contents mentioned in previous chapters.

The 2D and 3D woven fabric preforms were infused with epoxy resin using the vacuum bagging resin infusion technique. The epoxy resin was infused at room temperature using the VBRI process shown in Fig. 3.2 *(Chapter 3).* The epoxy, curing time and temperature were the same as used in the previous studies in this thesis. All the specimens were ~5 mm thick. The volume contents of in-plane fibres and z-binder for the different materials are given in Table 9.1.

Table 9-1: *Volume fractions of in-plane fibres and z-binder in the 2D laminate and 3D woven composites.*

Z-binder	In-Plane Fibre Volume Fraction	Z-binder Volume Content
None	0.39	-
Steel	0.35	Low
	0.33	High
Copper	0.36	Low
	0.35	High
Carbon	0.38	Low
	0.34	High

9.2.2 Tensile testing

The tensile properties of the 2D laminate and 3D woven composites were measured using dog bone-shaped specimens. The gauge section of the specimens was 80 mm long x 25 mm wide, as shown in Fig. 9.1, and loading was applied in the warp direction which is also the alignment direction of the z-binder rows. The tensile tests were performed at a displacement rate of 1.0 mm/min according to ASTM D3039 [230] specifications using a 100 kN MTS machine. E-glass fibre-epoxy composite tabs were bonded to the specimen ends to prevent crushing within the vice grips of the machine. The longitudinal strain was measured using a 25 mm extensometer attached to the gauge section of the tensile specimen. According to the standard, the Young's modulus was determined over the strain range of 0.01% to 0.03%. A minimum of four samples were tensile tested for each type of composite material.

Acoustic emission (AE) monitoring was performed during the tensile tests. The AE hits were recorded using an AE sensor, which was a single wide-band piezoelectric transducer (WD sensor) mounted on the tensile specimen. The sensor, which was used to monitor the initiation and accumulation of damage under increasing tensile strain to failure, was connected to a 2/4/6 Preamplifier and PCI-2 AE system (Pacific Acoustics Corporation), and the signal was analysed using AEwin software. The AE parameters are shown in Fig. 9.2 and 9.3 respectively.

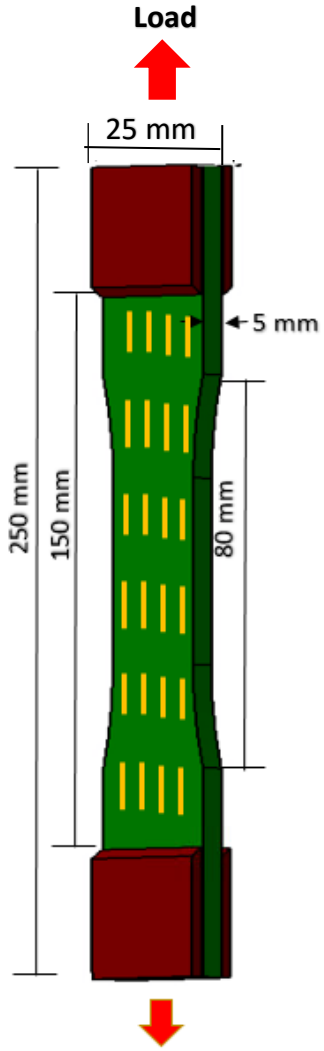

Fig. 9.1: *Schematic of tensile test specimen. The rows of z-binders were aligned parallel with the tensile load direction, which is indicated by the arrows.*

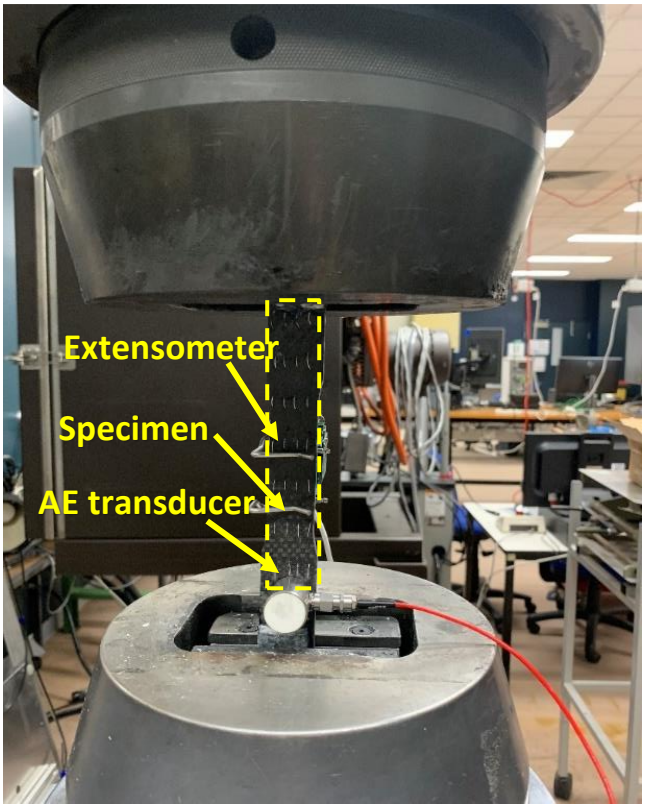

Fig. 9.2: *Tensile test with AE transducer.*

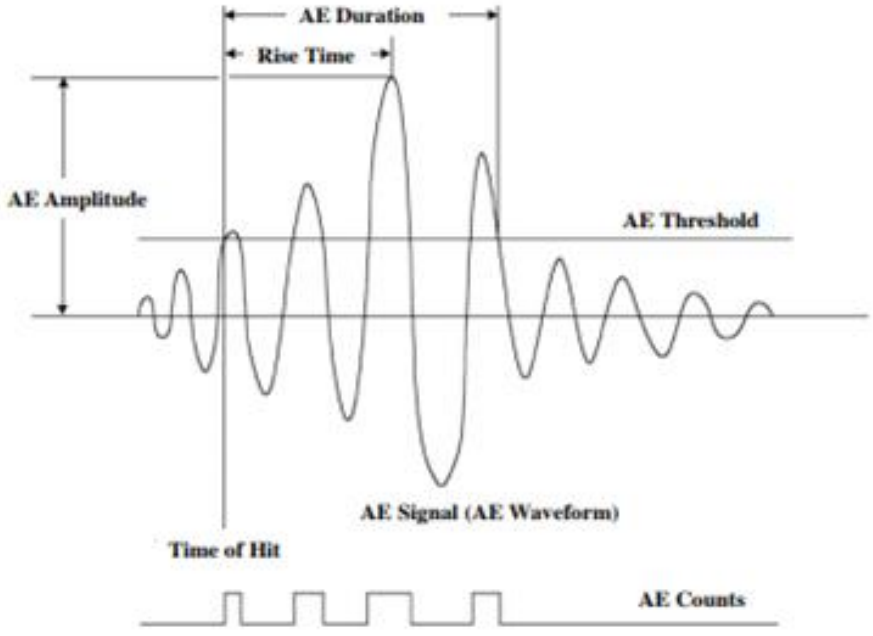

Fig. 9.3: *A schematic display depicting the AE parameters in a single AE hit.*

9.2.3 Compression testing

The compressive properties of the composites were measured according to ASTM D7137 specifications. The specimens were 100 mm wide x 150 mm long, and were loaded (like the tensile samples) along the warp direction. The samples were axially compressed at an end-shortening rate of 0.5 mm/min until failure. The ends of the sample were clamped whereas the sides were laterally supported using anti-buckling guides, as shown in Fig. 9.4. Three samples of each type of composite material were compression tested. The DIC setup was used for measuring the surface strains during testing, and further details on the DIC technique are given in Chapter 7.

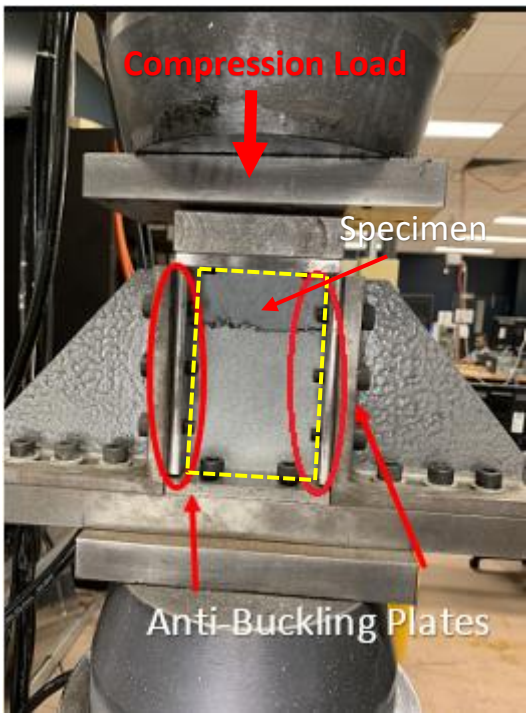

Fig. 9.4: *Compression test fixture with anti-buckling guides.*

9.2.4 Flexural testing

The flexural properties of the composites were measured using the four-point bend test method following ASTM D7264 [231], with a support span-to-thickness ratio of 32:1. The samples were tested at the centre-point deflection rate of 1 mm/min using a 50 kN Instron testing machine, as shown in Fig. 9.5. A linear variable differential transducer (LVDT) was used to measure the displacement during the flexural test, and from this the flexural modulus was determined. The specimen dimensions and loading configuration are shown in Fig. 9.6. Four

samples of each type of composite material were tested. In this study steel z-binder specimens were not tested.

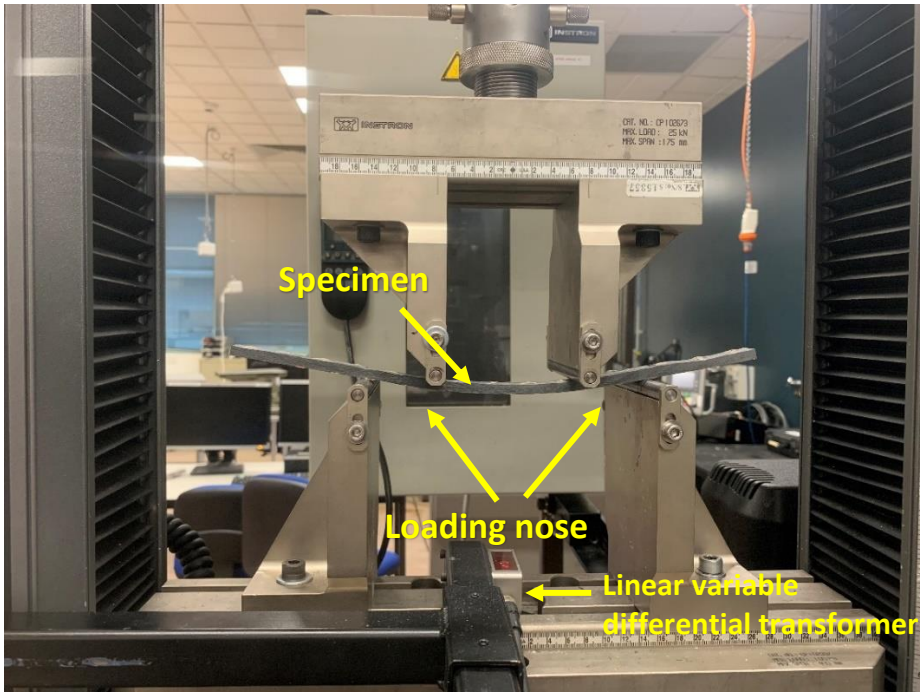

Fig. 9.5: *Flexural test setup.*

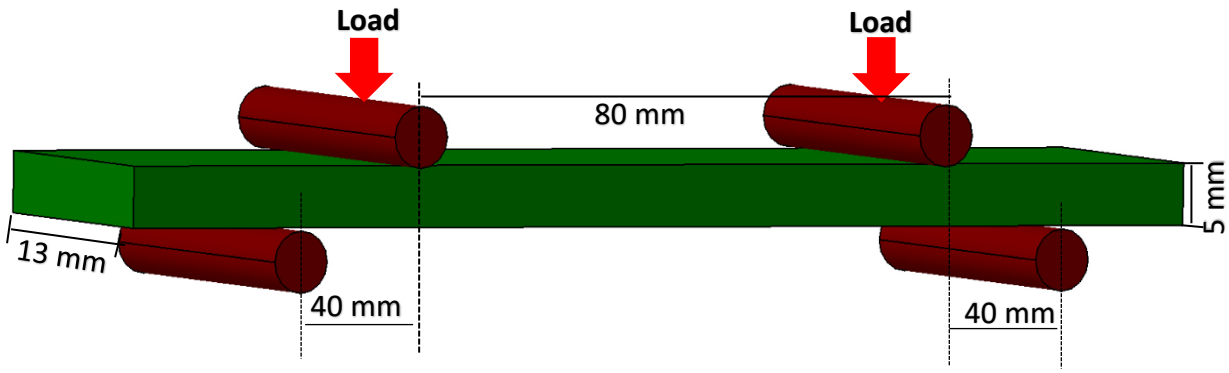

Fig. 9.6: *Schematic of flexural test.*

9.3 RESULTS AND DISCUSSION

9.3.1 Tensile properties of 2D and 3D composites

Examples of the stress-strain curves for the 2D laminate and a 3D woven composite (with the steel z-binder) when subjected to multiple tensile tests are shown in Figs. 9.7 and 9.8. The curves show some scatter in the results, with the variability typically under ~10%. Therefore, any difference in properties between the materials over ~10% can be considered statistically significant. Stress-strain curves for the 2D laminate and different types of 3D woven composites at the low and high z-binder contents are presented in Figs. 9.9 and 9.10, respectively. The curves for the 3D composites are nearly linear elastic to failure, and do not show any significant non-linear deformation behaviour. This is different to the tensile stress-strain response measured by Cox et al. [36] and Callus et al. [37], who both reported a 'kink' in the curve due to plastic straightening of the load-bearing tows which had been crimped by the z-binders. The weave architectures and processes were different to those used in this study, which may account for the absence of tow straightening in the 3D woven composites studied here. The curves in Fig 9.9 and 9.10 also show that the tensile failure stress of the different types of 3D woven composites were similar (i.e. within the bounds of experimental scatter), and the average failure stress values were lower than the 2D laminate. The reductions to the failure stress were similar for both the low and high volume content of z-binder used in the 3D woven composites. The z-binders did not alter significantly the Young's modulus of the composite material.

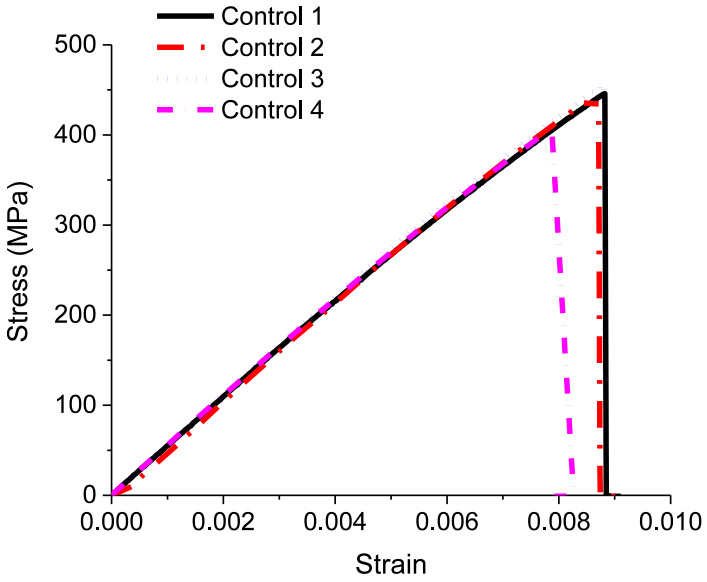

Fig. 9.7: *Multiple tensile stress-strain curves measured for the 2D laminate.*

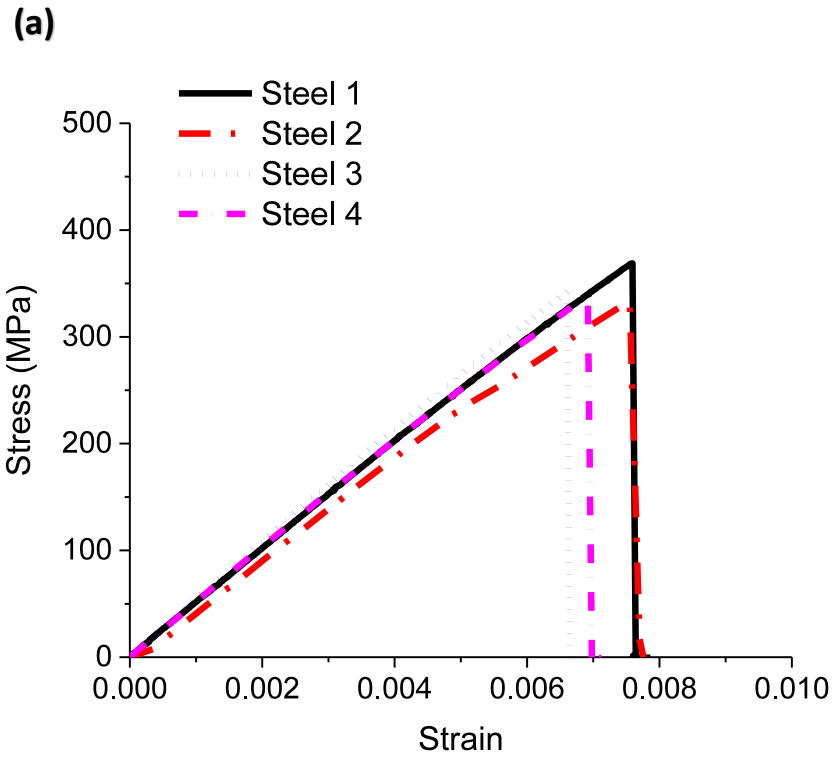

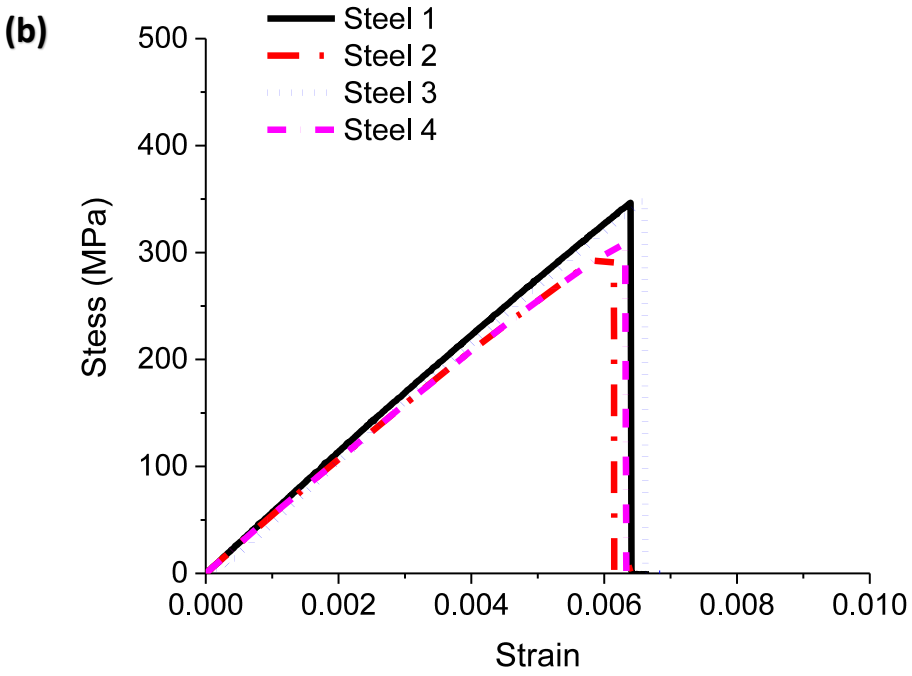

Fig. 9.8: *Multiple tensile stress-strain curves for the 3D composite reinforced with steel z-binder: (a) low and (b) high contents.*

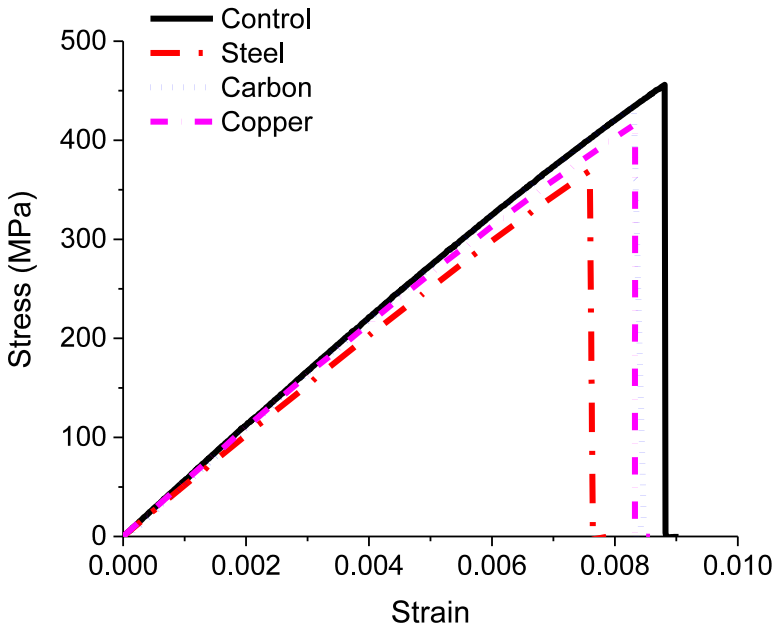

Fig. 9.9: *Tensile stress-strain curves for the 2D laminate and the 3D woven composites with the low volume content of z-binders.*

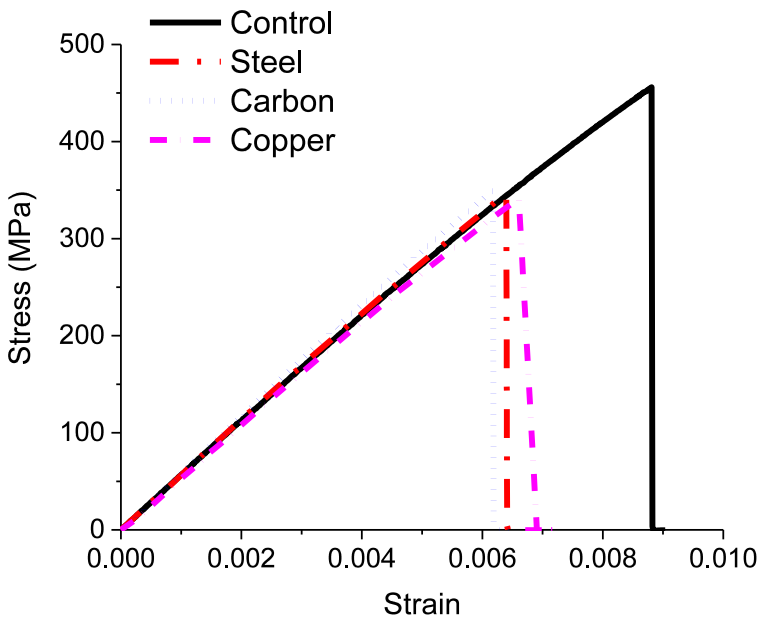

Fig. 9.10: *Tensile stress-strain curves for the 2D laminate and the 3D woven composites with the high volume content of z-binders.*

The effects of the material type and volume content of the z-binder on the tensile strength and modulus are shown in Figs. 9.11 and 9.12**.** The results show that all the z-binders reduce the tensile strength, but do not cause a significant change to the modulus. Similar reductions to the tensile properties of 3D woven composites have been reported elsewhere [31, 36, 165, 228, 232]. The strength of all three types of 3D woven composite was lower than the 2D laminate, although the magnitude of the reduction was not affected significantly by either the z-binder type or z-binder content. The reductions to the strength can be attributed to several factors, which are the reduced fibre volume content (Table 1) and fibre/ply waviness caused by the z-binders. Callus et al. [37] and Cox et al. [36] found that the z-binder architecture has no significant effect on tensile modulus, however the tensile failure stress is controlled by the amount of crimp in the warp (load-bearing) yarns. Stig et al. [223] observed that the tensile strength is significantly lower in 3D composites compared with 2D laminate. The crimp in the 3D composites cause premature failure since the load acted to straighten the fibre yarns to such an extent that the matrix failed. Fig. 9.11 and 9.12 show no significant reduction in the tensile strength and modulus with increasing z-binder volume content. Mouritz and Cox [228] assessed the effect of z-binder content on the tensile strength and

found little or no dependency on the areal density of z-binders, and observed that the reduction is almost always within the 20% of the 2D laminate, and often within 10%.

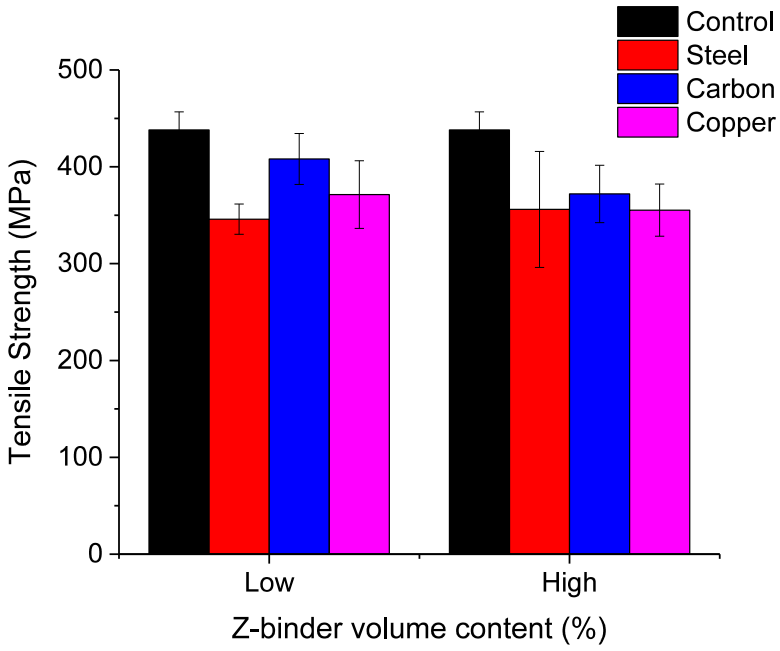

Fig. 9.11: *Tensile strength of 2D laminate and different types of 3D woven composites.*

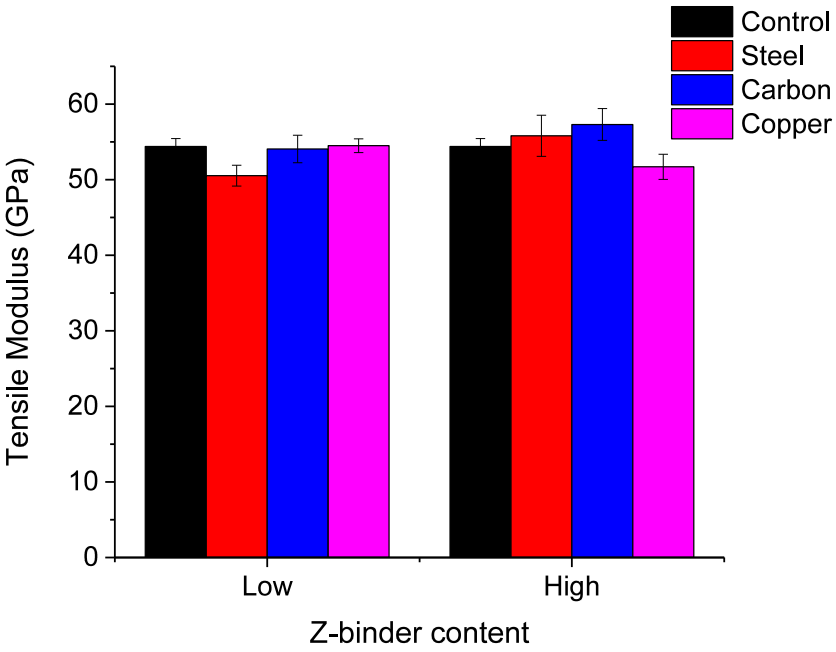

Fig. 9.12: *Tensile modulus values of 2D laminate and different types of 3D woven composites.*

Acoustic emission events recorded during tensile testing of the composite samples are shown in Fig. 9.14**.** The number of AE events are normalised to the total number at final failure of specimen. The AE events are caused mostly by matrix cracking, fibre-matrix interfacial cracking and fibre fracture. A progressive increase in the number of acoustic emission events with increasing applied tensile strain for steel, copper and carbon z-binder is shown in Fig. 9.13 (a, b, c). A rapid rise in the number of AE counts in the tests conforms to the cumulative failure probability of the fibre breakage during the tensile test. The number of counts recorded for 3D woven composites for low and high volume contents is same as of the number of counts for 2D laminate. As previously discussed, fibre rupture is the dominant failure mechanism in the 3D composites and a reason for the reduction to the tensile strength. Fig. 9.14 (a, b) reveals that the tensile properties of 3D woven composites are not affected by the volume content of metal z-binders. The total number of acoustic events increased at the same rate for the low and high volume contents.

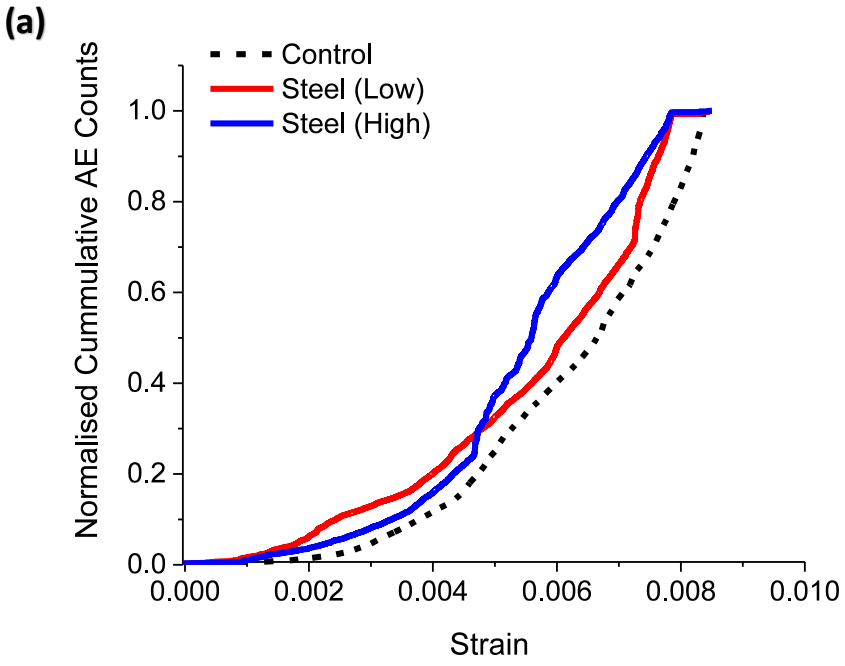

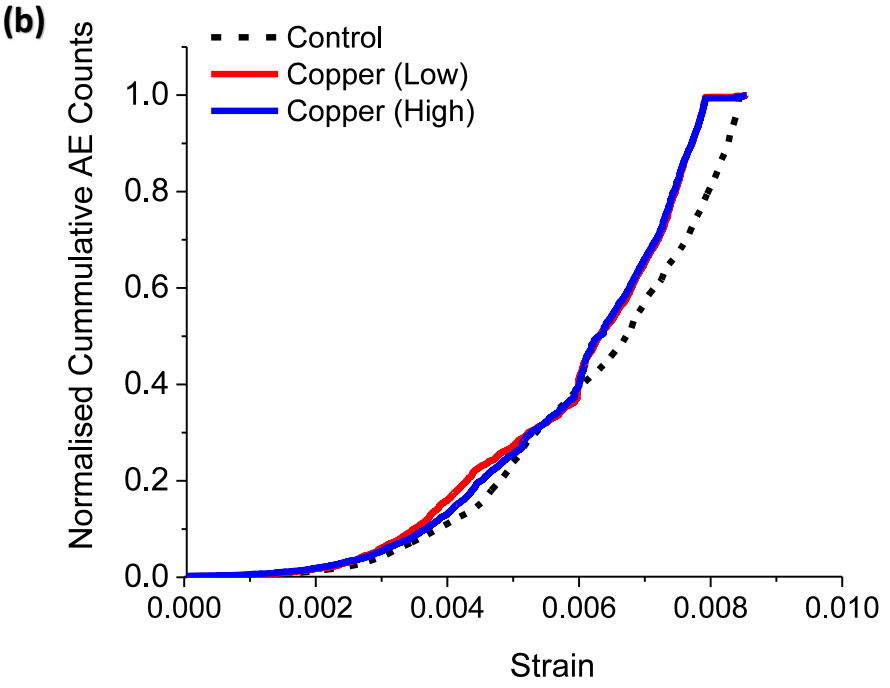

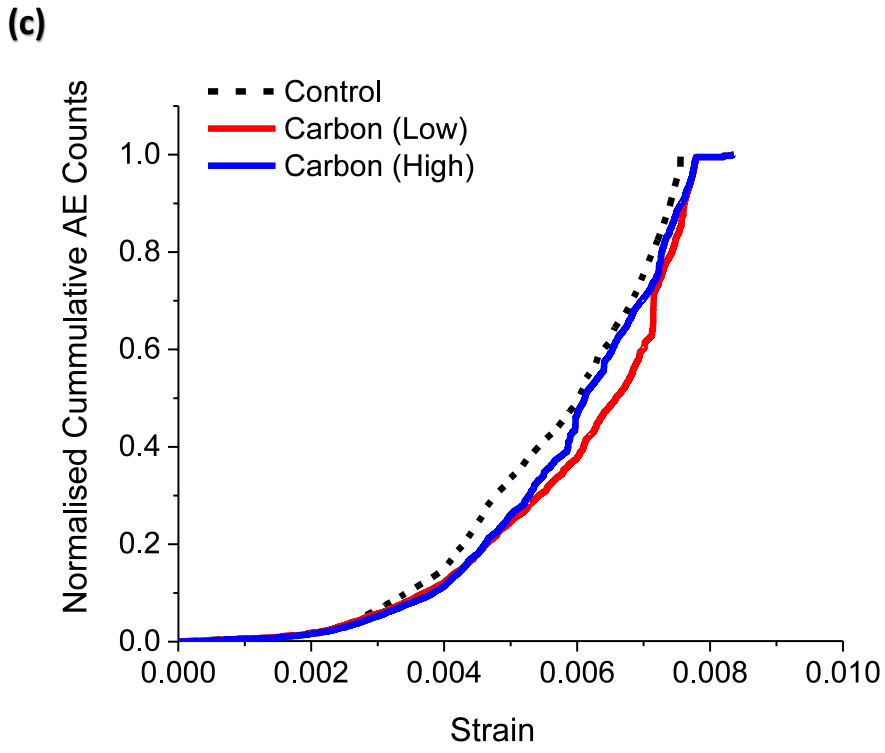

Fig. 9.13: *Effect of z-binder content on normalised AE hits vs strain during the tensile test for the (a) steel (b) copper (c) carbon 3D composites compared with 2D laminate.*

The 2D laminate failed by fibre fracture of the load-bearing (0°) plies, with significant matrix cracking in the 90° plies under tension loading as shown in Fig. 9.14. The tensile failure mode of the 3D woven composites, irrespective of the material type and volume content of the z-binder, was initiated by cracking prior to final rupture. It is believed that the cracking initiated in the locations of in-plane fibre waviness and out-of-plane crimping of the load-bearing fibres**.** The wavy plies near the z-binders attempt to straighten in the loading direction, and this generates a high shear stress in the surrounding polymer matrix. The tensile strength was also reduced by the broken fibres caused by the insertion of z-binders. Also, the tensile strength was reduced by lowering the fibre content.

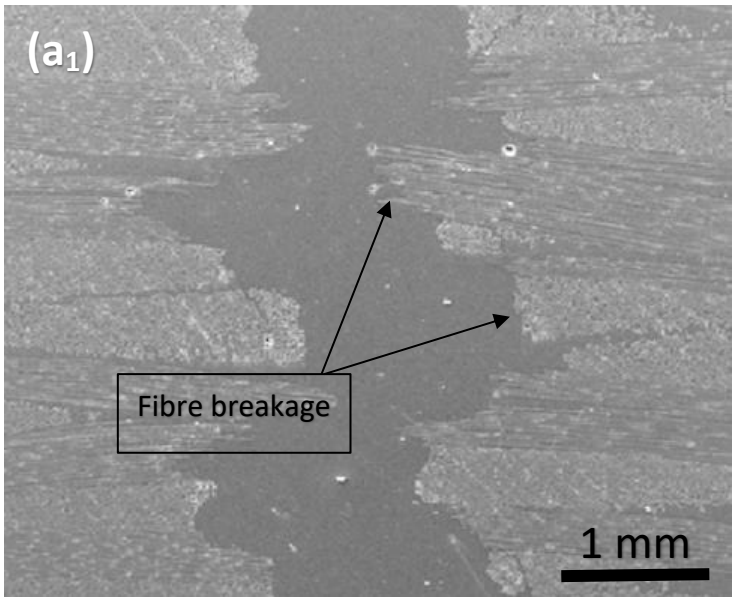

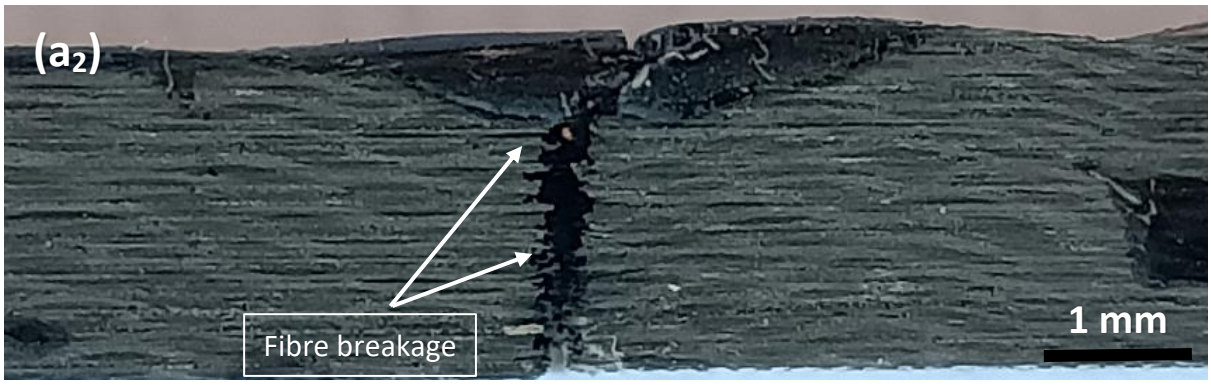

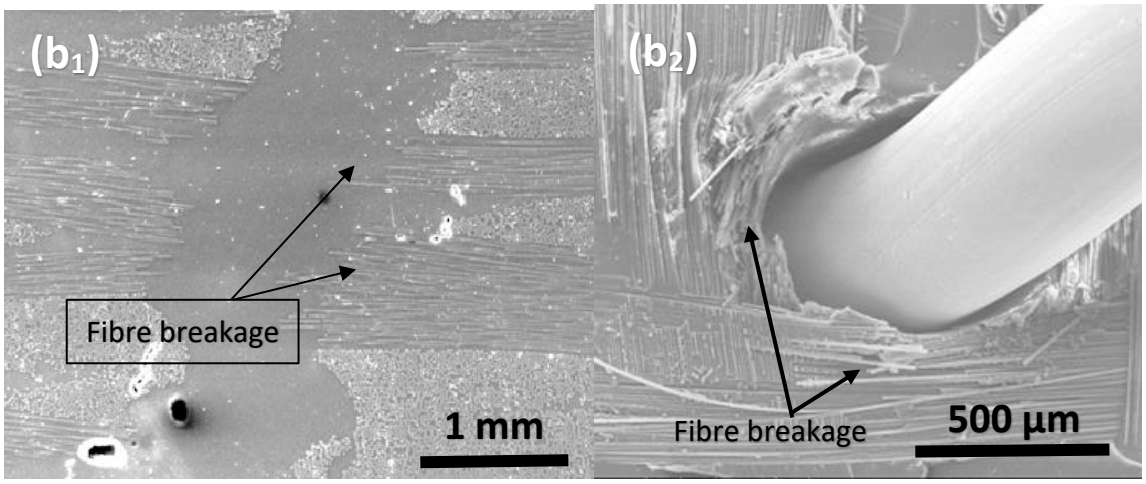
(b1)
Fibre breakage
1 mm
(b2)
Fibre breakage
500 µm

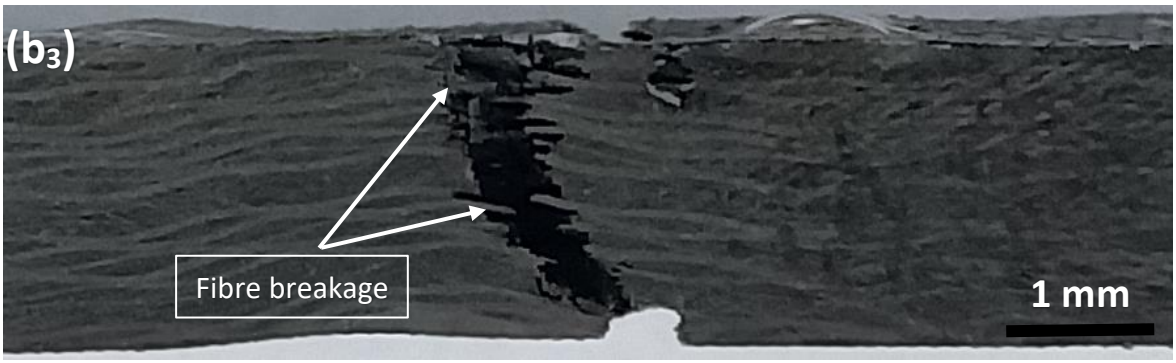
(b3)
Fibre breakage
1 mm

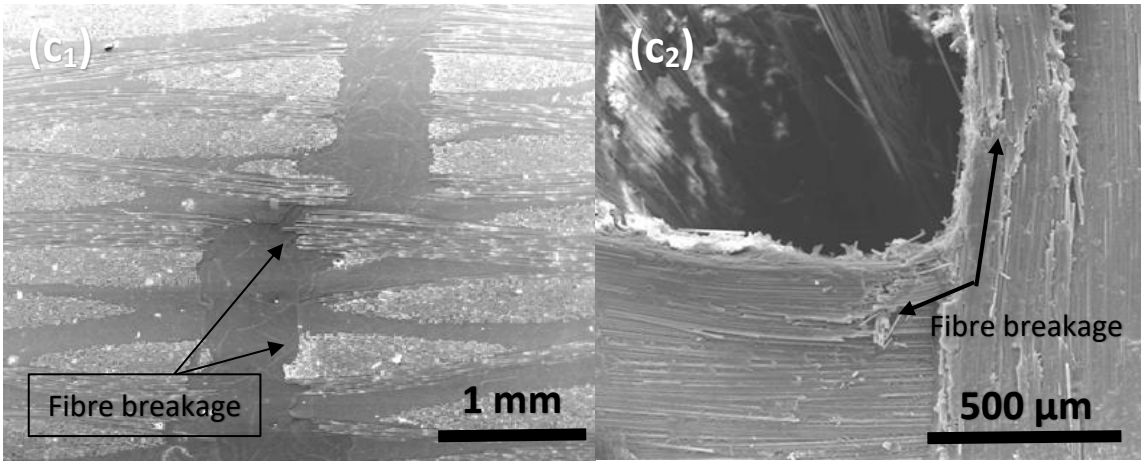
(c1)
Fibre breakage
1 mm
(c2)
Fibre breakage
500 µm

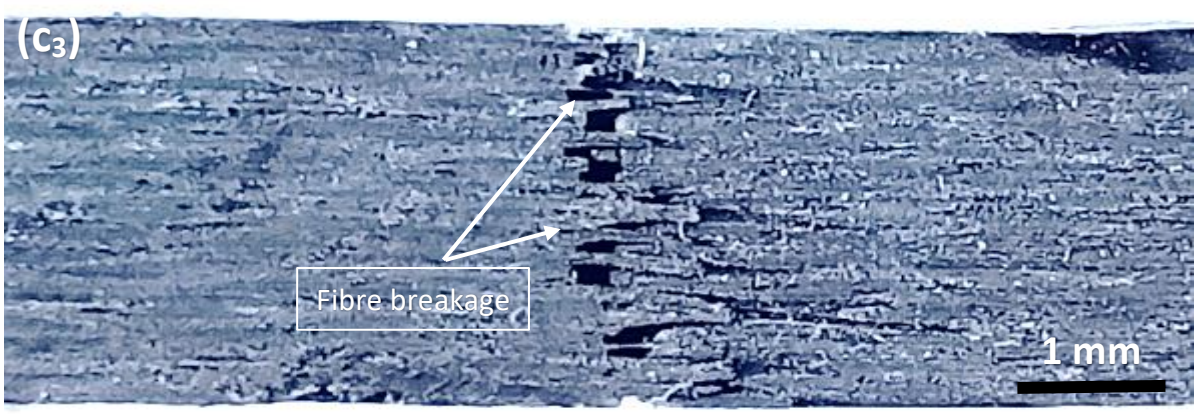
(c3)
Fibre breakage
1 mm

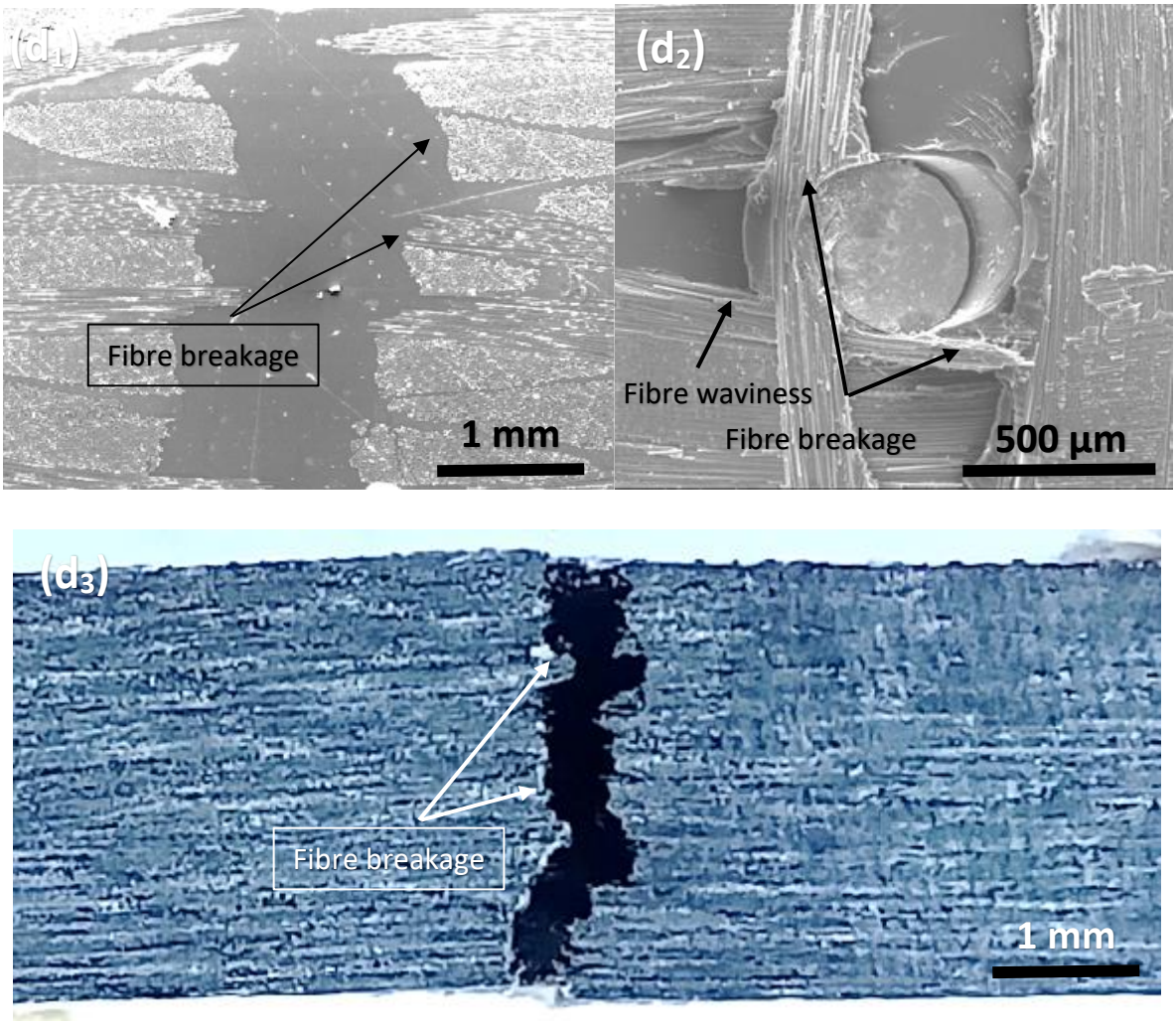

Fig. 9.14: *Fracture tensile specimens of (a) 2D laminate and 3D composites containing z-binders made of (b) steel, (c) carbon and (d) copper.*

9.3.2 Compression Properties of 2D and 3D Woven composites

Compressive stress-strain curves measured for the 2D laminate and 3D woven composites are presented in Figs. 9.15 – 9.18. The curves (Figs. 9.15 and 9.16) show the repeatability of the compression tests, and the scatter is in the range of 10% - 20%. The curves (Fig. 9.17, 9.18) show the applied load increased linearly with the strain until failure of the material. The 3D composites experienced around 50% reduction in compression load compared to the control laminate. The reduction is due to micro-buckling/kinking of the load-bearing tows, which was aided by the increased waviness and crimp of the z-binders. The z-binders also reduced the compressive modulus of the 3D composites. Similar to the tensile

results, the reductions to the compressive failure stress were similar for the low and high volume contents of z-binder.

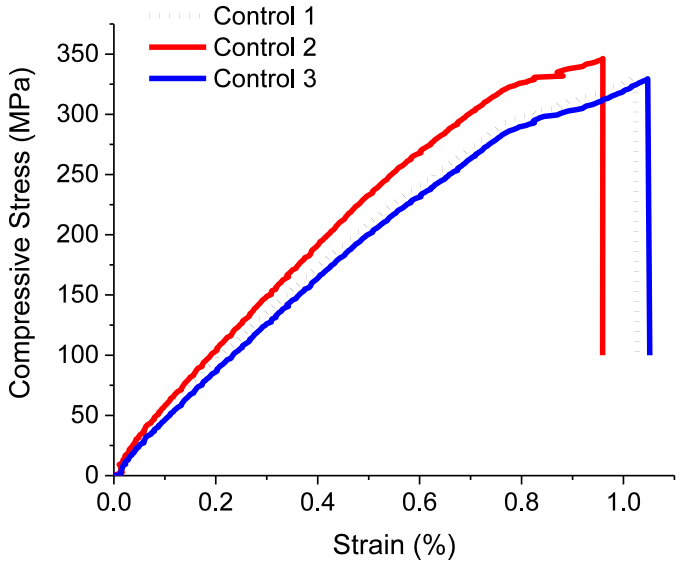

Fig. 9.15: *Compression stress-strain curves from repeated tests of the 2D composite.*

(a)

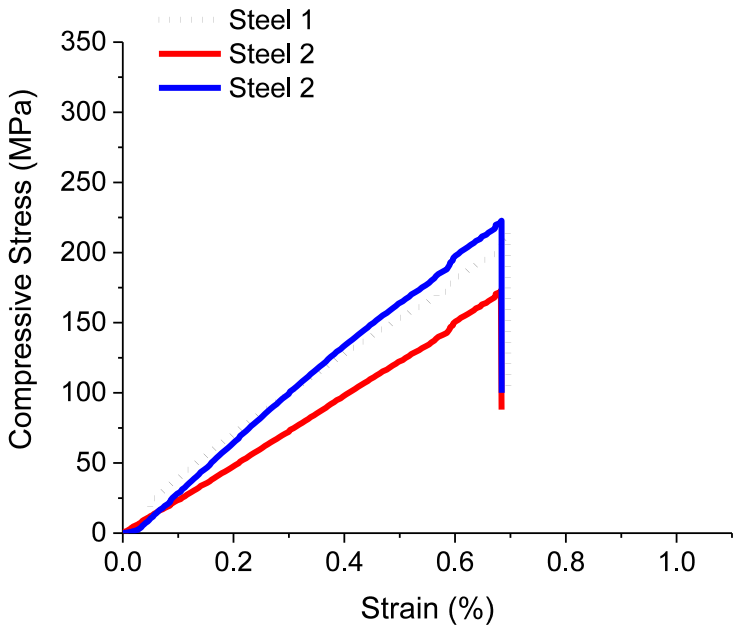

(b)

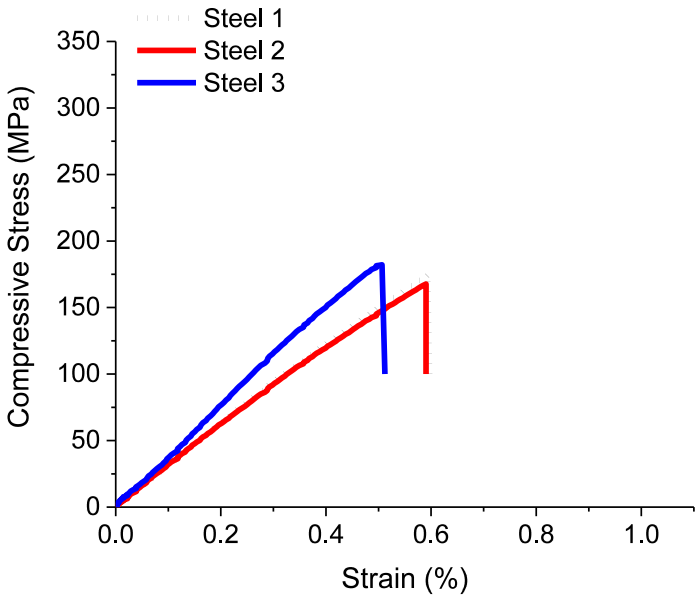

Fig. 9.16: *Compression stress-strain curves from repeated tests of the 3D woven composite reinforced with steel z-binder at the (a) low and (b) high z-binder contents.*

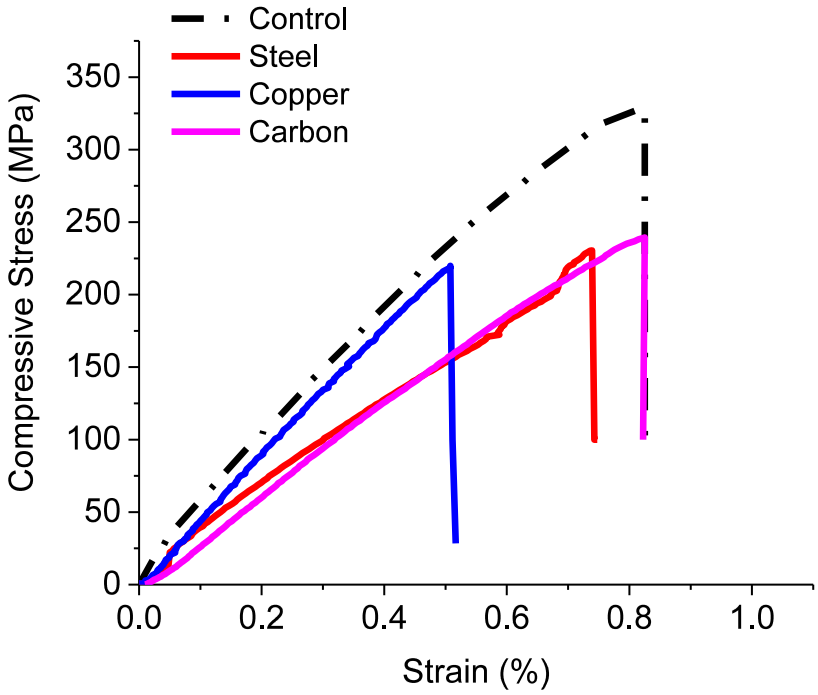

Fig. 9.17: *Compression stress-strain curves of the 2D laminate and 3D woven composites with the low z-binder content.*

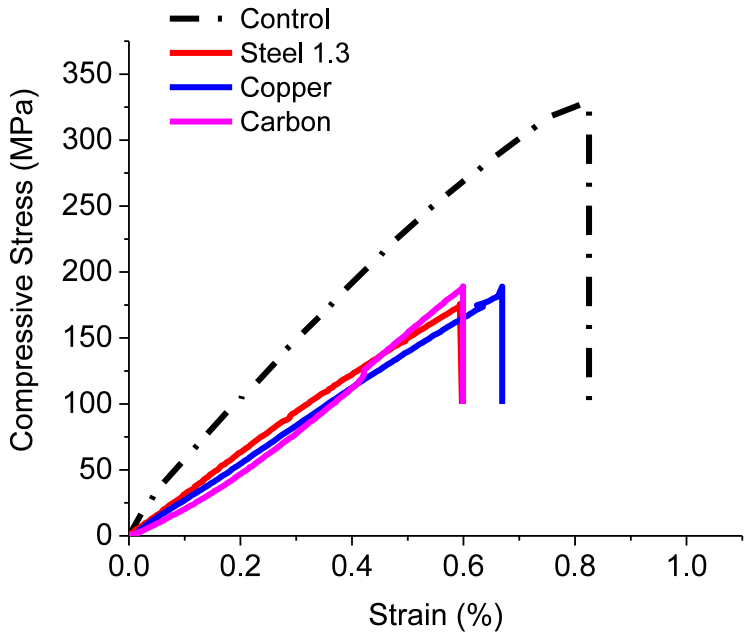

Fig. 9.18: *Compression stress-strain curves of the 2D laminate and 3D woven composites with the high z-binder content.*

The compression properties of the 2D and 3D woven composites are shown in Figs. 9.19 and 9.20. The reduction to the compression modulus of the 3D composites is due to several factors, including the increased fibre waviness and the lower fibre volume content. The compression strengths for the all the 3D woven composites are much lower than the 2D laminate. The compressive failure stress of 3D woven materials are reduced by microstructural damage caused by the z-binders, as reported in [31, 32, 176]. The reduction is due to the in-plane fibre waviness and out-of-plane fibre crimping [176-178] as well as the lower in-plane fibre volume content. Furthermore, finite element modelling [24, 30, 176] reveals that the fibre waviness and crimping caused by woven z-binders lowers the critical stress required to initiate kinking of the load-bearing fibres.

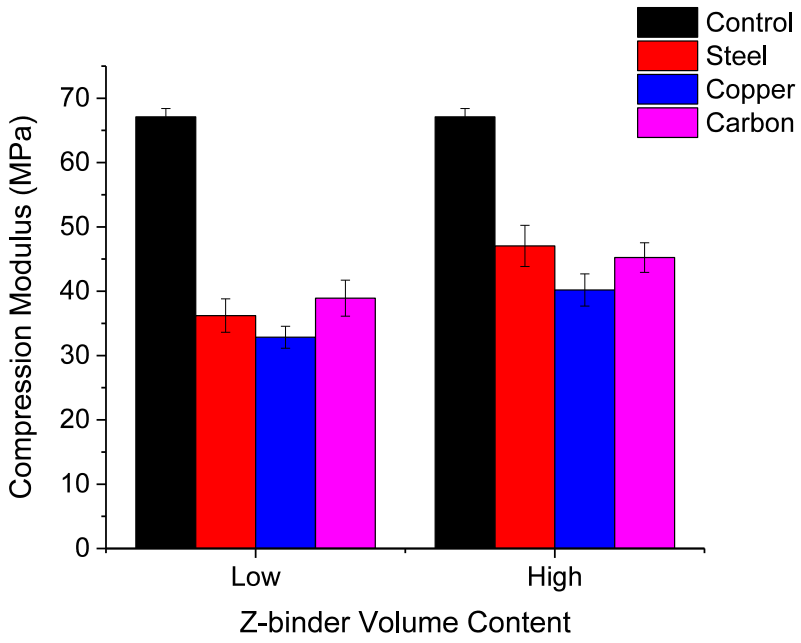

Fig. 9.19: *Compression modulus values of the 2D laminate and different types of 3D woven composites. The error bars represent variation (standard deviation).*

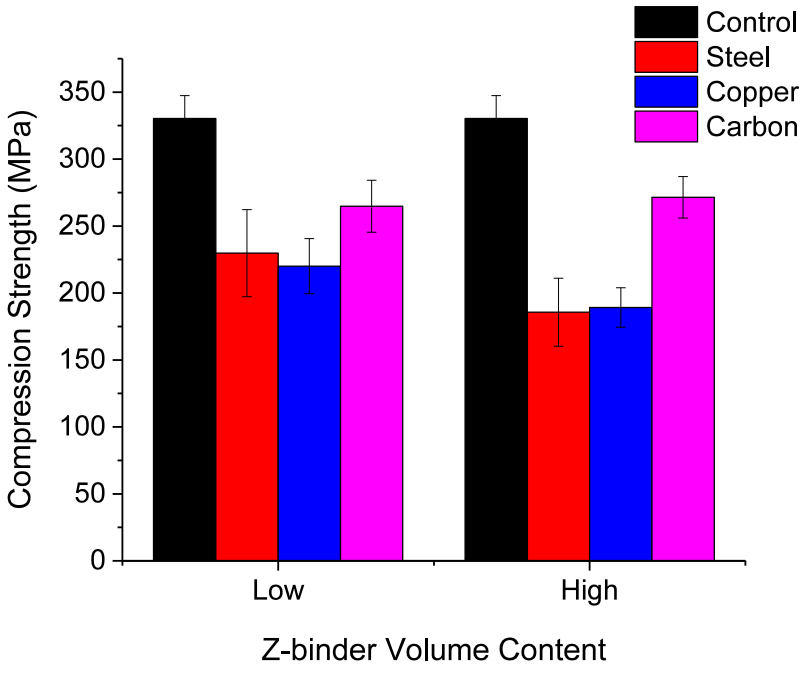

Fig. 9.20: *Compression strength values of the 2D laminate and different types of 3D woven composites. The error bars represent variation (standard deviation).*

Measurements of the compression strain fields using the DIC technique provide further insight into the effect of the z-binders on the deformation behaviour of the 3D woven composites under increasing strain. Compression surface strain (ε_{yy}) maps measured for the 2D laminate and 3D woven composites are presented in Fig. 6.13. The DIC-generated strain maps were recorded at compressive strains of 30%, 50% and just below 100% of the final failure strain of the test specimen. The 2D laminate shows a relatively uniform strain field over the surface until the point of failure, which is expected. In contrast, all the 3D laminates show high strain concentrations in the locations of the z-binders. This reveals that the z-binders acted as geometric stress raisers, and the mismatch in the strain at the z-binder and in the surrounding CFRP material increased with the applied compressive strain. This strain concentration effect caused a localised build-up of stress at the z-binder sites, thereby causing the initiation of damage which reduces the compressive failure stress.

(a)

% of failure strength	30%	50%	~100%
Control	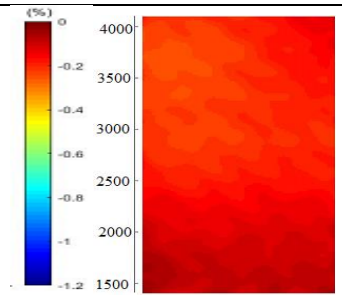		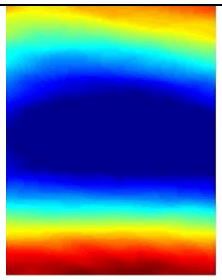
Steel (Low)	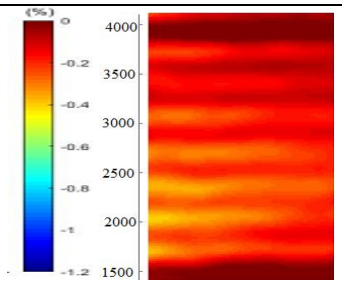	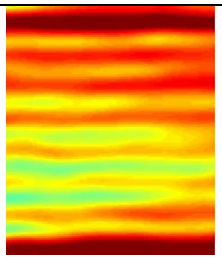	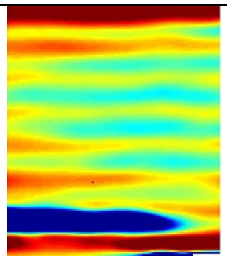
Carbon (Low)	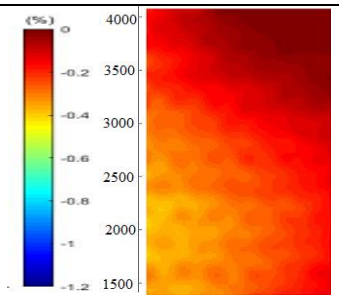	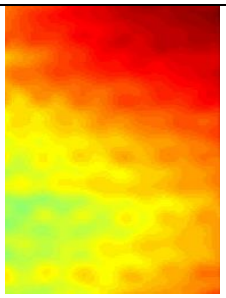	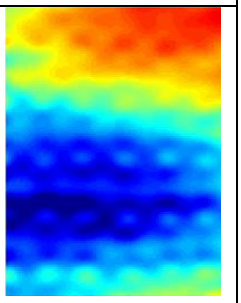
Copper (Low)	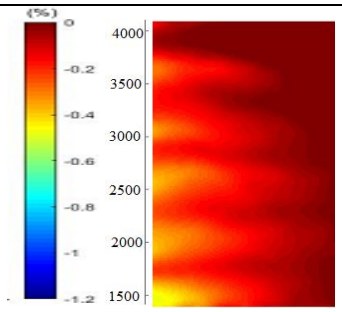	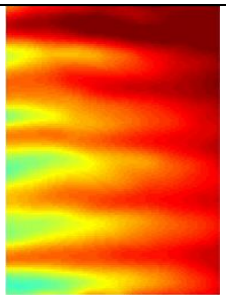	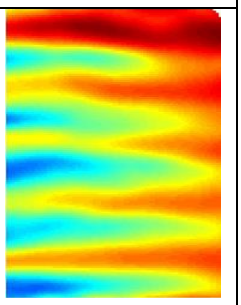

(b)

% of failure strength	30%	50%	~100%
Control	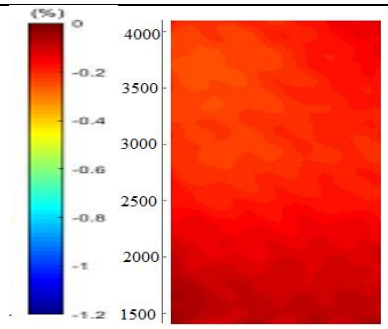	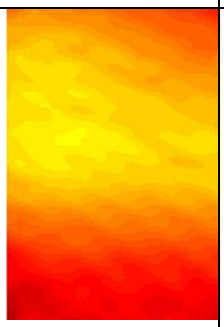	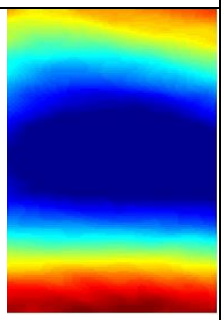
Steel (High)	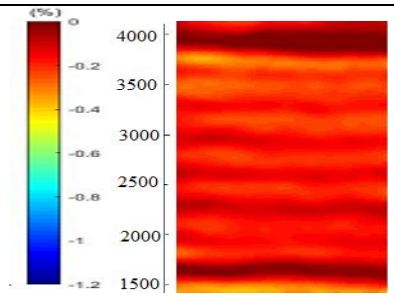	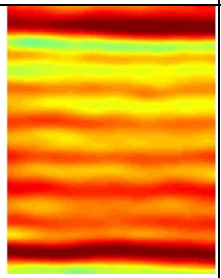	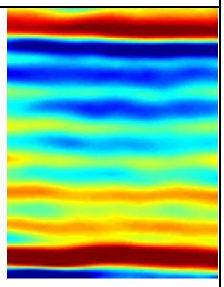
Carbon (High)	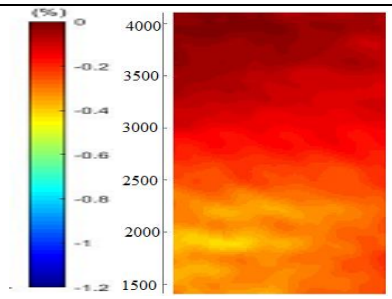	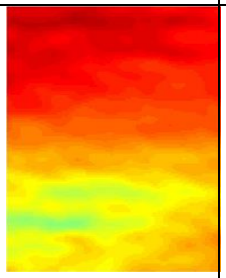	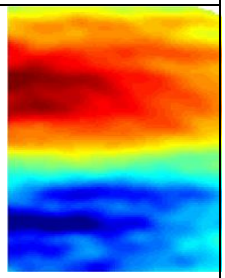
Copper (High)	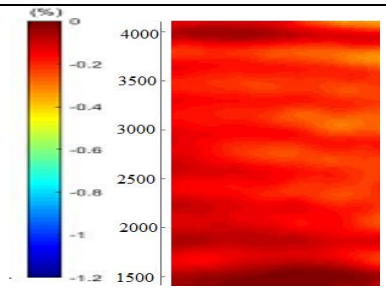	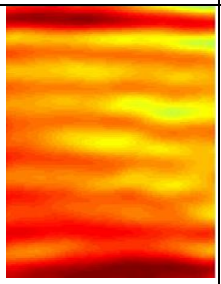	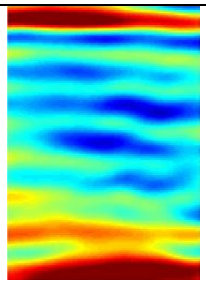

Fig. 9.21: *Compression surface strain (ε_{yy}) maps measured at 30%, 50% and just prior to 100% of the compressive failure strain for the 2D (control) laminate and the 3D woven composites with (a) low and (b) high volume content of z-binders.*

9.3.2 Flexural properties of 2D and 3D woven composites

The flexural stress-strain curves for the 2D and 3D woven composites are shown in Fig. 9.22 - 9.24. The curves for the 2D laminate generally show good repeatability based on multiple tests (Fig. 9.22). The stress-strain curves for 3D woven composite containing carbon z-binder for four repeated tests are shown in Fig. 9.23, and again the results show good repeatability. The stress-strain curves for the different types of 3D woven composites are mostly linear elastic to failure (Figs. 9.24 - 9.25), which is similar to that measured under tension and compression loads. The flexural properties show similar results for low and high volume content of z-binder.

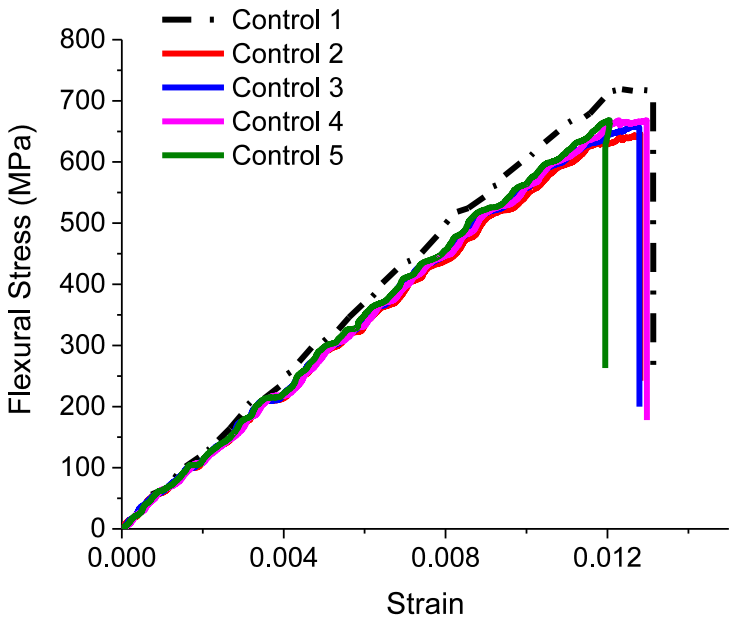

Fig. 9.22: *Flexural stress-strain curves from repeated tests of the 2D composite.*

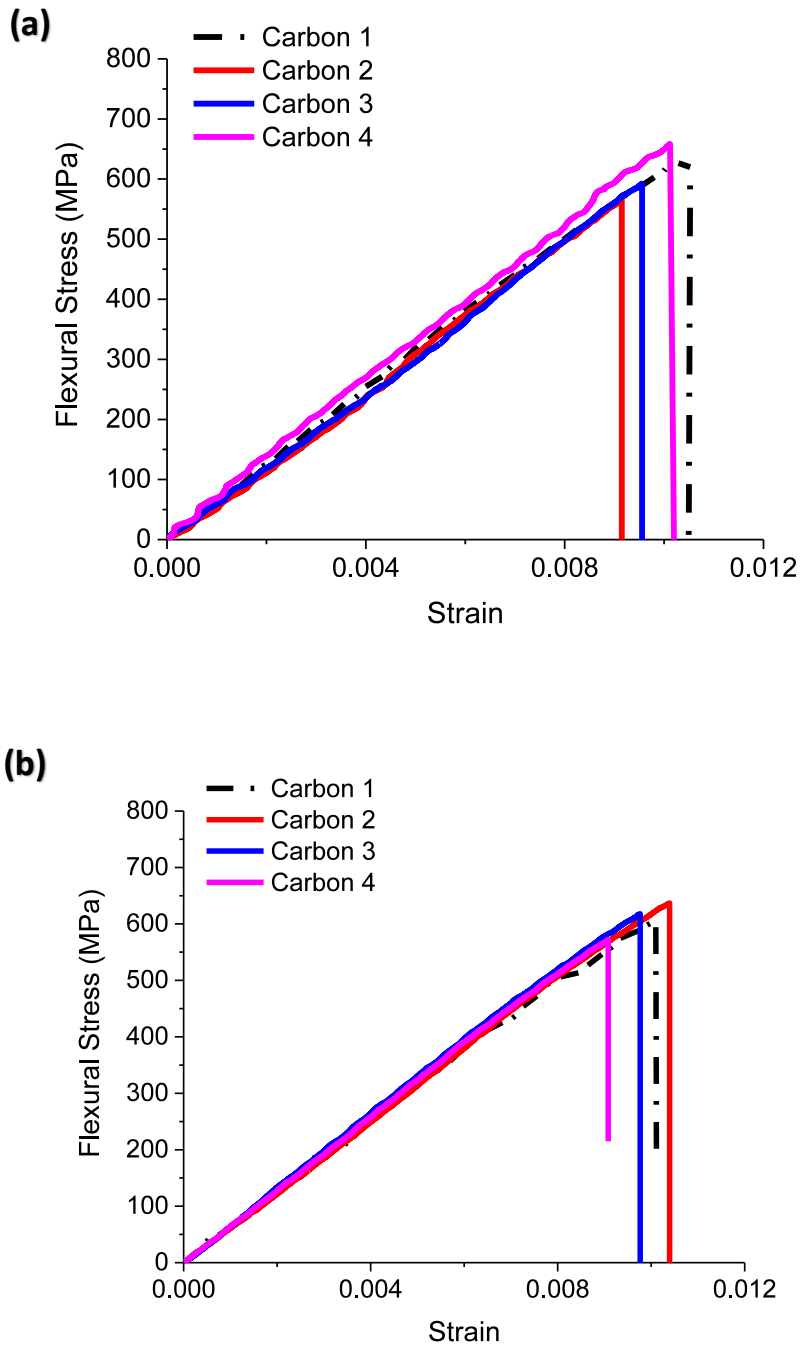

Fig. 9.23: *Flexural stress-strain curves from repeated tests of the 3D woven composite with a (a) low and (b) high content of carbon z-binders.*

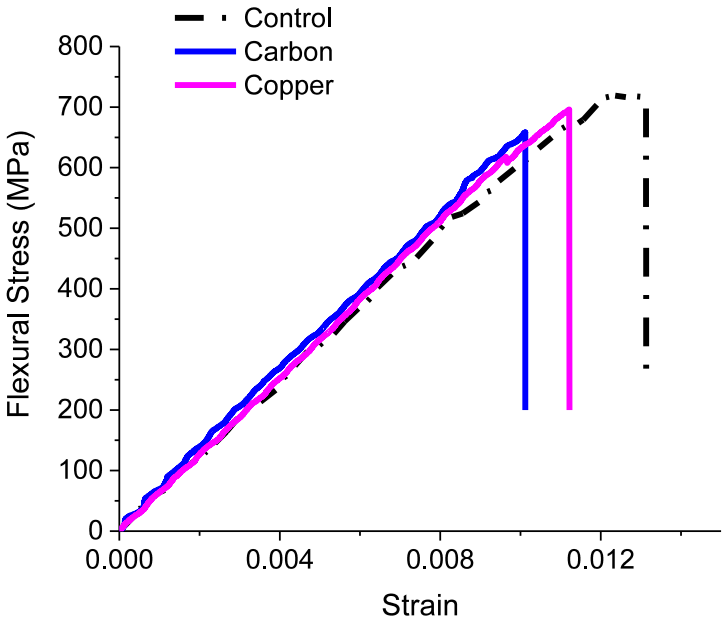

Fig.9.24: *Flexural stress-displacement curves of the 2D laminate and 3D woven composites with the low z-binder content.*

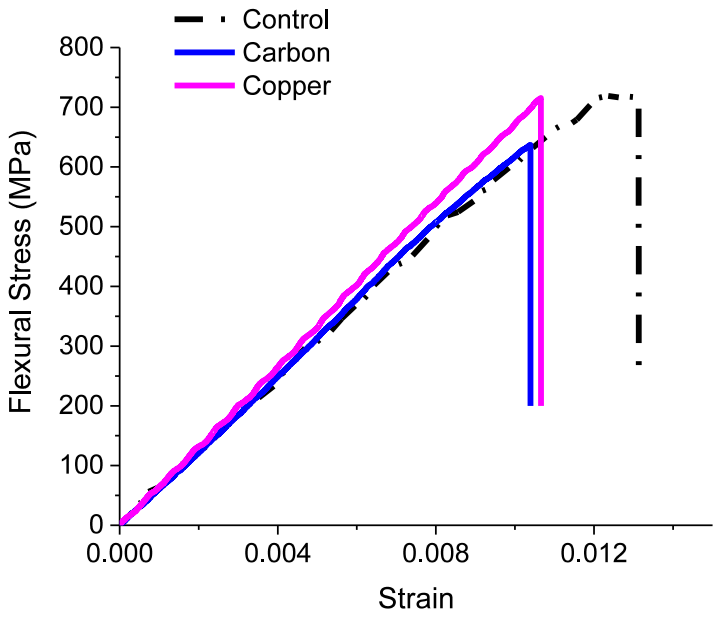

Fig. 9.25: *Flexural stress-displacement curves of the 2D laminate and 3D woven composites with the high z-binder content.*

Figs. 9.26 and 9.27 show the effect of z-binder volume content on the flexural strength and flexural modulus. The flexural strength and modulus of the 3D composites were not affected when woven through-thickness with carbon or copper z-binders. The 3D composites showed no statistically significant reduction to the in-plane modulus and strength compared to the 2D laminate. All the flexural results for 3D woven composites are within the bounds of scatter. Similar to tensile and compression properties, the flexural properties were also not significantly affected when the z-binder volume content was increased.

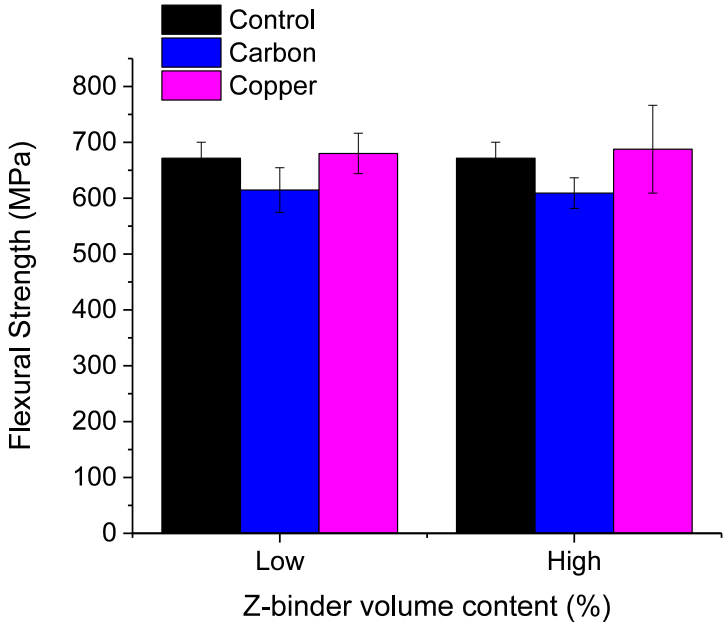

Fig. 9.26: *Flexural strength values of the 2D laminate and different types of 3D woven composites. The error bars represent variation (standard deviation).*

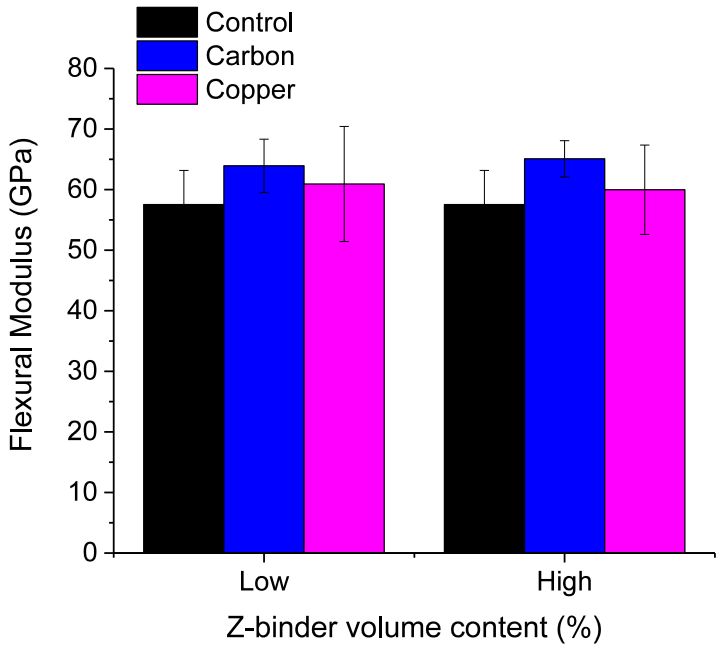

Fig. 9.27: *Flexural modulus values of the 2D laminate and different types of 3D woven composites. The error bars represent variation (standard deviation).*

9.4 CONCLUSION

The effect of z-binder material and volume content on the tensile, compressive and flexural properties of 2D and 3D woven composite has been investigated. The effect of the metal z-binders on the microstructure and mechanical properties of the 3D woven composites are similar to the carbon fibre z-binder. The microstructure of the composite is changed by insertion of z-binder, with increased in-plane fibre waviness, reduced fibre content, broken and damaged fibres. These defects are the main reasons of reductions to the mechanical properties of the 3D woven composites. The tensile and flexural modulus and strength of the 3D composite remain same with increasing volume content of z-binder. However, the compression properties are reduced substantially by waviness of the load-bearing fibres together with the reduced fibre content and increasing the resin-rich regions near the z-binder location. Under compression loading, the z-binders induce localised regions of high strain concentration which lowers the applied compressive stress needed to initiate failure by microbuckling/kinking of the load-bearing fibres. The tensile, compression and flexural properties were not significantly affected with increasing volume content of z-binder.

Chapter 10: Conclusions and Future Research

10.1 Main Conclusions

This PhD thesis has presented an original experimental research study into 3D orthogonally woven composites reinforced in the through-thickness direction with metal or carbon z-binders. The main deliverables of this study were improvements to the (i) modes I and II interlaminar fracture toughness properties, (ii) modes I and II interlaminar fatigue resistance, (iii) impact damage resistance, (iv) electrical conductivity properties, (v) *in-situ* damage detection functionality and (vi) structural properties of T-joints. The detrimental effect of z-binders on the in-plane mechanical properties of 3D woven composites was also explored.

The modes I and II interlaminar fracture toughness and interlaminar fatigue resistance properties of 3D woven composites reinforced with copper, steel or carbon z-binders were investigated in Chapter 3 and 4. The effects of the material properties and volume content of the z-binders on these properties was experimentally investigated. Also, the interlaminar toughening and fatigue strengthening mechanisms for the different types of z-binder were identified. It was found that the steel z-binders caused an exceptionally high mode I interlaminar fracture toughness value (~28 kJ/m^2), which is the highest toughness value ever reported for a toughened composite. The carbon z-binder and, to a much lesser extent, the copper z-binder were also effective at increasing the mode I interlaminar toughness. The steel and carbon z-binders formed a long bridging process zone along the mode I delamination crack which led to the high mode I interlaminar fracture toughness. Also, these z-binders broke within the composite material and were then pulled-out, and this contributed to the high mode I toughening effect. The copper z-binders were less effective at increasing the mode I interlaminar fracture toughness, and this is because they formed a relatively short crack bridging zone and fractured at the delamination crack plane without significant pull-out. The study revealed that large improvements to the mode I interlaminar toughness is gained using z-binders made of a high strength, ductile material (e.g. steel) that can form a long bridging process zone and that fractures within the composite material and therefore

needs to be pulled-out. The improvement to the mode II interlaminar toughness properties using the z-binders was less than the mode I properties. Furthermore, the three types of z-binder induced similar improvements to the mode II toughness, although the carbon was slightly more effective than the steel or copper. Similar to mode I loading, the z-binders formed a long bridging process zone along the delamination shear crack which increased the mode II interlaminar fracture toughness. The metal z-binders sustained plastic shear deformation that was localised to the mode II delamination crack plane, but they did not break due to the relatively short shear sliding displacements between the opposing crack surfaces. The carbon z-binders experienced localised shear deformation leading to transverse fracture under mode II loading, and this was due to their failure strain being much lower than the metal z-binders.

The z-binders improved the mode I interlaminar fatigue resistance of the 3D woven composites. The mode I fatigue strengthening effect was dependent on both the material type and volume content of z-binders. The copper z-binder provided the smallest improvement to the mode I fatigue resistance of the composite material due to its relatively low fatigue strength. Steel z-binders provided a higher improvement to the mode I fatigue resistance due to its higher fatigue strength and its capacity to partially pull-out after fatigue-induced fracture, which generated bridging traction loads that opposed fatigue crack growth. The carbon z-binder increased the mode I fatigue properties the most due to its high tensile fatigue strength and also its capacity to pull-out under mode I cyclic loading. It was found the improvement to the mode II interlaminar fatigue strength was less sensitive to the type of z-binder material than the mode I fatigue properties. Similar to static mode II fracture toughness, the mode II fatigue properties were increased by the z-binders forming a large-scale bridging process zone along the delamination crack.

Chapter 5 presented an experimental study to demonstrate the use of z-binders to increase the electrical conductivity of 3D woven composites. The through-thickness conductivity was increased by the z-binders, with the magnitude of the improvement controlled by the material type and volume content. The z-binders created a continuous conductive pathway for current flow in the through-thickness direction, thereby greatly increasing the electrical conductivity in this direction. In the case of the copper z-binders,

which had the lowest resistivity of the three materials tested, the through-thickness conductivity was increased by over three orders of magnitude. The z-binders also increased the longitudinal conductivity of the composite material, although the improvement was less than for the through-thickness conductivity. The improvements to the electrical properties of the 3D woven composites can be predicted using rule-of-mixtures analysis.

The increase to the electrical properties of the 3D woven composites can be used for the *in-situ* detection of mode I delamination cracks, as reported in Chapter 6. Due to the increased electrical conductivity caused by the z-binders, the changes to the resistivity of the 3D woven composite due to delamination crack growth can be monitored. The resistivity increased with the delamination length, and is dependent on the type and volume content of z-binder. This study demonstrated that z-binders can be used to provide 3D woven composites with a structural health monitoring functionality to detect the growth of mode I delaminations.

Chapter 7 presented the experimental investigation into the impact damage resistance and compression-after-impact properties of 3D woven composites containing copper, steel or carbon z-binders. This study proved that z-binders increased the impact damage resistance, and this was due to their interlaminar toughening effect which resists the growth of impact-induced delamination cracks. However, the post-impact compressive strength of the 3D woven composites was lower or similar to the control laminate despite the lower amount of impact damage.

The structural properties of T-joints reinforced with z-binders was experimentally investigated for the stiffener load condition in Chapter 8. The z-binders were not effective at increasing the load-at-first failure of the T-joint, which involved cracking within the delta-fillet region where the z-binders were absent. However, the z-binders increased both the ultimate load and absorbed energy capacity of the T-joint via interlaminar toughnening of the skin/flange section. The structural properties of the T-joint increased with the volume content of z-binders. The improvement to the T-joint properties was also dependent on the type of z-binder material, with copper being the least effective and steel being the most effective at increasing the ultimate load and absorbed energy capacity. The z-binders made of carbon and

steel were capable of strengthening the skin/flange section to such a high level that large-scale delamination-type cracking in the skin/flange section was suppressed, and instead the T-joint failed via fracture of the laminate skin. Based on comparative analysis of published data presented in chapter 8, the steel z-binder was capable of increasing the percentage ultimate load of the T-joint more than other toughening techniques such as nanoparticles, interleaving, stitching, tufting and z-pinning.

Chapter 9 presented an experimental investigation into the in-plane mechanical properties of the 3D woven composites. The effects of material type and volume content of the z-binder on the tensile, compressive and flexural properties of 3D woven composites was investigated. The microstructure of the composite was changed due to the z-binder, which included in-plane fibre waviness, reduced fibre content, and broken and damaged fibres. The tensile and flexural properties of the 3D woven composites were not affected significantly with increasing z-binder content. However, the compression properties were substantially reduced due primarily to increased waviness of the load-bearing fibres which lowered to critical stress to initiate kinking. DIC analysis revealed that stress was concentrated at the sites of the z-binders under compressive loading due to the locally reduced stiffness caused by fibre waviness, and this lowered the kinking failure stress.

10.2 Future Research

This PhD research provides a large body of experimental work on the properties of 3D woven composites. However, key challenges and unsolved research problems exist with these materials. This section briefly identifies several research topics worthy of further exploration to advance further the understanding of 3D woven composites.

FE models have been developed to calculate the modes I and mode II interlaminar fracture toughness properties for 3D woven composites [65, 66], but there are no models that can predict the delamination fatigue properties. The effects of both the material type and volume content of the z-binders on the interlaminar fatigue properties needs to be considered for the FE model. Also, further research is needed into the electrical properties of 3D woven composites by using other highly conductive and high strength materials (e.g.

titanium alloys) as well as other z-binder architectures (e.g. layer interlock). Research is required into the thermal conductivity properties of 3D woven composites, which is expected to be improved significantly by using highly thermally conductive z-binder materials (e.g. copper). The effects of the material type and volume content of the z-binder on the through-thickness and longitudinal thermal properties of 3D woven composites is worthy of investigation.

Research is also required towards the development of an FE model to calculate the structural properties of T-joints containing woven z-binders. In addition, other types of z-binders with high strength properties, such as titanium alloy, can also be considered for the strengthening of T-joints. The properties of multifunctional T-joints containing metal z-binders are also a topic of future investigation, including the control of their structural, damage tolerance, electrical, thermal and damage detection properties via the judicious choice of the volume content, material type and weave architecture of the z-binders.

References

1. Australian-Transport-Safety-Bureau. *Australian aviation wildlife strike statistics 2008 – 2017*. 2008-2017 [cited 2019 13 March]; Available from: https://www.atsb.gov.au/publications/2018/ar-2018-035/.
2. Rouchon, J. and Bos, M.J., *Fatigue and damage tolerance evaluation of structures: the composite materials response*, in *Symposium of the International Committee on Aeronautical Fatigue*. 2009.
3. Dutton, S., Kelly, D., and Baker, A., *Composite materials for aircraft structures.* American Institute of Aeronautics and Astronautics, 2004.
4. Lin, K.Y. and Styuart, A.V., *Probabilistic approach to damage tolerance design of aircraft composite structures.* Journal of Aircraft, 2007. **44**(4): p. 1309-1317.
5. Jones, S. *Drone crash into Boeing 737 jet plane*. 2017 [cited 2020; Available from: https://www.mirror.co.uk/news/world-news/drone-crashes-boeing-737-jet-9574073.
6. Chandarana, N., Sanchez, D.M., Soutis, C., and Gresil, M., *Early damage detection in composites during fabrication and mechanical testing.* Materials (Basel, Switzerland), 2017. **10**(7): p. 685.
7. Curtis, P.T., *Multifunctional polymer composites.* Advanced Performance Materials, 1996. **3**(3): p. 279-293.
8. Greenhalgh, E. and Hiley, M., *The assessment of novel materials and processes for the impact tolerant design of stiffened composite aerospace structures.* Composites Part A: Applied Science and Manufacturing, 2003. **34**(2): p. 151-161.
9. Dransfield, K., Baillie, C., and Mai, Y.-W., *Improving the delamination resistance of CFRP by stitching—a review.* Composites Science and Technology, 1994. **50**(3): p. 305-317.
10. Sankar, B.V. and Zhu, H., *The effect of stitching on the low-velocity impact response of delaminated composite beams.* Composites Science and Technology, 2000. **60**(14): p. 2681-2691.
11. Kelkar, A.D., Mohan, R., Bolick, R., and Shendokar, S., *Effect of nanoparticles and nanofibers on Mode I fracture toughness of fiber glass reinforced polymeric matrix composites.* Materials Science and Engineering: B, 2010. **168**(1): p. 85-89.
12. Deconinck, P., Capelle, J., Bouchart, V., Chevrier, P., and Ravailler, F., *Delamination propagation analysis in tufted carbon fibre-reinforced plastic composites subjected to high-velocity impact.* Reinforced Plastics and Composites, 2014. **33**(14): p. 1353-1363.
13. Sohn, M.-S. and Hu, X.-Z., *Mode II delamination toughness of carbon-fibre/epoxy composites with chopped Kevlar fibre reinforcement.* Composites Science and Technology, 1994. **52**(3): p. 439-448.
14. Meyers, R., *Encyclopedia of complexity and systems science*. 2009: Springer New York. p. 1283-1302.
15. Huang, T., Wang, Y., and Wang, G., *Review of the mechanical properties of a 3D Woven composite and its applications.* Polymer-Plastics Technology and Engineering, 2018. **57**(8): p. 740-756.
16. Chen, X. and Yang, D., *Use of 3D angle-interlock woven fabric for seamless female body armor: Part 1: Ballistic evaluation.* Textile Research Journal, 2010. **80**(15): p. 1581-1588.

17. Aiman, D.P.C., Yahya, M.F., and Salleh, J., *Impact properties of 2D and 3D woven composites : A review.* American Institute of Physics, 2016. **1774**(1): p. 020002.
18. Guess, T.R. and Reedy, E.D., *Comparison of interlocked fabric and laminated fabric kevlar 49/epoxy composites.* Journal of Composites, Technology and Research, 1985. **7**(4): p. 136-142.
19. Chou, S., Chen, H.-C., and Wu, C.-C., *BMI resin composites reinforced with 3D carbon-fibre fabrics.* Composites Science and Technology, 1992. **43**(2): p. 117-128.
20. Voß, S., Fahmy, A.A., and West, H.A., *Impact tolerance of laminated and 3-dimensionally reinforced graphite-epoxy panels.* Material Science, 1993: p. 591-596.
21. Cantwell, W.J. and Morton, J., *The impact resistance of composite materials — a review.* Composites, 1991. **22**(5): p. 347-362.
22. Bilisik, K., *Multiaxis three-dimensional weaving for composites: A review.* Textile Research Journal, 2012. **82**(7): p. 725-743.
23. Dickinson, L., Mohamed, M., and Bogdanovich, A. *3D weaving: what, how and where*. in *in 44 th International SAMPE Symposium and Exhibition*. 1999.
24. Tong, L., Mouritz, A.P., and Bannister, M.K., *Chapter 5 - 3D woven composites*, in *3D fibre reinforced polymer composites*, Tong, L., Mouritz, A.P., and Bannister, M.K., Editors. 2002, Elsevier Science: Oxford. p. 107-136.
25. Kamiya, R., Cheeseman, B.A., Popper, P., and Chou, T.-W., *Some recent advances in the fabrication and design of three-dimensional textile preforms: a review.* Composites Science and Technology, 2000. **60**(1): p. 33-47.
26. Bogdanovich, A.E. and Mohamed, M.H., *Three-dimensional reinforcements for composites.* SAMPE, 2009. **45**: p. 8-28.
27. Mahadik, Y. and Hallett, S.R., *Effect of fabric compaction and yarn waviness on 3D woven composite compressive properties.* Composites Part A: Applied Science and Manufacturing, 2011. **42**(11): p. 1592-1600.
28. Gokarneshan, N. and Alagirusamy, R., *Weaving of 3D fabrics: A critical appreciation of the developments.* Textile Progress, 2009. **41**(1): p. 1-58.
29. Mouritz, A.P., Bannister, M.K., Falzon, P.J., and Leong, K.H., *Review of applications for advanced three-dimensional fibre textile composites.* Composites Part A: Applied Science and Manufacturing, 1999. **30**(12): p. 1445-1461.
30. Mouritz, A.P., *6 - Three-dimensional (3D) fibre reinforcements for composites*, in *Composite Reinforcements for Optimum Performance*, Boisse, P., Editor. 2011, Woodhead Publishing. p. 157-199.
31. Dai, S., Cunningham, P.R., Marshall, S., and Silva, C., *Influence of fibre architecture on the tensile, compressive and flexural behaviour of 3D woven composites.* Composites Part A: Applied Science and Manufacturing, 2015. **69**: p. 195-207.
32. Saleh, M.N. and Soutis, C., *Recent advancements in mechanical characterisation of 3D woven composites.* Mechanics of Advanced Materials and Modern Processes, 2017. **3**(1): p. 12.
33. Lee, B., Leong, K.H., and Herszberg, I., *Effect of weaving on the tensile properties of carbon fibre tows and woven composites.* Reinforced Plastics and Composites, 2001. **20**(8): p. 652-670.
34. Lee, L., Rudov-Clark, S., Mouritz, A.P., Bannister, M.K., and Herszberg, I., *Effect of weaving damage on the tensile properties of three-dimensional woven composites.* Composite Structures, 2002. **57**(1): p. 405-413.

35. Rudov-Clark, S., Mouritz, A.P., Lee, L., and Bannister, M.K., *Fibre damage in the manufacture of advanced three-dimensional woven composites.* Composites Part A: Applied Science and Manufacturing, 2003. **34**(10): p. 963-970.
36. Cox, B.N., Dadkhah, M.S., Morris, W.L., and Flintoff, J.G., *Failure mechanisms of 3D woven composites in tension, compression, and bending.* Acta Metallurgica et Materialia, 1994. **42**(12): p. 3967-3984.
37. Callus, P.J., Mouritz, A.P., Bannister, M.K., and Leong, K.H., *Tensile properties and failure mechanisms of 3D woven GRP composites.* Composites Part A: Applied Science and Manufacturing, 1999. **30**(11): p. 1277-1287.
38. Kuo, W.-S. and Ko, T.-H., *Compressive damage in 3-axis orthogonal fabric composites.* Composites Part A: Applied Science and Manufacturing, 2000. **31**(10): p. 1091-1105.
39. McGrath, G.C., *Fracture and toughening in fibre reinforced polymer composites*. in Rubber Toughened Engineering Plastics, ed. Collyer, A.A. 2012: Springer, Dordrecht. p. 57-89.
40. Kim, J.-K., Mai, Y.-W., and Mai, Y.-W., *Chapter 8 - Improvement of interlaminar fracture toughness with interface control*, in *Engineered Interfaces in Fiber Reinforced Composites*, Kim, J.-K., Mai, Y.-W., and Mai, Y.-W., Editors. 1998, Elsevier Science Ltd: Oxford. p. 329-365.
41. Coleman, J.N., Khan, U., Blau, W.J., and Gun'ko, Y.K., *Small but strong: A review of the mechanical properties of carbon nanotube–polymer composites.* Carbon, 2006. **44**(9): p. 1624-1652.
42. Veedu, V.P., Cao, A., Li, X., Ma, K., Soldano, C., Kar, S., Ajayan, P.M., and Ghasemi-Nejhad, M.N., *Multifunctional composites using reinforced laminae with carbon-nanotube forests.* Nature Materials, 2006. **5**(6): p. 457-462.
43. Mouritz, A.P., *Review of z-pinned composite laminates.* Composites Part A: Applied Science and Manufacturing, 2007. **38**(12): p. 2383-2397.
44. Prasad M.S. , Venkatesha C.S., and Jayaraju T., *Experimental methods of determining fracture toughness of fiber reinforced polymer composites under various loading conditions.* Journal of Minerals and Materials Characterization and Engineering, 2011. **10**(13): p. 1263-1275.
45. Rocha-Rangel, E., *Fracture toughness determinations by means of indentation fracture*, in *Nanocomposites with unique properties and applications in medicine and industry*. 2011, IntechOpen.
46. Mouritz, A.P., Baini, C., and Herszberg, I., *Mode I interlaminar fracture toughness properties of advanced textile fibreglass composites.* Composites Part A: Applied Science and Manufacturing, 1999. **30**(7): p. 859-870.
47. Vinson, J.R. *Sandwich structures: past, present, and future*. 2005. Dordrecht: Springer Netherlands.
48. Byun, J.-H., Gillespie, J.W., and Chou, T.-W., *Mode I delamination of a three-dimensional fabric composite.* Journal of Composite Materials, 1990. **24**(5): p. 497-518.
49. Guénon, V.A., Chou, T.W., and Gillespie, J.W., *Toughness properties of a three-dimensional carbon-epoxy composite.* Journal of Materials Science, 1989. **24**(11): p. 4168-4175.
50. Arendts, F.J., K, D., and Brandt, J., *Advanced textile structural composites--status and outlook*, in *International conference on advanced composite materials*. 1993: United States.

51. Yan, W., Liu, H.-Y., and Mai, Y.-W., *Mode II delamination toughness of z-pinned laminates.* Composites Science and Technology, 2004. **64**(13): p. 1937-1945.
52. Tong, L. and Sun, X., *Bending effect of through-thickness reinforcement rods on mode I delamination toughness of DCB specimen. I. Linearly elastic and rigid-perfectly plastic models.* International Journal of Solids and Structures, 2004. **41**(24): p. 6831-6852.
53. Rugg, K.L., Cox, B.N., and Massabò, R., *Mixed mode delamination of polymer composite laminates reinforced through the thickness by z-fibers.* Composites Part A: Applied Science and Manufacturing, 2002. **33**(2): p. 177-190.
54. Ashton, T., Negre, P., and Langer, J. *Interlaminar damage resistance of Z fiberTM reinforced structural CFRP*. in *Extended abstracts of the 13th international conference on composite materials*. 2001.
55. Tanzawa, Y., Watanabe, N., and Ishikawa, T. *Interlaminar delamination toughness and strength of 3-D orthogonal interlocked fabric composite*. in *Proceedings of 11th International Conference on Composite Materials*. 1997.
56. Friedrich, K., *Application of fracture mechanics to composite materials*. Vol. 6. 2012: Elsevier.
57. Jain, L.K., Dransfield, K.A., and Mai, Y.-W., *On the effects of stitching in CFRPs—II. Mode II delamination toughness.* Composites Science and Technology, 1998. **58**(6): p. 829-837.
58. Fishpool, D.T., Rezai, A., Baker, D., Ogin, S.L., and Smith, P.A., *Interlaminar toughness characterisation of 3D woven carbon fibre composites.* Plastics, Rubber and Composites, 2013. **42**(3): p. 108-114.
59. Trabelsi, W., Michel, L., and Othomene, R., *Effects of stitching on delamination of satin weave carbon-epoxy laminates under mode I, mode II and mixed-mode I/II loadings.* Applied Composite Materials, 2010. **17**(6): p. 575-595.
60. Wicks, S.S., de Villoria, R.G., and Wardle, B.L., *Interlaminar and intralaminar reinforcement of composite laminates with aligned carbon nanotubes.* Composites Science and Technology, 2010. **70**(1): p. 20-28.
61. Jain, L.K. and Mai, Y.-W., *Analysis of stitched laminated ENF specimens for interlaminar mode II fracture toughness.* International Journal of Fracture, 1994. **68**(3): p. 219-244.
62. Wood, M.D.K., Sun, X., Tong, L., Katzos, A., Rispler, A.R., and Mai, Y.-W., *The effect of stitch distribution on Mode I delamination toughness of stitched laminated composites – experimental results and FEA simulation.* Composites Science and Technology, 2007. **67**(6): p. 1058-1072.
63. Pingkarawat, K., Wang, C.H., Varley, R.J., and Mouritz, A.P., *Effect of mendable polymer stitch density on the toughening and healing of delamination cracks in carbon–epoxy laminates.* Composites Part A: Applied Science and Manufacturing, 2013. **50**: p. 22-30.
64. Stegschuster, G., Pingkarawat, K., Wendland, B., and Mouritz, A.P., *Experimental determination of the mode I delamination fracture and fatigue properties of thin 3D woven composites.* Composites Part A: Applied Science and Manufacturing, 2016. **84**: p. 308-315.
65. Ladani, R.B., Pingkarawat, K., Nguyen, A.T.T., Wang, C.H., and Mouritz, A.P., *Delamination toughening and healing performance of woven composites with hybrid z-fibre reinforcement.* Composites Part A: Applied Science and Manufacturing, 2018. **110**: p. 258-267.

66. Ladani, R.B., Nguyen, A.T.T., Wang, C.H., and Mouritz, A.P., *Mode II interlaminar delamination resistance and healing performance of 3D composites with hybrid z-fibre reinforcement.* Composites Part A: Applied Science and Manufacturing, 2019. **120**: p. 21-32.
67. Wilkinson, M.P. and Ruggles-Wrenn, M.B., *Fatigue of a 3D orthogonal non-crimp woven polymer matrix composite at elevated temperature.* Applied Composite Materials, 2017. **24**(6): p. 1405-1424.
68. Carvelli, V., Gramellini, G., Lomov, S.V., Bogdanovich, A.E., Mungalov, D.D., and Verpoest, I., *Fatigue behavior of non-crimp 3D orthogonal weave and multi-layer plain weave E-glass reinforced composites.* Composites Science and Technology, 2010. **70**(14): p. 2068-2076.
69. Judawisastra, H., Ivens, J., and Verpoest, I., *The fatigue behaviour and damage development of 3D woven sandwich composites.* Composite Structures, 1998. **43**(1): p. 35-45.
70. Ladani, R.B., Wang, C.H., and Mouritz, A.P., *Delamination fatigue resistant three-dimensional textile self-healing composites.* Composites Part A: Applied Science and Manufacturing, 2019. **127**: p. 105626.
71. Mouritz, A.P., Pingkarawat, K., Pegorin, F., Stegschuster, G., and Wendland, B., *Improving the delamination fatigue properties of textile composites using through-thickness reinforcement*, in *TEXCOMP-12 Conference,* . 2015: Raleigh, NC, USA. p. 1-8.
72. Brandt, J., Drechsler, K., and Arendts, F.J., *Mechanical performance of composites based on various three-dimensional woven-fibre preforms.* Composites Science and Technology, 1996. **56**(3): p. 381-386.
73. Ko, F.K. and Hartman, D. *Impact behavior of 2-D and 3-D glass/epoxy composites*. in *Materials Science for the Future: 31 st International SAMPE Symposium and Exhibition*. 1986.
74. Brandt, J., Drechsler, K., Mohamed, M., and Gu, P. *Manufacture and performance of carbon/epoxy 3-D woven composites*. in *International SAMPE Symposium and Exhibition*. 1992.
75. Adanur, S., Tsao, Y.P., and Tam, C.W., *Improving fracture resistance of laminar textile composites by third direction reinforcement.* Composites Engineering, 1995. **5**(9): p. 1149-1158.
76. Baucom, J.N. and Zikry, M.A., *Evolution of failure mechanisms in 2D and 3D woven composite systems under quasi-static perforation.* Journal of Composite Materials, 2003. **37**(18): p. 1651-1674.
77. Baucom, J.N. and Zikry, M.A., *Low-velocity impact damage progression in woven E-glass composite systems.* Composites Part A: Applied Science and Manufacturing, 2005. **36**(5): p. 658-664.
78. Luo, Y., Lv, L., Sun, B., Qiu, Y., and Gu, B., *Transverse impact behavior and energy absorption of three-dimensional orthogonal hybrid woven composites.* Composite Structures, 2007. **81**(2): p. 202-209.
79. Lv, L., Sun, B., Qiu, Y., and Gu, B., *Energy absorptions and failure modes of 3D orthogonal hybrid woven composite struck by flat-ended rod.* 2006. **27**(4): p. 410-416.
80. Walter, T.R., Subhash, G., Sankar, B.V., and Yen, C.F., *Damage modes in 3D glass fiber epoxy woven composites under high rate of impact loading.* Composites Part B: Engineering, 2009. **40**(6): p. 584-589.

81. King, R.S., Stewart, G., McIlhagger, A.T., and Quinn, J.P., *The influence of through-the-thickness binder yarn count on fibre volume fraction, crimp and damage tolerance within 3D woven carbon fibre composites.* Polymers and Polymers Composites, 2009. **17**(5): p. 303-312.
82. Gerlach, R., Siviour, C.R., Wiegand, J., and Petrinic, N., *In-plane and through-thickness properties, failure modes, damage and delamination in 3D woven carbon fibre composites subjected to impact loading.* Composites Science and Technology, 2012. **72**(3): p. 397-411.
83. Chen, F. and Hodgkinson, J.M., *Impact behaviour of composites with different fibre architecture.* Proceedings of the Institution of Mechanical Engineers, Part G: Journal of Aerospace Engineering, 2009. **223**(7): p. 1009-1017.
84. Potluri, P., Hogg, P., Arshad, M., Jetavat, D., and Jamshidi, P., *Influence of fibre architecture on impact damage tolerance in 3D woven composites.* Applied Composite Materials, 2012. **19**(5): p. 799-812.
85. Behera, B. and Dash, B., *Mechanical behavior of 3D woven composites.* Materials and Design, 2015. **67**: p. 261-271.
86. Ding, Y., Wenger, W., and McIlhagger, R., *Structural characterization and mechanical properties of 3-D woven composites.* Broadening horizons with advanced materials and processes, 1993: p. 1-9.
87. Saleh, M.N., Yudhanto, A., Potluri, P., Lubineau, G., and Soutis, C., *Characterising the loading direction sensitivity of 3D woven composites: Effect of z-binder architecture.* Composites Part A: Applied Science and Manufacturing, 2016. **90**: p. 577-588.
88. Yousaf, Z., Potluri, P., and Withers, P.J., *Influence of tow architecture on compaction and nesting in textile preforms.* Applied Composite Materials, 2017. **24**(2): p. 337-350.
89. Umer, R., Alhussein, H., Zhou, J., and Cantwell, W., *The mechanical properties of 3D woven composites.* 2017. **51**(12): p. 1703-1716.
90. Sun, F., Sun, Y., Zhang, Q., Zhang, D., and Chen, L., *Experimental investigation on bending behavior of 3D non-crimp orthogonal composite.* 2014. **33**(20): p. 1869-1878.
91. Shigang, A., Rujie, H., and Yongmao, P., *A numerical study on the thermal conductivity of 3D woven C/C composites at high temperature.* Applied Composite Materials, 2015. **22**(6): p. 823-835.
92. Schuster, J., Heider, D., Sharp, K., and Glowania, M., *Thermal conductivities of three-dimensionally woven fabric composites.* Composites Science and Technology, 2008. **68**(9): p. 2085-2091.
93. Gowayed, Y. and Hwang, J.-C., *Thermal conductivity of composite materials made from plain weaves and 3-D weaves.* Composites Engineering, 1995. **5**(9): p. 1177-1186.
94. Sharp, K., Bogdanovich, A.E., Tang, W., Heider, D., Advani, S., and Glowiana, M., *High through-thickness thermal conductivity composites based on three-dimensional woven fiber architectures.* American Institute of Aeronautics and Astronautics, 2008. **46**(11): p. 2944-2954.
95. Tanzawa, Y., Watanabe, N., and Ishikawa, T., *Interlaminar fracture toughness of 3-D orthogonal interlocked fabric composites.* Composites Science and Technology, 1999. **59**(8): p. 1261-1270.
96. Tamuzs, V., Tarasovs, S., and Vilks, U., *Delamination properties of translaminar-reinforced composites.* Composites Science and Technology, 2003. **63**(10): p. 1423-1431.

97. Seltzer, R., González, C., Muñoz, R., Llorca, J., and Blanco-Varela, T., *X-ray microtomography analysis of the damage micromechanisms in 3D woven composites under low-velocity impact.* Composites Part A: Applied Science and Manufacturing, 2013. **45**: p. 49-60.
98. Kerber, A., Gargano, A., Pingkarawat, K., and Mouritz, A.P., *Explosive blast damage resistance of three-dimensional textile composites.* Composites Part A: Applied Science and Manufacturing, 2017. **100**: p. 170-182.
99. Treiber, J., Cartié, D., and Partridge, I. *Determination of crack bridging laws in tufted composites*. in *ICCM International Conferences on Composite Materials*. 2009.
100. Ladani, R.B., Ravindran, A.R., Wu, S., Pingkarawat, K., Kinloch, A.J., Mouritz, A.P., Ritchie, R.O., and Wang, C.H., *Multi-scale toughening of fibre composites using carbon nanofibres and z-pins.* Composites Science and Technology, 2016. **131**: p. 98-109.
101. Morales, A., *Structural stitching of textile preforms.* Advanced Materials, 1990: p. 1217-1230.
102. Srivastava, V.K., Gries, T., Veit, D., Quadflieg, T., Mohr, B., and Kolloch, M., *Effect of nanomaterial on mode I and mode II interlaminar fracture toughness of woven carbon fabric reinforced polymer composites.* Engineering Fracture Mechanics, 2017. **180**: p. 73-86.
103. Ravindran, A.R., Ladani, R.B., Zavabeti, A., Daeneke, T., Wu, S., Kinloch, A.J., Wang, C.H., Kalantar-Zadeh, K., and Mouritz, A.P., *Liquid metal synthesis of two-dimensional aluminium oxide platelets to reinforce epoxy composites.* Composites Science and Technology, 2019. **181**: p. 107708.
104. Hsieh, T.H., Kinloch, A.J., Masania, K., Sohn Lee, J., Taylor, A.C., and Sprenger, S., *The toughness of epoxy polymers and fibre composites modified with rubber microparticles and silica nanoparticles.* Journal of Materials Science, 2010. **45**(5): p. 1193-1210.
105. Zeng, Y., Liu, H.-Y., Mai, Y.-W., and Du, X.-S., *Improving interlaminar fracture toughness of carbon fibre/epoxy laminates by incorporation of nano-particles.* Composites Part B: Engineering, 2012. **43**(1): p. 90-94.
106. Kuwata, M. and Hogg, P.J., *Interlaminar toughness of interleaved CFRP using non-woven veils: Part 1. Mode-I testing.* Composites Part A: Applied Science and Manufacturing, 2011. **42**(10): p. 1551-1559.
107. Lee, S.-H., Kim, H., Hang, S., and Cheong, S.-K., *Interlaminar fracture toughness of composite laminates with CNT-enhanced nonwoven carbon tissue interleave.* Composites Science and Technology, 2012. **73**: p. 1-8.
108. Beckermann, G.W. and Pickering, K.L., *Mode I and Mode II interlaminar fracture toughness of composite laminates interleaved with electrospun nanofibre veils.* Composites Part A: Applied Science and Manufacturing, 2015. **72**: p. 11-21.
109. Park, B.Y. and Kim, S.C., *A study of the interlaminar fracture toughness of a carbon-fiber/epoxy composite containing surface-modified short kevlar fibers.* Composites Science and Technology, 1998. **58**(10): p. 1599-1606.
110. Wang, W.X., Takao, Y., Matsubara, T., and Kim, H.S., *Improvement of the interlaminar fracture toughness of composite laminates by whisker reinforced interlamination.* Composites Science and Technology, 2002. **62**(6): p. 767-774.
111. Mouritz, A.P. and Jain, L.K., *Further validation of the Jain and Mai models for interlaminar fracture of stitched composites.* Composites Science and Technology, 1999. **59**(11): p. 1653-1662.

112. Cartié, D.D.R., Troulis, M., and Partridge, I.K., *Delamination of Z-pinned carbon fibre reinforced laminates.* Composites Science and Technology, 2006. **66**(6): p. 855-861.
113. Pingkarawat, K. and Mouritz, A.P., *Comparative study of metal and composite z-pins for delamination fracture and fatigue strengthening of composites.* Engineering Fracture Mechanics, 2016. **154**: p. 180-190.
114. Pegorin, F., Pingkarawat, K., Daynes, S., and Mouritz, A.P., *Influence of z-pin length on the delamination fracture toughness and fatigue resistance of pinned composites.* Composites Part B: Engineering, 2015. **78**: p. 298-307.
115. McCarthy, R.F.J., Haines, G.H., and Newley, R.A., *Polymer composite applications to aerospace equipment.* Composites Manufacturing, 1994. **5**(2): p. 83-93.
116. Joshi, S.P. and Sun, C.T., *Impact induced fracture in a laminated composite.* Composite Materials, 1985. **19**(1): p. 51-66.
117. Yang, T., Wang, C.H., Zhang, J., He, S., and Mouritz, A.P., *Toughening and self-healing of epoxy matrix laminates using mendable polymer stitching.* Composites Science and Technology, 2012. **72**(12): p. 1396-1401.
118. Su, K.B., *Delamination resistance of stitched thermoplastic matrix composite Laminates*, in *Advances in thermoplastic matrix composite materials*, Newaz, G.M., Editor. 1989, ASTM International: West Conshohocken, PA. p. 279-300.
119. Pingkarawat, K., Wang, C.H., Varley, R.J., and Mouritz, A.P., *Healing of fatigue delamination cracks in carbon–epoxy composite using mendable polymer stitching.* Journal of Intelligent Material Systems and Structures, 2014. **25**(1): p. 75-86.
120. Hojo, M., Nakashima, K., Kusaka, T., Tanaka, M., Adachi, T., Fukuoka, T., and Ishibashi, M., *Mode I fatigue delamination of Zanchor-reinforced CF/epoxy laminates.* International Journal of Fatigue, 2010. **32**(1): p. 37-45.
121. Aymerich, F., Priolo, P., and Sun, C.T., *Static and fatigue behaviour of stitched graphite/epoxy composite laminates.* Composites Science and Technology, 2003. **63**(6): p. 907-917.
122. Khan, M.Z.S. and Mouritz, A.P., *Fatigue behaviour of stitched GRP laminates.* Composites Science and Technology, 1996. **56**(6): p. 695-701.
123. Aymerich, F., Onnis, R., and Priolo, P., *Analysis of the fracture behaviour of a stitched single-lap joint.* Composites Part A: Applied Science and Manufacturing, 2005. **36**(5): p. 603-614.
124. Aymerich, F., *Effect of Stitching on the Static and Fatigue Performance of Co-Cured Composite Single-Lap Joints.* Composite Materials, 2004. **38**(3): p. 243-257.
125. Cartié, D.D.R., Laffaille, J.-M., Partridge, I.K., and Brunner, A.J., *Fatigue delamination behaviour of unidirectional carbon fibre/epoxy laminates reinforced by Z-Fiber® pinning.* Engineering Fracture Mechanics, 2009. **76**(18): p. 2834-2845.
126. Riccio, A., *2 - Delamination in the context of composite structural design*, in *Delamination Behaviour of Composites*, Sridharan, S., Editor. 2008, Woodhead Publishing. p. 28-64.
127. Yao, L., Sun, Y., Guo, L., Alderliesten, R.C., Benedictus, R., Zhao, M., and Jia, L., *Fibre bridging effect on the Paris relation of mode I fatigue delamination in composite laminates with different thicknesses.* International Journal of Fatigue, 2017. **103**: p. 196-206.
128. Pegorin, F., Pingkarawat, K., and Mouritz, A.P., *Comparative study of the mode I and mode II delamination fatigue properties of z-pinned aircraft composites.* Materials & Design 2015. **65**: p. 139-146.

129. Zhang, A.Y., Liu, H.-Y., Mouritz, A.P., and Mai, Y.-W., *Experimental study and computer simulation on degradation of z-pin reinforcement under cyclic fatigue.* Composites Part A: Applied Science and Manufacturing, 2008. **39**(2): p. 406-414.
130. Donough, M.J., Gunnion, A.J., Orifici, A.C., and Wang, C.H., *Scaling parameter for fatigue delamination growth in composites under varying load ratios.* Composites Science and Technology, 2015. **120**: p. 39-48.
131. Ladani, R.B., Wu, S., Kinloch, A.J., Ghorbani, K., Mouritz, A.P., and Wang, C.H., *Enhancing fatigue resistance and damage characterisation in adhesively-bonded composite joints by carbon nanofibres.* Composites Science and Technology, 2017. **149**: p. 116-126.
132. Pegorin, F., Pingkarawat, K., Daynes, S., and Mouritz, A.P., *Mode II interlaminar fatigue properties of z-pinned carbon fibre reinforced epoxy composites.* Composites Part A: Applied Science and Manufacturing, 2014. **67**: p. 8-15.
133. Pegorin, F., Pingkarawat, K., Daynes, S., and Mouritz, A. *Delamination fatigue properties of z-pinned carbon-epoxylLaminate using metal or composite rods*. in *20th International Conference on Composite Materials (ICCM20)*. 2015.
134. Kuilla, T., Bhadra, S., Yao, D., Kim, N.H., Bose, S., and Lee, J.H., *Recent advances in graphene based polymer composites.* Progress in Polymer Science, 2010. **35**(11): p. 1350-1375.
135. Spitalsky, Z., Tasis, D., Papagelis, K., and Galiotis, C., *Carbon nanotube–polymer composites: chemistry, processing, mechanical and electrical properties.* Progress in Polymer Science, 2010. **35**(3): p. 357-401.
136. Sengupta, R., Bhattacharya, M., Bandyopadhyay, S., and Bhowmick, A.K., *A review on the mechanical and electrical properties of graphite and modified graphite reinforced polymer composites.* Progress in Polymer Science, 2011. **36**(5): p. 638-670.
137. Hannemann, B., Backe, S., Schmeer, S., Balle, F., Breuer, U.P., and Schuster, J., *Hybridisation of CFRP by the use of continuous metal fibres (MCFRP) for damage tolerant and electrically conductive lightweight structures.* Composite Structures, 2017. **172**: p. 374-382.
138. Taipalus, R., Harmia, T., Zhang, M.Q., and Friedrich, K., *The electrical conductivity of carbon-fibre-reinforced polypropylene/polyaniline complex-blends: experimental characterisation and modelling.* Composites Science and Technology, 2001. **61**(6): p. 801-814.
139. Markov, A., Fiedler, B., and Schulte, K., *Electrical conductivity of carbon black/fibres filled glass-fibre-reinforced thermoplastic composites.* Composites Part A: Applied Science and Manufacturing, 2006. **37**(9): p. 1390-1395.
140. Mohd Radzuan, N.A., Yusuf Zakaria, M., Sulong, A.B., and Sahari, J., *The effect of milled carbon fibre filler on electrical conductivity in highly conductive polymer composites.* Composites Part B: Engineering, 2017. **110**: p. 153-160.
141. Pozegic, T.R., Hamerton, I., Anguita, J.V., Tang, W., Ballocchi, P., Jenkins, P., and Silva, S.R.P., *Low temperature growth of carbon nanotubes on carbon fibre to create a highly networked fuzzy fibre reinforced composite with superior electrical conductivity.* Carbon, 2014. **74**: p. 319-328.
142. Zhang, D., Ye, L., Deng, S., Zhang, J., Tang, Y., and Chen, Y., *CF/EP composite laminates with carbon black and copper chloride for improved electrical conductivity and interlaminar fracture toughness.* Composites Science and Technology, 2012. **72**(3): p. 412-420.

143. Pegorin, F., Pingkarawat, K., and Mouritz, A.P., *Controlling the electrical conductivity of fibre-polymer composites using z-pins.* Composites Science and Technology, 2017. **150**: p. 167-173.
144. Grigoriou, K., Ladani, R.B., and Mouritz, A.P., *Electrical properties of multifunctional Z-pinned sandwich composites.* Composites Science and Technology, 2019. **170**: p. 60-69.
145. Chung, D., *Damage detection using self-sensing concepts.* Proceedings of the Institution of Mechanical Engineers, Part G: Journal of Aerospace Engineering, 2007. **221**(4): p. 509-520.
146. Zantout, A.E. and Zhupanska, O.I., *On the electrical resistance of carbon fiber polymer matrix composites.* Composites Part A: Applied Science and Manufacturing, 2010. **41**(11): p. 1719-1727.
147. Abry, J.C., Bochard, S., Chateauminois, A., Salvia, M., and Giraud, G., *In situ detection of damage in CFRP laminates by electrical resistance measurements.* Composites Science and Technology, 1999. **59**(6): p. 925-935.
148. Prabhakaran, R., *Damage assessment through electrical resistance in graphene fibre-reinforced composites.* Experimental Techniques, 1990. **14**(1): p. 16-20.
149. Schulte, K. and Baron, C., *Load and failure analyses of CFRP laminates by means of electrical resistivity measurements.* Composites Science and Technology, 1989. **36**(1): p. 63-76.
150. Vavouliotis, A., Paipetis, A., and Kostopoulos, V., *On the fatigue life prediction of CFRP laminates using the Electrical Resistance Change method.* Composites Science and Technology, 2011. **71**(5): p. 630-642.
151. Wang, X. and Chung, D.D.L., *Real-time monitoring of fatigue damage and dynamic strain in carbon fiber polymer-matrix composite by electrical resistance measurement.* Smart Materials and Structures, 1997. **6**(4): p. 504-508.
152. Wen, J., Xia, Z., and Choy, F., *Damage detection of carbon fiber reinforced polymer composites via electrical resistance measurement.* Composites Part B: Engineering, 2011. **42**(1): p. 77-86.
153. Grammatikos, S.A. and Paipetis, A.S., *On the electrical properties of multi scale reinforced composites for damage accumulation monitoring.* Composites Part B: Engineering, 2012. **43**(6): p. 2687-2696.
154. Li, C., Thostenson, E.T., and Chou, T.-W., *Sensors and actuators based on carbon nanotubes and their composites: A review.* Composites Science and Technology, 2008. **68**(6): p. 1227-1249.
155. Böger, L., Wichmann, M.H.G., Meyer, L.O., and Schulte, K., *Load and health monitoring in glass fibre reinforced composites with an electrically conductive nanocomposite epoxy matrix.* Composites Science and Technology, 2008. **68**(7): p. 1886-1894.
156. Gao, L., Thostenson, E.T., Zhang, Z., and Chou, T.-W., *Sensing of damage mechanisms in fiber-reinforced composites under cyclic loading using carbon nanotubes.* Advanced Functional Materials, 2009. **19**(1): p. 123-130.
157. Ladani, R.B., Wu, S., Kinloch, A.J., Ghorbani, K., Zhang, J., Mouritz, A.P., and Wang, C.H., *Improving the toughness and electrical conductivity of epoxy nanocomposites by using aligned carbon nanofibres.* Composites Science and Technology, 2015. **117**: p. 146-158.
158. Zhang, B., Allegri, G., and Hallett, S.R., *An experimental investigation into multi-functional Z-pinned composite laminates.* Materials & Design, 2016. **108**: p. 679-688.

159. Pegorin, F., Pingkarawat, K., and Mouritz, A.P., *Electrical-based delamination crack monitoring in composites using z-pins.* Composites Part A: Applied Science and Manufacturing, 2018. **104**: p. 120-128.
160. Wu, S., Ladani, R.B., Ravindran, A.R., Zhang, J., Mouritz, A.P., Kinloch, A.J., and Wang, C.H., *Aligning carbon nanofibres in glass-fibre/epoxy composites to improve interlaminar toughness and crack-detection capability.* Composites Science and Technology, 2017. **152**: p. 46-56.
161. Hufenbach, W., Gude, M., Ebert, C., Zscheyge, M., and Hornig, A., *Strain rate dependent low velocity impact response of layerwise 3D-reinforced composite structures.* International Journal of Impact Engineering, 2011. **38**(5): p. 358-368.
162. Bandaru, A.K., Chavan, V.V., Ahmad, S., Alagirusamy, R., and Bhatnagar, N., *Low velocity impact response of 2D and 3D Kevlar/polypropylene composites.* International Journal of Impact Engineering, 2016. **93**: p. 136-143.
163. Herb, V., Martin, E., and Couégnat, G., *Damage analysis of thin 3D-woven SiC/SiC composite under low velocity impact loading.* Composites Part A: Applied Science and Manufacturing, 2012. **43**(2): p. 247-253.
164. Chou, S., Chen, H.-C., and Chen, H.-E., *Effect of weave structure on mechanical fracture behavior of three-dimensional carbon fiber fabric reinforced epoxy resin composites.* Composites Science and Technology, 1992. **45**(1): p. 23-35.
165. Tan, P., Tong, L., Steven, G.P., and Ishikawa, T., *Behavior of 3D orthogonal woven CFRP composites. Part I. Experimental investigation.* Composites Part A: Applied Science and Manufacturing, 2000. **31**(3): p. 259-271.
166. Ghosh, R. and De, S., *Z-fiber influence on high speed penetration of 3D orthogonal woven fiber composites.* Mechanics of Materials, 2014. **68**: p. 147-163.
167. Zhang, D., Sun, Y., Chen, L., and Pan, N., *A comparative study on low-velocity impact response of fabric composite laminates.* Materials & Design, 2013. **50**: p. 750-756.
168. Asaee, Z., Shadlou, S., and Taheri, F., *Low-velocity impact response of fiberglass/magnesium FMLs with a new 3D fiberglass fabric.* Composite Structures, 2015. **122**: p. 155-165.
169. Wang, X., Hu, B., Feng, Y., Liang, F., Mo, J., Xiong, J., and Qiu, Y., *Low velocity impact properties of 3D woven basalt/aramid hybrid composites.* Composites Science and Technology, 2008. **68**(2): p. 444-450.
170. Vaidya, A.S., Vaidya, U.K., and Uddin, N., *Impact response of three-dimensional multifunctional sandwich composite.* Materials Science and Engineering: A, 2008. **472**(1): p. 52-58.
171. Kazemianfar, B., Esmaeeli, M., and Nami, M.R., *Response of 3D woven composites under low velocity impact with different impactor geometries.* Aerospace Science and Technology, 2020. **102**: p. 105849.
172. Naik, R. and Logan, C., *Damage resistant materials for aero-engine applications*, in *40th Structures, Structural Dynamics, and Materials Conference and Exhibit*. 1999. p. 1451-1475.
173. Chiu, C.H., Lai, M.H., and Wu, C.M., *Compression failure mechanisms of 3-D angle interlock woven composites subjected to low-energy impact.* 2004. **12**(4): p. 309-320.
174. Jones, E., *Documentation for Matlab-based DIC code, Version 4.* University of Illinois, Champaign County, Illinois, , 2015.
175. Evci, C. and Gülgeç, M., *An experimental investigation on the impact response of composite materials.* International Journal of Impact Engineering, 2012. **43**: p. 40-51.

176. Hu, X., Ying, Z., Cheng, X., and Wu, Z., *Effect of Z-binder tension and internal micro-structure on damage behavior of 3D orthogonal woven composite.* Journal of Industrial Textiles, 2019. **49**(5): p. 551-571.
177. Wu, C., Gu, Y., Luo, L., Xu, P., Wang, S., Li, M., and Zhang, Z., *Influences of in-plane and out-of-plane fiber waviness on mechanical properties of carbon fiber composite laminate.* Journal of Reinforced Plastics and Composites, 2018. **37**(13): p. 877-891.
178. Greenhalgh, E.S., *6 - The influence of fibre architecture in the failure of polymer composites*, in *Failure Analysis and Fractography of Polymer Composites*, Greenhalgh, E.S., Editor. 2009, Woodhead Publishing. p. 279-355.
179. Wang, C.H. and Duong, C.N., *Bonded and repairs of composite airframe structures*. 2015: Elsevier.
180. Faulkner, S.D., Kwon, Y.W., Bartlett, S., and Rasmussen, E.A., *Study of composite joint strength with carbon nanotube reinforcement.* Journal of Materials Science, 2009. **44**(11): p. 2858-2864.
181. Burkholder, G.L., Kwon, Y.W., and Pollak, R.D., *Effect of carbon nanotube reinforcement on fracture strength of composite adhesive joints.* Journal of Materials Science, 2011. **46**(10): p. 3370-3377.
182. Takeda, T. and Narita, F., *Fracture behavior and crack sensing capability of bonded carbon fiber composite joints with carbon nanotube-based polymer adhesive layer under Mode I loading.* Composites Science and Technology, 2017. **146**: p. 26-33.
183. Ravindran, A.R., *Multi-scale interlaminar toughening of fibre polymer composites*. 2019, RMIT University.
184. Deng, S., Djukic, L., Paton, R., and Ye, L., *Thermoplastic–epoxy interactions and their potential applications in joining composite structures – A review.* Composites Part A: Applied Science and Manufacturing, 2015. **68**: p. 121-132.
185. Verma, K.K., Sandeep, D., Sugun, B., Athimoolaganesh, S., Gaddikeri, K.M., and Sundaram, R. *Novel design of cocured composite 'T'Joints with integrally woven 3D inserts*. in *5th World Conference on 3D Fabrics and Their Applications*. 2013.
186. Burns, L.A., Mouritz, A.P., Pook, D., and Feih, S., *Bio-inspired design of aerospace composite joints for improved damage tolerance.* Composite Structures, 2012. **94**(3): p. 995-1004.
187. Burns, L., Mouritz, A.P., Pook, D., and Feih, S., *Strengthening of composite T-joints using novel ply design approaches.* Composites Part B: Engineering, 2016. **88**: p. 73-84.
188. Shenoi, R.A. and Hawkins, G.L., *Influence of material and geometry variations on the behaviour of bonded tee connections in FRP ships.* Composites, 1992. **23**(5): p. 335-345.
189. Cartié, D.D.R., Dell'Anno, G., Poulin, E., and Partridge, I.K., *3D reinforcement of stiffener-to-skin T-joints by Z-pinning and tufting.* Engineering Fracture Mechanics, 2006. **73**(16): p. 2532-2540.
190. Vazquez, J.T., Castanié, B., Barrau, J.-J., and Swiergiel, N., *Multi-level analysis of low-cost Z-pinned composite joints: Part 2: Joint behaviour.* Composites Part A: Applied Science and Manufacturing, 2011. **42**(12): p. 2082-2092.
191. Koh, T.M., Feih, S., and Mouritz, A.P., *Experimental determination of the structural properties and strengthening mechanisms of z-pinned composite T-joints.* Composite Structures, 2011. **93**(9): p. 2222-2230.

192. Koh, T.M., Feih, S., and Mouritz, A.P., *Strengthening mechanics of thin and thick composite T-joints reinforced with z-pins.* Composites Part A: Applied Science and Manufacturing, 2012. **43**(8): p. 1308-1317.
193. Bianchi, F., Koh, T.M., Zhang, X., Partridge, I.K., and Mouritz, A.P., *Finite element modelling of z-pinned composite T-joints.* Composites Science and Technology, 2012. **73**: p. 48-56.
194. Park, Y.-B., Lee, B.-H., Kweon, J.-H., Choi, J.-H., and Choi, I.-H., *The strength of composite bonded T-joints transversely reinforced by carbon pins.* Composite Structures, 2012. **94**(2): p. 625-634.
195. Huan, D., Li, Y., Tan, Y., Zhang, X., and Xiao, J., *On the assessment of the load-bearing capacity of Z-pinned composite T-joint under out-of-plane tension.* Journal of Reinforced Plastics and Composites, 2017. **36**(22): p. 1639-1650.
196. Li, M., Chen, P., Li, X., and Gong, N., *Experimental and numerical study on the tensile properties of T-joints with low Z-pin volume density.* Polymer Composites, 2020. **41**(1): p. 258-270.
197. Kim, C.H., Jo, D.H., and Choi, J.H., *Failure strength of composite T-joints prepared using a new 1-thread stitching process.* Composite Structures, 2017. **178**: p. 225-231.
198. Stickler, P.B. and Ramulu, M., *Damage progression analyses of transverse stitched T-joints under flexure and tensile loading.* Advanced Composite Materials, 2006. **15**(2): p. 243-261.
199. Wood, M.D.K., Tong, L., Luo, Q., Sun, X., Katzos, A., and Rispler, A.R., *Failure of stitched composite L-Joints under tensile loading — Experiment and simulation.* 2009. **28**(6): p. 715-742.
200. Yang, T., Zhang, J., Mouritz, A.P., and Wang, C.H., *Healing of carbon fibre–epoxy composite T-joints using mendable polymer fibre stitching.* Composites Part B: Engineering, 2013. **45**(1): p. 1499-1507.
201. Bigaud, J., Aboura, Z., Martins, A.T., and Verger, S., *Analysis of the mechanical behavior of composite T-joints reinforced by one side stitching.* Composite Structures, 2018. **184**: p. 249-255.
202. Stickler, P.B. and Ramulu, M., *Investigation of mechanical behavior of transverse stitched T-joints with PR520 resin in flexure and tension.* Composite Structures, 2001. **52**(3): p. 307-314.
203. Yang, Q.D., Rugg, K.L., Cox, B.N., and Shaw, M.C., *Failure in the junction region of T-stiffeners: 3D-braided vs. 2D tape laminate stiffeners.* International Journal of Solids and Structures, 2003. **40**(7): p. 1653-1668.
204. Gilchrist, M.D., Kinloch, A.J., Matthews, F.L., and Osiyemi, S.O., *Mechanical performance of carbon-fibre- and glass-fibre-reinforced epoxy I-beams: I. Mechanical behaviour.* Composites Science and Technology, 1996. **56**(1): p. 37-53.
205. Schmidt, R.P. and Kalser, D.A., *Woven preform for structural joints, US Patent US6874543B2*. 2002.
206. Amirul Islam, M., *9 - 3D woven structures and methods of manufacture*, in *Woven Textiles*, Gandhi, K.L., Editor. 2012, Woodhead Publishing. p. 264-313.
207. Sugun, B. and Sandeep, D., *Development of single-layer 3D 'T' profile with fillet for composite 'T' joints.* Journal of Industrial Textiles, 2016. **46**(3): p. 887-900.
208. Yan, S., Zeng, X., Brown, L., and Long, A., *Geometric modeling of 3D woven preforms in composite T-joints.* 2018. **88**(16): p. 1862-1875.

209. Soden, J.A., Weissenbach, G., and Hill, B.J., *The design and fabrication of 3D multi-layer woven T-section reinforcements.* Composites Part A: Applied Science and Manufacturing, 1999. **30**(3): p. 213-220.
210. Wang, Y. and Soutis, C., *Fatigue behaviour of composite T-Joints in wind turbine blade applications.* Applied Composite Materials, 2017. **24**(2): p. 461-475.
211. Yan, S., Zeng, X., and Long, A., *Experimental assessment of the mechanical behaviour of 3D woven composite T-joints.* Composites Part B: Engineering, 2018. **154**: p. 108-113.
212. Yan, S., Zeng, X., and Long, A., *Meso-scale modelling of 3D woven composite T-joints with weave variations.* Composites Science and Technology, 2019. **171**: p. 171-179.
213. Yan, S., Zeng, X., and Long, A., *Effect of fibre architecture on tensile pull-off behaviour of 3D woven composite T-joints.* Composite Structures, 2020. **242**: p. 112194.
214. Ali, M., Kausar, F., Shahid, S., Zeeshan, M., Nawab, Y., Riaz, R., Memon, A.A., Mengal, N., and Anjum, A.S., *Novel derivatives of 3D woven T-shaped composites with improved performance.* The Journal of The Textile Institute, 2019. **110**(2): p. 267-273.
215. Clegg, H., Dell'Anno, G., Partridge, I.K.J.A.i.A., and Spacecraft Science, A.I.l.J., *Creating intersections in composite structures using Tufting and 3D woven connectors.* Advances in Aircraft and Spacecraft Science, 2019. **6**(2): p. 145-156.
216. Sharp, K., Bogdanovich, A., Boyle, R., Brown, J., and Mungalov, D., *Wind blade joints based on non-crimp 3D orthogonal woven Pi shaped preforms.* Composites Part A: Applied Science and Manufacturing, 2013. **49**: p. 9-17.
217. Abbasi, S., Ladani, R.B., Wang, C.H., and Mouritz, A.P., *Improving the delamination resistance of fibre reinforced polymer composites using 3D woven metal Z-Filaments.* Composites Science and Technology, 2020: p. 108301.
218. Zhang, B., Allegri, G., Yasaee, M., Hallett, S.R., and Partridge, I.K., *On the delamination self-sensing function of Z-pinned composite laminates.* Composites Science and Technology, 2016. **128**: p. 138-146.
219. Jain, L.K. and Mai, Y.-W., *On the effect of stitching on mode I delamination toughness of laminated composites.* Composites Science and Technology, 1994. **51**(3): p. 331-345.
220. Jain, L.K. and Mai, Y.-W., *Determination of mode II delamination toughness of stitched laminated composites.* Composites Science and Technology, 1995. **55**(3): p. 241-253.
221. Cox, B.N., Massabò, R., and Kedward, K.T., *Suppression of delaminations in curved structures by stitching.* Composites Part A: Applied Science and Manufacturing, 1996. **27**(12): p. 1133-1138.
222. Lomov, S.V., Ivanov, D.S., Truong, T.C., Verpoest, I., Baudry, F., Vanden Bosche, K., and Xie, H., *Experimental methodology of study of damage initiation and development in textile composites in uniaxial tensile test.* Composites Science and Technology, 2008. **68**(12): p. 2340-2349.
223. Stig, F. and Hallström, S., *Assessment of the mechanical properties of a new 3D woven fibre composite material.* Composites Science and Technology, 2009. **69**(11): p. 1686-1692.
224. Yu, B., Blanc, R., Soutis, C., and Withers, P.J., *Evolution of damage during the fatigue of 3D woven glass-fibre reinforced composites subjected to tension–tension loading observed by time-lapse X-ray tomography.* Composites Part A: Applied Science and Manufacturing, 2016. **82**: p. 279-290.

225. Saleh, M.N., Lubineau, G., Potluri, P., Withers, P.J., and Soutis, C., *Micro-mechanics based damage mechanics for 3D orthogonal woven composites: experiment and numerical modelling.* Composite Structures, 2016. **156**: p. 115-124.
226. Gnaba, I., Legrand, X., Wang, P., and Soulat, D., *Through-the-thickness reinforcement for composite structures: A review.* Journal of Industrial Textiles, 2019. **49**(1): p. 71-96.
227. Velmurugan, R. and Solaimurugan, S., *Improvements in Mode I interlaminar fracture toughness and in-plane mechanical properties of stitched glass/polyester composites.* Composites Science and Technology, 2007. **67**(1): p. 61-69.
228. Mouritz, A.P. and Cox, B.N., *A mechanistic interpretation of the comparative in-plane mechanical properties of 3D woven, stitched and pinned composites.* Composites Part A: Applied Science and Manufacturing, 2010. **41**(6): p. 709-728.
229. Reedy, E.D. and Guess, T.R., *Additional Comparisons of Interlocked Fabric and Laminated Fabric Kevlar 49/Epoxy Composites.* Journal of Composites, Technology and Research, 1986. **8**(4): p. 163-168.
230. ASTMD3039, *Standard test method for tensile properties of polymer matrix composite materials*. 2017, West Conshohocken, PA: ASTM International.
231. ASTMD7264, *Standard Test Method for flexural properties of polymer matrix composite material*. 2015, ASTM International: West Conshohocken, PA.
232. Bannister, M.K., Braemar, R., and Crothers, P.J., *The mechanical performance of 3D woven sandwich composites.* Composite Structures, 1999. **47**(1): p. 687-690.